Influence of a nanoantenna on the rates of organic molecules : single molecule study

Remigiusz Trojanowicz

université PARIS-SACLAY

Influence of a nanoantenna on the rates of organic molecules: single molecule study

Influence d'une nanoantenne sur les taux de molécules organiques : étude par molécules uniques

Thèse de doctorat de l'université Paris-Saclay

École doctorale n°572 : Ondes et Matière (EDOM)
Spécialité de doctorat : Physique
Graduate School : Physique. Référent : Faculté des sciences d'Orsay

Thèse préparée dans l'unité de recherche **SPEC** (Université Paris-Saclay, CEA, CNRS), sous la direction de **Fabrice CHARRA**, Directeur de Recherche CEA et le co-encadrement de **Simon VASSANT**, Chercheur CEA

Thèse soutenue à Paris-Saclay, le 12 Décembre 2023, par

Remigiusz TROJANOWICZ

Composition du Jury

Membres du jury avec voix délibérative

Elizabeth BOER-DUCHEMIN Professeure, Université Paris-Saclay	Présidente
Jérôme WENGER Directeur de recherche, Institut Fresnel, CNRS, Université Aix-Marseille	Rapporteur & Examinateur
Mathieu MIVELLE Chargé de recherche (HDR), Institut des NanoSciences de Paris	Rapporteur & Examinateur
Vahid SANDOGHDAR Directeur de recherche, Max Planck Institute for the Science of Light	Examinateur

THÈSE DE DOCTORAT

NNT : 2023UPASP200

université PARIS-SACLAY
ÉCOLE DOCTORALE
Ondes et matière (EDOM)

Titre : Influence d'une nanoantenne sur les taux de molécules organiques : études par molécules uniques

Mots clés : nanophotonique, Microscopie a sonde locale, nanoantenne, plasmonique, molecule unique

Abstract : Comprendre la photophysique des émetteurs quantiques piégés dans des matrices solides et contrôler leurs propriétés avec des nanoantennes revêt une grande importance dans le développement de dispositifs optoélectroniques et de technologies quantiques. Il existe de nombreuses publications sur les systèmes à molécule unique et à nanoantennes, mais les études se concentrent principalement sur la dynamique des états singules. Mais les molécules fluorescentes ont des états triplets sombres et à longue durée de vie, qui agissent (avec la durée de vie de la fluorescence) comme une limitation physique du flux maximum (appelé ''effet de goulot d'étranglement'') et rendent impropres leur utilisation comme source de photons a la demande. Il existe également des dispositifs électroluminescents organiques, basés sur des molécules qui présentent une relaxation triplet radiative (phosphorescence) ou subissent une fluorescence retardée activée thermiquement. Pour de tels dispositifs, le taux de peuplement et de dépeuplement de l'état triplet devraient être augmentés. Dans l'ensemble, il existe de nombreuses applications potentielles des nanoantennes, en fonction de leur effet sur la dynamique des états triplets.

Dans cette thèse, je réalise des expériences sur des molécules uniques de terrylène piégées dans un film de para-terphényle inférieur à 30 nm d'épaisseur. En utilisant la dépendance à la polarisation d'excitation et à l'intensité des processus photophysiques, je propose un modèle 3D qui décrit les taux auxquelles les transitions se produisent et l'orientation de l'émetteur. À l'aide de la microscopie à sonde à locale, je mène des expériences sur la même molécule avec et sans la présence de la nanoantenne. Cela permet des mesures quantitatives et une distinction entre les changements réversibles et les changements non réversibles. Enfin, je compare l'influence de la nanoantenne diélectrique (fibre de verre tire) et plasmonique (pyramide d'or nanofabriquée).

Une étude de population a montré des variations de molécule-à-molécule beaucoup plus faibles que d'autres rapports dans la littérature. Deux transitions optiques triplet-triplet discernables avec un croisement intersystème inversé subséquent (photo-induit) ont été identifiées. Les moments dipolaires de transition liés à l'absorption singulet, à la fluorescence et à l'une des deux absorptions triplet sont colinéaires. La section efficace d'absorption de l'état fondamental singulet est presque identique parmi les molécules. La section efficace de la transition triplet-triplet, qui n'est pas colinéaire avec le moment dipolaire d'émission, varie considérablement entre les molécules. Le spectre de fluorescence a montré des variations molécule à molécule des intensités relatives des bandes liées aux transitions vibroniques. Cela indique des changements dans les facteurs de Franck Condon, et donc la déformation géométrique de l'émetteur. Le type de déformation reste flou. La majorité des molécules mesurées ont connu une multiplication par 2 des excitations des états singulet et triplet et du taux d'émission en présence de la nanoantenne diélectrique. En conséquence, la pointe diélectrique a favorisé le dépeuplement du singulet excité de manière sélective par fluorescence, a réduit la population du triplet et a accéléré son dépeuplement de manière sélective vers le singulet excité. La nanoantenne plasmonique affecte la dynamique de la population de la même manière, mais avec facteurs differents. L'antenne en fibre de verre tirée maintient la pureté d'un émetteur de photons uniques, tandis que la pyramide d'or introduit une grande photoluminescence. Le système pyramide-molécule peut difficilement être considéré comme un émetteur de photons uniques.

Le comportement des émetteurs quantiques piégés dans une matrice solide constitue un problème majeur dans la conception de dispositifs basés sur des molécules uniques. Les résultats obtenus ici sont une preuve de concept selon laquelle des mesures optiques pourraient être utilisées pour résoudre ce problème, tandis que les nanoantennes montrent comment la fonctionnalité de tels dispositifs pourrait être davantage modifiée.

université PARIS-SACLAY
ÉCOLE DOCTORALE
Ondes et matière (EDOM)

Title : Influence of a nanoantenna on the rates of organic molecules : single molecule study

Keywords : nanophotonics, Scanning Probe Microscopy, nanoantenna, plasmonics, single molecule

Abstract : Understanding the photophysics of quantum emitters trapped in solid matrices and controlling their properties with nanoantennas is of great importance in the development of optoelectronic devices and quantum technology. There is plenty of literature on single molecule and nanoantenna systems, but mainly on the singlet state dynamics. Fluorescent molecules have dark and long-lived triplet states, which act (with fluorescence lifetime) as a physical limitation of the maximum flux (so-called ''bottle-neck effect''), thus rends them unsuitable for on-demand single photon source. There are also organic light emitting devices, based on molecules that have a radiative triplet relaxation or undergo thermally activated delayed fluorescence. For such devices, triplet population and depopulation should be increased. Overall, there are plenty of potential applications of nanoantennas, depending on the effect on the emitter triplet dynamics.

I carry out experiments on single terrylene molecules trapped in a sub-30 nm para-terphenyl film. Using the excitation polarization- and intensity-dependence of photophysical processes, I propose a 3D model that describes the rates of transitions and the orientation of the emitter. Using Scanning Probe Microscopy, I conduct experiments on the same molecule with and without the presence of the nanoantenna. This enables quantitative assesment and discrimination of the reversible changes from the non-reversible ones. Finally, I compare the influence of dielectric (pulled glass fiber) and plasmonic nanoantenna (nanofabricated gold pyramid).

The population study has shown smaller molecule-to-molecule variation than other reports on the same system. Two distinguishable triplet-triplet optical transitions with subsequent (photoinduced) reversed intersystem crossing are found. The transition dipole moments related to the singlet absorption, fluorescence and one of the two triplet absorptions are collinear. The cross-section of singlet ground state absorption is nearly identical among the molecules. The cross-section of the triplet-triplet transition, that is not colinear with the emission dipole moment, varies between the molecules significantly. The fluorescence spectrum has shown molecule-to-molecule variations in the relative intensities of the bands related to vibronic transitions. This indicates changes in Franck Condon Factors, and thus the geometrical deformation of the emitter. Type of deformation remains unclear.

Most of the measured molecules experienced a 2-fold enhancement of the singlet and triplet states excitations and the emission rate in the presence of the dielectric nanoantenna. In consequence, the dielectric tip has promoted excited singlet depopulation selectively through fluorescence, reduced the triplet population and accelerated its depopulation selectively back to the excited singlet. The plasmonic nanoantenna affects the population dynamics similarly, but with different magnitudes. The pulled glass fiber antenna maintains a single photon emitter purity, while the gold pyramid introduces large photoluminescence, and thus pyramid-molecule system can be hardly considered as a single photon emitter.

Behavior of quantum emitters trapped in solid matrix is a big issue in designing devices based on single molecules. The results obtained here are a proof-of-concept that optical measurements could be used to tackle this problem, while nanoantennas show how the functionality of such devices could be further modified.

Table of Contents

Preface

Studies of the interaction between light and matter date back to the 5th century BC [1]. The interaction between light and matter was difficult to explain back then because the nature of light itself wasn't clear until the 20th century. In 1690, Huygens proposed the wave theory of light, and in 1865, Maxwell published work on the theory of the electromagnetic field. In 1900, quantum theory of light began as Planck proposed that electromagnetic energy has to be emitted in quantized amounts. In 1905, wave-particle duality of light was introduced by Einstein, and in 1924, de Broglie suggested that the same applies to matter. Finally, in 1926, Schrödinger introduced wave mechanics, which can describe particles placed in the force field and, thus a full understanding of light-matter interaction. A complete picture of the light-matter interaction also requires the inclusion of the environment accommodating a particle interacting with light. In the 1940s, Purcell discovered how this interaction could be enhanced through a change in the so-called local density of states that can be understood through the Fermi golden rule introduced in a book published by Fermi in 1950 (but developed by Dirac in 1927) [2]. Altogether, with recent technology development that enables experiments at the nanoscale and single photon resolution, those findings give motivation to this thesis, which investigates light-matter interaction in the nanoenvironment. More precisely, how does the photophysics of a single molecule change when approached by a metallic or dielectric nanoobject, and can it be applied to create a more efficient light source?

Recently, the field of the single photon sources has been dominated by quantum dots, NV centers, and 2D materials. However, single-molecule-based devices are still promising materials in the development of quantum technologies such as nonlinear elements and transducers [3]. If we think of a single molecule as a light source, then what is usually desired is less power consumption and more radiated power – simply put, better efficiency. To tackle this issue, scientists have came up with optical nanoantennas. An optical antenna is an object that can ''*convert free-propagating optical radiation to localized energy, and vice versa*'' [4]. However, to choose an optimal nanoantenna for a given single molecule, one has to first create a complete description of this molecule's photophysics. For such a description, a single molecule is not just a light source – it is a quantum light source. Every time a photon emitted by a single molecule is detected, it

means that prior to the detection event, this quantum light source has undergone various types and a number of processes. Each of those processes is probabilistic and changes the quantum state of the emitter. The properties, timescales, and probabilities of those processes need to be well understood in order to predict what will be the effect of a plasmonic or dielectric nanoantenna on the temporal behavior of the photon flux coming from a single molecule. The dark triplet state is responsible for a ''bottle-neck effect'', which constitutes a physical limitation (together with fluorescence lifetime) to the maximum photon flux that a fluorophore can emit. Therefore, an ideal nanoantenna should prevent population of the dark triplet or accelerate the dark triplet depopulation, while also accelerating the excited singlet depopulation via fluorescence. Compared to the singlet dynamics, the triplet dynamics has been often neglected in nanoantenna-single molecule studies that can be found in the literature.

There are several methodological approaches to perform such studies. We have decided to use Scanning Probe Microscopy (SPM) as it provides exceptional control over the positioning of the nanoantenna with respect to the molecule. The very same single molecule can be then measured with and without the presence of nanoantenna to obtain quantitative data. As a single molecule, we have chosen terrylene in para-terphenyl because this system is well-known in the literature and has proven to be incredibly photostable even at room temperature. Special measures were adapted to verify the stability of the emitters and molecule-nanoantenna alignment, which is showcased throughout the manuscript.

In the first chapter of this manuscript, I introduce the fundamentals of photophysics, followed by a review of the studies on terrylene and specifically terrylene in para-terphenyl. Subsequently, I introduce the basic properties of a nanoantenna and describe what kind of mechanisms are behind its effect on a single molecule. Finally, I present the photon statistics in quantum light sources and discuss models used to describe the photon flux of a single molecule.

In the second chapter, I present the methods and technical/experimental details, which constitute an important ''know-how'' of nanoantenna-single molecule experiments.

In the third chapter, I focus solely on the photophysics of terrylene in a sub-30 nm para-terphenyl thin film. I present a large population study to verify the timescales of different processes and the molecule-to-molecule variations. I show results from ''Power Scan'' and ''Polarization Scan'' that are used to describe transition's timescales and their transition dipole moment orientation in space.

In the fourth chapter, I present the results of the experiments with dielectric (pulled glass fiber) and plasmonic (gold pyramid) nanoantennas. Once approached with a nanoantenna of each type, I analyze the changes in rates and translate them into intuitive quantities that describe temporal behavior of a single molecule light source such as the average time spent in the dark triplet state and the average time spent in the emissive state.

Résumé étendu en française

Les études sur l'interaction entre la lumière et la matière remontent au Ve siècle av. J.-C. [1]. L'explication de l'interaction entre la lumière et la matière était difficile à cette époque car la nature de la lumière elle-même n'était pas claire avant le XXe siècle. En 1690, Huygens proposa la théorie ondulatoire de la lumière, et en 1865, Maxwell publia des travaux sur la théorie du champ électromagnétique. En 1900, la théorie quantique de la lumière commença lorsque Planck proposa que l'énergie électromagnétique devait être émise en quantités quantifiées. En 1905, Einstein introduisit la dualité onde-particule de la lumière, et en 1924, de Broglie suggéra que cela s'appliquait également à la matière. Enfin, en 1926, Schrödinger introduisit la mécanique ondulatoire, qui peut décrire les particules placées dans le champ de force et ainsi permettre une compréhension complète de l'interaction lumière-matière. Une image complète de l'interaction lumière-matière nécessite également l'inclusion de l'environnement accueillant une particule interagissant avec la lumière. Dans les années 1940, Purcell découvrit comment cette interaction pouvait être améliorée par un changement dans la soi-disant densité locale des états, compréhensible grâce à la règle d'or de Fermi introduite dans un livre publié par Fermi en 1950 (mais développée par Dirac en 1927) [2]. Dans l'ensemble, avec le récent développement technologique permettant des expériences à l'échelle nanométrique et à une résolution de photon unique, ces découvertes motivent cette thèse qui explore l'interaction lumière-matière dans le nanoenvironnement. Plus précisément, comment la photophysique d'une molécule unique change-t-elle lorsqu'elle est approchée par un nanoobjet métallique ou diélectrique, et peut-elle être appliquée pour créer une source de lumière plus efficace ?

Récemment, le domaine des sources de photons uniques a été dominé par les points quantiques, les centres NV et les matériaux 2D. Cependant, les dispositifs basés sur une molécule unique demeurent des matériaux prometteurs dans le développement de technologies quantiques telles que les éléments non linéaires et les transducteurs [3]. Si l'on considère une molécule unique comme une source de lumière, ce qui est généralement souhaité est une consommation d'énergie réduite et une puissance rayonnée accrue - en d'autres termes, une meilleure efficacité. Pour résoudre cette question, les scientifiques ont développé des nanoantennes optiques. Une antenne

optique est un objet qui peut "convertir le rayonnement optique libre en énergie localisée, et vice versa" [4]. Cependant, pour choisir une nanoantenne optimale pour une molécule unique donnée, il faut d'abord créer une description complète de la photophysique de cette molécule. Pour une telle description, une molécule unique n'est pas simplement une source de lumière - c'est une source de lumière quantique. Chaque fois qu'un photon émis par une molécule unique est détecté, cela signifie qu'avant l'événement de détection, cette source de lumière quantique a subi divers types et un certain nombre de processus. Chacun de ces processus est probabiliste et modifie l'état quantique de l'émetteur. Les propriétés, les échelles de temps et les probabilités de ces processus doivent être bien compris pour prédire l'effet d'une nanoantenne plasmonique ou diélectrique sur le comportement temporel du flux de photons émis par une molécule unique. L'état sombre triplet est responsable d'un "effet d'étranglement", qui constitue une limitation physique (avec la durée de vie de la fluorescence) à la puissance maximale de photon qu'un fluorophore peut émettre. Par conséquent, une nanoantenne idéale devrait empêcher la population de l'état sombre triplet ou accélérer la dépopulation de l'état sombre triplet, tout en accélérant également la dépopulation du singulet excité par fluorescence. Comparée à la dynamique du singulet, la dynamique du triplet a souvent été négligée dans les études sur les nanoantennes et les molécules uniques que l'on trouve dans la littérature.

Il existe plusieurs approches méthodologiques pour mener de telles études. Nous avons décidé d'utiliser la microscopie à sonde locale, car elle offre un contrôle exceptionnel sur le positionnement de la nanoantenne par rapport à la molécule. La même molécule unique peut ensuite être mesurée avec et sans la présence de la nanoantenne pour obtenir des données quantitatives. En tant que molécule unique, nous avons choisi le terrylene dans le para-terphenyl, car ce système est bien connu dans la littérature et s'est révélé incroyablement photostable même à température ambiante. Des mesures spéciales ont été adaptées pour vérifier la stabilité des émetteurs et l'alignement molécule-nanoantenne, ce qui est présenté tout au long du manuscrit.

Dans le premier chapitre de ce manuscrit, j'introduis les fondamentaux de la photophysique, suivi d'une revue des études sur le terrylène, et plus particulièrement sur le terrylène dans le para-terphényle. Ensuite, j'expose les propriétés fondamentales d'une nanoantenne et je décris les mécanismes qui sous-tendent son effet sur une molécule

unique. Enfin, je présente les statistiques des photons dans les sources de lumière quantique et je discute des modèles utilisés pour décrire le flux de photons d'une molécule unique.

Dans le deuxième chapitre, je présente les méthodes et les détails techniques/expérimentaux, qui constituent un savoir-faire important des expériences sur les nanoantennes et les molécules uniques.

Dans le troisième chapitre, je me concentre uniquement sur la photophysique du terrylene dans un film mince de para-terphenyle de moins de 30 nm. J'effectue une étude de population étendue pour vérifier les échelles de temps des différents processus et les variations de molécule à molécule. Je présente des résultats issus de "Scan de Puissance" et de "Scan de Polarisation" qui sont utilisés pour décrire les échelles de temps de transition et l'orientation du moment dipolaire de transition dans l'espace.

Dans le quatrième chapitre, je présente les résultats des expériences avec des nanoantennes diélectriques (fibres de verre étirées) et plasmoniques (pyramide en or). Une fois approchée par une nanoantenne de chaque type, j'analyse les changements de taux et les traduis en quantités intuitives décrivant le comportement temporel d'une source de lumière d'une seule molécule, telles que le temps moyen passé dans l'état sombre triplet et le temps moyen passé dans l'état émissif.

Chapter 1

In this Chapter, I present fundamental concepts of photophysics and definitions used throughout this thesis. I start with a short introduction to transitions occurring in an organic molecule. Subsequently, I take a closer look at the mechanisms behind them. Finally, I show how the timescales of the transitions are related to their probability in time. The reader with a photophysical background can skip directly to the summary in Section 1.1.6, where I define the questions that will be answered through the manuscript.

1. Introduction

1.1. Fundamentals

1.1.1. Light-matter interactions

Light, being an oscillating electromagnetic field, can interact with matter composed of particles. In the macroscopic view, we can identify transmission, reflection, scattering, absorption, and luminescence phenomena. All those interactions originate from quantum mechanics. The matter of a particular, well-defined composition can be considered a system. This composition results in the system having its intrinsic properties. Subsequently, those properties define the system's behavior and response to the perturbation (such as a photon). The state is a mathematical concept that assigns a set of variables of various meanings to the system so its behavior or response is reproduced within the scope of observation. For instance, some objects deform under tension, so we assign different values of hardness to them and define hardness as resistance to deformation. In quantum mechanics, the quantum state is described by its wave function, the square of which defines the probability of possible outcomes of observations. Photon is a quantum of the electromagnetic field. Light-matter interaction is a perturbation to the system's quantum state and can be written as a Hamiltonian that investigates the behavior of a charged particle (dipole) in the electromagnetic field. As a consequence of this perturbation, quantum state changes, which is referred to as transition.

To be less abstract, let's define the system studied in the scope of this thesis. An organic molecule is a carbon-containing compound composed of two or more atoms bound

through chemical (covalent) bonds. A covalent bond is created when two atoms donate an electron to form a shared pair of electrons. According to Molecular Orbital Theory, electrons participating in bond creation are shared by the whole molecule, and the spatial distribution of electrons with particular energy is called a molecular orbital [5]. Linear Combination of Atomic Orbitals is a method used to calculate molecular orbital wavefunction from the combination of atomic orbital wavefunctions of electrons. As two atomic orbitals contribute, we obtain 2 molecular orbitals. One is a lower energy orbital, occupied by two electrons of opposite spins (Pauli's exclusion), and is called a bonding orbital. The other is an empty higher energy orbital. In a molecule, multiple orbitals will be formed (equal to the number of atomic orbitals combined). The orbital with the highest energy and having paired electrons is called the Highest Occupied Molecular Orbital (HOMO) or a ground state. The orbital of the lowest energy and having no electrons is called the Lowest Unoccupied Molecular Orbital (LUMO) or an excited state. Photon in the visible range (1,6-3,1 eV) has an energy corresponding to the HOMO-LUMO gap of many organic compounds. In the quantum mechanics description, this situation may be viewed as follows [1]. Lets assume that wave function Ψ of the electron that occupies LUMO of the molecule has a form of:

$$\Psi_{LUMO}(\vec{r},t) = \exp\left(-\frac{iE_{LUMO}t}{\hbar}\right)\varphi_{LUMO}(\vec{r}) \tag{1.1}$$

Which is a solution to the Schrödinger equation, where $\vec{r}$ refers to coordinate, t to time, E_{LUMO} to the energy of the LUMO orbital, $\hbar$ is a reduced Planck's constant and φ_{LUMO} represents the time-independent factor of the wavefunction. When the electron undergoes the HOMO-LUMO transition, its probability distribution function is given by the square of the linear combination of HOMO and LUMO state from Equation 1.1:

$$\begin{aligned}\Psi^*\Psi = {} & |A_1|^2|\varphi_1|^2 + |A_2|^2|\varphi_2|^2 \\ & + A_1^* A_2 \varphi_1^* \varphi_2 \exp\left(\frac{-i(E_{HOMO}-E_{LUMO})t}{\hbar}\right) \\ & + A_1 A_2^* \varphi_1 \varphi_2^* \exp\left(\frac{i(E_{HOMO}-E_{LUMO})t}{\hbar}\right)\end{aligned} \tag{1.2}$$

Where $A_{1/2}$ are time-dependent amplitudes that are slowly varying with respect to exponential factors (thus taken as constants). Equation 1.2 shows that probability distribution is coherently oscillating at:

$$\omega = \frac{(E_{HOMO} - E_{LUMO})}{\hbar} \qquad 1.3$$

Promoting the electron from its HOMO to its LUMO also requires a change in electron density distribution in the molecule. This spatial rearrangement has a vector associated with it. This is mathematically expressed by a transition dipole moment. If the energy of a photon is equal to the energy difference of the two quantum states (Equations 1.3) and its polarization isn't perpendicular to the transition moment, the molecule can increase or dissipate its internal energy through the absorption and emission process, respectively. The energy exchange between a photon and a quantum system is not stepwise but oscillates at Rabi frequency. In solids at room temperature, the coherence is compromised by phonons, and this phenomenon cannot be observed [6]. Depending on the spins of unpaired electrons in the excited state, either a singlet (spin multiplicity equal to 1) or a triplet (spin multiplicity equal to 3). Any process that provides a direct pathway to change the system's state is called a transition. In the case above, electron's energy state has changed, so an electronic transition has occurred. Transitions taking place in organic molecules are discussed in the following Subsection 1.1.2.

1.1.2. Transitions

Transitions can be divided into electronic, vibrational, rotational and a mixture of those such as vibronic or rovibrational, which imply either changes solely in electronic, vibrational and rotational states or simultaneous changes in many states like vibrational and electronic or rotational and vibrational, respectively. Upward transitions are referred to as excitation, while downward as relaxation/deexcitation. Any transition that changes energy has a transition moment. However in the scope of this thesis, whenever referring to it, I consider solely electronic state transition.

In organic molecules, the excited electronic state with the lowest energy corresponds typically to the HOMO-LUMO transition but not always [7]. Jablonski diagram is commonly

used to represent transitions on the molecular energy diagram – Figure 1-1. Typical notation of electronic states goes as S0 for the ground state, S1 for the first excited singlet state, and T1 for the first excited triplet state (and so on for the higher states). Absorption (Abs) is a vertical transition (straight blue line) in which the energy of a photon is converted into the system's internal energy by promoting it to the higher energy state. Fluorescence (Fluo) and Phosphorescence (Ph) are vertical radiative transitions in which photon emission results in a transition between the same multiplicity states within nanoseconds (straight green line) or states of different multiplicity, which takes from microseconds up to seconds (straight red line), respectively. Internal Conversion (IC) and Intersystem Crossing (ISC) are non-radiative horizontal transitions between states of the same (wavy purple line) and different (wavy blue line) multiplicity, respectively. Vibrational Relaxation (VR) is a non-radiative vertical transition between vibrational levels that dissipates energy (wavy yellow line). This dissipation can occur inter- or intramolecularly through collisions or vibrational redistribution, respectively, and is said to occur within picoseconds. Intermolecular dissipation can also result in the relaxation of the excited state by transferring its energy to another entity. Such phenomena and entity is called quenching and a quencher, respectively. Intermolecular processes sometimes result in photobleaching, which means that due to irreversible photochemical changes, the molecule no longer emits light upon deexcitation. Relaxations resulting in photon emission, or lack of it, are commonly referred to as 'bright' (Fluo, Ph) or 'dark' (VR, IC, ISC).

For a large population of molecules (law of large numbers), state occupancy defines a fraction of the population that can be found in the particular state. In the case of a single molecule, state occupancy refers to the probability that the molecule is in a given state at a given time. When occupancy increases or decreases, the probability of being in a state changes and I refer to it as population or depopulation, respectively. The evolution of population and depopulation as a function of time defines the dynamics of state occupancy. Transitions cause these dynamics. For instance, ISC is populating T1, and Fluo is depopulating S1. This dynamics is related to the timescales of different transitions. Timescales of transitions in Figure 1-1 are only illustrative and depend heavily on the molecule and its environment.

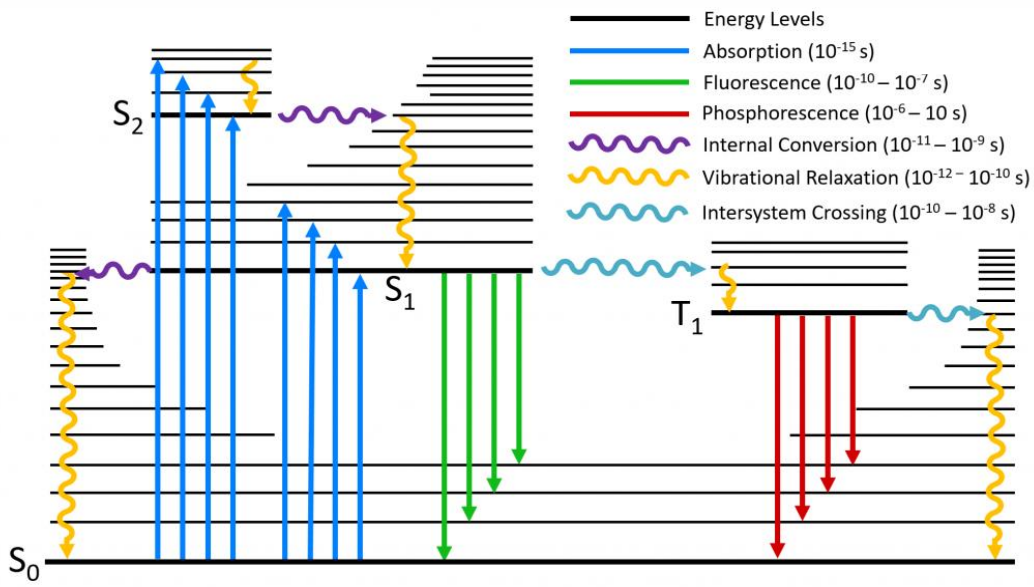

Figure 1-1. Jablonski diagram showing common photophysical processes in a single molecule and their typical time in the legend. Processes involving photons are illustrated using straight lines, while non-radiative process are depicted using wavy lines. [8].

There are special rules that define whether transition can occur, which are called Selection rules. They are based on the total spin, total orbital momentum, and symmetries [9]. Group Theory is applied for symmetry considerations of molecular transitions. Molecules are assigned to point groups based on their symmetry elements (structure). Allowance of the transitions can be readily found in the tables using irreducible representation. Transitions between states of different spin multiplicity are formally forbidden by selection rules [10] and occur through other phenomena. Radiative and non-radiative transitions are discussed in detail in the subsequent Subsections 1.1.3 and 1.1.4.

1.1.3. Radiative transitions

Transitions depicted in Figure 1-1 occur between discrete energy levels but are theoretically limited by the Uncertainty Principle of Heisenberg, which states that linewidth is lifetime-limited. In practice, collisional and Doppler broadening heavily affect the intrinsic linewidth [9]. Figure 1-2 presents absorption and fluorescence spectra of terrylene (T) in toluene taken at excitation wavelength of 560 nm. Difference between the energy of a wavelength at maximum absorption and at maximum emission is called a Stokes shift or anti-Stokes shift - if positive or negative, respectively. Stokes shift comes

from intra- and intermolecular dissipation, while anti-Stokes shift from absorption of additional energy. Kasha's rule states that regardless of excitation wavelength, I quote: ''*The emitting electronic level of a given multiplicity is the lowest excited level of that multiplicity*'' [11]. This means that emission occurs only due to S1-S0 and T1-S0 transitions for Fluo and Ph, respectively. Radiative transition can occur as well through vibronic transition which is responsible for the pattern seen in Figure 1-2. The intensity of the band related to the vibronic transition depends on the Franck-Condon Factor (FCF) as thus an overlap between wavefunction of the excited and ground state being in non-zero vibrational level. If normalized absorption and fluorescence spectra do not form a mirror image, it implies that molecular geometry is different in those two states.

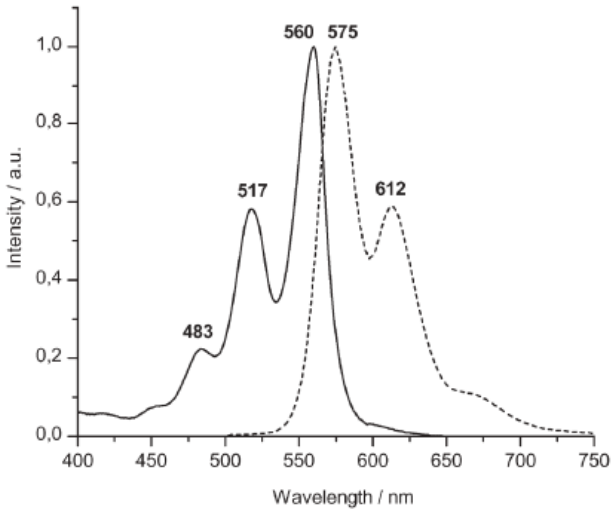

Figure 1-2.Absorption (solid line) and emission (dashed line) spectra of terrylene (T) in toluene (excitation wavelength 560 nm) [12].

1.1.4. Non-radiative transitions

Non-radiative transitions follow the Energy Gap Law (EGL), which states that the probability of non-radiative relaxation depends exponentially on the energy gap between electronic states. This can be explained intuitively [13] – the larger the energy gap between the lower and upper states, the higher the required quantum number of vibrational levels in the lower state (to match the energy of the upper state). Simultaneously, vibrations of higher energy increase the probability as smaller vibrational quantum number is required for a given energy gap. Again, this corresponds to FCF and thus overlap between

wavefunctions - higher vibrational levels have typically lesser overlap with a relaxed state.

Besides EGL, ISC is also spin-forbidden (unlike IC and VR). Direct singlet-triplet transition is forbidden due to the orthogonality of their wavefunctions. There are 3 interactions that enable ISC transition: spin-orbit coupling (SOC), electronic spin-spin coupling (ESSC), and hyperfine interaction (HFI) [14]. SOC comes from the coupling of the spin and orbital angular momentum [15], ESSC considers the interaction of two electronic spins, and HFI arises due to the interaction of nuclear spin with electronic spin. Based on those interactions, decreasing the S1-T1 bandgap and intensifying the coupling are amongst the most popular methods for ISC enhancement [16].

In general, the coupling matrix can be expended to identify 5 experimentally distinguishable mechanisms: direct spin-orbit coupling $H_{mn}^{(1)}$, vibronically induced spin-orbit coupling $H_{mn}^{(2)}$, mixed vibronic and spin-orbit coupling $H_{mn}^{(3)}$, resonant spin-orbit coupling $H_{mn}^{(4)}$ and vibronically induced resonant spin-orbit coupling $H_{mn}^{(5)}$ [17]. In the 1st mechanism, nuclear coordinate remains at equilibrium, unlike the 2nd mechanism (analogically to 4th and 5th). Mechanisms 1st and 4th must be allowed by symmetry. Mechanisms 2nd and 5th must include vibration that would favor coupling of symmetry forbidden transition. The 3rd, 4th, and 5th terms treat ISC analogically to IC by introducing energy gap dependence. Even a simple molecule such as naphthalene (2 fused benzene rings) was shown to follow predominantly the 4th or 5th mechanism. Experiments required for the differentiation of ISC mechanisms include isotope substitution, temperature effect, spin polarization, and vibronic selection [17].

In organic molecules, ISC occurs efficiently accordingly to El-Sayed rules when low-lying nπ*-ππ* transitions are present [18]. However, planar aromatic hydrocarbons (such as T studied herein) lack nonbonding n-orbitals and possess the lowest-lying excited states formed by 2pz, drastically reducing the interaction predicted by those rules [19]. In such a case, ISC is expected to compete with IC as vibrational levels should participate in the transition.

1.1.5. Rates

The average time that molecule spends in the initial state before transitioning can be described by the transition rate - the inverse of loosely given timescales in Figure 1-1. This rate is a is described by the Fermi golden rule, in which a quantum system undergoes a transition from an initial state to a final state due to a perturbation. Change in probability $dProb$ in time dt of such transition can be expressed as rate k_{if} [20,21]:

$$k_{if} = \frac{dProb}{dt} = \frac{2\pi}{\hbar^2}\left|M_{if}\right|^2\rho(f) \qquad 1.4$$

where M_{if} represents the matrix element of the perturbation Hamiltonian between initial and final states, $\rho(f)$ is a density of final states per unit energy close to the final level E_f. Equation 1.4 implies that the transition rate is affected by the environment that this molecule is placed in. The transitions are governed by quantum mechanics and thus are inherently probabilistic. The Cumulative Distribution Function (CDF) refers to the probability that the molecule is yet to undergo or has undergone transition within the time interval <0, t> and rate k_{if} is its parameter:

$$CDF(t) = e^{-k_{if}t} \; or \; 1 - e^{-k_{if}t} \qquad 1.5$$

The inverse of k_{if} is called the time constant τ_{if}. If there are j processes that facilitate the transition between two states, they are referred to as channels – e. g. IC-VR and Fluo would be a non-radiative and radiative channel of S1-S0 transition, respectively. For j channels, the CDF takes a form of:

$$CDF(t) = e^{-(\Sigma_j kj)t} = e^{-k_{tot}t} \qquad 1.6$$

Where the parameter k_{tot} becomes the overall rate of transition and is a sum of all the rates involved. The inverse k_{tot} is called a lifetime τ. For single-channel transitions, the time constant is simultaneously the lifetime. Lifetime is considered an average time spent

in state *i*, before transitioning to state *f*. From Equation 1.6, it becomes evident that the highest rate dominates the overall rate.

Analogically to parallel pathways connecting 2 states, one can think about serial connections of the rates that make a pathway with an overall rate. If the channel requires 2 or more subsequent processes, it is not a transition per se. Transition, by definition, connects 2 states directly. A sequence of processes implies a sequence of states. In this case, CDF cannot be described as an exponential distribution:

$$CDF(t) \neq e^{-\left(\frac{1}{\sum_J \frac{1}{kj}}\right)t} \neq e^{-k_{tot}t} \tag{1.7}$$

However, if we recall the Jablonski diagram (Figure 1-1), transitions between electronic states sometimes include VR, e.g. IC-VR for T1-S0. Here is when the timescales (ratio of rates) of the processes become crucial. It's intuitive that if one process is much faster than the other, it has a negligible time contribution and effectively CDF is approximated by a slower process. Under certain circumstances Equation 1.7 becomes a good approximation of CDF. The requirements for this approximation are discussed in Appendix A.

The efficiency of *X* state population (or depopulation) via channel *i* is a fraction of all *j* channels contributing:

$$\eta_{k_i}^{\pm X} = \frac{k_i}{\sum_j kj} \tag{1.8}$$

Where $\pm X$ specifies state of interest and transition direction - sign '+' and '-' for population and depopulation, respectively. Rate k_i corresponds to the channel under consideration. A process with a much lower rate than the others has a negligible contribution to the efficiency.

The sequence of processes that started with absorption in the ground state and finished with a relaxation back to the ground state is called a primary process [13]. Herein, the primary process is referred to as a cycle instead, since the word 'process' is used

extensively throughout this manuscript in various contexts. Quantum Yield (QY) is a parameter which reflects a number of realizations of a certain cycle as a fraction of all the cycles that have taken place:

$$QY_{k_{if}} = \frac{M\ events\ of\ process\ k_{if}}{N\ events\ of\ excitation} \qquad 1.9$$

Note the conceptual difference between QY and η. QY is an absolute reference and thus is divided by all excitation events (every cycle has to start with an excitation), while η refers to a particular state dynamics (relative reference). In some cases, the two are equivalent and are used interchangeably, e. g. intersystem crossing in organic molecules $QY_{ISC} = \eta_{k_{ISC}}^{-S2}$.

1.1.6. Summary

In this Section, I've shortly reminded how and why light interacts with a matter such as an organic molecule. I've presented possible transitions and discussed some of them in detail. I've introduced the concept of the rate at which transition occurs, which can be affected by an environment.

In the next Sections I will look for answers:

1) What is the structure and energy diagram of T?
2) What kind of experiments are necessary to built the Jablonski diagram of the particular system and its timescales?
3) What are the transitions and rates at which T undergoes them, and how are they affected by the environment for instance, a dielectric or metallic nanoobject?
4) What is the mechanism (if single) behind ISC in T, and can we use an antenna to gain some information about it?

1.2. Terrylene photophysics

The goal of this thesis is to investigate how an antenna affects a single molecule to, in perspective, finely tune photon source properties. It is necessary to have a deep understanding of the physics and properties of the system studied to later consider why and how an antenna would affect them. The reader unfamiliar with terrylene and

terrylene in para-terphenyl is recommended to give a special attention to Sections 1.2.1 and 1.2.3, prior to moving to the summary in Section 1.2.9.

In this Section, I introduce the intrinsic properties of Terrylene (T). I summarize major results concerning the photophysics of T in gas, liquids, and solids, especially in p-terphenyl (pT). Terrylene in p-terphenyl (T/pT) was extensively studied in the past and is presumably the most stable single molecule system at room temperature (RT). Subsections are implemented to narrow down the discussion to one particular factor at once and identify its influence. This work is meant to provide complete review on all the studies that offer a valuable insight into terrylene photophysics and what factors can affect it. Major factors are discussed in the subsections below and some of them were moved to Appendix B.

Most of the experimental studies cited below were carried out by groups of (in chronological order): William Moerner [22–25], Thomas Basche [26–30], Urs Wild [31–34], Michel Orrit [35–43] and Boleslaw Kozankiewicz [38,39,44–52]. William Moerner is also considered a pioneer in the single molecule field itself, being the first one to detect optically a single molecule in 1989, for which he was awarded a Nobel Prize in chemistry in 2014.

1.2.1. Structure and energy diagram of Terrylene

T belongs to the family of rylenes and is an aromatic compound composed of 3 naphthalene building blocks – the structure of T and pT is presented in Figure 1-3. T is made solely of carbon and hydrogen atoms (sp^2 hybridization), and thus doesn't satisfy El-Sayed rules for efficient ISC in organic molecules [18]. It possesses a D_{2h} point group symmetry with A_g ground state for which only $B_{1\text{-}3u}$ transitions are allowed via electric dipole operator (photon) [53]. The first excited state S1 is a HOMO-LUMO transition (π-π^*) with a transition dipole moment oriented along the long axis of the molecule [54,55]. The transitions calculated from simulations and identified experimentally are presented in Table 1-1.

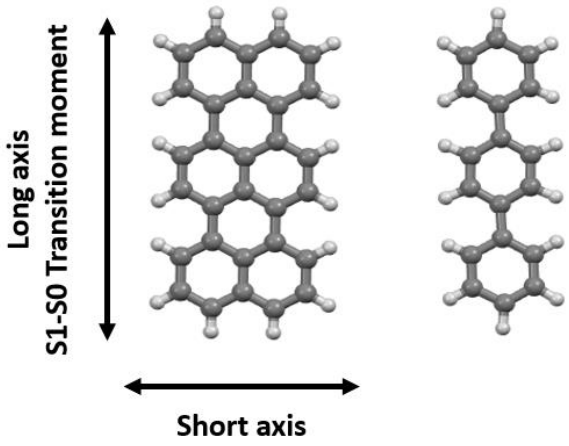

Figure 1-3. Structure of terrylene (left) and p-terphenyl (right) downloaded from Cambridge Structural Database - carbon atoms in grey and hydrogen in white.

Table 1-1. Energy of the 0-0 Franck Condon transitions, irreducible representation and experimental molar extinctions.

Transition	Energy [eV] (irreducible representation if given)				Molar extinction (λ) [10^{-16} cm^{-2}]
	Simulation [56]	Simulation [57]	Simulation [49]	Experimental [58]*	
|E(S0-S1)|	2,29	2,07-2,50 (B_{3u})	~2,2 (B_{1u})	2,23	7,80 (557 nm)
|E(S0-T1)|	1,10		~1 (B_{1u})		
|E(S0-T2)|	2,33		~2,2 (A_g)		
|E(S0-T3)|			~2,6 (B_{3g})		
|E(S0-S2)|		3,09-3,68 (B_{2u})			
|E(S1-S2)|				1,38	14,91 (892 nm)
|E(T1-T5)|	2,34			2,26	10,32 (549 nm)

|E(T1-T6)|	2,40			2,42	3,45 (512 nm)
Stimulated emission				2,18	8,94 (570 nm)

*tetra-t-butyl-terrylene in benzene and cyclohexane (soluble derivative of terrylene), extinction coefficients ε were given in M^{-1} cm^{-1} and converted to cross-sections σ in cm^{-2} according to the formula: $\sigma = 3 * \frac{\ln(10)\cdot 10^3 \cdot \varepsilon}{N_A}$, where N_A is the Avogadro number and factor 3 in front correct the random orientation to the perfect alignment the excitation polarization.

There is an overall agreement across numerical and experimental studies when it comes to the energy of the transitions. T undergoes 2 singlet and 2 triplet transitions in the UV-Vis range. Triplet transition occurs between T1 and T5 or T6. Transition S0-S1, S1-S2, T1-T5, and T1-T6 were found experimentally by Meyer et al. using ultrafast spectroscopy and have molar extinction within an order of magnitude [58]. Though the two triplet-triplet transitions weren't assigned by Meyer et al., they match in energy with the simulations of T5 and T6 levels [56]. Moreover, transitions are of similar energy, which means that the same wavelength promotes S1 as well as T5 and T6 population. Transitions not verified experimentally include T1-S0, T2-S0 (symmetry forbidden), and T3-S0 – all being spin-forbidden. Maximum of stimulated emission lays 0,11 eV below E(S0-S1). Small Stokes shift is most likely due to solvent dissipation and shell reorganization (experiments were done in a solution).

1.2.2. Vibronic transitions

The geometry (symmetry) of a molecule may not be the same in the excited state as in the ground state, which affects Franck-Condon Factors. As a result, a molecule may lose mirror symmetry in the absorption and emission spectrum or change its point group. Moreover, geometry may be additionally disturbed when placed in the solid matrix. Fluorescence excitation spectroscopy can be used to identify vibronic excitations, and fluorescence spectroscopy to recognize vibronic relaxations. Modes of the energy modes in the range 900-1600 cm^{-1} are usually densely spaced in organic molecules as individual,

combinatory, and overtone modes can be found [9]. It is therefore preferred to compare modes that are well-separated and can be assigned with high certainty to a vibration of a specific symmetry.

Results from the literature as concerns T are contradictory - one vibronic excitation line was found at ~243-256 cm^{-1} in T/pT at 5 K, but two vibronic excitation lines at 245-248 cm^{-1} (ν_{11}) and 255-258 cm^{-1} (ν_{13}) were found in T/pT at 4,2 K [47, 28]. Lines ν_{11} and ν_{13} were attributed to symmetric long-axis C-C stretch and skeleton torsion, respectively. It should be noted that in the first study, authors have investigated single molecules one by one, while in the second study excitation spectrum of an ensemble was taken. The authors claim that from a planar excited to non-planar ground state 2 lines are seen, while for the reverse, only ν_{11} is allowed. Regardless, both vibronic lines are seen in the fluorescence spectrum. In crystals such as naphthalene [46,59] and di-substituted naphthalene [60], terrylene has shown vibronic excitation lines: at ~240 cm^{-1} and ~260 cm^{-1} and at ~180 cm^{-1} and ~250 cm^{-1}, respectively. This was explained by symmetry lowering from D_{2h} to D_2 and C_{2h}, respectively. Additionally, for vibronic excitations of T, twice the maximum theoretical flux of purely electronic transition at infinite power were observed [47,48], which authors explained by steady-state population effect. Figure 1-4 presents experimental fluorescence spectra of T/pT with vibrational modes taken from the reference [28]. Around half of the emission integral intensity comes from 0-0 and mentioned ν_{11} and ν_{13} lines in the form of a band spanning from 570 to 590 nm. Another band is long and flat and spans over 600 nm to 640 nm. Assignment of the molecular vibrations in this range wasn't presented in the reference.

In polyethylene matrix, terrylene exists in 2 different spectral populations (not just lines). This was attributed to amorphous and crystalline regions, where T is subjected to different geometry distortions [24].

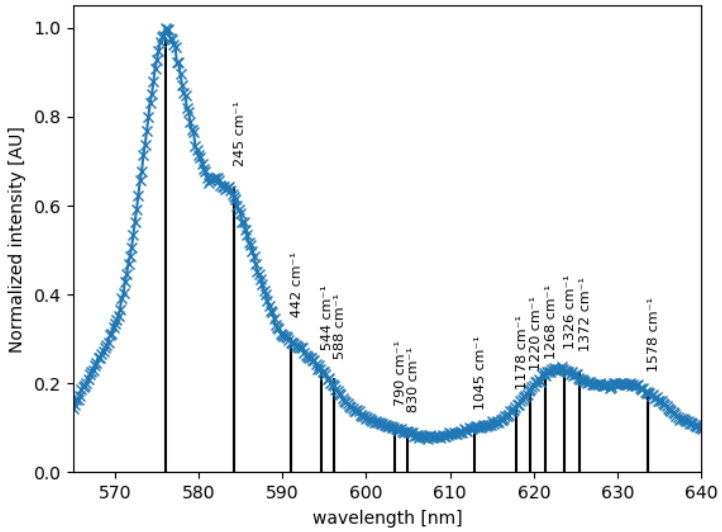

Figure 1-4.Experimental fluorescence spectrum of T/pT with vibrations assigned according to the reference [28] and taking 576 nm as 0-0 transition line. Vibrations closer than 20 cm^{-1} to each other were reduced to single vibration for clarity.

To conclude, it must be considered that excited and ground state of T/pT may have a different point group due to structural deformation. However, the degree of the structural deformation and the quantitative effect it may have on photophysics is not clear. Qualitatively lowering to C_{2h} or D_2 would allow transitions to A_u and B_u or B_1, B_2, and B_3. Therefore, it wouldn't have much of an impact on the allowed transitions, according to Table 1-1.

1.2.3. Rates of transitions

In order to give meaning, to the rates, I present a simplified energy diagram scheme of T - Figure 1-5. The rate of S0-S1 excitation is referred to as k_{12} (excitation rate), the rate of S1-S0 relaxation as k_{21} (spontaneous emission rate), the rate of ISC from S1 to T1 as k_{23}, and the rate of T1-S0 relaxation as k_T. A series of transitions involving T1-T5/T6 excitation, T5/T6-S2 reversed ISC, and S2-S1 relaxation is modeled as a single transition with an effective rate k_{32}.Studies have shown that k_{32} is linear with excitation power [32,45]. Rates k_{12} and k_{32} are products of the absorption coefficients of this transition (σ_{12} and σ_{32}) and pump intensity *I(P)* that depends on the power density. While σ_{12} is the absorption cross-section of the S0-S1 transition, σ_{32} is a cross-section of the T1-T5/T6 transition only

if the time spent in T1 prior to transitioning to T5/6 is at least 100 times larger than the time spent in the T5/6-S1 pathway. From now on, I will use this nomenclature throughout the rest of manuscript whenever referring to the rates.

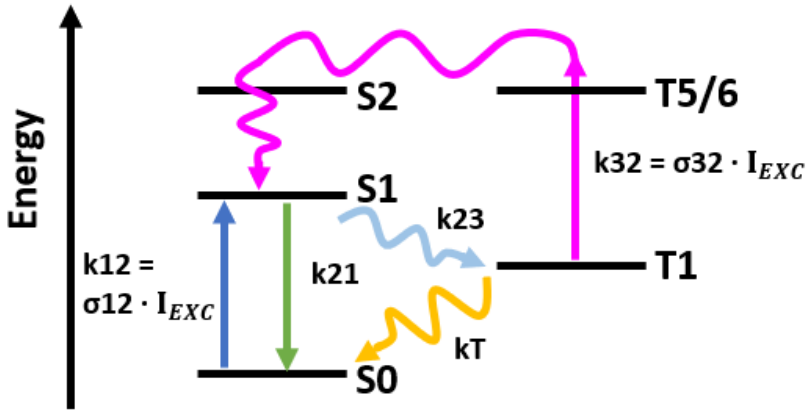

Figure 1-5. Energy diagram scheme based on Table 1-1.

The keyword 'terrylene' yields 320 results in the Mendeley search engine. In Table 1-2, I gather all the results from terrylene studies that include information on any of the molecular rates. The goal of this literature review is to compare results and point out experimental differences. For each study, matrix (or environment) and temperature are noted – unless not given in the reference, then room-temperature (RT) is assumed.

First and foremost, not all the rates are studied equally. Rate k_{21} is the most often studied rate with the value of ~250 MHz (~4 ns) [31,61], followed by k_{23} and k_T (up to double digit kHz range, besides Fleury et al [32]). Only 3 and 1 out of 23 studies report k_{32} and k_{21}, respectively. Studies are carried out at LT and RT. Whenever a single reference reports k_{21} at few K and at RT, the rate always increases or remains constant but never decreases. Lowering of k_{21} could happen if thermal expansion, and a resulting decrease in density, was to significantly lower LDOS. Increase in k_{21} comes most likely from a thermal effect on the rate of non-radiative relaxation. A specific case in which material could undergo phase transition between two temperature regimes is also possible. Most of the polymers show large lifetime changes, which suggest variations of intersystem crossing, quenching of the excited state or IC with temperature – similarly to the shorter lifetime in the air (positions 1-2), which are caused by oxygen quenching. Nevertheless, none of the above is the case of T/pT, which shows no difference upon temperature change according to

Harms et al. [31] (238 and 244 MHz). Results reported for this rate vary within 20% when comparing different studies in the same matrix and at the same temperature. Deviation larger than 20% can be found in the case of T/pT, as bulk crystals have around 5 times larger rates than spin-coated thin films. This comes from the dependence on the orientation, thickness, and depth inside the matrix [62]. Moreover, lifetime was shown to be emission wavelength dependent for T/pT: 4,25 ns at 580 nm, 3,33 ns for 600 nm, 3,90 ns for 627 nm, and 3,32 ns for 685 nm [31]. Therefore, the difference in k_{21} rate may have, besides intrinsic, plenty experimental origins such as spectrum of the collected flux (filters etc.) and crystal thickness.

The rate of T1-S0 relaxation, k_T, is within an order of magnitude throughout different studies in the pT matrix (single to low double digits kHz), while rate k_{23} has a large deviation within a single study and between them – 0,1-14,7 kHz for position 22 and 120-2300 kHz for position 21. If we recall, the ISC process has to originate from a particular interaction. It's qualitatively difficult to say whether spin-spin (ESSC), spin-orbit (SOC), or electron spin with nuclear spin(HFI) vary so much from molecule-to-molecule to explain 2 orders of magnitude differences.

Another huge deviation by a factor of 1000 between the studies takes place in the case of counts at saturation in the anthracene matrix – 750 000 cps (position 5) and 300 cps (position 7). Those differ by preparation method and temperature – spin-coating and RT, instead of sublimation and liquid helium, but the same rates (±20%) besides k_T (2 orders of magnitude). This discrepancy is discussed by Yuce et al. [63], as they suggest that intermolecular ISC is not present at RT, thus the counts are higher.

Recalculating cross-section of S0-S1 transition from Table 1-1 yields $7{,}8 \cdot 10^{-16}$ cm^2 compared to $1\text{-}8 \cdot 10^{-17}$ cm^2 of position 21 and thus are consistent within one order of magnitude. The orientation of the molecules studied in position 21 is unknown, and thus the obtained σ_{12} is biased by an unknown angle between the orientation of the transition dipole moment and polarization of the excitation.

Counts saturation curve of T/pT system deviate from the shape of the typical saturation curves due to its power-dependent triplet depopulation. There are 2 possibilities to include this dependence – by considering a T1-S0 transition as power-dependent or by

introducing an additional power-dependent depopulation pathway that originates from the reversed ISC. Both of those interpretations of k_{32} can be found in the literature.. In one study [64], it is modeled as $k_{32} = k_T * \beta I(P)$, which suggests that T1-S0 (IC and VR) are power-dependent and parameter β has a unit of inversed intensity. In the two other studies [32,45], $k_{32} = \sigma_{32} I(P)$, which means that it is a separate transition with a absorption cross-section, which gives a unit of inverse intensity multiplied by Hertz. One should be careful when reading the study [41], which shows that at 1000 kW/cm^2 rate k_{32}~50 kHz and then for this exact measurement (and many others), in the table therein, gives $\sigma_{32} = 0{,}05 \frac{Hz*cm}{kW}$, which would give merely 50 Hz and not 50 kHz if recalculated as $\sigma_{32} * I$. Therefore, the authors might have lost 3 orders of magnitude in unit conversion or a manuscript typo. In consequence, the two studies give also σ_{32} that varies by 3 orders of magnitude. Moreover, the authors [45] cite reference [32] to prove that they find consistent k_{23}, when k_{23} in the both studies yields 0,1-10kHz and 0,1-1MHz, respectively.

If I assume that there is a typo in the print and I recalculate the values myself by looking at the graphs presented therein, the two studies at the same power of 1 MW/cm^2 report k_{32} of 50 kHz and 200 kHz, respectively [32,45]. This means that σ_{32} in fact differ by a factor of 4, which seems reasonable as the power density of a laser spot (and scattering losses) were not accounted for.

Lastly, there is one report on ~30 nm thick T/pT in which radiative rate quantum yield (QY_R) of 0,97 and 1 was found based on 2 molecules [62], but no k_{23} was given, which is needed to calculate exact non-radiative contribution. Therefore, T/pT can be approximated as a near-unity QY_R system.

To conclude, experimental factors that affect the determination of the rates are the spectrum of the photons collected, power density distribution in the sample and its thickness, preparation method, and the temperature at which measurements are carried. Intrinsic factors that affect the rates are the orientation of a molecule and molecule-to-molecule variation, whose origin is rarely specified. In the 20 nm thick pT, spontaneous emission rate is ~50MHz and is 5-times smaller than in the bulk. The S0-S1 absorption cross-section in the bulk crystal (10^{-17}cm^2) is one order of magnitude smaller than in the solution. In the bulk, the power-dependent triplet depopulation coefficient is on the order of 50-200 kHz/MW*cm^{-2}. Also in the bulk, the direct T1-S0 relaxation is mostly <20 kHz

and the intersystem crossing rate in the kHz and MHz range was reported. Rates found have significant molecule-to-molecule variations, up to one order of magnitude within single study, but only a couple of molecules are typically measured. Moreover, not all the 3-level system rates are calculated in each study. This Subsections shows that large population study has not been reported up to date. Such study should include all of the rates at play and look for the possible causes of such large differences between the molecules.

Table 1-2. Literature summary of T's rates in various environments – T (temperature), σ_{12} (absorption cross-section), Rsat (counts at saturation), k_{21} (spontaneous emission rate), k_{23} (ISC), σ_{32} (triplet-triplet cross-section), k_T (triplet lifetime of T1-S0 transition), Ref (reference).

N	Matrix	T [K]	σ_{12} /Rsat	k_{21} [MHz]	k_{23} [kHz]	σ_{32} [kHz/MW*cm^{-2}]	k_T [kHz]	Ref
1	Air (on SiO_2)	RT		355				65
2	Air (on h-BN)	RT		290				65
3	Neon	260-280		37				66
4	Argon	260-280		250				66
5	Anthracene	RT	/0,8M	278	10^3		700	63

N	Matrix	T [K]	σ_{12} /Rsat	k_{21} [MHz]	k_{23} [kHz]	σ_{32} [kHz/MW*cm^{-2}]	k_T [kHz]	Ref
6	Anthracene	1,5	/250	317	10^3		2	38
7	Anthracene	4,2	/300	317	10^3		1,8	39
8	Polyethylene	4,2/RT		222/222				31
9	Hexane	4,2/RT		227/227				31
10	Polystyrene	4,2/RT		208/303				31
11	PVB	4,2/RT		204/227				31
12	PMMA	4,2/RT		204/265				31
13	PMMA	RT		323		$3\ 10^{-2}$ [cm^2/kWs]		64
14	2,3-DCN		/40k		0,7-1,3		1,8-3,6	60
15	P-terphenyl	4,2/RT		238/244				31
16	p-terphenyl	1,4	/0,6M	310*	1,9-2,0		1,7-2,0	26

N	Matrix	T [K]	σ_{12} /Rsat	k_{21} [MHz]	k_{23} [kHz]	σ_{32} [kHz/MW*cm^{-2}]	k_T [kHz]	Ref
17	p-terphenyl	RT	/>1,4M		>27		>56	30
18	p-terphenyl	2		278				67
19	p-terphenyl	1,4			<1		2	27
20	p-terphenyl	1,5			<1		4**	68
21	p-terphenyl	RT	1,4-7,5 10^{-17} cm^2	120-300	120-2300	~200	3-14	32
22	p-terphenyl	5-300K			0,1-14,7	~50 (if typo in the ref)	2,5-19,0	45
23	Sub-30 nm p-terphenyl	RT		40-66				62

*calculated from linewidth

** for the x,y triplet sublevels

1.2.4. Temperature

As seen in Table 1-2, temperature can change the studied system drastically, and since k_{21} was already discussed, below I will focus on the dynamics of the triplet state. This dynamics is regulated by 3 main pathways - T1 population (k_{23}), depopulation to S0 (k_T), and cross-section of the transition providing depopulation to S1 (σ_{32}).

Dipolar interactions of triplet electrons lift degeneracy in triplet sublevels in molecules that belong to D_{2h} symmetry. Decays of in-plane sublevels are an order of magnitude faster than out-of-plane ones [69]. Terrylene in p-terphenyl shows biexponential decays that evolve into monoexponential decays as the temperature is increased above 17,5 K and 20,5 K for 2 subpopulations [51]. In both cases, spin-lattice relaxation (through Raman or Orbach process) provides coupling of the triplet sublevels resulting in a transition to single exponential at a certain temperature [49,56]. Besides that, subpopulations also had different time constants and amplitudes of the autocorrelation function, which was explained as 2 different intersystem crossing mechanisms populating preferentially different triplet sublevels – S1-T1 intersystem crossing into in-plane sublevels and S1-T2-T1 thermally activated intersystem crossing into out-of-plane sublevel. According to the calculations, the energy gap between S1 and T2 levels is 40 meV, and thus nearly double the thermal energy (25 meV at RT) [49,56].

Note that according to Table 1-1. [49] S1-T2 is symmetry forbidden (and spin forbidden) and thus should have a vibronic-spin-orbit coupling character. To prove the vibronic character, the same authors decided to work on this system at different temperatures, and they found up to a 100-fold increase in k_{23} rate over the range of 5-300 K [45]. Results from the paper are presented in Figure 1-6 – average values of many molecules measured at each temperature and their population standard deviation. Clearly, average values of all the transitions that regulate T1 dynamics increase with the temperature. Two of them (k_T and σ_{32}) seem to reach a plateau at 200 K, while k_{23} increases over the entire range. However, error bars show that this doesn't apply to all molecules. For instance, authors have found at 300 K molecules with k_{23} of 1,5±1 kHz and 42±30 kHz and at 100 K a molecule with k_{23} of 3,0±2,5 kHz. Taking into consideration also error bars, it is without a doubt that k_{23} and σ_{32} behave differently below 50 K and above 50 K, but an exact trend is unclear. From this, it could seem that a temperature above 100 K (8 meV, 64 cm^{-1}) is somewhat an activation energy. It is unclear why and how such energy increases ISC (k_{23}) and rISC (σ_{32}) as this energy if 4 times smaller than the lowest vibrational level of T (250 cm^{-1}).

The possibility that the findings described above shouldn't be viewed just as thermal energy supply to the system as they might be influenced by matrix phase transition cannot

be disregarded. Pentacene in pT was studied to reveal the potential coupling of the guest to the host phenyl rings due to pT phase transition at 193 K [70].

To conclude, without a doubt, rates were shown to vary with temperature. Results were interpreted by thermal activation of vibrational modes above 100 K. However, the vibrational mode of the lowest energy corresponds to 350 K (thermal energy) and thus it is possible that findings may be connected to matrix phase transition instead. The triplet depopulation follows a monoexponential distribution at RT.

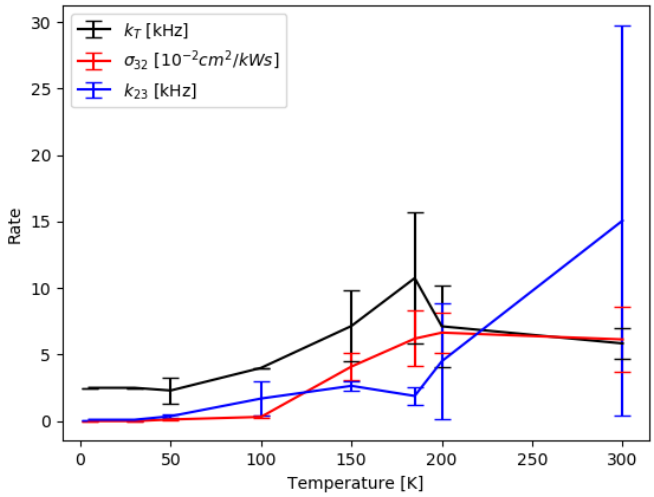

Figure 1-6. Average rates describing T1 population (k_{23}), depopulation to S0 (k_T) and cross-section of the transition providing depopulation to S1 (σ_{32}) in T/pT measured at different temperatures [45]. Error bars calculated from their population standard deviation. Original units from the reference kept, regardless of unit conversion error suspected.

1.2.5. Position inside the matrix

As rates have shown very large variations, it could be expected that T can occupy different sites in pT that provide a different environment and modify its photophysical properties. Therefore, it is necessary to investigate how this host-guest system behaves.

Terrylene in p-terphenyl co-sublimated crystals at LT can occupy 4 crystalline sites (X1-X4), which are substitutions of 4 crystallographically inequivalent p-terphenyl molecules inside the unit cell and in-between layers [26,52]. Sites X1 and X4 undergo reversible and irreversible light-induced frequency changes, respectively. The authors explained

reversible frequency switching: it is analogous to the case of pentacene in p-terphenyl, in which reorientation of the host's central phenyl ring causes spectral diffusion of emitters within a few lattice spacings [71]. Interlayer traps have shown photon flux similar to site X1 and a couple of times smaller than sites X2 and X4.

On the other hand, in the spin-coated T/pT films of around 20 nm thickness, the c-axis of crystal and out-of-sample direction were proven to be coincident [55]. This relation is lost in thick crystals. However, spin-coated crystals are inhomogeneous. Terrylene can occupy a fixed position or diffuse. As was shown in spin-coated T/pT with a thickness of a few hundred nanometers, T can move with a nearly nm^2/ms speed [25]. Instead of being random, diffusion has preferential directions within a given area, which was attributed to the crystal defects. Diffusing molecules photobleach over 30 times faster than fixed ones and tend to be misaligned with the c-axis of the crystal. Superior photostability and preferential c-axis orientation of the fixed molecules provide extreme advantages to T/pT system over any other system for single molecule and antenna studies.

To sum up, crystallographic sites were found at low temperatures but those don't exist anymore at RT as pT undergoes the phase transition at 193 K [70]. Nevertheless, in sub-30 nm films at RT, T was shown to have preferential out-of-plane alignment, which gives a particular doughnut image and suggests not random organization.

1.2.6. Orientation

Orientation of the emitter and its transition dipole is of great interest to provide a complete understanding of the radiation source. A few methods allow extracting orientation of the radiating dipole: the image plane, back focal plane, and polarization-resolved imaging or photon flux [72, 73]. In case of more than one emission dipole, their relative orientation can be defined through polarization-resolved fluorescence spectroscopy [74]. Polarization-resolved Total Internal Reflection Fluorescence (pol-TIRF) allows tracking of the biomacromolecules' orientation and positions if the emitter linked to it has a specific binding conformation [75]. Additionally, the 3D orientation of the host affects the emitter's intrinsic properties. Methods used depend on the host itself and take advantage of its properties – crystals using Transmission Electron Microscopy and anisotropic bulks using Fourier Transformed InfraRed, Raman, and Nuclear Magnetic

Resonance [76,77]. Note that methods based on the polarization-resolved emission signal carry no other information than the orientation of the radiating dipole. On the other hand, observation of the emission with polarization-resolved excitation relates to the orientation of the absorption dipole moment.

I have found no reports that would present rates of T and its orientation with respect to excitation. Due to this fact, in the scope of my thesis, I will collect photon statistics during pol-TIRF scan and polarization-resolved emission. This allows us to track the evolution of all 3-level system rates as a function of polarization.

1.2.7. Photobleaching

Oxygen is a principal factor that affects the photobleaching of organic molecules, and the accessibility to oxygen varies with the depth inside the film.

Photoexcited T is known to generate singlet oxygen, from the triplet oxygen ground state, through triplet-triplet annihilation. This reaction is diffusion (and thus temperature) dependent [78]. The study of T in 9,10-dibromoanthracene matrix has shown that the reaction requires a formation of a weak Van der Waals complex between T in a triplet state and oxygen in a ground state [50]. Therefore, (oxygen-borne) photobleaching of T varies between systems and could depend on the diffusion of oxygen in a matrix. Oxygen is also known to affect the triplet lifetime of organic molecules [33]. In a helium gas atmosphere in 2,3-dimethylnaphtalene crystals, it was suggested that T jump in intensity or even photobleaching can occur due to structural deformation of the host matrix [44].

1.2.8. Local environment

Ideally, the rate at which transition occurs is constant (time-independent). In practice, transient changes in the system may occur and result in a distribution of rates for a single transition. The power law of triplet state decay has been shown for terrylene in polymers [79] and in crystals for other molecules [80]. This is believed to be caused by modifications of the local environment, such as photochemical byproducts (eg. photoinjections, singlet oxygen [37]) in ordered medium or density changes in the disordered medium [81,82]. In Chapter 3, back and forth measurements (Scans) are treated as a measure of temporal stability.

1.2.9. Summary

In this Section, I've presented the structure, electronic energy levels, and transition moments of T to identify allowed transitions. I've recalled studies on the vibronic transitions that show geometry changes between ground and excited states. I've gathered the rates of T found in various experimental studies and discussed the differences between them. I've identified a cause and a consequence to discuss how external and internal factors affect the photophysics of T/pT and T in other solid matrixes.

There are plenty of factors that cause variations in the k_{21}, and any σ_{12} smaller than the molar extinction could be potentially explained by an unknown orientation of a molecule with respect to the polarization of the laser excitation. Meanwhile, k_{23} varies by a factor of 10 within a single study (T/pT), and molecule-to-molecule variation is a typical argument recalled (see population standard deviation at 300 K in Figure 1-6). However, those variations have to originate from EGL, SOC, ESSC, and HFI (Section 1.1.4). For instance, if k_{23} were to change through a change in S1-T1 (EGL), I hypothesize that other rates and vibronic pattern in the fluorescence spectrum (Section 1.2.2) should also exhibit some changes. Therefore there should be some spectral correlation between molecules within a low k_{23} or high k_{23}.

Stark-effect study [36] (Appendix B.d), which doesn't correspond directly to my topic, has proven to be the most stimulating. The authors have suggested very particular changes in molecular structure that would affect the π-conjugation of T. Change in the π-conjugation has to directly impact the fluorescence spectrum (HOMO-LUMO), maybe even rates and orientation of the transition dipole moment. It is unknown what extent of changes is expected. Therefore, it becomes a question itself, how large are the changes in other rates and are they correlated with variation in k_{23}?

It could seem that photophysics of T/pT was already extensively studied. However, in thin films, only spontaneous emission rate was reported. Typically, very few molecules are reported and not all the rates at play are calculated within one study. A comprehensive study that would attempt to connect all those results together is missing. Thus, literature lacks 1) a large population study of T/pT, 2) the triplet dynamics in nanoscale films 3) all

of the rates reported at once 4) connection between the rates and the fluorescence spectrum 5) information about the orientation of the transition dipole moments.

Below I set the experimental goals and indicate in parenthesis what is the main process affected by it

1) thickness of the film doesn't vary significantly (spontaneous emission rate)
2) power density distribution of incident excitation inside the film is accounted for (cross-sections of the transitions)
3) fluorescence (vibronic) spectrum of measured T (molecular structure)
4) photostability of the emitter is well verified (*CDF*)
5) polarization-resolved emission is taken, so called ''Analyzer Scan'' (orientation of the S1-S0 transition dipole moment)
6) all the rates are calculated for each molecule to look for a correlation between them (molecule-to-molecule variability)
7) measurement should cover a wide range of power (minimize calculation uncertainty)
8) rates are measured at different polarization of the excitation laser (verification of allowed transition dipole moments)
9) molecule-to-molecule variation should be linked to factors and mechanisms behind it

1.3. Nanoantennas

In this Section, I briefly introduce the general properties of an optical antenna and present state-of-the-art review. The reader familiar with nanoantennas is recommended to give special attention to Sections 1.3.8 and 1.3.9, prior to moving to the summary in Section 1.3.10.

I focus on the nanoantennas that are used in the visible range and divide them into 2 categories - plasmonic and dielectric. I explain why and how those antennas affect the photophysics of a single molecule through the review of the state-of-the-art. Experimental studies on the single-molecule emitters and plasmonic antennas are much more abundant in the literature. Therefore, the part dedicated to plasmonic antennas is dominated by empirical findings. The part devoted to dielectric antennas covers mostly theoretical studies. All the studies on T/pT system are gathered in a single separate paragraph,

regardless of the antenna type. Finally, a separate subsection is devoted to measurements of the triplet state dynamics.

An optical antenna can be defined as an object that, in a controlled manner, modifies optical radiation and can serve as a receiver or a (typically) transmitter [4]. The emitter-nanoantenna systems offers several advantages as:

1) energy concentration, which means that the same excitation rate can be achieved at lower input power, analogically to lowering the power consumption of the light source

2) control over the radiation pattern, which means that instead of spreading the radiation power over the dipole radiation pattern, radiated power can be concentrated into the desired solid angle

3) polarization change, which means that it can work as somewhat of a polarizer to the light emitter by a radiating dipole

4) rates modification, which means that, in an ideal case, one gets to control not only the intensity of the light source but also the temporal distribution of the emitted photons (photon statistics)

1.3.1. Antenna properties

The rate at which transition occurs is related to the density of states ρ and is described by the Fermi golden rule (Section 1.1.2). The role of the optical antenna is to alter the density of optical states and thus modify the rate of a transition. First experiments were carried out with the molecule of interest placed near planar surfaces and in cavities to find out that both radiative and non-radiative rates can be modified [83]. A total description of physics behind it requires introduction of the coupling constant g of the interactions between the quantum system (molecule) and the light electromagnetic field:

$$g = \mathrm{d}\sqrt{\frac{\hbar\omega}{2\varepsilon_0 \mathrm{V}}} \qquad 1.10$$

with d the emission transition dipole moment, ω the transition frequency, ε_0 the vacuum dielectric constant, and V the mode volume. Two regimes of coupling can be distinguished – weak and strong coupling. The latter occurs when $g > k, \kappa$, where k and κ are inverse of the excited state lifetime and photon lifetime in a cavity [84]. Strong coupling results in the formation of a hybrid light-matter state between the confined optical mode and the excited state. Actually, the Rabi frequency at which energy exchanges between molecule and electromagnetic field is larger than all system decay rates.

Strong coupling was observed at RT in molecule-antenna studies using an emitter placed in a sub-1nm polymer matrix [85]. Since our T/pT system has a sub-30 nm, I do not expect to observe a strong coupling, so I limit my discussion to a dipole in a weak coupling regime only.

Semi-classical treatment of the Purcell effect can be derived. A dynamic dipole $d(t)$ placed in an inhomogeneous environment will experience its own scattered field $E_s(r_0, t)$ that can be written as oscillator motion:

$$\frac{d^2}{dt^2}d(t) + k_0\frac{d}{dt}d(t) + \omega_0^2 d(t) = \frac{Q}{m}E_s(r_0, t) \qquad 1.11$$

Where k_0 and ω_0 are the initial decay rate and resonance frequency. The driving force is equal to charge Q and mass m multiplied by scattered field E_s. In fact, the resonance frequency shift is so small in a weak coupling regime that it is usually neglected. Which yields the Purcell factor PF:

$$PF = \frac{k}{k_0} = 1 + \frac{6\pi\varepsilon_0}{|d|^2}\frac{1}{q^3}Im\{d^* \cdot E_s(r_0)\} = \frac{P_R + P_{NR}}{P_0} \qquad 1.12$$

Where q is a wavenumber and r_0 indicates the emitter position [86]. $P_{R/NR}$ represents power dissipated in radiative and non-radiative relaxations. Total dissipated power in free space using the vacuum local density of states (LDOS) $\rho_0 = \frac{\omega^2}{\pi^2 c^3}$ can be expressed as:

$$P_0 = \frac{\omega^4}{12\pi\varepsilon_0 c^3}|d|^2 \quad 1.13$$

LDOS is defined as the number of available optical states per Hz within a given volume at the dipole location. Change in the LDOS caused by an antenna can be directly evaluated from the dissipated power ratio. If the LDOS is purely radiative, it is proportional to the ratio of the emitter photon flux with the antenna F and the emitter photon flux without the antenna Fo:

$$\rho_p(r_0, \omega) = \frac{\omega^2}{\pi^2 c^3}\frac{P}{P_0} \propto \frac{F}{F_0} \quad 1.14$$

Where notation ρ_p accounts for the partial density of states due to the dipole's orientation.

Optical antenna shape and dimensions are designed so it fulfills its role at a given range of frequencies. Every resonance of the antenna has its Q-factor which is a measure of the antenna's damping and is equal to the ratio of its center frequency f_{res} to the bandwidth Δf set by 3dB loss (FWHM for a Gaussian shape):

$$Q - factor = \frac{f_{res}}{\Delta f} \quad 1.15$$

The Q-factor for a optical mode n can be defined using this optical mode's volume V_n, its angular frequency ω and the Purcell factor PF at this frequency:

$$Q - factor = \frac{PF\omega^3 V_n}{6\pi c^3} \quad 1.16$$

The antenna can be characterized by its efficiency and directivity, which comes from the modification of the emitter's QY_R and radiation pattern, respectively [87]. This modification can be interpreted in the framework of the Purcell effect and modulation of

LDOS. Optical antenna efficiency ϵ_R is described as the ratio or power dissipated with P_R' and without antenna P_R, including intrinsic QY_R of molecule and antenna loss P_{loss}:

$$\epsilon_R = \frac{\frac{P_R'}{P_R}}{\frac{P_R'}{P_R} + \frac{P_{loss}}{P_R} + \frac{1 - QY_R}{QY_R}} \quad 1.17$$

This shows that emitters with low QY_R can exhibit high radiative optical antenna efficiency as it's a relative measure. An interplay of the increase in the radiation power and the lost power depends on the radiative and non-radiative contribution to the LDOS that the emitters experiences, when placed in the proximity of objects with a complex dielectric function [88].

The directivity of the antenna describes the angular power density p in a given direction (radial θ and azimuthal φ angles):

$$D(\theta, \varphi) = \frac{4\pi}{P_R} p(\theta, \varphi) \quad 1.18$$

Directivity can have a large effect on the observed photon flux. Optics can only collect a limited solid angle (numerical aperture).

Sometimes instead of evaluating the directivity, only the modification of the collection efficiency C_{EFF} by the antenna is assessed. The term collection efficiency C_{EFF} is used, which indicates the fraction of the total photon flux emitted F that the optical set-up collects and detects R:

$$C_{EFF}(\lambda, \theta, \varphi, \dots) = \frac{R}{F} \propto C_{OBJECTIVE} * C_{TRANSMISSION} * C_{DETECTOR} \quad 1.19$$

The exact value of C_{EFF} can vary for each experiment. Factors such as transmission through the optical path $C_{TRANSMISSION}$ and detector efficiency $C_{DETECTOR}$ depend on the spectrum of the flux. The solid angle of the objective is constant (Numerical Aperture, NA),

however fraction of radiated power within that solid angle can change depending on the radiation pattern of the emitter. The intrinsic pattern is defined by the orientation of the emitter (radiating oscillating dipole) and then modified by the nanophotonic environment – for T/pT thickness of the film, distance from the surface, and refractive index of the material used as sample support [87].

1.3.2. Electromagnetic reciprocity

Antennas obey Lorentz reciprocity which can be interpreted as, I quote: ''relative excitation rate for a plane wave incident from a certain direction is equal to the relative emitted power in that direction'' [89]. This leads to the relation:

$$\frac{k_{exc}'(\theta,\varphi)}{k_{exc}(\theta,\varphi)} = \frac{D(\theta,\varphi)}{D_0}\frac{k_R'(\theta,\varphi)}{k_R(\theta,\varphi)} \qquad 1.20$$

This relation yields equal excitation and radiative enhancement for a perfect 2-level system if the radiation pattern is not strongly affected by the presence of an antenna (no change in directivity) within the solid angle of the objective. There exists another case in which excitation enhancement can be lower or equal to the radiative enhancement, and it occurs when the quasi-static approximation fails – the electromagnetic field inside the antenna is not uniform due to the relative size of the wavelength. Authors have showcased two examples: sub-micro particle and nanoparticle on a mirror [90]. For a plane wave excitation and dipole radiation, it was proven (through multipolar decomposition) that only odd modes contribute to excitation, while all modes contribute to radiation. In experiments with organic molecules, excitation occurs at a laser excitation wavelength, while emission has a spectrum covering a range of wavelengths. In the following case, LDOS (and enhancement) is not necessarily equal.

1.3.3. Overview

The optical antenna has its role, and in order to fulfill it the best, its properties are adjusted. In this subsection, I present some of the more popular optical antennas, which can be divided into a few categories based on factors such as working frequency, material,

plasmonic effect, shape, coatings, and a number of individual elements that the antenna consists of.

1) Size - antenna dimensions have to be chosen such that strong interaction with the electromagnetic field at the wavelength of interest is achieved. Since single molecules are excited in the visible, nanoantennas are usually used. Nanoantenna is an antenna with one of its dimensions in the nanoscale. From now on, I shift my considerations from a general case of an optical antenna to the nanoantennas.

2) Shape - Starting from a shape, which influences the distribution of the field scattered, popular antennas used in single-molecule experiments are (from the simplest to more complex) tips [91], nanospheres [92], nanorods [93] and monopoles [94], multipoles [95], dimers [96], nanocavities [97], nanoparticle-on-mirror [98], antenna-in-box [99], bowtie [100], apertures [101], Yagi-Uda [102]. More sophisticated structures offer better control over the quality factor, field confinement, and directivity.

3) Fabrication - Depending on the nanoantenna complexity, different fabrication methods have to be used. Wet-chemistry synthesis creates nanoparticles with a random distribution of various shapes and sizes. Nanofabrication methods such as electron beam-, photolithography as well as focused ion beam milling provide control over the size and shape within instrumental spatial resolution. Nanofabrication offers direct control over the positioning of the nanoantenna, and synthesized nanoparticles can be manipulated through DNA origami. DNA origami provides an attachment for the emitter and nanoantenna, thus allowing fine distance tuning, which is used to place the emitter inside hotspots but far enough from the surface to avoid extensive quenching [98,103].

4) Material properties - To discuss how the material affects nanoantenna efficiency, I assume a monomer spherical antenna, either dielectric or metallic (plasmonic), with a diameter within quasi-static approximation and working in the visible range. Major differences arise due to the real and imaginary parts of the refractive index of the constitutive material. Absorption of plasmonic antennas due to intra- or interband transitions lowers antenna efficiency [104]. In contrast, dielectric antennas have negligible absorption.

5) Interaction with light - The mechanism of the field intensity enhancement is different for the two antennas. In dielectric antennas, it arises from the scattering by a relatively high refractive index (compared to the surroundings) and thus offers lesser confinement than near-fields originating from coherent oscillations of free electrons in the plasmonic analogs. Moreover, a metallic antenna can be simplified to the electric modes, while in dielectrics, magnetic modes appear additionally (in the case of a nanoantenna as specified in the assumptions above). Plasmonic antennas have a low Q due to the high damping of the plasmonic modes, while dielectric antennas support high Q factors due to low losses.

6) Selectivity - The presence of magnetic and electric modes creates additional opportunities. Control over electric and magnetic modes offers selective enhancement of transitions [105, 106]. Tuning wavelength for a particular phase relationship between the two moments in dielectric antennas can result in forward or backward scattering (Kerk conditions) [107], thus providing wavelength-dependent directivity. Depending on the phase relation between the incident and scattered field, hot and cold spots are created that lead to an increase (Purcell) and decrease of the LDOS, respectively [108].

In a very simplified view, the efficiency of the nanoantenna can be simplified to 2 functions – absorption and scattering cross-section. I simulate a gold sphere of a 80 nm diameter suspended in a medium with a unity refractive index (no substrate). Figure 1-7 presents COMSOL simulations of the absorption and scattering cross-section compared with Mie theory [109] by applying the python package Miepython. COMSOL simulations were done following references [110,111] and using the dielectric function by McPeak et al. [112]. Previously introduced lost power P_{loss}, enhancement in the radiated power P'_R/P_R and LDOS relate to the absorption, scattering, and sum of the two cross-sections. It could be expected, based on Figure 1-7, that in the air this nanoparticle cannot be an efficient optical antenna below 580 nm as losses are larger than radiated power enhancement. In fact, each nanoantenna has its own QY_R, meaning that energy transferred to it from the emitter, can result in radiative and non-radiative deexcitation. Moreover, the orientation and distance of the emitter from the nanoantenna, as well as the excitation angle of incidence, strongly influences overall performance. Influence of these factors is described based on the experimental findings in the following subsections.

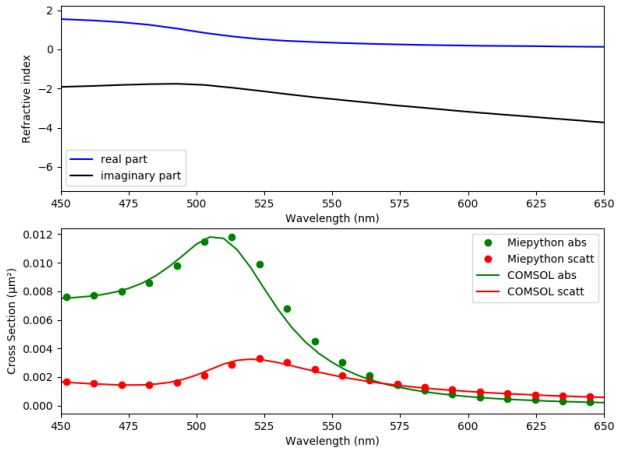

Figure 1-7. Real and imaginary part of refractive index (upper) [112] used for the calculations of 80 nm gold nanoparticle absorption and scattering cross-sections using analytical solutions from Mie theory (Miepython package) and COMSOL software.

1.3.4. Single molecule and nanoantenna studies: history

The number of studies on single molecules with nanoantennas is overwhelming. Experimental findings in this field started appearing in the 80s and led to cited over 8100 times work of Katrin Kneipp in 1997, who was the first to observe a single molecule Raman scattering [113]. If we narrow down the scope to the single molecule emitters and nanoantennas, we can identify subsequent revolutionary works in the field by the teams of: Lukas Novotny in 2006 [88] who measured distance-dependence of nanoantenna fluorescence enhancement, Vahid Sandhoghar in 2006 who measured distance-dependence of emitter's lifetime [114], Jaime Gomez Rivas in 2007 who abandoned cumbersome SNOM configuration for high throughput methods [115], William Moerner in 2009 who introduced a bow-tie nanoantenna concept [116] and Jeremy Baumberg in 2016 who achieved strong coupling at room temperature [85]. Those studies mark the milestones in the field as it evolves from observation of the photon flux to photon statistics, tackling experimental approaches, through the design of nanophotonic environments for optimal performance up to the mixing of photonic and exciton states without surface contact.

Throughout 20 years since those ground-breaking achievements, the most attention was directed to the emitter's orientation, Purcell effect, photon flux enhancement, and

directivity of various nanoantenna designs. These days, the mechanism of the nanoantenna itself is well understood [88,117–119], and there are even a couple of experimental studies on T/pT system interacting with a nanoantenna [61,92,96,114]. What has been overlooked so far in the experimental studies with the nanoantennas is the triplet state dynamics. Even though emitters in the studies with the nanoantennas are sometimes modelled as 3-level systems with a triplet state, only rates related to the singlet are recalculated from the experimental data [120]. The effect of the nanophotonic environment on the triplet dynamics is presented in a separate subsection.

Below I summarize some of the most recent findings based on (mostly experimental) studies on the single molecule emitter (mostly) and optical antenna, especially works by Vahid Sandoghdar [62,96,114,121–125], Lucas Novotny [88,126], Michel Orrit [127], Nicolas Bonod [105,120,128–133], Niek Van Hulst [89,93,95,99,101,106,108,134,135], Phillip Tinnefeld [103,136,137], and Stefan Maier [138,139].

1.3.5. Working configurations

Nanoantenna and single-molecule experiments can be carried out in several ways, which I will shortly introduce here. First off, a conceptual difference between the spacer and matrix has to be discussed first. The primary role of the spacer is to define an approximate distance between the antenna and the emitter, while their relative orientation is random if the emitter is free to rotate. Meanwhile, the matrix is used to provide photostability and fixing of the emitter's orientation. Spacers can be made of biomacromolecules, DNA origami, alkyl chains, polymers, or inorganic thin films [140]. Matrixes are usually composed of the last two or organic crystals. The latter has a particular property as orientation is fixed but not randomly - they have a preferential orientation (pT thin films) or specific crystallographic sites (pT at low temperature). Recall that interaction of the molecule and electromagnetic field depends on the relative orientation of the transition dipole and the polarization. Therefore, ideal system would leave the emitter with no degrees of freedom while allowing control over nanoantenna-emitter distance.

Experimental configuration is important for the sake of dynamic range. In Scanning Probe Microscopy (SPM), a nanoantenna is attached to the probe and approached over the emitter fixed inside the matrix (Figure 1-8A). The nanoantenna-emitter distance can be

controlled down to the distance of the emitter from the matrix surface (probe contact point). This configuration suffers from snapping in- and out-of-contact in out-of-plane direction at tens of nm distance. In this range, in-plane displacement is preferred to measure distance dependence. However, such displacement changes the relative orientation of the emitter and nanoantenna.

In confocal mode 1) matrix with emitters is spin-coated directly onto the nanoantennas, which results in random but fixed distance and orientation 2) nanoantennas are immersed in the solution with the emitters, which results in random diffusion (Figure 1-8B), unless a spacer is used so that distance is fixed, but emitter is still free to rotate (Figure 1-8C). The second method is especially popular and is called Fluorescence Correlation Spectroscopy (FCS).

There is one crucial advantage of the SPM system over the confocal system. The former allows measurements on the emitter and on the emitter-nanoantenna system while working with the very same single molecule. Nanoantenna, also serving as a probe, can be readily retracted or approached, therefore a nanoantenna effect can be verified without concerns about molecule-to-molecule variations. In contrast, in the confocal system antenna is fixed, and therefore antenna effect is effectively deduced by comparing different single molecules. It may not seem like a problem, but recall large molecule-to-molecule variations in rates reported.

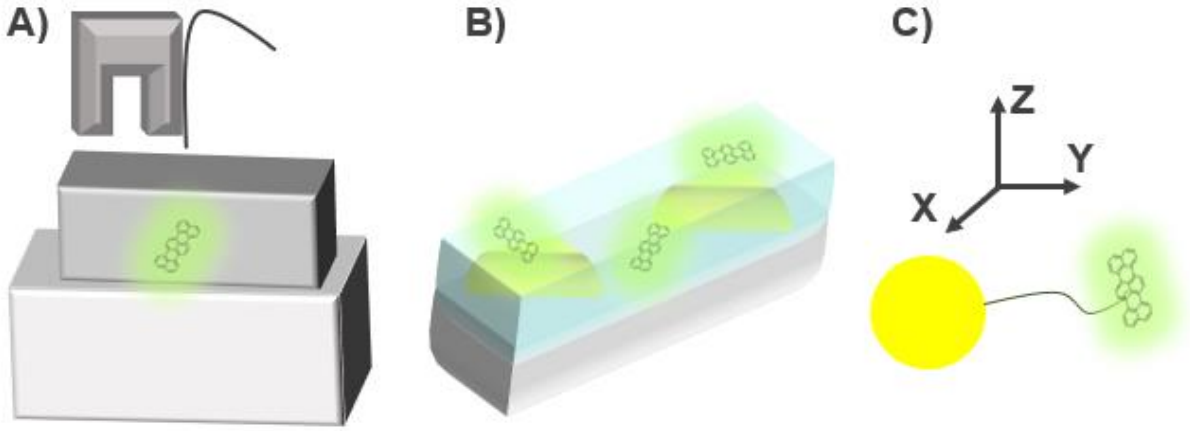

Figure 1-8. Schematic representation of A) SPM working mode with emitter inside the matrix B) confocal working mode with the emitters diffusing around the nanoantennas inside a solution C) nanoantenna with a spacer that leaves emitter free to rotate but fixes distance.

1.3.6. Single molecule emitter and plasmonic antennas

1.3.6.1. Size- and distance-dependence

One of the first such studies came in 2007, where gold nanoparticles of 15 nm diameter with Alexa fluorophore attached by double-stranded DNA nucleotide of lengths up to 40 nm were used to track lifetime changes [121] – configuration as in Figure 1-8B with DNA being a spacer as in Figure 1-8C.

Purcell Factor was shown to take sigmoidal ('S' shape), with the highest gradient at 15-25 nm distance. The sigmoidal curve were shown to depend on the plasmon spectrum of the gold nanoparticles. The increase in LDOS didn't result in photon flux enhancement, because of the low efficiency of this nanoantenna – large imaginary part of gold dielectric function decrease the QY_R due to quenching (energy transfer). Calculations have shown that the larger the gold nanoparticle, the larger distance over which it affects the lifetime.

A more advanced study came in *Nature* in 2014, where DNA origami was used to control the distance and position of the emitter (Atto647N) with respect to a 20 nm diameter gold nanoparticles [136]. For certain positions, the excitation rate and the radiative rate remained constant, while the non-radiative rate was increasing up to 10-fold. Authors have explained by considering cold spots and hot spots. If plasmonic nanosphere is placed

in the cartesian system and the electric field of the excitation illumination has no Z-axis component, then cold spots are created at Z-axis displacements (above and below the nanosphere), while hot spots are present around the nanosphere. Authors have argued that if emitter is placed in the cold spots, experiences no enhancement of excitation nor emission from the plasmon but is still prone to losses due to energy transfer between a dipole and a metallic nanosphere. The experiment was troubled by free rotation of the emitter As the emitter is free to rotate, it will experience different enhancements for tangential (suppressed) and radial (increased) orientation with respect to the nanosphere. Mentioned lack of excitation rate enhancement is explained by orientation averaging. Further on, at a fixed distance of 11,5 nm and for NP of diameters of 20, 40, and 80 nm, changes in k_R, k_{NR}, k_{EX}, and QY are further investigated, but authors report no clear correlation between excitation and radiative rate change. They suspect various orientations of the emitter inside origami structures to be at fault. This experiment highlights how the experiments with freely rotating emitter are difficult to interpret and often show inconsistencies.

1.3.6.2. Orientation-dependence

As shown in the subsection above, rotation of the emitter is a big obstacle in the nanoantennas studies. To give some quantitative idea on this topic, in Figure 1-9, I present the results of a simulation of QY modification and LDOS change taken from a reference [141]. Perfect unity single emitter emitting at 600 nm was studied as a function of the distance and orientation to the AuNP of 100 nm. While LDOS is the greatest near the surface of the antenna, QY approaches 0 because the contribution of non-radiative states of LDOS dominates (within 10 nm from the surface). Note that the spatial distribution of changes in LDOS and QY depends strongly on the dipole orientation with respect to the surface. For an arbitrarily orientated dipole, those distributions can be obtained by the decomposition into relative radial and tangential components.

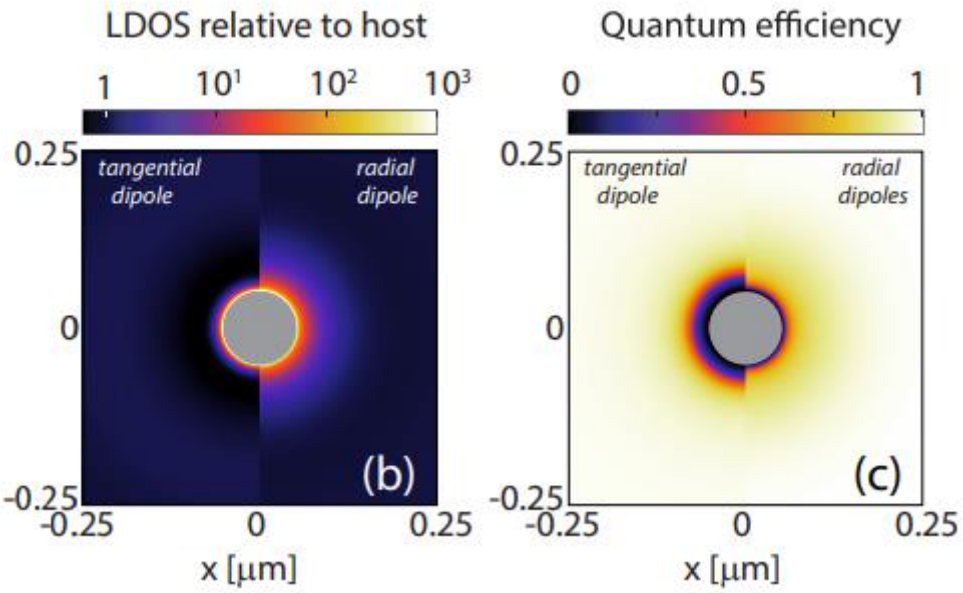

Figure 1-9. Relative LDOS (left) and modified QY (right) of a perfect unity QY emitter around 100 nm AuNPs for tangential and radial dipole orientation (emission wavelength 600 nm) [141].

1.3.6.3. Radiation pattern

The radiation pattern of the emitter also varies with its orientation, distance, and nanoantenna. Simulation of the radiation pattern for tangential point dipole emitting at 600 nm at various distances from 80 nm AgNP, both embedded in a matrix of n=1.5, were done assuming a perfect objective that collects all photons in -X direction hemisphere (Figure 1-10a) [130]. Collected photons are normalized to all photons emitted and defined as a reflected power. The total decay rate and reflected power are tracked as the distance between the emitter and the antenna's center. Both were expended up to the multipole of order 30 for the calculations (Figure 1-10b, surface at 40 nm). Total decay shows very large discrepancies between dipole approximation and multipole expansion below 20 nm away from the surface as dark multipole modes start to contribute significantly to the LDOS. On the other hand, the reflected power is well reproduced by dipole approximation and shows a nearly 2-fold change between the emitter placed at 19 nm (Figure 1-10c) and 9 nm away from the surface (Figure 1-10d).

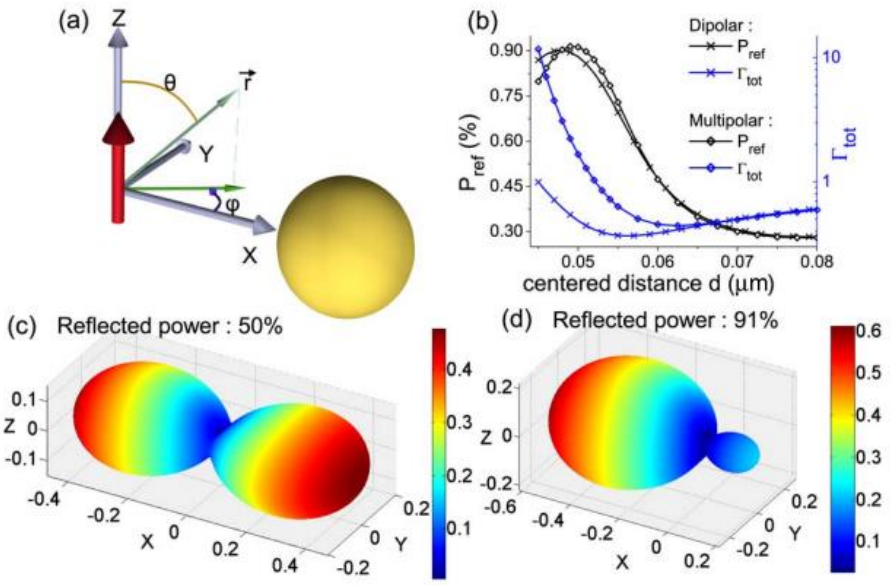

Figure 1-10. Emitter modelled as point dipole with tangential orientation and 80 nm AgNP –(a). Reflected power (black) and total decay (blue) as distance from AgNP varies using dipolar approximation (cross) and multipole expansion (diamonds)- (b). 3D plots of radiation pattern at 19 nm (c) and 9 nm (d) from the surface [[130]*].*

1.3.6.4. Photon flux Enhancements

As Koenderink pointed out in his state-of-the-art review [141], the scientific field is in need of an absolute figure of merit that would allow direct comparison between the efficiency of the different systems. Overall enhancement of the photon flux is a result of nanoantenna's influence on the excitation, emission, radiative contribution to the deexcitation and radiation pattern of the emitter. Those enhancements are assessed by investigating the ratios (with and without nanoantenna) of k_{12}, k_{12}, QY_R, directivity depicted through polar plots or C_{EFF}, respectively. Reporting flux enhancement gives information on the consequence but not the mechanisms involved.

One of the highest reported fluorescence enhancements of a plasmonic nanoantenna reported in the literature is above 5000-fold [103]. Yet, this enhancement is actually obtained from the comparison with a quenched dye, and that enhancement falls below 500 when compared with the emitter's intrinsic flux. In fact, the emitter's *QY* plays an important role in the overall enhancement - the lower the *QY*, the larger the enhancement in the photon flux [126]. Numerical simulations for a gold nanorod have shown that if all

the variables are kept constant, and just QY of the emitter is varied, the enhancement factor changes from around 100 to 100 000 for the emitter with intrinsic $QY=1$ and $QY=10^{-4}$, respectively [127]. A very low QY emitter enhanced greatly by the antenna doesn't necessarily produce more photons than a high QY emitter with a modest enhancement.

1.3.6.5. Emitter spectrum and nanoantenna resonance

Spectral overlap of the molecular absorption, molecular fluorescence, and nanoantenna's absorption and scattering cross-sections play an important role in the antenna effect. Previously, I have mentioned that the antenna's has radiative LDOS, which relates to the scattering spectrum and absorption spectrum (through nanoantenna's QY_R). Part of the radiative LDOS that is available for the molecule is not simple to define specifically. The molecule can be approximated as the electric dipole, but this is not always the case for the nanoantenna. Radiative LDOS can be composed of multipoles that have various spatial (and vectorial) distributions specific to the excitation field components, photonic environment and antenna. Distance, orientation and emission wavelength of the emitter will define what part of the radiative LDOS becomes available for the emitter (is seen by the emitter).

The antenna's absorption is more complex. The energy transferred from the emitter to the nanoantenna can result in nanoantenna luminescence (radiative relaxation) or thermal dissipation (ohmic loss, nonradiative relaxation). To simplify, one can say that overlap between the emitter's absorption and the antenna's scattering spectrum results is related to the excitation component, while the overlap between the emitter's fluorescence and the antenna's scattering spectrum relates to the emission. Therefore, the antenna and the emitter must be carefully chosen to satisfy those overlap conditions. Antenna's scattering and single emitter's emission spectrum are easily accessible experimentally, while single-molecule excitation spectrum requires a more complex set-up [142]. Thus, absorption spectrum of a population is used instead.

Scattering of the antenna can be readily tuned for maximum overlap if the emitter's excitation and emission are not significantly redshifted (small Stokes-shift). Otherwise, a compromise has to be made. Gold nanorods were proposed to tackle large Stokes shift fluorophores. They enable to optimize excitation in green with transverse LSPR and

emission in red with longitudinal LSPR. Such an approach is questionable for a single molecule as those modes are separated spatially and are perpendicular. Nevertheless, experimentally a 4-fold photon flux enhancement compared with nanosphere was observed [143].

For antennas that are not as easily produced (top-down fabrication), it is desired to predict the scattering spectrum in the design step. Aluminum-coated monopole antennas fabricated by Focused Ion Beam (FIB) have shown that the resonant frequency of a nanoantenna differs from a $\lambda/4$ resonance in classical antennas. Material properties at optical frequencies differ strongly from perfect electric conductor used in radio-frequency antenna theory. When excited at 514 nm a monopole antenna with a perfect electric conductor of 20 nm diameter resonates if it has a length of ~100 nm, while 20 nm diameter aluminum monopole is resonant with this excitation if the nanoantenna has a length of 70 nm [144].

Scattering sphere-like Ag nanoantenna, 150 nm AuNP, and Au nanoshells were investigated [145,146] on different substrates to show inhomogeneous broadening or even peak splitting in the scattering spectrum (LSPR). The transition from simple Lorentzian to bi-Lorentzian shape occurred when switching from s-polarized to p-polarized excitation at 79° incidence. Authors have explained that the dielectric surface positioned below the plasmonic object causes non-uniform screening of electromagnetic field related to plasmon oscillation. This leads to the surface-hybridized plasmonic modes, which can even result in the activation of a dark quadrupolar mode (no far field radiation). A shift of the resonant wavelength up to 40 nm was observed experimentally when switching between the substrates of the refractive index of 1,34 and 1,75. Besides the absolute shift of the dipolar and the quadrupolar mode in the scattering spectrum, also their relative shifts vary with the refractive index of the substrate – Figure 1-11.

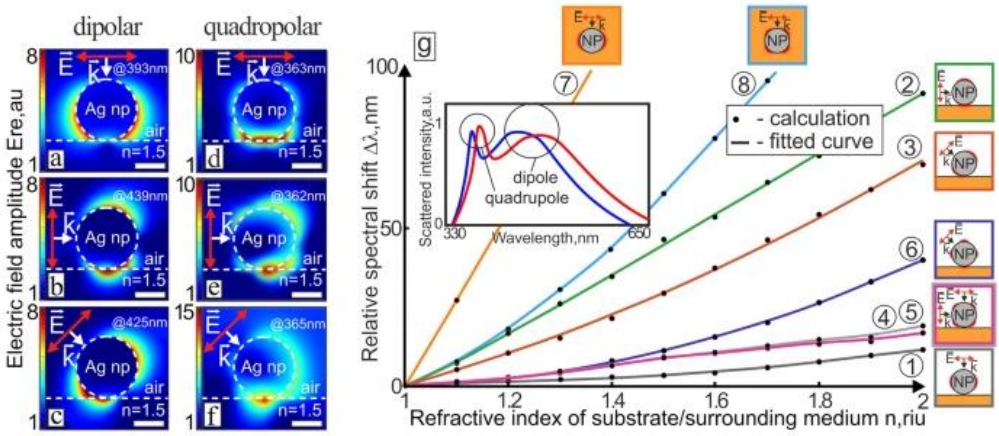

Figure 1-11. Simulations of electric field amplitude around 100 nm AuNP in air placed on dielectric substrate at various incidence angles of p-polarization for dipolar (a-c) and quadrupolar (d-f) modes. Relative shifts of dipolar and quadrupolar modes resonant wavelength – 1-6 correspond to cases a-f, respectively. Isotropic dielectric environment case for dipolar and quadrupolar mode on curves 7-8. Inset presents a typical scattering spectrum of scatterer on a substrate of n=1.2 (blue) and n=1.3 (red) [[146]*].*

Besides the dispersion of the scattering, simulations can retrieve the field vectors around antenna. Vectorial field depends on the polarization of the incident light and follows antenna symmetry. It was shown that the orientation of the emitters can be assessed by performing polarization-resolved maps. To do this, monopole and bowtie nanoaperture optical antennas fabricated by focused ion beam were used in SNOM on terrylene diimide doped PMMA [95,101]. Especially bowtie nanoaperture antenna has a highly asymmetric spatial field distribution of electric field's X, Y and Z-components. Patterns recorded when the antenna is scanned above the emitter were used to resolve it's in-plane orientation.

1.3.6.6. Transition selection

In plasmonic antennas, transition selection is based mostly on spectral selection. The antenna of a high Q-factor is tuned for the wavelength of a wanted transition. In consequence, LDOS is enhanced within a given spectral range. The opposite approach is also theoretically possible, as the antenna could be tuned to suppress LDOS in the spectral range of unwanted transition. As Purcell factor defines how the transition rate is enhanced (and is proportional to Q-factor/V, Section 1.3.1), ideally a small mode volume V and a high Q-factor are desired.

Resonant microcavity and plasmonic hotspots can be compared to describe the interplay between the Q-factor and mode volume. The first provides extremely high Q-factors (photonic mode) but large mode volumes. The other provides smaller Q-factor (plasmonic mode) but a much smaller mode volume. Exact numbers vary drastically for different designs so to give at least an order of magnitude – optical cavities have a Q-factor of several thousands and mode volume of λ^3, while plasmonic antennas have a Q-factor of a few tens and mode volume of $10^{-5}\lambda^3$ [147]. In the end, Purcell Factors, being proportional to Q-factor/V, are similar for cavities and plasmonic antennas. The cavities are tuned by the varying spacing of the mirrors or active medium, while for plasmonic nanoparticles either shape or size are adjusted.

As an example for cavity resonator, Terrylene molecules were placed in a micro-resonator based on two silver mirrors and T-doped adhesive tuned in resonance with a zero-phonon line. This configuration has been shown to cut the vibronic transitions entirely [148].

A typical example of a plasmonic antennas are Gold nanorods. The coupling of Rhodamine 800 was studied as a function of nanorods length in the weak coupling regime [93]. Nanorods with a length in the range of 80-140 nm allowed to tune the relative ratio of zero-phonon and the vibronic sideband in the emission spectrum by a factor of 25.

1.3.7. Emitter and dielectric antennas

Studies with a single emitter and dielectric antennas are not as abundant in the literature as in the case of their plasmonic analogs. There are hardly any experimental reports that investigate single molecule emitters. Rare-earth ions, 2D materials, and quantum dots are used instead. The modest electric field intensity enhancement of dielectric nanoantennas can't offer the spectacular headlines of huge fluorescence increase and single molecule detection as plasmonic antennas do. Instead, in this field, most of the effort has been put into light manipulation, e. g. Kerker effect. The quantum emitter and dielectric antenna field share many notions and characteristics with photonic crystals and metasurfaces fields, so it is difficult to define advances specific to the former. This subsection involves theoretical and experimental studies to discuss various quantum emitters in proximity to the dielectric antenna. As dielectric materials have negligible absorption outside of bandgap transitions, *QY* remains unchanged and is not considered.

It was shown that for a plasmonic particle of a given diameter, a hypothetical dielectric particle with the same diameter can perfectly reproduce its scattering spectrum and electric field intensity distribution [131]. To achieve this, imaginary and real parts of plasmonic particle permittivity have to be used to recalculate complex permittivity of equivalent dielectric. For example, the complex permittivity of 50 nm AgNP around 300 nm yields 0+3i, while an equivalent dielectric particle would have 100+4i. Work wasn't verified experimentally as materials with such properties do not exist in the visible range. The authors do not discuss the extinction spectrum, and 5 multipoles are required for hypothetical dielectric to reproduce the response of metallic dipole.

Below I present a short review of quantum emitters studied in the proximity to the dielectric surface [124], microsphere [132], nanosphere [149], tip [150,151], dimer pillars nanogaps [138,139,152], and resonators [129].

1.3.7.1. Fluorescence enhancement

Experiments on the 1-5 μm latex microspheres in the FCS configuration were carried out [132]. The microspheres drastically change the distribution of the excitation field and, in consequence, volume probed by the excitation. Measurements were normalized for the effective intensity that molecules experience. Up to a 5-fold increase in the fluorescence flux was observed. Fluorescence enhancement is evaluated using a so-called parameter 'count rate per molecule' rather than the overall count rate. Authors measure an autocorrelation function but only for a measurement of diffusion.

The studies on the influence of dielectric antenna on the rates of a quantum emitter were conducted on silicon pillar nanogaps with crystal violet and Alexa647 fluorophores in FCS [152] in 2016[144]. Both fluorescent molecules in nanogaps exhibit over a 200-fold fluorescence enhancement while detection volume is reduced 3600 times. The same experiments were carried out on gold pillars nanogaps for reference – for tuning to Alexa647, both had a 20 nm gap, but dielectric and metallic pillars were of 170 nm and 80 nm diameter, respectively. The authors show that for 20 nm gap detection volume and fluorescence enhancement is nearly equal for both types of nanogaps. Authors have collected bunching curves to evaluate the number of molecules inside a probed volume.

Similar experiments were conducted on monolayer WSe_2 [139] in 2021. Single-photon source creation in the 2D material requires a strain, which means that photon flux cannot be directly compared to the no-nanoantenna situation. To provide some frame of reference, authors carry out experiments on non-gap glass nanopillar (n=1.5 instead of 4 for Si). The authors simulate a dipole emitting at 750 nm and excited at 638 nm placed in the nanogap. At a constant gap but as a function of pillar radius in the range 150-300 nm Purcell factor stays constant (~30), while the excitation rate changes from nearly 40 to less than 10 as the radius increases. Simultaneously, C_{EFF} for the objective above substrate decreases 2-fold.

1.3.7.2. Collection efficiency

The biggest loss in the C_{EFF} usually comes from the NA of the microscope objective. To tackle this problem, authors have chosen thin film T/pT (T has a preferential out-of-plane orientation) and subsequently designed a layered structure of refractive index n1=1,78, n2=1,50, and n3=1. Radiation of the emitter in such a structure gets redirected into one half-space (high refractive index layer), where the NA=1,65 objective is placed. The middle layer consists of 20 nm T/pT placed at 200 nm depth within a few hundred nm thick PVA (n2). The authors refer to electromagnetic calculations, which show that for such a large thickness contrast, the emitter can be effectively treated as a dopant in PVA, and the presence of pT matrix is ignored (thus study is not summarized in Section 1.3.8). This planar dielectric antenna has achieved $C_{OBJECTIVE}$ of 96% [124].

1.3.7.3. Transition selection

Transition selectivity of the dielectric antenna can be achieved through another mechanism than just spectral selection. While the optical response of the metallic particles with a radius much smaller than the wavelength can be approximated by an electric dipole, dielectric analogs support multipolar modes of both electric and magnetic components. This leads to the splitting of the modified LDOS into magnetic and electric Purcell factors. Transition selectivity can be achieved through the design of the antennas that enhances or suppresses electric or magnetic dipole transition in quantum emitters. Such studies were reported for lanthanide ions having d->f orbitals magnetic dipole transitions [105,153].

1.3.7.4. Thermal effects

Plasmonic nanostructures can only be used below a certain threshold to ensure their shape stays intact. While intensity enhancement around dielectric antennas is lower than plasmonic, so does its heat conversion. Using Nile Red in PMMA as thermal probes, experiments on silicon and gold 20 nm nanogap dimer nanopillars were carried out [138]. Excitation field enhancement and temperature for metallic and dielectric antennas are evaluated. The authors highlight that in order to recover the same Raman signal – which scales as $(E/E_0)^4$ – dielectric equivalent requires 5 times higher input excitation. Nevertheless, at this 5-fold higher power ($5I_0$), heating is still 75% lower compared to the gold equivalent at I_0.

1.3.8. Terrylene in p-terphenyl

Work on T/pT system by the group of Sandoghdar consists of experimental works using silver [62], gold nanoparticle monomers [61,92,114] and dimers [96], as well as glass or chromium-coated tips [150] and planar dielectric antenna [124]. All of the studies were carried out in SPM configuration – Figure 1-8A.

In the spin-coated matrix down to sub-30 nm, terrylene changes its lifetime from around 4 ns to 15-25 ns. Lifetime depends on the depth within the film and dipole orientation [62]. Orientation of the T emission dipole, which coincides with the long axis of the molecule, was calculated using back focal plane images to yield around 15±5° tilt. Recorded curves of the lifetime as a function of distance from the silver mirror for 2 molecules were fitted to obtain QY of 0.98 and 1, which supports near-unity quantum emitter approximation.

Besides the characterization of the molecule, Sandoghdar also developed a method to characterize 3D dimensions of a AuNP attached to glass fiber [154] and to find plasmon's QY_R when modeled as a point dipole [62].

Experiments on a single molecule and plasmonic nanoantenna were done with AuNP of 100 nm attached to the glass fiber and scanned above a single T in sub-30 nm pT [114] (Figure 1-12). Fluorescence enhancement and lifetime reduction were recorded as a function of lateral and perpendicular displacement. Lateral scan yields FWHM of 65 nm, while the perpendicular shows that the nanoantenna effect is confined up to 10 nm.

Perpendicular scans show a 22-fold decrease in lifetime and a 13-fold increase in fluorescence signal at the contact point, compared to retracted 300 nm away from the surface. The direct relation between near-field intensity and fluorescence enhancement was shown using two different laser sources (532 and 488 nm). The authors reported that AuNP doesn't change emission pattern significantly [114]

Dielectric and metallic antenna effect on a 45 nm T/pT matrix was studied using pulled glass fiber and chromium-coated glass fiber [150]. The dielectric tip with FWHM of 35 nm introduced a 2-fold reduction of the lifetime and a 2-fold enhancement of the photon flux, while the chromium-coated tip gave 1,6-fold fluorescence enhancement and FWHM of 150 nm.

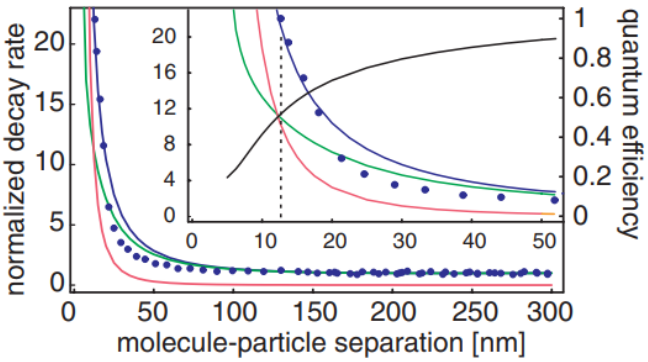

Figure 1-12.Radiative, non-radiative and total decay rates (green, pink and blue) calculated for T tilted at 15° and experimental data points (blue circles) as a function of the distance between the molecule and 100 nm AuNP nanoantenna. Inset shows zoomed range up to 50 nm and calculated QY (black line) [114].

The role of the substrate was studied in 20 nm T/pT using glass, sapphire, or cubic zirconia. Results have shown that the lower the refractive index of the substrate, the longer the lifetime – from 20 ns on the glass to 11 ns on zirconia [61]. Subsequently, approaching 80 nm AuNPs attached to glass fiber have shown decay enhancement of around 4 and 7 (each based on 5 molecules) for glass and zirconia, respectively. Results given in this study seem at first contradictory with previously reported 22-fold decay enhancement by the same team in the same system, substrate, and same laser excitation wavelength, but using 100 nm instead of 80 nm AuNP [114]. Also, the same group reports in theoretical calculations that it's indeed 80 nm AuNP that should provide maximal

enhancement and not 100 nm. However, decay can change by a factor of 10 due to different depths inside the film [92].

1.3.9. Triplet dynamics

The dielectric environment is known to strongly affect ISC in the donor-acceptor molecules. Those molecules undergo so-called Spin-Orbit Charge-Transfer ISC (SOCT-ISC) as photoinduced charge transfer species has drastically altered SOC matrix elements. Simulations on the commercially available thermally-activated delayed fluorescent compound TXO-TPA showed that ISC rate and reversed ISC are 2 and 3 orders higher, respectively, in toluene than in the vacuum [155]. And thus, ISC based on SOCT is affected by the environment.

The ISC rate can also be affected when a strong coupling regime is achieved. This is somewhat anticipated as the excited state of a molecule couples with light to create hybrid states. Those hybrid states have different energy and therefore different ISC rates by the EGL. Erythrosine B was studied in an optical cavity, and 5 orders of magnitude increase in ISC rate was found when compared with a molecule alone [156]. This also proves that hybrid states can collapse to non-coupled molecular states (T1 in this case).

An experimental study on Rhodamine 6G water-glycerol (3:1) solution in metallic nanoapertures (configuration as Figure 1-8B) was reported [157]. Authors have found a 7,1-fold and 1,6-fold increase in triplet population and depopulation rate, respectively. Plasmonic effects near the surface of the nanoaperture are suspected to cause those changes. It's worth noticing that rates found for the molecule alone are consistent with another study in water at pH 9 [158]. Consistency across different studies is not as obvious as it may seem even for such a popular dye as Rhodamine 6G. The rates of Rhodamine 6G in ethanol reported in scientific publications were summarized in a review [158] and ISC rates found are in the range 0,46-28 MHz (2 orders of magnitude variation). In the next Section, I will present how those rates are calculated and consider whether such a large deviation between studies, whether it's T or a popular Rhodamine 6G, is molecule-to-molecule variation or maybe some experimental factors are at fault.

1.3.10. Summary

In this Section, I've presented how and why nanoantenna affects excitation, emission, QY_R, and radiation pattern of the emitter. I've discussed advantages and disadvantages of various working configurations and different types of nanoantennas. Factors that affect the interaction between the nanoantenna and emitter, such as their spectrum, distance, and relative orientation, were discussed based on experimental and theoretical studies. I've paid special attention to summarizing reports on the T/pT system.

Studies found in the literature often refer to the random orientation of the emitter or molecule-to-molecule variations to explain some inconsistencies. This Section really highlights the superiority of the T/pT system. Fixed transition moment and preferential orientation of the molecule should allow experiments with a nanoantenna that are repeatable (or correlated) across a population. SPM configuration (that I will use in my experiments) offers dynamic range and nanoantenna effect investigation of the very same single molecule, thus bypassing molecule-to-molecule variation issues. Nanoantenna approached above the surface of the sub-30 nm pT is expected to work in a weak coupling regime. Emission and excitation are expected to be enhanced due to the increase of LDOS (Purcell and reciprocity rule). Alteration of the singlet state dynamics was already studied with a nanoantenna by Sandoghdar group, but a full model of T/pT was not solved. If hybrid states are not formed, then triplet dynamics shouldn't be affected by EGL. The Purcell effect is expected to accelerate the S1-S0 electronic transition but not vibrational relaxation in S1 state. It is not obvious how the triplet population will change, as according to El-Sayed rules and experimental studies, a vibrational mode is expected to participate in ISC of T.

Finally, single-molecule studies report rates that vary from molecule to molecule and also between studies. This is not just a case of T/pT, but also of T in anthracene or even as popular dyes such as Rhodamine 6G. In the next Section, I will have a closer look at how rates are calculated and verify if, in the case of T/pT, using different models results in calculating different rates.

1.4. Molecule as a single photon emitter

In the Sections above, I've presented fundamental concepts of photophysics, as well as particular properties of T/pT system and nanoantenna effect. Now, I move on to the discussion of photon statistics, and when required, I refer to the information gathered on T/pT to investigate the expected behavior of this system.

Light consists of photons, and the temporal behavior of a photon flux can be used to determine the statistical properties of the light (photon statistics). Single molecules belong to the group of single emitters, which is a subcategory of single photon sources. They constitute of isolated systems that are deterministic (photons emitted on demand by external control), such as single atoms and ions, color centers, single molecules, quantum dots, and mesoscopic quantum wells [159]. Photon sources can be classified based on their photon statistics.

1.4.1. Fundamentals of photon statistics

A single molecule with a radiative deexcitation is a light source. Yet, its statistics differ from other typical light sources such as a laser or a black body. Emitted photons are numerous realizations of a cycle (primary process). In the scope of photon statistics, the rate of every transition contributing to the cycle is a random variable having a well-defined probability space. In consequence, emission events have a particular distribution of spacing in time.

1.4.1.1. Classification

In this subsection, I very briefly introduce a more profound treatment of photon statistics based on [6,160]. The electromagnetic field consists of photons whose number is discrete, and so is the field. I limit myself to a case of light in an optical cavity with a single mode (wavevector). The energy of the electric field can be treated as a quantum harmonic oscillator having energy levels E_n given by:

$$E_n = \left(n + \frac{1}{2}\right)\hbar\omega \qquad 1.21$$

Where $\hbar\omega$ is a quanta of electromagnetic field energy. In this context, transition results in photon creation (n+1) and annihilation (n-1) and the number of photons refer to state's number n. Absorption and emission events can be viewed as such changes in the state's number. Mean photon number $<n>$ can be evaluated if the source is observed over a period longer than any characteristic timescale (photophysics). Shot noise is a fluctuation of photons number (variance) emitted by a source. A coherent source of photons with a time-independent intensity has a probability distribution that takes a form of a Poisson distribution $P(n)$ with a variance Δn that is considered a shot noise limit:

$$P(n) = \frac{\langle n\rangle^n}{n!} e^{-\langle n\rangle} \qquad 1.22$$

$$\Delta n = \langle n\rangle^{\frac{1}{2}} \qquad 1.23$$

Plank photon probability $P_T(n)$ follows the Boltzmann distribution and describes a thermal source with a variance Δn_T (fluctuations):

$$P_T(n) = \frac{\langle n\rangle^n}{(1+\langle n\rangle)^{1+n}} \qquad 1.24$$

$$\Delta n_T = \langle n\rangle + \langle n\rangle^2 \qquad 1.25$$

Fluctuations are used to classify light sources based on their statistics. Super-Poissonian, Poissonian, and Sub-Poissonian statistics refer to noise above, equal, and below the shot noise limit. A sub-Poissonian source has a noise smaller than a source with constant intensity and is viewed as a quantum property. In the next subsection, I will have a closer look at the temporal behavior of those sources.

1.4.1.2. Antibunching and bunching

Probability distributions of light sources imply a particular temporal behavior of the photon flux. Figure 1-13 represent probability distributions (left) and photons as a function of time (right) for 3 different sources, all fixed to $\langle n\rangle$=5 within the time interval.

Single-photon emitter is a theoretical source with a constant time difference between 2 subsequent photons, while coherent light and thermal light have to follow distributions presented above in Equations 1.22 and 1.24, respectively. Herein, I refer to the time difference between two subsequent photons as interphoton time. All 3 sources have a very different interphoton time, which is constant for a single-photon emitter (blue) but tends to be more and more grouped in the case of coherent (green) and thermal light (orange). The second-order coherence function can be applied:

$$g^{(2)}(\tau) = \frac{\langle I(t)I(t+\tau)\rangle}{\langle I(t)\rangle^2} \qquad 1.26$$

This function expresses how light intensity I at the given time t is correlated with itself after a delay τ. The value of$g^{(2)}$ at different delays reflects photon grouping. If $g^{(2)} < 1$ or > 1 incoming flux is antibunched or bunched, respectively. The antibunching is observed within fluorescence lifetime regime, while bunching is observed in the regime of the emitter's blinking (intermittency). Under the slow ISC approximation, it is ensured that antibunching regime is a few orders of magnitude faster than the bunching regime.

At a zero-delay time, $g^{(2)}$ takes values of 1 for a coherent light, 2 for a thermal light, and *(n-1)/n* for a quantum light source, where *n* is a discrete number of photons in a *n* energy levels as described in Equation 1.21 (Fock state, to be more precise). A single molecule can be viewed as having one state. Its $g^{(2)}(0) = 0$ which means that photons always arrive one by one, regardless of light intensity. In practice, $g^{(2)}(0) = 0{,}5$ is used as a generally accepted limit that proves single photon nature of the emitter.

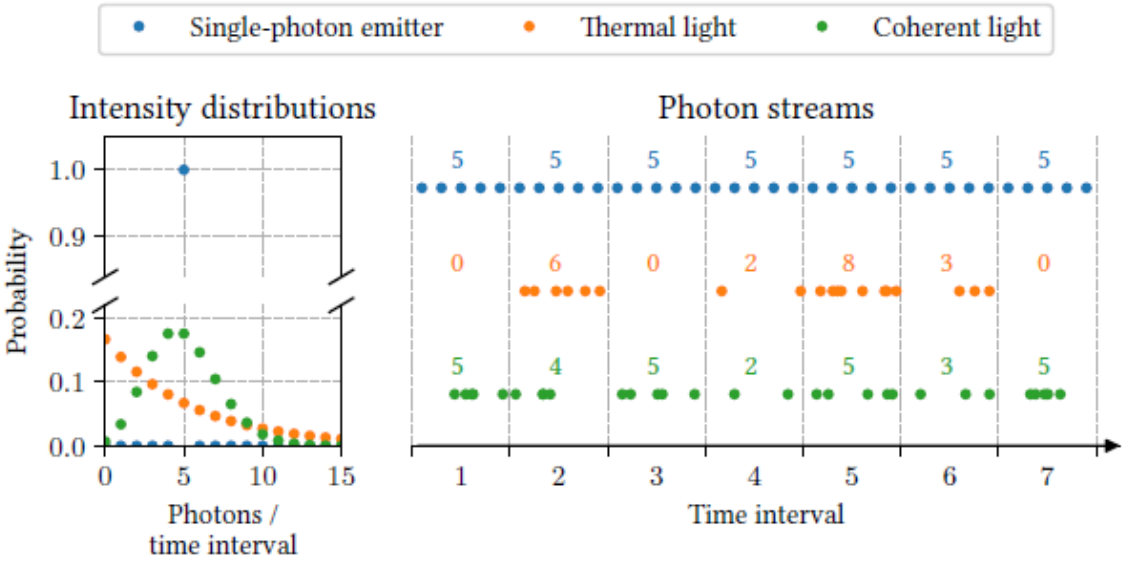

Figure 1-13. Probability distributions (left) and photons depicted as a function of time with their number within each time interval for 3 light sources Single-photon emitter (blue), thermal (orange), and coherent (green) [[160]*].*

1.4.2. Model considerations

Now that we have seen some general properties of a quantum light source, such as antibunching and bunching, I apply information on the photophysics of T/pT to review mathematical models. In Figure 1-14, I present some mathematical models used in single-molecule studies – A) a 2-level system, B) a 3-level system with a monodirectional 2-3 pathway, and C) a 3-level system with a bidirectional 2-3 pathway. Model C) looks a lot like Figure 1-5 (the Jablonski diagram of T/pT) since rISC is incorporated as 3-2 pathway. In the literature, T/pT is treated as a model B). However only 1 of the studies [161] has compared an experimental photon flux with a calculated photon flux (imposed by calculated rates). First, I will recall the meaning of the rates seen in Figure 1-14, and later on, I will investigate models B) and C) and verify if that for T/pT these 2 models are equivalent, even if they seem conceptually different.

In the mathematical model, states are reduced to levels *L*. Rate k_{12} is an excitation rate of the system - transition from a ground state S0 to first excited singlet state S1. This rate depends on the pump intensity and molecule absorption cross-section. Rate k_{21} is a spontaneous emission rate – transition from S1 to S0 being a sum of non-radiative k_{NR} and

radiative relaxation k_R. For molecules with QY_R close to 1, k_{21} occurs through VR-F, and in case of QY_R close to 0, it yields the rate of IC-VR. In thin films (Table 1-2) F in T/pT occurs within 15-25 ns and is more than 100 times slower than typical VR (ps regime). Rate k_{23} is an ISC rate and corresponds to S1-T1 transition (ISC-VR). As mentioned earlier, T/pT is a near-unity quantum yield emitter, and thus k_{NR} is around 100 times slower. Rate k_{32} involves a sequence from T1, through T5/6 to S1, while k_T is a direct T1-S0 transition without intermediate electronic levels.

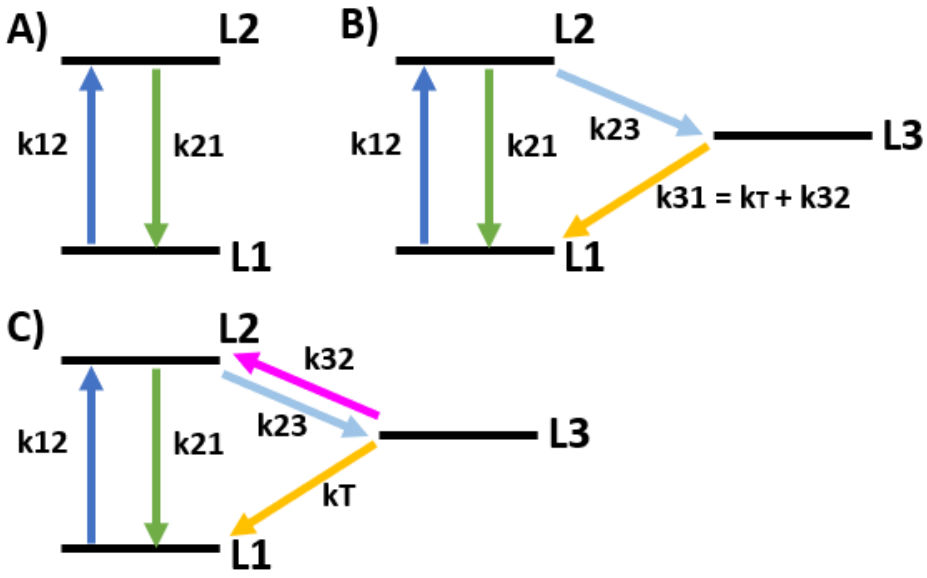

Figure 1-14. Typical mathematical models used in photon statistics studies: 2-level system (A), 3 level with uni- (B) and bidirectional (C) pathway between levels 2 and 3.

Model C) differs from model B) as triplet depopulation k_{31} is separated into k_T being a direct transition between the triplet and ground state, while k_{32} is a pathway from the triplet to the excited singlet state.). Solutions for model B) are well-known in the literature [20,160], and scientific community commonly takes advantage of slow ISC approximation [32,158,162–164].

Treatment of model C) is analogical to the model B) (Appendix C), but the state dynamics is written as:

$$\frac{d}{dt}L1(t) = -k_{12} * L1(t) + k_{21} * L2(t) + k_T * L3(t) \quad 1.27$$

$$\frac{d}{dt}L2(t) = k12 * L1(t) - (k_{21} + k_{23}) * L2(t) + k_{32} * L3(t) \quad 1.28$$

$$\frac{d}{dt}L3(t) = k_{23} * L2(t) - (k_{32} + k_T) * L3(t) \quad 1.29$$

Transition *L3-L1* for model C) is abbreviated as k_T to avoid confusion with rate k_{31} of model B) (Appendix C). The formulas for the parameters *P* and *Q* change accordingly:

$$P = k_{12} + k_{21} + k_{23} + k_{32} + k_T; \quad 1.30$$

$$Q = k_{12}(k_T + k_{32} + k_{23}) + k_{23}k_T + k_{21}(k_T + k_{32})$$

In the case of T/pT, slow intersystem crossing approximation is commonly used ($k_{12}, k_{21} >> k_T, k_{32}, k_{23}$) [162]. The solutions within the slow ISC approximation:

$$\lambda_2 = -(k_{12} + k_{21}) \quad 1.31$$

$$\lambda_3 = -(k_{32} + k_T + \frac{k_{12}\,k_{23}}{\lambda_2}) \quad 1.32$$

$$A = \frac{k_{12}k_{23}}{(k_{32} + k_T)\lambda_2} \quad 1.33$$

Note that correlation function parameters within slow ISC are identical for model B) and C) as term $(k_{32} + k_T)$ substitutes for k_{31} (Appendix C). However, photon flux is not identical as part of the T1 returns to the bright S1 state. The photon flux of the models B) and C) was compared using population method and Monte Carlo simulations in Appendix

D to show that difference. It was proven therein that photon flux difference (for typical rates of T/pT) is negligible (0,2%) and formula of model B) can be used:

$$F = \frac{k_{12}k_R k_{31}}{\lambda_2 \lambda_3} \tag{1.34}$$

That yields identical photon flux as formula of model C) in the slow ISC approximation (Appendix D):

$$F = \left(\frac{1}{k_{21}} + \frac{1}{k_{12}}\right)^{-1} \left(\frac{1}{1+A}\right) \frac{k_R}{k_{21}} \tag{1.35}$$

1.4.3. Telegraph parameters

If one uses a single molecule as a light source, it is more intuitive to discuss quantities originating from the implications of those rates on the temporal behavior of the photon flux. The light source made of a single molecule with bright and dark transitions has periods, when it does and doesn't emit photons, so called fluorescence intermittency. The light source that spends a lot of time not emitting photons is not very applicable. It's thus much more straightforward to recalculate those so-called telegraph parameters from the rates. Exemplary 'telegraph' signal of the photon emission events in time is presented on Figure 1-15.

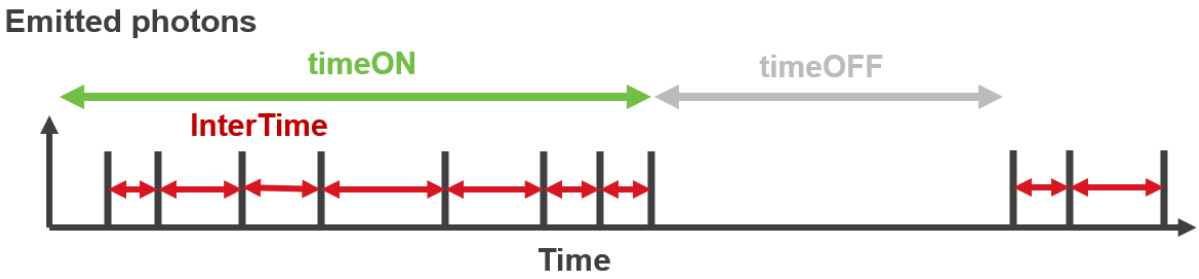

Figure 1-15. Exemplary behavior of photon emission events in time and telegraph parameters such as InterTime – time between subsequent photon emissions, timeON – interval of repeatable photon emissions and timeOFF – interval of no photon emission events.

Using slow ISC approximation, I reconstruct parameters such as *timeOFF*, *timeON*, $timeON_{flux}$, *totON*, which refer to:

1) average duration of time that light source spends not emitting light (*timeOFF*)

2) the average duration of time that the source spends emitting on repeat (*timeON*)

3) number of photons emitted within average *timeON*

4) fraction of total time that light source spends in *timeON*

$$timeOFF = \frac{1}{k_{31}} = \frac{1}{k_T + k_{32}} \tag{1.36}$$

$$timeON = \frac{1}{k_{23}}\left(1 + \frac{k_{21}}{k_{12}}\right) \tag{1.37}$$

$$timeON_{flux} = C_{EFF}\frac{k_{21}^R}{k_{23}} \tag{1.38}$$

$$totON = \frac{timeON}{timeON + timeOFF} = \frac{1}{1 + A} \tag{1.39}$$

Note that all the equations above are identical for model B) and C) (within slow ISC approximation).

1.4.4. Summary

In this Section, I've presented the basics of photon statistics and introduced models that are used to describe T/pT photophysics. I've chosen a model based on T/pT photophysics to write the set of differential equations that describes the population dynamics (under the slow ISC approximation), which is a classical treatment found in the literature. I've compared this classical differential equation approach with the ''population-approach'' that interprets the photon flux as series of Markov process realizations (Monte Carlo

simulations). Under slow ISC approximation, models B) and C) are nearly identical (0,2% photon flux difference) and their solutions to the set of differential equations of population dynamics (under the slow ISC approximation) are also. Finally, rates are translated into intuitive quantities that describe the light source behavior in time as the telegraph signal with bright and dark periods, and the fraction of time spent in the bright period.

Chapter 2

To carry out experiments on a single molecule, a complicated optical set-up is required. Such a set-up becomes even more complicated, when one wants to finely control the position of a nanoantenna (attached to the probe), with respect to a single molecule by using Scanning Probe Microscopy (SPM) technique. Additionally, this set-up needs to be automatized in order to perform various measurements on a single molecule with and without nanoantenna prior to photobleaching.

To understand how rates are calculated and how the orientations of the transition dipole moments are found, a reader must be familiar with Time Tagged Time-Resolved (TTTR) measurements and the field distribution in sub-30 nm pT. The molecules presented in Chapter 3 are measured with Power, Polarization and Analyzer Scans. Those Scans require introduction, because measurement protocol differs from typical single-molecules studies that collect TTTR measurements at a couple of different excitation intensities.

To perform those Scans a user much be able to dynamically control the power and polarization of the laser beam. For the field distribution simulation/calculation, The Point Spread Function (PSF), angle of incidence at the sample and k-vector space of the incident beam must be verified experimentally. To measure the fluorescence spectrum and Scans on the very same single molecule, automatized and fast switching between different modes is required (attaching the optical components to motorized- and flip-mounts). To ensure good signal-to-noise ratio (SNR), spatial and spectral selections are necessary by introducing pinholes and filters. Finally, to avoid manipulation-induced mechanical drifts, which are crucial for emitter-nanoantenna measurements, all the translations on the sample and (ideally) measurement mode changes should be controlled from a CPU.

Moreover, this chapter contains details on the fabrication and characterization of the probe and sample, as well as SPM system used to align the probe (nanoantenna) with a single molecule and keep it fixed for the time measurement (~1 minute). The concept of keeping two objects fixed at nanoscale is very debatable, so it's necessary to investigate the magnitudes of different drifts and assess the acceptable range.

If the reader is experienced with the single-molecule studies and SPM, Chapter may be skipped, besides Sections 2.1.4 and 2.1.5 that are necessary to understand results presented in Chapter 3 and 4.

2. Materials and Methods

2.1. Optical set-up

2.1.1. Major blocks

The optical set-up is very complicated and rather than discussing the components in the optical path, its easier to identify blocks (composed of components) that are used to perform specific operations – Figure 2-1. Overall, for the scope of the study it is necessary to:

1. Power control – controls the power and polarization of the incident beam
2. Beam shaping - control the beam at the input of the microscope objective (divergence, diameter, Gaussian beam profile, polarization)
3. Imaging mode - switches between various light sources, controls the angle of incidence at the sample and the k-vector space of the beam
4. Sample stage – micromanipulation and nanopositioning
5. Detection path – switches between planes (image, Fourier), and various measurements (optical image, spectroscopy, TTTR measurements) with spatial and spectral selection (pinhole and filters)

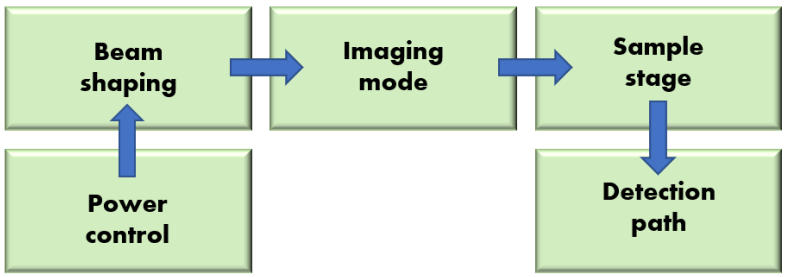

Figure 2-1. Block diagram of the optical set-up.

2.1.2. Full scheme

The full scheme optical set-up is presented in Figure 2-2. and its legend in Figure 2-3. Note that elements constituting major blocks are not always in chronological order, e.g., the laser line filter belongs to beam shaping but is placed close to the sample stage as autofluorescence accumulates throughout the path.

Power control unit is composed of the laser (532 nm) and motorized half-wave plate and the fixed polarizer (analyzer) that allows precise and dynamic power adjustment. Beam shaping is composed of the single mode optical fiber for mode-cleaning, telescope (optional) to control beam diameter and divergence laser line filter to cut autofluorescence. Imaging mode is composed of a mirror to switch between light sources, wide-field lens on a flip and mirror on the translation to focus (or not) the beam in the back-focal plane of the objective (wide-field or focused beam illumination) and adjusted the angle on incidence onto a sample to switch between normal incidence and Total Internal Reflection Fluorescence (TIRF). Sample stage serves as a holder and besides the microscope objective, it has micrometer screws to make large displacements on the sample and piezoelectric stage for displacement with nanometer precision. Detection path is composed of telescopes to switch between image plane and Fourier plane (direct space and k-vector space), pinhole and filters for spatial and spectral selection, beam-splitter to sent 10% of the signal to the camera (to observe optical image) and motorized mirror to switch between TTTR measurements and spectroscopy.

The characterization of the optical set-up such as: laser stability, direct space on camera, point-spread function, spectrophotometer calibration were all performed and gave respective values: <2%/h, 64 pixel/μm (100X, oil objective) at binning 1, FWHM=1,5 μm (TIRF lens 50 cm, oil objective 100X) and λ=-8.52$\frac{nm}{pixel^2}$x^2 + 0,21$\frac{nm}{pixel}$x + 508nm for grating 600mm, blazed at 500nm and position 610.

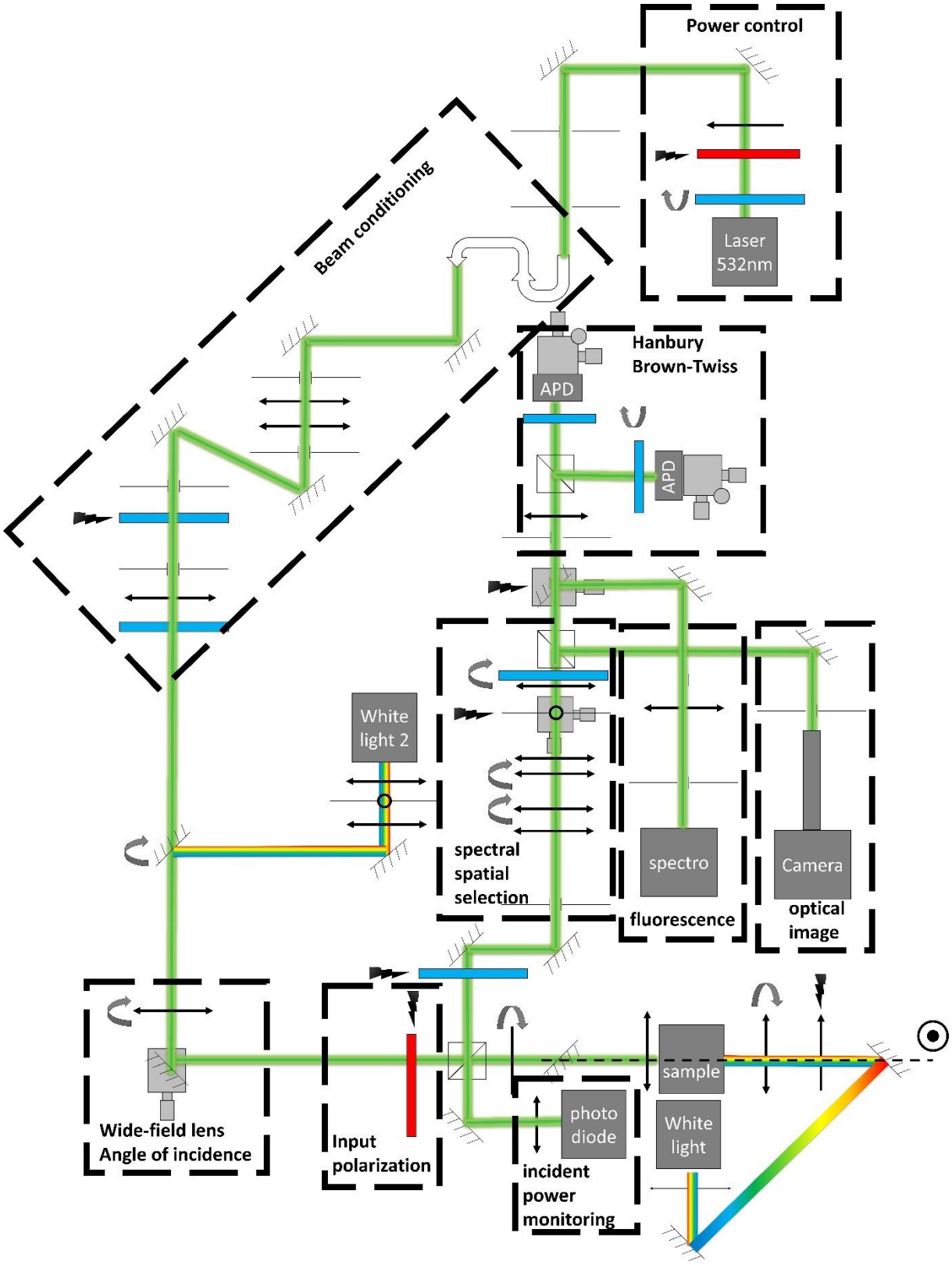

Figure 2-2. Scheme of the optical set-up with particular functionalities marked in dashed boxes with the descriptions.

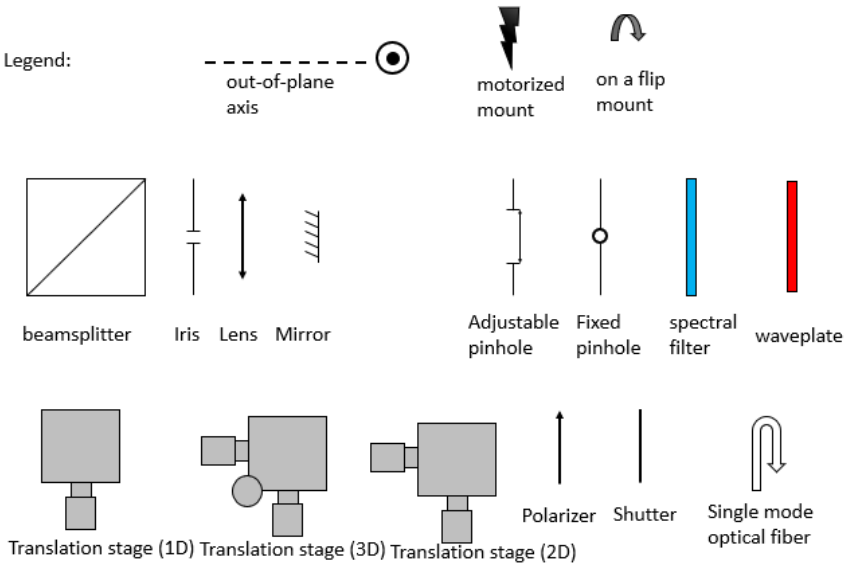

Figure 2-3. Legend of the symbols used for optical components in the optical set-up scheme.

The models and manufacturers of the most important devices/components used can be found in Table 2-1.

Table 2-1. Manufacturers and models of the most important components and devices.

Components and devices	model
Laser	532nm
Laser spectral cleaning	Semrock LL01-532-12.5
Laser polarization cleaning	Glan-Thompson polarizer
Microscope objective	Olympus, 100X, NA 1.3
Beam splitters	Thorlabs BS013/022/025
Laser cut-off filter	Semrock LP03-532RE-25

Camera	Hamamatsu Orca Flash 4.0
spectrophotometer	Andor Shamrock 193i + Andor iDus DU401A-BVF
Photon counters filters	Semrock 632/148 BrightLine HC
Photon counters	SPCM-AQRH-16
Time Correlated Single Photon Counting module	Picoharp 300
Scanning Probe Microscopy module	Nanonis BP3 + PI P-620.ZCL
Nanopositioning sample stage	MadcityLabs Nano-PDQ

2.1.3. Time Tagged Time-Resolved measurements

To understand jargon used throughout the manuscript, reader must be familiar with the Time Correlated Single Photon Counting (TCSPC) technique and some definitions I introduced herein.

TCSPC is a technique that allows assigning the time of an event (photon detection or pulsed laser trigger) and detector ID (for multiple detectors). Instrument Picoharp 300 used herein does so with 4 ps resolution. To perform TTTR measurements typically Hanbury Brown-Twiss (HBT) configuration is used (marked in a dashed box in Figure 2-2) – 2 single photon counters are aligned with 50/50 beam splitter (pinholes and filter for stray light/background reduction). Herein, I work with continuous-wave laser at 532 nm.

Some definitions are required to understand data treatment of TTTR measurements:

- Macrotime – time measured since the start of the measurement that every event is being assigned
- Deadtime – period of time for which detector becomes irresponsive after the detection event (90 ns)
- Intrachannel time– Macrotime difference if 2 subsequent detection events are on the same channel
- Interchannel time – Macrotime difference if 2 subsequent detection events are on different channels
- Interphoton time – Macrotime difference between subsequent detections events, regardless of the channel
- Timetrace – detection events grouped with an arbitrary bin size and plotted against the Macrotime
- PhotonPair (PP) –2 subsequent detection events with time window with an upper limit of $\frac{1}{C_{EFF}k_{21}}$ [165] (herein, typical C_{EFF}~0,05% and k_{21}=50 MHz, yields a window of 100 ns)
- START-STOP – histogram of PhotonPairs, where each PP is assigned its interphoton time

For the more intuitive understanding, timetrace with the definitions is presented in Figure 2-4.

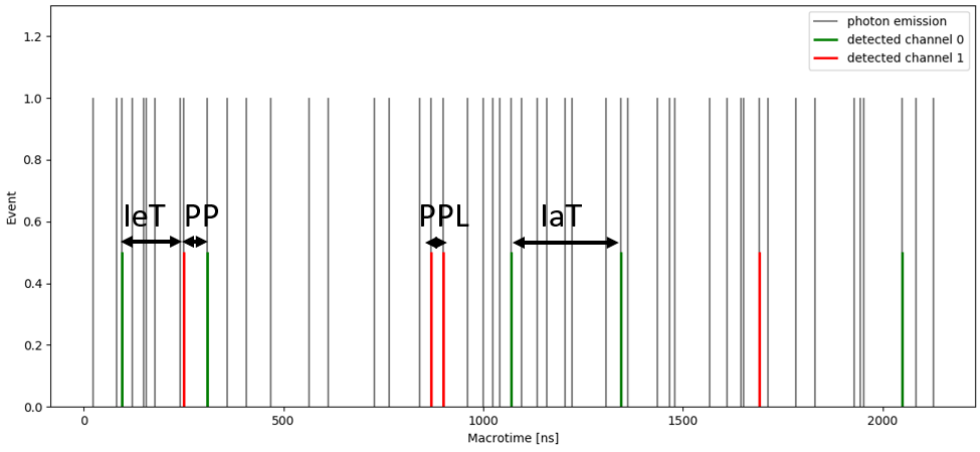

Figure 2-4.Timetrace (bin size 1 ns) of simulated photon flux showing photons emitter by an emitter (grey), photons detected on channels 0 and 1 (green and red), Interchannel time

(IeT), Intrachannel time (IaT), PhotonPair (PP), PhotonPair lost as intrachannel<deadtime (PPL),

2.1.3.1. START-STOP

As briefly explained above, START-STOP is simply a histogram of PPs (Y-axis), where each PP has its own interphoton time (X-axis) - Figure 2-5. To create such histogram, interphoton times must be discretized with a certain bin size (don't confuse with TTTR resolution). In order to get a good fit of the antibunching curve (monoexponential function) bin size is kept at least 5-fold smaller than the fitted time constant ($1/\lambda_2$). Confidence level is difficult to assess, because the statistical noise in START-STOP is also complicated to evaluate.

In order to approximate the antibunching part of a $g^{(2)}(\tau)$ correlation function with a START-STOP measurement, certain time window must be applied. This window cannot be smaller than 5 times the investigate time constant (so that the exponential reaches a plateau) and cannot be larger than $\frac{1}{C_{EFF}k_{21}}$ used [165].

Additionally, one has to ensure that the time interval of 3 (or more) photons isn't counted as the time interval between 2 photons. To do this, I take advantage of the Monte Carlo simulation that I've developed in Chapter 1. To verify if START-STOP is consistent with the $g^{(2)}$ at the time window of 100 ns, I plot the START-STOP simulation and overlay it with the theoretical formula.

I ran the simulation for 3 different k_{12} (10 MHz, 50 MHz, and 150 MHz) and constant $k_R = k_{21} = 50\ MHz$. The set-up C_{EFF} of 0,05 was used. The results are shown in Figure 2-5. Interphoton times are calculated as positive for a PP of channel 0 before channel 1 sequence and negative for a PP of channel 1before channel 0 sequence. Both yield consistent antibunching parameters λ_2 within the fit error. Between the theoretical and experimental λ_2, there is a mismatch of 3%, 7% and 0%, for each k_{12}, respectively.

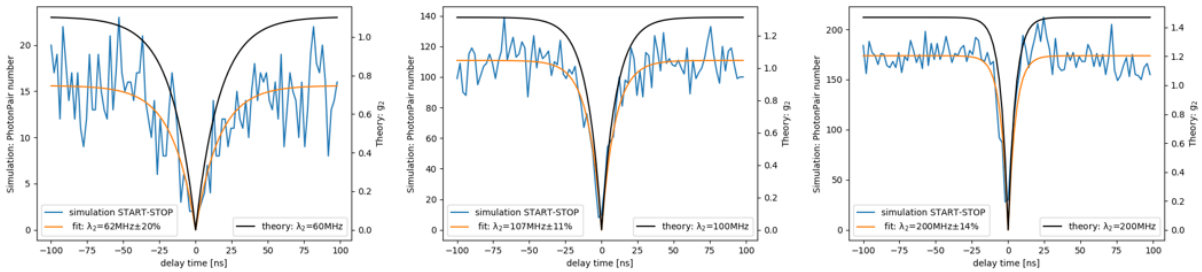

Figure 2-5. START-STOP measurements of the simulated photon flux (blue), fit of the START-STOP measurement (orange) and theoretical g_2 function (black). Rates used for the simulation $k_{12} = 10\ MHz$ (left), 50 MHz (center) and 100 MHz (right), other rates kept constant: $k_{21} = 50\ MHz$, $k_{23} = 15\ kHz$, $k_{32} = 21\ kHz$ and $k_T = 3\ kHz$. Set-up C_{EFF} set to 0,05. Window set to 100 ns.

Naturally START-STOP (histogram of PPs) and g_2 (correlation) have different y-axis units. It is possible to convert START-STOP measurement into $g_M^{(2)}$ by performing normalization according to Kurtsiefer et al. [166]:

$$g_M^{(2)} = \frac{\text{START} - \text{STOP}}{2R_1R_2} * \frac{ACQ}{bin\ size} \qquad 2.1$$

Where, R_1R_2 is the product of counts on each detector in HBT configuration, ACQ is the measurement acquisition time. Subsequently $g_M^{(2)}$ is the measured correlation function (background-biased) and relates to pristine (background-free) $g^{(2)}$ as given in Sontheimer [160]:

$$g_M^{(2)} = \frac{g^{(2)} + 2b + b^2}{1 + 2b + b^2} \qquad 2.2$$

Where $b = \frac{1}{SNR} = \frac{R_{pT}}{R_{T/pT}}$ is the inverse of signal-to-noise ratio (SNR) and thus ratio of the counts collected from pT (background) and collected from the emitter (T/pT).

2.1.3.2. PhotonPair Fraction

As mentioned in Chapter 1, to verify the rates calculated, I will compare experimental flux with the flux that those rates should yield. To do this, I need to know set-up C_{EFF} and k_R/k_{21}.

To the best of my knowledge, there is no analytical expression that calculates the number of PP given the rates of the emitter. Similarly to the subsection above, I take advantage of Monte Carlo simulation to find an approximate value of the product of $C_{EFF} * k_R/k_{21}$ using the PhotonPair Fraction (PPF), which is a percentage of all the photons detected that are counted as the PP. Note that PPF is independent of the rates related to the triplet population if the number of photons detected during $timeOFF$ (background of stray light photons) is negligible. For the exact value of $C_{EFF} * k_R/k_{21}$ background should be accounted for.

In Figure 2-6, I plot PPF as a function of k_{12} for $k_{21} = 50\ MHz$ and $C_{EFF} * k_R/k_{21}$ of 0.05. As the excitation rate increases, PP makes up for a bigger and bigger fraction of the total photons detected. In Chapter 3, I will use the presented here PPF method to prove that sub-30 nm T/pT system can be approximated with the ideal case in the low power regime, and set-up's C_{EFF} can be calculated (assuming T/pT is a near-unity quantum yield system).

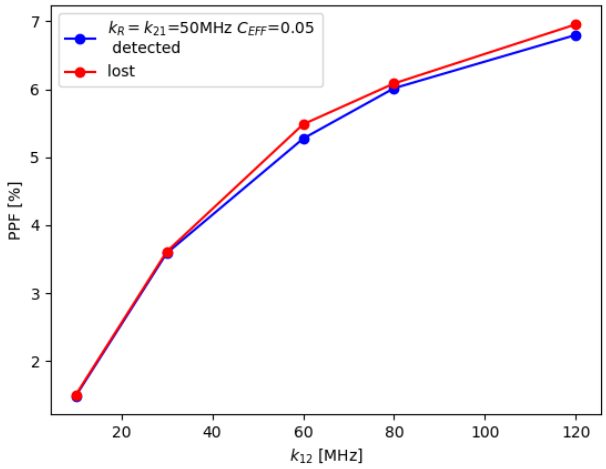

Figure 2-6. PhotonPair Fraction (PPF) for a near-unity quantum yield emitter at C_{EFF}=0.05 and k_{21}=50 MHz as the function of k_{12} that was detected (blue) and lost in the deadtime (red).

2.1.3.3. Counts correction

To match the theoretical and experimental counts, I also have to account for the counts lost in the deadtime. If intrachannel time is smaller than the deadtime, the second photon is lost (not counted). Flux lost can be approximated very intuitively –if the 1st photon is detected, then 2nd photon detected has a 50% chance to be incident on the same channel (photon lost) or different channel (PP). Therefore, lost flux is at least equal a to the number of PP detected. Lost flux will be slightly bigger because of the Nth photon that is incident on the detectors after 2 photons made a PP (both are in the deadtime). In my set-up and T/pT, only the 3rd photon is non-negligible term (lifetime ~20 ns, deadtime ~90 ns, C_{EFF} ~0,05).

Once again, I can use the Monte Carlo simulation to track fraction of the photon flux that would be lost experimentally as a function of k_{12} and fixed $k_{21} = 50\ MHz$. I present the result in Figure 2-6. PPF detected (blue line) is slightly smaller that the PPF lost (red line) in the large power regime ($k_{12} = \sigma_{12} * I$) but almost identical in the low power regime due to that 3rd photon term.

While Monte Carlo simulation is the most precise way to get counts lost in the deadtime, there is an approximation of this loss according to Sontheimer [160]:

$$R_{corr} = \frac{1}{1 - R_M \tau_{DEAD}} R_M \qquad 2.3$$

Where R_{corr} and R_M are deadtime-corrected and measured counts on the detector and τ_{DEAD} is the deadtime. I refer to this formula as an approximation as it is inherently independent of the photon statistics. I can take an abstract example of a pulsed laser source with 100 ns repetition period, which would result in 10 MHz counts but no loss (deadtime 90 ns). Meanwhile, Monte Carlo simulation depends on the rates of the emitter (photon statistics) and thus is plotted as a function of excitation rate (k_{12}) for fixed emission rate (k_{21}) and fixed C_{EFF}. Nevertheless, both methods yield nearly identical deadtime correction in counts – Figure 2-7. Throughout the manuscript Equation 2.3 is used for counts correction, because both corrections are identical, while Monte Carlo simulation is computationally very expensive.

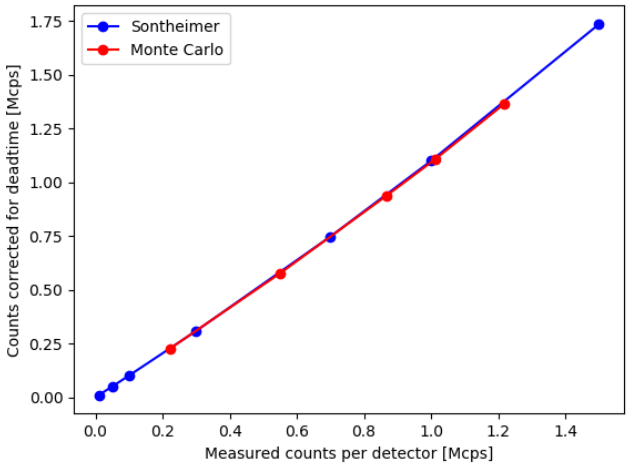

Figure 2-7. Counts corrected for deadtime as a function of counts measured by a detector with 90 ns deadtime according to the Monte Carlo simulation and Sontheimer [[160]*].*

2.1.4. Measurement types

Throughout this manuscript there are several measurement types discussed such as Power Scan, Polarization Scan and Analyzer Scan. Those Scan characterizes emitter in domains of excitation intensity and space. Thus, they allow to calculate the transition rates with a (slightly modified) typical approach found in the literature (Power Scan) and to find the orientation of the excitation transition dipole moments with their cross-sections (Polarization Scan). However, relaxations and horizontal transitions are independent of the excitation polarization, thus the orientation of the emission dipole has to be measured separately (Analyzer Scan) and serves as a validation of Angle Scan results.

2.1.4.1. Power and Polarization Scans

The idea behind Scans comes from the concept of the so-called ''photon budget'', which is the number of photons that a single molecule emits prior to photobleaching, or changing its photophysics (unexplained changes in the photon statistics, which may come from spectral jumps, photodamage etc.). To conduct good experiments, one has to mindfully distribute this photon budget across various measurements (fluorescence, TTTR etc.). Typical Power Scan records a total of 10^8 counts, while Polarization Scan around half of that. For experiments with the nanoantenna, those scans are carried out 3 times to get

pre-, approached and post- measurements (sometimes even repeated again). I estimate that total number of counts detected is a bit shy of 10^9. As will be shown in Chapter 3, set-up C_{EFF}~0,045, which means that the total number of photons emitted by molecules is the order of 10^{10}. This is an extraordinary photostability, but still not an infinite number. The measurements need to be not only quick and automatized, but each measurement needs to have parameters (speed, power range, acquisition time) adjusted to collect as little photons as required to perform fits and calculations with acceptable uncertainties.

Power and Polarization Scans are simply TTTR measurements at different incident excitation power and excitation polarization, respectively. However, those measurements are not taken as a series of separate measurements but rather as two measurements (either power or polarization is varied continuously). Subsequently, those measurements are separated into smaller ''measurements'' by dividing the acquisition time into time segments (data points) and treating them separately. The main motivation behind this approach is that the emitter is monitored continuously, and thus any spectral instabilities are readily visible. This is a great advantage compared to taking several measurements, each at different but fixed power (or polarization).

In the sequence of several measurements, the emitter is not observed in-between measurements and spectral instabilities are visible only after fully treating the file, which is not efficient. Also, the time in-between measurements is not negligible compared to the measurement acquisition time and results from communication between devices (Picoharp, motorized translations and rotations, CPU), but this technical discussion is beyond the scope of this work. In short, Scans perform a TTTR measurements synchronized with a motorized element that varies power (or polarization) continuously and thus they are very time-efficient and robust.

Evolution of the excitation power P and excitation polarization angle α_{EXC} for each Scan is shown in Figure 2-8. Polarization Scan is slightly simpler as half-waveplate rotates with a constant angular velocity (20 deg/s) at fixed incident power. The polarization angle α_{EXC} is defined as twice the angle readings on the half-waveplate. Power Scan is a bit more complicated, because it has somewhat of a bell-shape. Such a shape is due to the fact that incident power range has A) lower limit set by number of PPs required to build START-STOP histogram that can be fitted reliably B) upper limit set by photodamage to the

matrix. To get low uncertainty in the calculated rates its important to measure as wide power range as possible. And thus, Power Scan shape comes from the power-dependent acceleration (gradient of incident power change [mW/s]) so that the measurement spends more time in low power regime (more data points), but rapidly goes through high power regime (avoids photodamage). More precisely, accelerates with 1 deg/s^2 from the lowest power, up to the maximum velocity set to 10 deg/s and subsequently deaccelerates with 1 deg/s^2. Additionally, Time Scans are taken (fixed power and polarization) to verify emitter photostability prior to including the emitter in the dataset.

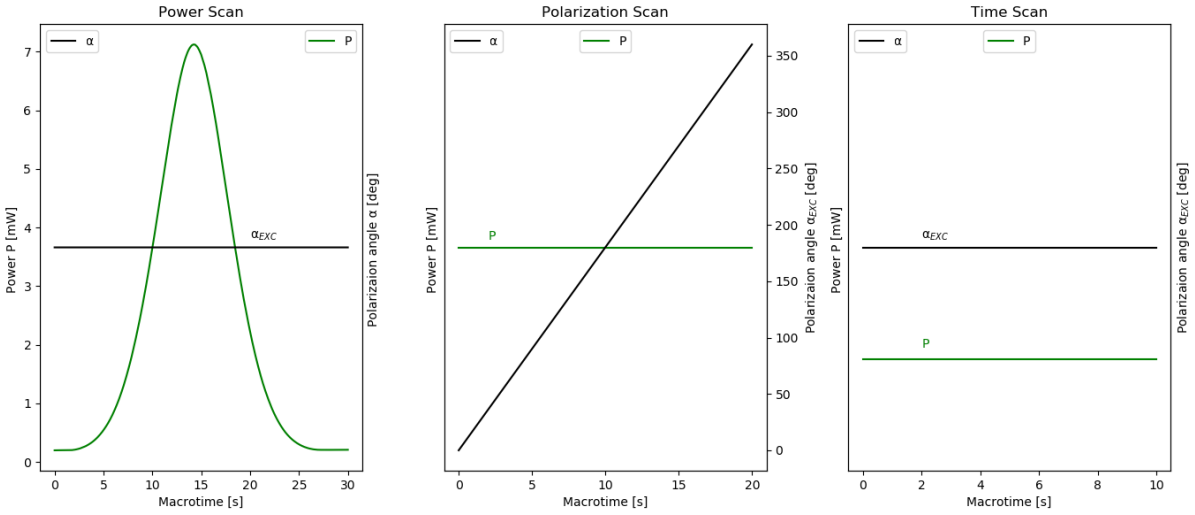

Figure 2-8. Incident excitation power (P) measured on the photodiode and the excitation laser polarization angle (α_{EXC}) during Power Scan (left), Polarization Scan (center) and Time Scan (right).

There are also other advantages of Power and Polarization Scans such that they directly show if there is a hysteresis in the system. As seen in Figure 2-8, excitation power is varied up and down, polarization is varied by 2 periods of cos^2 (360 deg). This is useful for measurements on the molecule alone (photodamage) and crucial for measurements in the nanoantenna-emitter systems as mechanical drift (spatial misalignment) is readily seen with hysteresis.

Typical protocol for a measurement of the emitter alone:

1) Polarization-resolved excitation
2) Fluorescence spectrum

3) Analyzer Scan
4) Power Scan
5) Polarization Scan
6) Bring in the tip, tip raster-scan (if emitter-nanoantenna)
7) Repeat 3 or 4 (if emitter-nanoantenna)
8) Retract the tip, repeat 3-4 (if emitter-nanoantenna)

Step 1 is used to find and fix the excitation polarization at the maximum counts (best SNR). Step 2 allows the assignment of the molecules to spectral subpopulations later on. Step 3 is used to find the emission dipole moment. Steps 4-5 are the measurements from which rates are calculated. Steps 6-8 are done if the experiments with a nanoantenna are carried out, then steps 3-4 become a pre-approached, step 6 is used for alignment, step 7 is the approached and step 8 the post-approached measurement.

Prior to proceeding with the measurement protocol, height of pT thin film is measured. The protocols omit some obvious but necessary practical steps like placing the molecule in the center of the laser spot, placing the pinhole, adjusting the focus, etc.

To sum up, there are technical and physical limitations to the single-molecule experiments. Scans can be finely adjusted to work in the optimal conditions required for high quality measurements.

2.1.4.2. Analyzer Scan

Analyzer Scan is a polarization-resolved emission (fluorescence) – analyzer is placed in front of the detector and counts are measured, while analyzer rotates. The emission is collected by the objective with a focal plane in XY. Detected photon flux R as a function of the analyzer angle α_A and can be fitted with a formula:

$$R(\alpha_A) = R * \cos^2(\alpha_A - \beta) \qquad 2.4$$

Where β is α_A at which counts reach maximum value. Subsequently, according to Fourkas [73], that assumes a radiating dipole placed in the homogenous environment, this can be used to calculate polar and azimuthal angles of the emission dipole moment (θ and φ).

The S0-S1 and S1-S0 transition dipole moments are collinear in the molecules with D_{2h} symmetry (such as terrylene).

2.1.5. Field distribution

To find the absorption cross-sections in Chapter 3, intensity at the location of the emitter should be known, but it's not measurable experimentally. The analytical expression (by Simon Vassant) and simulations (by Ludovic Douillard) were calculated in order to find how the electric field of a plane wave, incident at the angle of 51 deg, gets distributed in the sub-30 nm matrix of refractive index (n) of 1,8. The details can be found in Appendix E.

Prior to presenting the results, frame of reference and sample configuration has to be introduced –Figure 2-9. The glass slide (n=1,52) with sub-30 nm thin film of pT (n=1,8) in air (n=1) in placed above an oil-immersion objective (100X, NA=1,3). The plane wave (wavelength 532 nm) with an electric field amplitude of 1 V/m is incident onto the sample at 51 deg (Total Internal Reflection Fluorescence, TIRF).

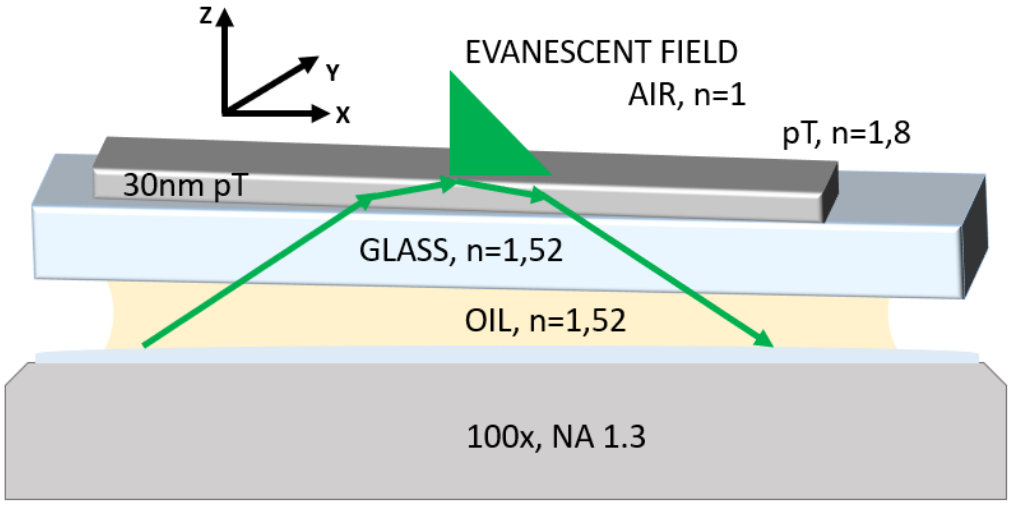

Figure 2-9. TIRF illumination mode and sample configuration.

Both simulation and analytical expression find the same field distribution, in which Ex, Ey and Ez (at a given depth inside pT) vary with the excitation polarization angle α_{EXC} as $a * \cos \alpha_{EXC}$, $b * \sin \alpha_{EXC}$ and $c * \cos \alpha_{EXC}$, respectively and *a, b, c* are amplitudes of the given

cartesian component of the electric field amplitude – Figure 2-10. The intensity $I = |E|^2$ is not constant, but changes with α_{EXC} from $(a + c)^2$ to b^2.

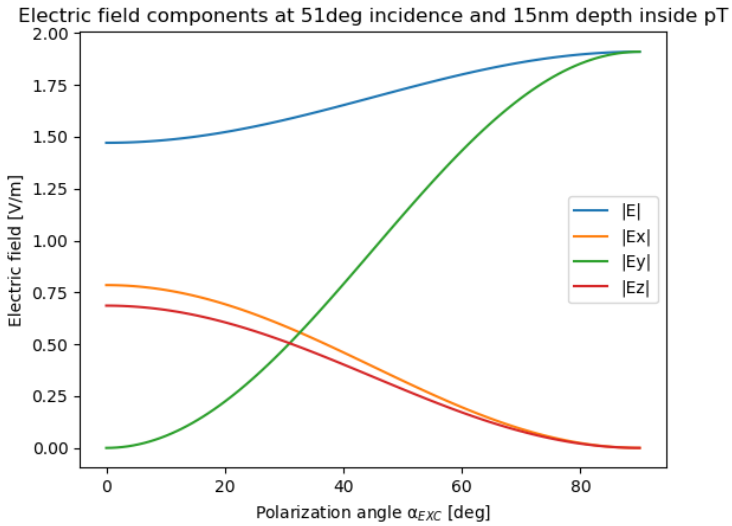

Figure 2-10. Evolution of the electric field amplitude cartesian components as the function of excitation polarization angle α_{EXC} at 15 nm depth inside pT.

Subsequently, the amplitude of each cartesian electric field components vary with the depth inside pT –Figure 2-11. As seen, Ey component is relatively constant, compared to Ex and Ez components that vary by a factor of 2 with the depth.

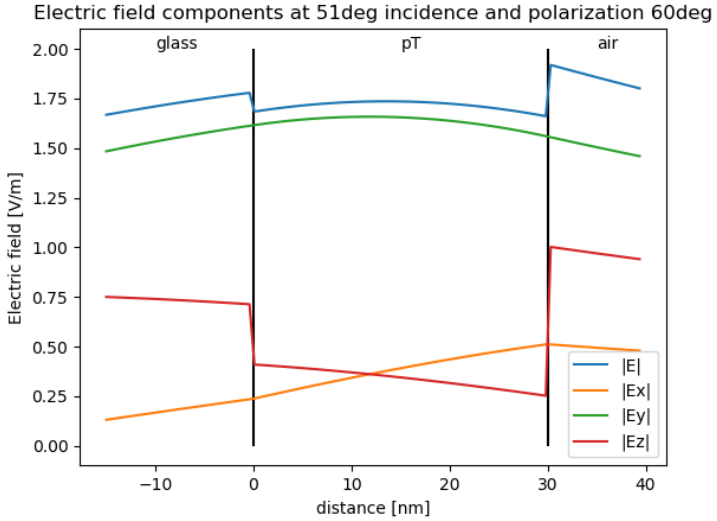

Figure 2-11. Evolution of the electric field amplitude cartesian components as the function of depth inside 30 nm pT thin film at α_{EXC} of 60 deg.

2.1.6. Summary

To sum up, I have presented a full scheme of the optical set-up, identified major blocks and marked groups of components responsible for certain functionalities. I have introduced defined some terms used in the context of TTTR measurements and shown how START-STOP measurement can be used as an approximation of the correlation function in the antibunching regime. Subsequently, I have shown how PPF can be used to calculate C_{EFF} of the system and how counts measured with detectors require correction due to their deadtime. I've presented schemes of the excitation power and polarization evolution during Power, Polarization and Analyzer Scans. Finally, I have discussed the field distribution in sub-30 nm pT, which is necessary to process Polarization Scans.

2.2. Scanning Probe Microscopy

Before describing the set-up and Scanning Probe Microscopy (SPM) technique, it should be recalled why such methodology is used here. Depositing nanoantenna on a substrate and then drop-casting or spin-coating the single molecules (bottom-up approach) is in fact much simpler. If drop-casting (solution) is used, the molecules are free to diffuse around the nanoantenna. In consequence, the orientation of the emitter and distance from the nanoantenna keeps on changing, which modifies the photon statistics. If spin-coating (solid matrix) is used, molecules are fixed, but distributed with random distance and orientation around the nanoantenna. In both cases, the very same single molecule cannot be measured without the nanoantenna. As it was mentioned repeatedly in Chapter 1, single-molecule studies show large molecule-to-molecule variations. Therefore, spin-coating and drop-casting methods should be carried on very large populations (with and without nanoantenna) to compare the population statistics.

Attaching a nanoantenna to the probe and bringing the probe near a single molecule fixed in a solid matrix has one crucial advantage over the bottom-up approach that can't be overseen. This methodology allows to perform the measurement on the very same emitter before and after bringing in the nanoantenna. This is extremely important, because one cannot assume that change in photon statistics is an (electromagnetic) effect of the nanoantenna and not the parasitic effect that originates from modifying the environment (thermal, mechanical) or molecule itself. After all, plasmonic nanoobjects

are known for plasmonic catalysis and hot carrier generation. The experimental Section of this manuscript (Chapter 3 and 4) gives a special attention to so-called pre- and post-approached measurements – the very same emitter is measured before bringing in the nanoantenna and then again, after the nanoantenna is retracted. Such methodology consisting of 3 measurements is an absolute measure of the nanoantenna effect.

In what follows basics of SPM and SPM control system are presented. Then probe and sample fabrication is shown, followed. Finally, review of various drifts and concept of keeping a nanoantenna aligned with a single molecule is discussed.

This Section constitutes essential part of the experimental know-how but is not required to understand the results presented in Chapter 3 and 4, therefore a reader may skip it entirely.

2.2.1. Basics

Scanning Probe Microscopy (SPM) uses a probe to gain various information from the sample, while performing raster scan over its surface. Based on the type of signal, SPM can be divided into several types like Scanning Tunneling Microscopy, Atomic Force Microscopy (AFM) and Near-field Scanning Optical Microscopy (SNOM). The last two are used throughout this thesis as height images of pT film (AFM) and counts images of single molecules (SNOM) are taken.

AFM is a technique is based on the forces between the sample and the probe. The forces at play can be divided into short-range (chemical, van der Waals), long-range interactions (magnetic and electrostatic) and adhesion forces depending on the environment [167]. The theory behind the AFM technique goes well above the scope of this thesis, and I restrict myself to an intuitive view. In the beginning of the AFM development, probes were made metallic foil and a sharp wire. The wire was used a tip to provide spatial resolution, while the foils deflected under such forces. Currently, resonators are used for AFM probes – having its resonant frequency f_{RES} and the resonance quality factor *Q-factor* (and amplitude of oscillation A_{OSC} and at a given AC driving voltage $V_{EXC}(f)$. Based on the direction of the oscillation, a normal mode (vertical) and shear-force mode (horizontal) are distinguished. The shear-force mode is preferred for the emitter-nanoantenna

studies, because oscillation in-plane results in lesser changes of the distance between the two, than the vertical oscillation.

Depending on the distance between the tip of the probe and the sample, so-called tip-sample distance (TSD), probe experiences forces of different magnitudes. Those forces results in perturbation of the probe oscillation (damping), which causes f_{RES} and A_{OSC} to change. Thus, the difference (Δf, ΔA_{OSC}) between free-standing probe parameters (f_{RES} and A_{OSC}) and upon interaction with the surface, can be used as a feedback signal to control TSD. Depending on the parameter used, amplitude modulation and frequency modulation modes are distinguished. The magnitude of the forces increases as TSD decreases, and so do the differences Δf, ΔA_{OSC}. And thus, one can use the nanopositioning (SPM control) system to manipulate the position of the probe, such that the differences stay at a certain value, and so in theory, TSD is fixed.

While silicon cantilevers are the most popular commercial probes, Tuning Fork (TF) is the most popular among the handmade probes (and less popular commercially available QPlus). TF has a body, 2 pins and 2 prongs made of a piezoelectric material and dimensions that define its f_{RES} (32 kHz and 100 kHz typically used for AFM). Handmade probes are made by attaching a sharp tip to one of the prongs. TF can be excited through mechanical agitation or with $V_{EXC}(f)$. While TF can support many eigen modes, in-phase in-plane prongs displacement is commonly used. The displacement of the prongs (deformation of the piezoelectric) generates displacement current I_{TF}. One of the two pins is connected to $V_{EXC}(f)$ and the other is used to detect I_{TF}. A scheme of the sheaf-force TF and pin connection is shown in Figure 2-12.

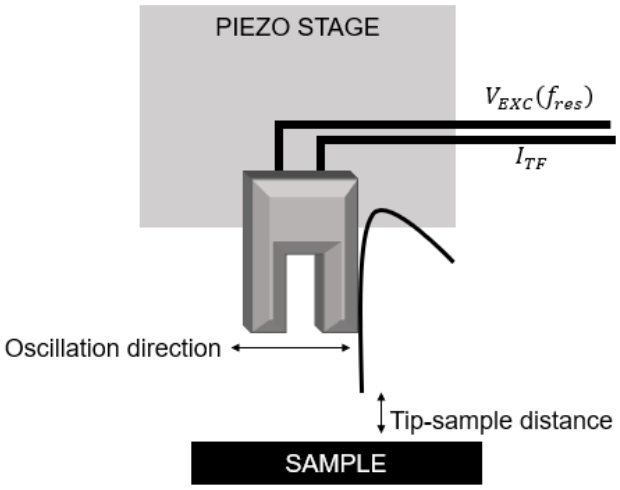

Figure 2-12. Shear force AFM configuration (center).

2.2.2. Control system

As mentioned above, the change in probe parameters Δf, ΔA_{OSC} is related to the forces and thus TSD. From now on, I will restrict myself to frequency modulation. In theory, if Δf can be kept around a fixed value, so will be TSD. This value is referred to as a setpoint and deviations from this value as frequency shift Δf. There are no absolute references that can link a setpoint to a given TSD as mechanical properties of the samples and probes vary. In fact, in shear force mode TSD is usually unknown, based on the magnitude of forces, TSD of ~10 nm is assumed [168], but exact values are rarely given. The sample and the probe are not really fixed – perfectly rigid assembly cannot be assumed. Both of them will move due to the mechanical drift, displace due to the random vibrations or even oscillate due to thermal motion. All of the above, considered as noise, will cause more or less rapid changes in TSD, which will reflect in deviations from the setpoint. Therefore, probe must be fixed onto the piezo stage and connected to the nanopositioning system, which is able to control the tip position relatively fast (µs-ms) and with a nanoscale precision – Figure 2-12.

Herein, I use Nanonis a commercially available SPM control system. A closed-loop feedback system is used for TSD regulation, scheme in Figure 2-13. Recall that I_{TF} originates from periodic displacement of the prongs, and thus this its an AC current with a phase and frequency. Nanonis takes user-defined setpoint (unknown TSD) and

compares it with the constantly monitored frequency of the probe. The difference between the two is an error signal that is passed to the controller. The controller calculates Z command, which is the displacement of piezostage in Z-axis (thus change in TSD) necessary to correct for the error signal. As TSD is unknown, necessary correction is unknown also and feedback loop parameters such as proportional gain and integral gain are adjusted by user. Up to this point, it may seem quite confusing how does the system work if there are so many unknowns. To understand AFM operation, one must consider system stability. If closed-loop parameters are maladjusted, the controller will send overestimated or underestimated Z command, so that TSD keeps oscillating and error signal oscillated also. The way to adjust the closed-loop parameters is to look for a near-zero error signal at as sensitive (proportional gain) and as fast (integral gain) response as possible, before entering instability (oscillation).

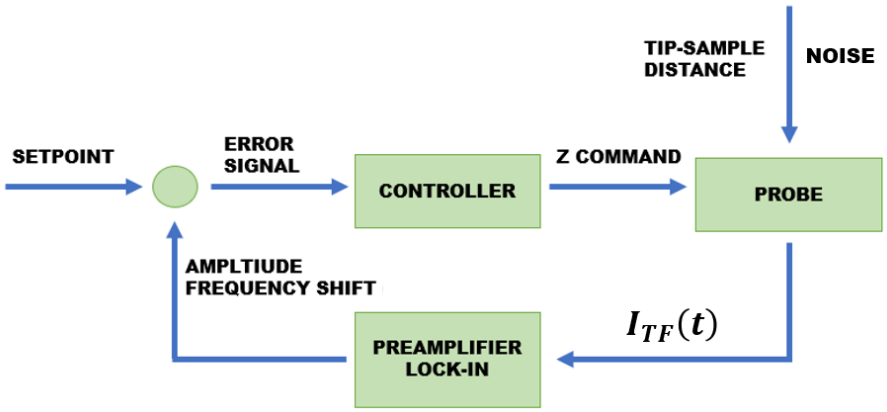

Figure 2-13. Closed-loop feedback in SPM control system using Tuning Fork probe.

Now that I've presented the probe working principle and feedback loop, the scheme of the SPM hardware is shown in Figure 2-14. The SPM system consists of a computer, Nanonis V3 (with OC4 and SC4 modules), nanopositioning XYZ stage (PI602), probe (nanoatenna glued onto the tuning fork), and signal conditioning block (preamplifier and filter).

Nanonis sends the voltage used to control the X, Y, and Z position of the probe to the nanopositioning stage – herein called Z/X/Y command voltage. Nanonis also supplies the voltage to agitate Tuning Fork (TF) oscillation called excitation voltage V_{EXC}. The output of the TF is amplified and filtered before sending it to the lock-in amplifier module of Nanonis. The input of the lock-in module has an additional external low-pass filter.

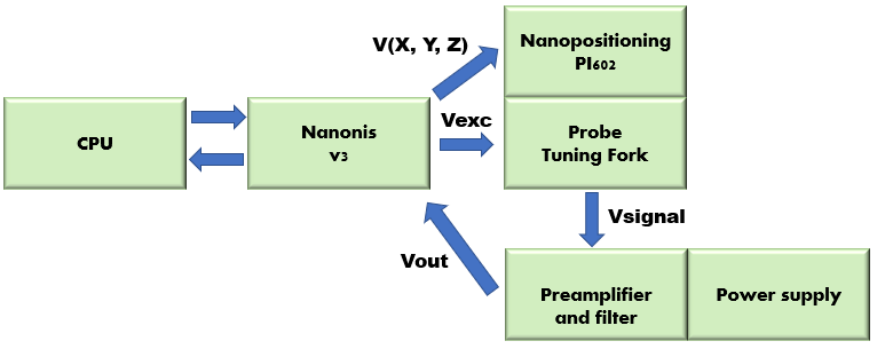

Figure 2-14. Scheme of the SPM control system involving (from left to right) computer, Nanonis system, the probe attached to the piezoelectric stage, and amplifier with a power supply.

2.2.2.1. Preamplifier

The scheme of the preamplifier is presented in Figure 2-15. The main role of the preamplifier is to amplify the picoampere-range current generated by the TF at small oscillations. A resistor of 100 $M\Omega$ is used to ensure a gain of 10^8 V/V. The preamp is placed as close as possible to the probe (~20cm in our setup) to avoid noise amplification and improve signal-to-noise ratio.

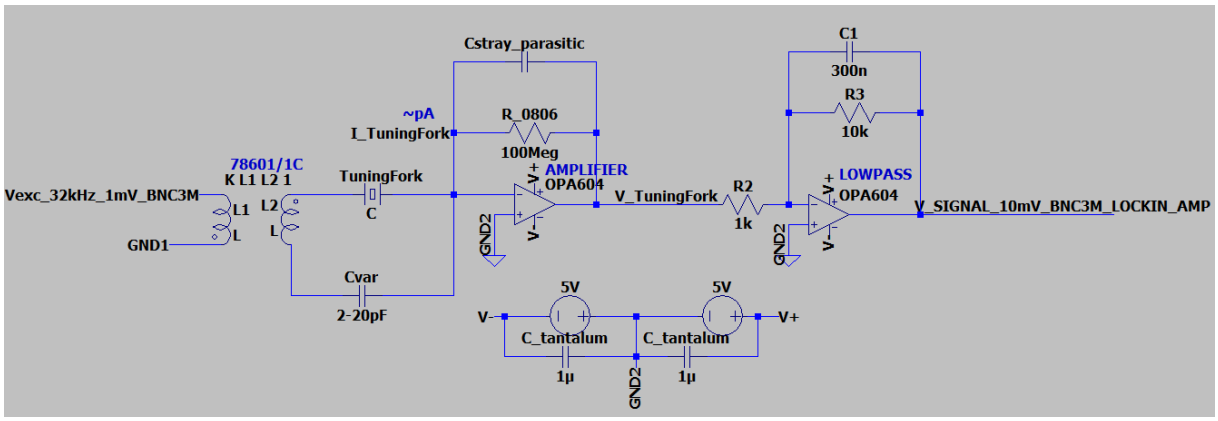

Figure 2-15. LT Spice scheme of the designed preamplifier.

2.2.3. Probe

Probe fabrication and nanoantenna attachment onto it, is one of the main challenges in the single molecule and nanoantenna experiments. In Chapter 4 probes made of pulled optical fiber (dielectric nanoantenna) or gold pyramid (plasmonic nanoantenna) glued

onto a TF are applied. Assessing the performance of the probe requires in-depth analysis of the electric signals and electronic components in the context of AFM experiment, which goes beyond the scope of this manuscript.

The probe is made of a TF and pulled glass fiber/gold pyramid are glued to it. The probe must be able to operate at the oscillation amplitude much smaller than the nanoantenna Radius of Curvature (RoC). By coupling light into the pulled glass fiber (dielectric nanoantenna) attached onto the TF, one can observe the tip with a microscope objective. Subsequently, TF can be driven with various V_{EXC}, which corresponds to the oscillation in the optical image. This allows to calibrate the driving voltage [V] into probe oscillation amplitude [m]. Such calibration cannot be performed with the gold pyramid.

2.2.3.1. Fabrication

An optical fiber (HP630 Thorlabs) was pulled using a fiber puller (P2000 Sutter Instruments), and a probe was fabricated on the home-made gluing set-up:

1) optical fiber is cut to ~1 m length, stripped of coating along 3cm in the middle, cleaned with iso-propyl alcohol (IPA), and pulled with a fiber puller
2) commercial tuning fork 32 kHz is decapped and soldered onto a pin header
3) pulled fiber is aligned and glued onto the prong's side with a super glue. After 15 minutes of drying, fiber is attached to the pin header using a large amount of epoxy glue and left overnight.

The reproducibility of the pulled fibers depends on the angle at which the fiber reduces its diameter (taper angle). The length over which diameter change occurs is called a taper. A stable regime is found when back-to-back pulls yield similar taper and post-pulling parameters. A full discussion on the various pulling parameters is irrelevant to the scope of this thesis. Once this regime is found, the apex of the fiber can be slightly adjusted using the hard pull parameter only without affecting the taper and taper angle.

I've found that the plateau can be varied between 30 nm and 400 nm (diameter) by controlling the pull parameter while keeping all the other setting constant. The final protocol pull of 150 was chosen. The high pull is more reproducible. Examples of the fibers pulled at different pulling parameters are shown in Figure 2-16.

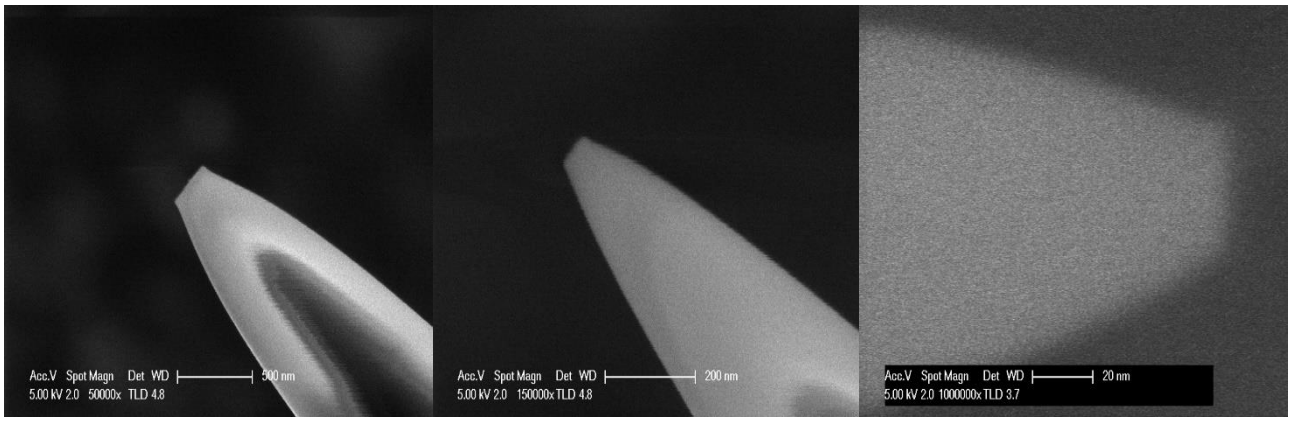

Figure 2-16. SEM images of the plateau at the tip of pulled fiber at different pull parameters: 200 nm at pull 40, 60 nm at pull 100, and 30 nm at pull 150.

It turns out that soldering a TF onto a pin header and gluing step is crucial for its SPM performance, and the scheme of the ideal probe is shown in Figure 2-17. Gluing a fiber onto the tuning fork, besides additional mass and fork imbalance, introduces a bending moment and torque that is transferred onto the fork. Experimentally, I’ ve observed that the distance between the front and back fixation of the fiber and fork should be kept minimal (short wires between pin header and fork body). Ideally, front and back fixation should be parallel to the prong. Additionally, any twisting of the fork and pin header axis should be avoided. Bending and torque result in the splitting of degenerated fork oscillation mode (thus reducing Q-factor) and drift of the TF resonant frequency.

To ensure this alignment, pin headers with a grove are preferred. Grove can be used for alignment with the prong’ s axis. The pin header body is used to handle the probe. A large amount of epoxy and overnight rest is necessary – fixations can misalign when handling. Finally, the rest of the ~1 m long optical fiber that is used to couple light should be fixed using adhesive tape to dampen and prevent transmission of dangling fiber vibrations onto the probe. In practice, AFM scans do not apply such constraints on the probe. However, staying approached above a molecule requires a reduced spatial drift and the probe parameters drift.

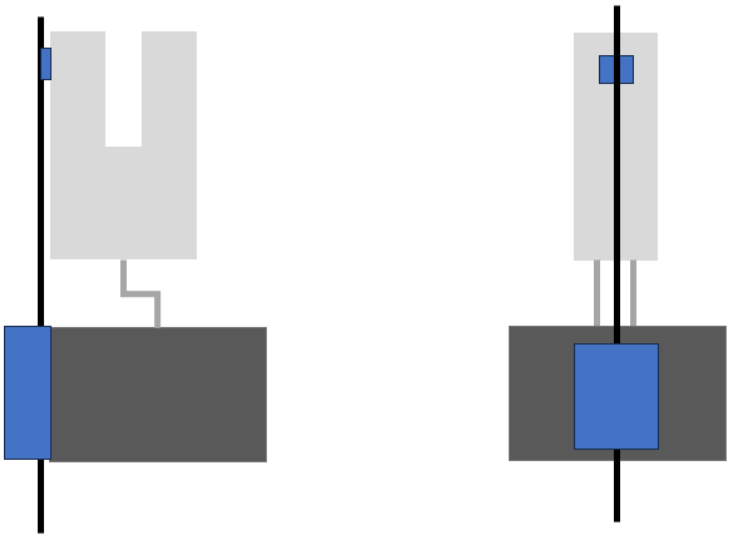

Figure 2-17. Side (left) and top(right) view of the ideal probe.

2.2.3.2. Calibration

To perform the real-space calibration of the probe oscillation amplitude, light is coupled into the fiber, and the probe is observed by the microscope objective. Bright-field images of the bright spot (light transmitted through fiber apex) at different driving voltages are collected – Figure 2-18. The distance of probe oscillation is measured in pixels and then recalculated to real-space.

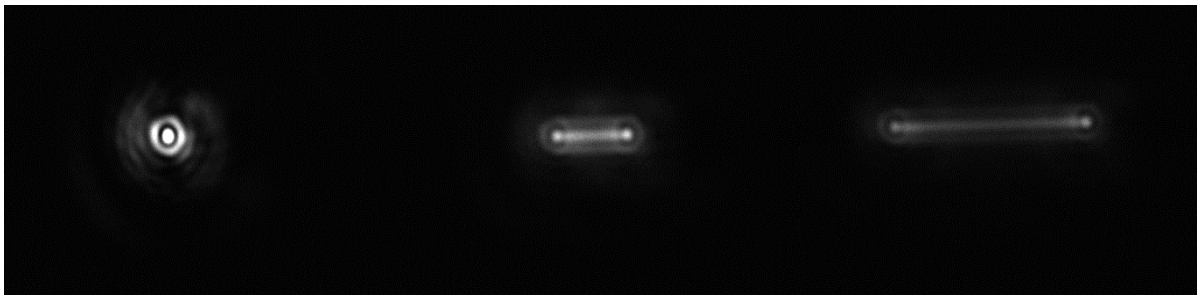

Figure 2-18. Images on the camera (tip with red diode coupled into fiber) at excitation of 0 V, 1 V and 3 V (left to right) applied to the probe of Q=2000 and f_{res}=32,6 kHz.

The real space displacement plotted against the applied excitation voltage returns a slope which is the probe's oscillation sensitivity (nm/mV). Different probes calibrated accordingly are shown in Figure 2-19.

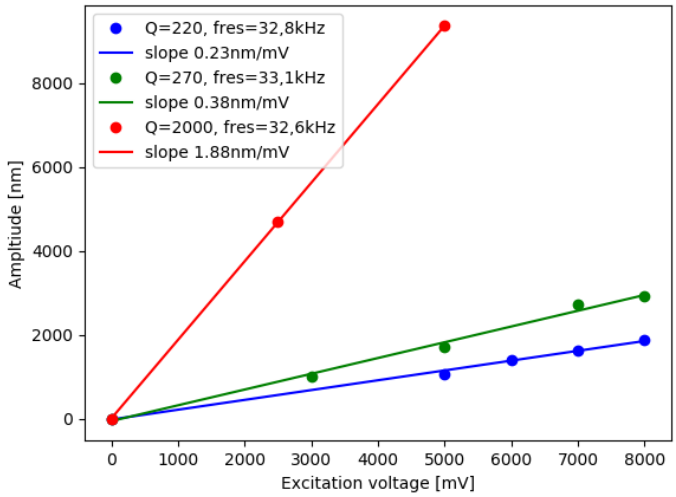

Figure 2-19. Examples (3 different probes) of calibration of tip oscillation sensitivity, amplitude of the real-space oscillation as a function of excitation voltage applied.

Amplitude of the oscillation is intrinsic to each probe. According to the energy balance method [169], it can be calculated as follows:

$$A_{OSC} = \sqrt{\frac{V_{DRIVE} * V_{READ} * Q}{2\pi * f_{RES} * SC * G}} \qquad 2.5$$

where A_{OSC} is the amplitude of oscillation in real-space [m], V_{DRIVE} and V_{READ} are the applied voltage and amplifier output, respectively, G is the gain of the transimpedance amplifier [V/A] and SC is the probe's spring constant.

Since I perform the calibration using the optical method, I can apply the energy balance method to recalculate the spring constant of our probes – knowing their V_{DRIVE}, V_{READ}, f_{RES}, Q and G from the Nanonis. I've calculated spring constant for 2 probes to recover values of 7,5 kN/m and 12 kN/m. Those values are consistent with the typical spring constant of the decapped tuning fork, which was reported to be around 15 kN/m [170]. Moreover, this property can be influenced by a gluing process [171]. I conclude that the optical method is a direct measurement, while the energy balance method should be carefully applied as glued probe stiffness is not the same as the stiffness of free TF.

2.2.4. Sample

Interaction between a single molecule and a nanoantenna has a nanoscale range, and therefore host matrix must be thin enough to allow it. Micrometer-wide narrow islands of sub-30 nm height can be readily found on the sample. However, molecules placed in small islands are less photostable and results of the field distribution cannot be used in this case (excitation wavelength is not much smaller than XY dimensions). In this Section, I show how from macroscopic to microscopic view, I have developed a method to readily find sub-30 nm islands spanning over tens of micrometers.

This Section constitutes essential part of the experimental know-how but is not required to understand the results presented in Chapter 3 and 4, therefore a reader may skip it entirely.

2.2.4.1. Fabrication

Samples were fabricated according to Pfab et al. [55]. Briefly, 20µl of T in 2 mg/ml pT/toluene solution was spin-coated at 1000/3000 rps for 30/5 s. Concentration of T was adjusted in dilution series and fluorescence wide-field images were observed to get desired density ~15 molecules/100 μm^2. It must be noted that pT film reproduces geometry of the holder used in the spin-coating. Metallic holder with engraved cross shape was fabricated. A protocol should always be adjusted for a holder used, and will not be reproducible with the holders of different patterns.

The concentration of 2 mg/ml yields somewhat of a triple cross pattern with a whitish film being the most outer (outside blue), a stripe pattern in the middle (blue-red), and very little pT in-between well-defined crosses (red-green) – Figure 2-20.

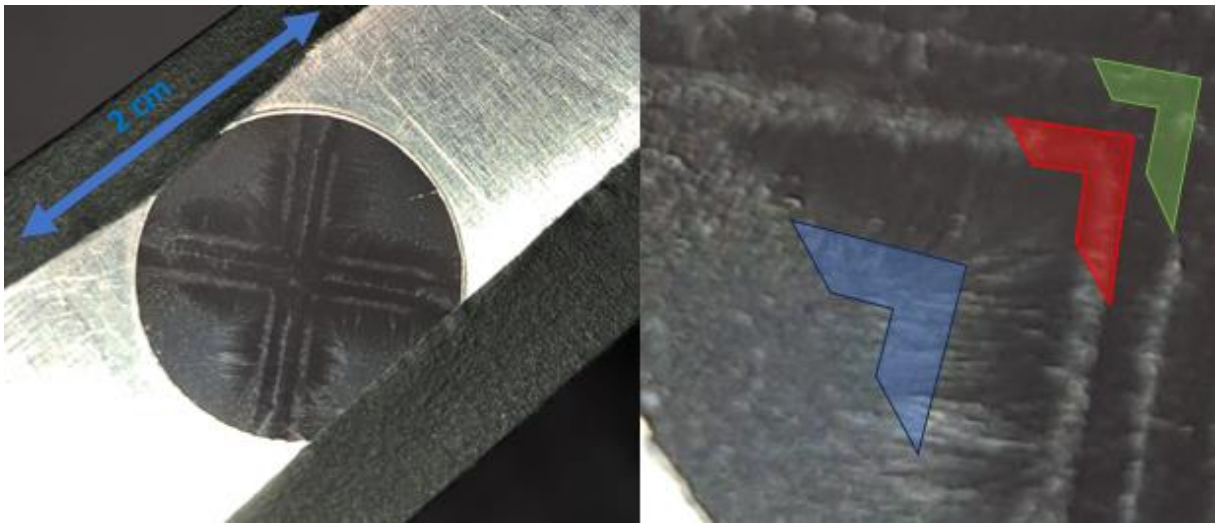

Figure 2-20. Macroscopic morphology of the spin-coated T/pT (left) and zoomed pattern transition of the 2 mg/ml sample (right). Microscope cover plate 2 cm x 2 cm.

It is visible with a naked eye that the thickness of the pT varies drastically on the sample (sub-20 nm to microscale crystals as verified by AFM). To find large area of the sub-30 nm thickness, I developed a protocol. Steps are shown in Figure 2-21 and require moving from the red to blue edge (Figure 2-20) on the sample.

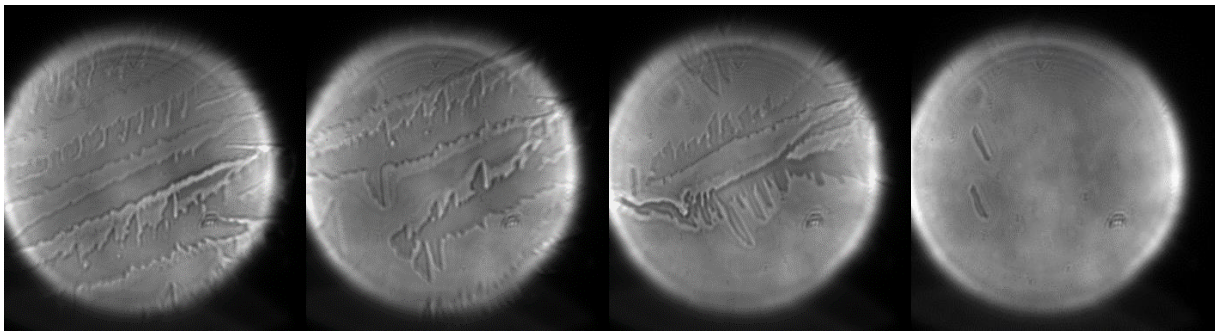

Figure 2-21. The evolution of pT matrix morphology (left to right) when moving along (2x) and perpendicularly (1x) to the long axis of the very thin islands.

To find the large areas of sub-30 nm thickness:

- Roughly position the sample within the stripes pattern area (very long and very narrow islands), which occupy a very large area of the sample so should be readily found
- Follow the long axis of the thin islands in the direction of islands widening

- As islands become wider some of them will start to merge together, at this point move either perpendicularly to the long axis or keep moving along
- Eventually, large areas with small defects having well oriented edges can be found due to the merging of the neighboring islands.

It has to be pointed out that emitters that measurements presented in Chapter 3 and 4 wouldn't be achieved without working within the large areas of continuous and flat sub-30 nm pT film. Its difficult to compare photon budget of emitters within narrow islands to 10^{10} photon budget in large areas. The emitters in narrow islands tend to have very unstable timetraces and rates (fluctuating even at constant polarization and power). Thus the photon budget is not really limited by photobleaching itself, but by number of photons that can be observed before the emitter changes its state in an unexplainable manner.

2.2.4.2. Height verification

The sample, which is microscope cover plate taped onto the metallic sample holder (Figure 2-20), should yield a height background defined by a plane in XYZ. Depending on the size and acquisition time, other factors have to be also considered for background correction. The drift keeps the fast-scan height background linear but modifies the slow-scan axis into a parabolic/exponential shape. In Figure 2-22. cross-section lines 1 and 2 show slow and fast-scan axis, respectively. I perform height background correction using command voltage and Gwyddion software.

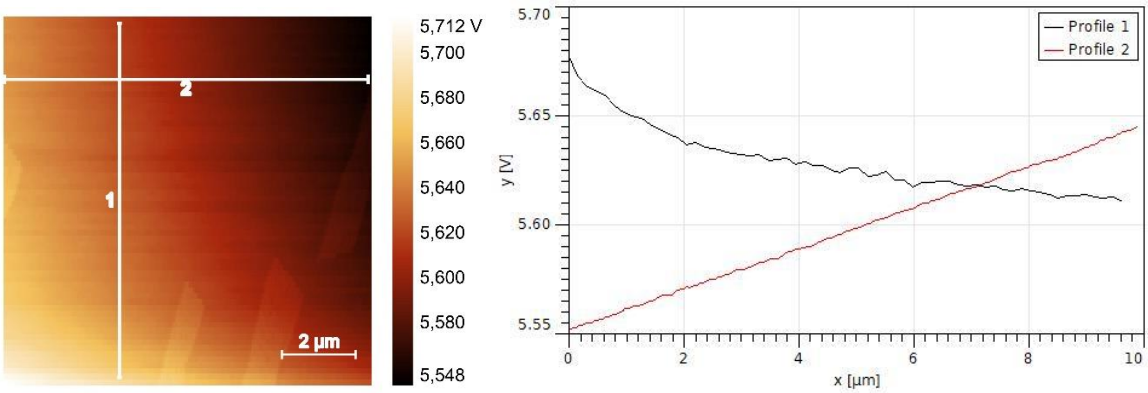

Figure 2-22. Z-command voltage image (left) with cross-section lines and voltage profiles of those lines (right).

After the background subtraction, I verify pT height and its variation within 100 μm^2 area. In Figure 2-23, height image and 2 profile lines of the sub-30 nm pT are presented. Line 1 verifies proper background correction and enables calculation of pT roughness ±1,9 nm. Line 2 represents cross-section through 2 defects (down to the glass slide surface) to verify a height of 20 nm. Due to the roughness of the film, I refer to it as sub-30 nm throughout this manuscript.

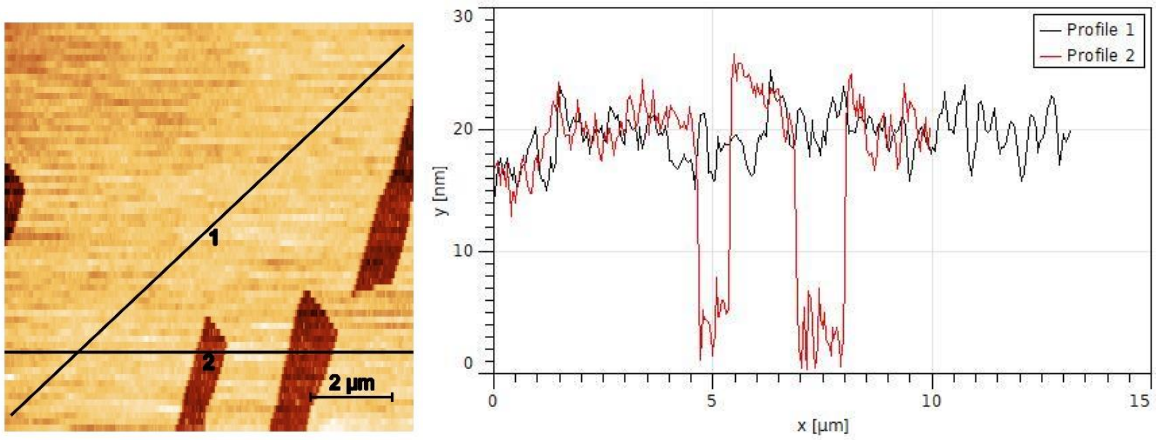

Figure 2-23. The height colormap with cross-sections (left) and their respective height profiles (right).

2.2.5. Single molecule and nanoantenna experiments

To perform experiments on single molecules with a nanoantenna, the two must be aligned and kept fixed during the measurement time. However, keeping two objects fixed at the nanoscale is impossible (drift, vibrations, noise etc.) and therefore a term ''to keep a nanoantenna fixed above a single molecule'' needs a quantitative definition for how long and what magnitude of misalignment is considered negligible. There are 3 factors contributing to the misalignment and they have different timescales.

First and the most obvious is the mechanical drift. Depending on the origin drift may have different velocities and time constants (if drift is exponential), however drift is typically unidirectional and relatively slow compared to 2 other misalignment factors below (Appendix F.a).

The second factor is the real-space oscillation amplitude (prongs displacement). It occurs at the frequency of the probe (32,8 kHz) and in XY plane. Though it has the average

displacement of 0, the instantaneous displacement goes from a negative amplitude to a positive amplitude of prong oscillation. To decrease this instantaneous displacement, a driving voltage V_{EXC} must be decreased. This was already discussed in Section 2.2.3.2.

Third and the most important is regulation. Ideally, error signal should be near-zero so that TSD is kept constant, but it is not the case in practice. Overall, average displace is 0, because tip will fluctuate (in Z-axis) around TSD value related to a setpoint. Timescale of this misalignment depends on the integral gain parameter of the feedback loop and is typically one order of magnitude slower. Recall experiments presented in Section 1.3.6.1., which show that for a plasmonic nanoantenna, even the nanoantenna-emitter distance changes of few nanometers can result in significant changes of photon flux. Thus it must be assessed experimentally what is the magnitude of those Z-axis fluctuations due to imperfect regulation (Appendix F.b).

2.2.6. Summary

To sum up, in order to paint a bigger photophysical picture of terrylene in sub-30 nm para-terphenyl, I have decided to carry out numerous measurements on the very same single molecule. Such experiments wouldn't be possible in many other host-guest system and wasn't even possible in T/pT, when measuring emitters in narrow islands. Based on the recorded measurements, I estimate that in the large, continuous areas of sub-30 nm, some emitters have a photon budget even reaching 10^{10} photons.

Though very large, this photon budget is not infinite. To use it to the fullest, I have placed optical components on the motorized mounts and established communication between the devices. This allows to carry out Scans, which register counts as excitation power or polarization is changing. Scans can be readily adjusted by a user, based on the photon statistics and budget of any emitter, to record necessary measurements with optimal SNR and perform calculation with optimal uncertainties.

Automatization of the set-up is also extremely important for emitter-nanoantenna measurements. After introducing SPM and presenting protocols for fabrication and characterization of the probe and sample, I have discussed various drifts. The mechanical drift and probe parameters drift that occurs right after mounting the probe on the set-up prevents from carrying out reliable experiments (nanoantenna-emitter misalignment).

Once probe is mounted, it is left to rest for one day and as little as required manual manipulations are performed on the set-up, when carrying out nanoantenna experiments. Once the manipulation-borne drift reduces, one has to consider other factors, because nanoantenna effect on the emitter depends on the distance from the emitter in nanoscale. I have assessed the SPM regulation. Results suggests that once average TSD is fixed by the setpoint, the regulation varies depending on the tip. The deviation from the average TSD (if treated as noise) has RMS < 1 nm, which I consider acceptable for the emitter-nanoantenna studies.

Chapter 3

If a single molecule is to be incorporated into a device (nanoantenna), one must be able to fully characterize photophysics of the molecule alone. This allows to predict the performance of such device (explain nanoantenna effect on the molecule). In Chapter 1, I've presented photophysics of terrylene and reviewed state of the art. There are numerous reports on T/pT system. The fluorescence lifetime was studied in the nanoscale thin films of pT and proven to be drastically different than in the bulk. The rates of other transitions are unknown in thin films, because 3-level model has only been reported in the bulk. Studies typically report measurements on very few molecules and show large molecule-to-molecule variations. It is unclear whether those variations originate from calculation uncertainties or photophysics, and if the latter, what are the ranges and causes of those variations for each transition rate. Moreover, T/pT has a very particular property as it's triplet depopulation is power-dependent. Though transition to higher triplet states was suggested as a root of this property, the transition dipole moment remains unspecified.

In fact, single-molecule studies very rarely report the orientation of the emitter or transition dipole moments. This is a consequence of the experimental method – typically the experiments are carried out by acquiring Time-Tagged-Time-Resolved (TTTR) measurements at a couple of different excitation intensities at fixed polarization. This method yields a couple of data points to perform the fit and calculate the rates. To better understand the photophysics of the emitter, it is necessary to record TTTR measurements at various excitation polarization and intensities, so that the 3-level model can be given the 3D dimensions. However, experiments on the single molecules are tedious and time-consuming, while simultaneously being time-restricted due to their photostability. To tackle this problem, I implemented Power and Polarization Scans, which are fully automatized TTTR measurements collected at varying excitation power and polarization. Those Scans are very robust as they can be optimized to minimize the irradiation dose (photostability), while providing high precision on the transition rates (Power Scan) and information about the orientation of transition dipole moments (Polarization Scan)

In this Chapter, I will look for the answers and discuss the questions raised in Chapter 1, by showcasing the experimental results. Principal questions include:

- How does the photophysics of T/pT in sub-30 nm films differ from the bulk crystals?
- What is the range of the population standard deviation for various rates for a large population of molecules?
- Can population standard deviation be viewed as molecule-to-molecule variation that originates from the photophysics, or is it simply a consequence of calculation uncertainties?
- Can the physical origins of those molecule-to-molecule variations be identified?
- Is the molecule-to-molecule variation correlated with the fluorescence spectrum; is there a correlation between the rates themselves?
- Can a 3D model of the emitter be reconstructed to provide a more complete understanding of the emitter photophysics?

3. Characterization of a single molecule

3.1. Power Scan

Power Scan subsection is composed of 3 main parts that contain exemplary step-by-step treatment of Power Scan on one of the measured T's, population statistics, and conclusions.

Note that Power Scan carries information about the orientation of the transition dipole moments, because rates are tracked as a function of incident power at fixed polarization. Therefore σ_{12} and σ_{32} calculated with Power Scans and presented in Section 3.1 are the excitation coefficients, defined as number of excitations per incident power and having a unit of Hz/mW. Those coefficients are related to the cross-section of the transition (σ_{12}^{CS} and σ_{32}^{CS}) given in cm^2. To calculate the cross-sections, it is necessary to know the field distribution inside the sub-30 nm pT film and the orientation of the transition dipole moments, which will be done in next Section of this Chapter (Section 3.2).

3.1.1. Sequential treatment (step-by-step)

Most of the equations were introduced already in Chapter 1 and notation holds. For the readers' comfort, I will repeat each equation that is subsequently plotted. Every measurement is collected during the acquisition time called Macrotime, as power is

varied. Subsequently, Macrotime is segmented into 200 ms bins and every bin is treated as a separated data point. Before each measurement, polarization of the excitation laser is rotated to find the maximum emission. This ensures the highest attainable dot product between the S0-S1 transition moment and polarization, but doesn't necessarily mean they are colinear.

The data treatments other than sequential fit were also investigated (Appendix G), namely all the autocorrelation functions were joined into a single 1D array and passed into the fitting. Such a treatment is inferior to the sequential treatment, and I suspect that python function scipy.curve_fit is not an optimal tool to use on such large non-linear 1D arrays (20 000 data points).

3.1.1.1. Time trace

I examine the counts Time trace (counts plotted against the Macrotime) of the T/pT, while the incident power varies and is observed simultaneously on the photodiode (Figure 3-1, upper right). This graph is also used for synchronization – assigning average incident power to each data segment. Luminescence from pT serves as a background (Figure 3-1, upper) and is taken few μm away from the emitter. The Signal-to-Noise Ratio (*SNR,* Figure 3-1, lower) defined as a ratio of the counts between emitter *R(T/pT)* and the background *R(pT)*:

$$SNR = \frac{R(T/pT)}{R(pT)} \qquad 3.1$$

The whole measurement is segmented into bins of 200 ms, identified by their macrotime, each one being considered to be acquired with constant incident power, to construct data points (here and throughout the entire manuscript). Time traces profiles of the emitter as of the background don't show clear differences between the upward and downward directions. Counts Time trace of T/pT shows smooth evolution in the counts as power is varied continuously (Figure 3-1, upper left). Time trace of the pT (background) contains some random (unknown origin) spikes in the counts that are beyond the detectors/statistical noise (Figure 3-1, upper right, around 20s). SNR Time Trace stays

above 20 during the entire measurement, which is a big advantage of sub-30 nm pT - less noise is accumulated through the nanoscale matrix path.

There are 2 main applications of the SNR – the background correction (introduced later in the thesis), and the dosage adjustment. In fact, SNR in Figure 3-1, lower is distorted (asymmetric with power) due to a transient increase of the background photoluminescence. Transient changes of the background can be viewed as photodamage (fatigue) of the matrix. Power Scans used here were developed taking into the account the SNR Time Traces - experiment duration and power range to tune into an optimal balance between photon flux and photostability of the sample. Such actions are referred to as ''photon budget optimization'', which can be understood as certain number of photons that one can, on average, extract from the emitter, prior to it's photobleaching/spectral jump/other photophysical instabilities.

Finally, each channel (detector) is plotted separately for technical investigation such as verification of the HBT alignment, power supply stability and eventual stray light detection.

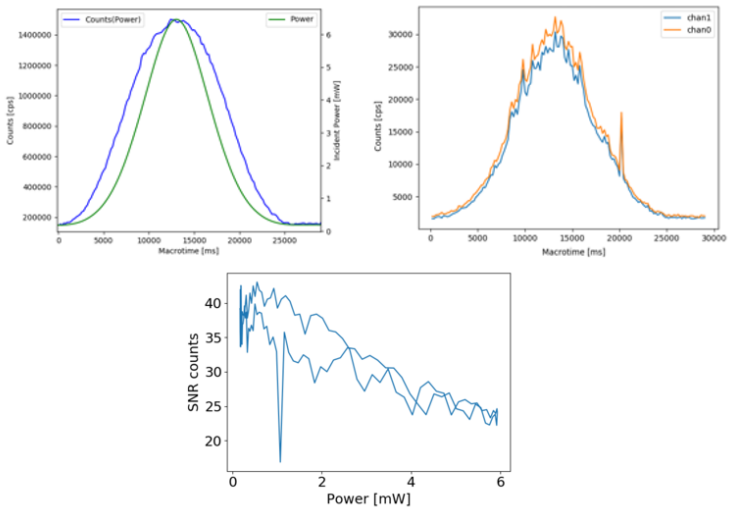

Figure 3-1. Counts on each channel (detector) from the single T/pT (upper left), pT taken a few μm away from the emitter (upper right) and SNR being the ratio of both (lower) as a function of power during Power Scan.

To conclude, Time trace shows that the emitter is stable and damage to the matrix is minor during Power Scan. Counts on each channel are identical in shape and almost identical in values, which proves that there are no technical issues with the HBT set-up.

3.1.1.2. Bunching (σ_{32}, k_T, k_{21}/σ_{12}, k_{23})

Within each 200ms bin, I use the cross-correlation between the two channels in the regime, where a delay is much larger than the antibunching time constant $1/|\lambda_2|$ (5-20ns). Considering that $|\lambda_3| \ll |\lambda_2|$, the emitter's autocorrelation function can be approximated as a bunching curve only:

$$g^{(2)}(\tau) = 1 - (1 + A)\, exp(\lambda_2 \tau) + A exp(\lambda_3 \tau) \xrightarrow{for\ \tau \gg \frac{1}{|\lambda_2|}} 1 + A exp(\lambda_3 \tau) \qquad 3.2$$

Fitting the bunching curve recovers 2 power-dependent parameters – bunching amplitude A with its uncertainty $\pm\Delta A$, and bunching rate λ_3 with its uncertainty $\pm\Delta\lambda_3$. Recall counts Time trace of T/pT (Figure 3-1, left) – the highest counts are found at macrotimes around 14 s (1,5 Mcps) and the lowest during 25-29 s (0,1 Mcps). In Figure 3-2, I plot the cross-correlation at two specific macrotimes corresponding to those two limit situations. In both cases, a bunching curve with a monoexponential shape can be fitted using Equation 3.2. This is consistent with double to monoexponential bunching curve change with temperature [51]. At the highest photon flux (Figure 3-2, left), fit uncertainty is a few times lower than at the lowest photon flux. This is why Power Scan was designed to stay longer at lowest power ranges – power gradient in time (dP/dt) is smaller in the low power regime, because the acceleration of power control unit is power-dependent. By doing this, I collect more data points at low power.

500

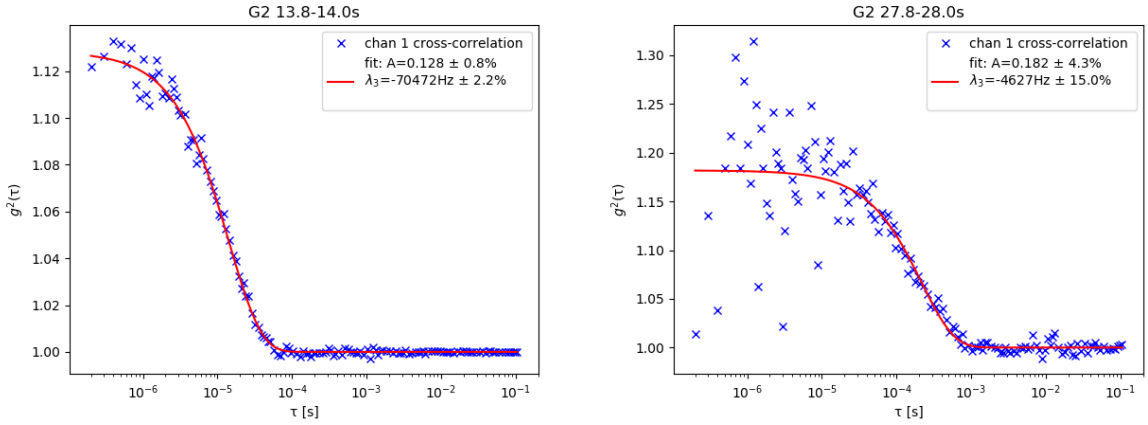

Figure 3-2. Cross-correlation of the two channels at two specific macrotimes corresponding to the frontier counts of 1,5 Mcps (left) and 0,1 Mcps (right) within 200 ms time segments of Power Scan; data points (blue crosses) and the fit (red line).

The bunching curves show perfect fit using a single exponential, which is a consistent with the literature - triplet states (3) have different relaxation rates at LT for terylene with D_{2h} symmetry, while at RT the levels are degenerated and have a single relaxation rate [reference].

None of the published papers cited in Chapter 1 have mentioned that the amplitude of the correlation depends on the SNR and thus requires a correction (I assume that haven't applied the correction). There are few works (thesis by B. Sontheimer and work done by the group of P. Grangier [160,172,173]) that show how such a correction should be applied, and so I follow this reference, to apply a correction given by the formula:

$$g^{(2)}(\tau) = g^{(2)}_{MEASURED}(\tau) * (SNR^{-2} + 2 * SNR^{-1} + 1) - (SNR^{-2} + 2 * SNR^{-1}) \quad 3.3$$

For a quantitative view, I plot 145 data points of raw and background corrected A (Figure 3-3, upper) and relative correction (Figure 3-3, lower) as the moving average of 5 data points, which shows that with SNR>20, correction is <10%.

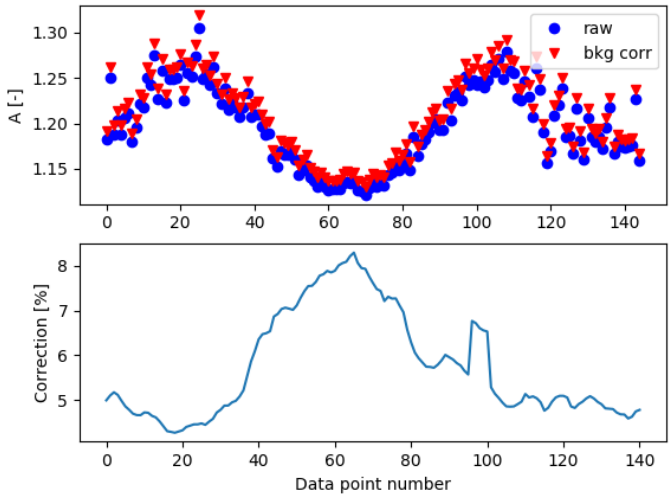

Figure 3-3. Raw (blue dots) and background corrected (red triangles) bunching amplitude A for every bin (200 ms time segment) during 29 s Power Scan (upper) and relative correction applied plotted as the moving average of 5 data points (lower).

Now I can move to the rate calculations. Recall the results of the cited studies on T/pT, which found that effective rISC rate (k_{32}) depends linearly on the excitation power – because this transition is actually a series of a vertical transition (triplet-triplet absorption) and horizontal transition (T5/6-S2). Its sum with a direct T1-S0 transition rate ($k_T + k_{32}$) can be calculated from the fitted values of λ_3 and A using the bunching regime only:

$$k_T + k_{32} = k_T + \sigma_{32} * P = \frac{1}{TimeOFF} = \frac{\lambda_3}{1 + A} \qquad 3.4$$

I plot $k_T + k_{32}$ as a function of the laser incident power (Figure 3-4). High linearity proves that synchronization is properly done (Figure 3-1, left). I proceed with a linear fit through all macrotimes and thus various power to extract σ_{32} (slope) and k_T (intercept). The linear fit returns low slope relative uncertainty $\delta\sigma_{32}/\sigma_{32} < 1\%$. Relative uncertainty $\delta k_T/k_T$ is an order of magnitude higher due to the small relative contribution of k_T to the value of the sum $k_T + k_{32}$ (in this power regime). Values of the fit, if the background correction isn't done, are also calculated (text in Figure 3-4, right). The effect of the

correction turns out to be negligible due to the fact that SNR is very high (>20) in sub-30 nm pT.

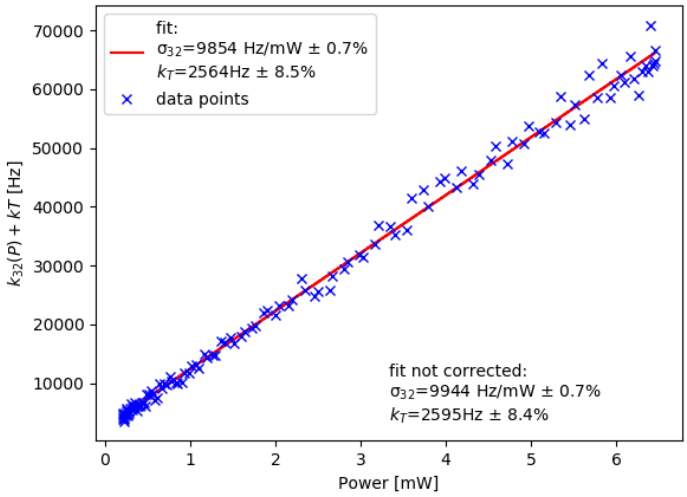

Figure 3-4. Sum of the $k_T + k_{32}$ as a function of the power assigned to each time segment, data points (blue crosses) and the fit (red line). Results of the linear fit $\sigma_{32} * P + k_T$ in the caption and without background correction in the text (right).

The rates k_{21} and k_{12} cannot be accessed directly using only the bunching regime (too many unknowns). However, the ratio $\frac{k_{21}}{\sigma_{12}}$ can be. This ratio can be understood as an incident power at which k_{12}=k_{21}. This incident power corresponds to the saturation intensity of 2-level system. Fitting the saturation curve is common procedure in single-molecule studies. However, power-dependent triplet relaxation of T/pT result in a deviation from the classical saturation curve, that assumes a constant triplet relaxation rate. Therefore, this treatment shouldn't be used for this system.

The value of k_{23} is then given as the inverse of *TimeON* limit as $P \to \infty$:

$$TimeON = \frac{1}{-\lambda_3 + \left(\frac{\lambda_3}{1+A}\right)} = \frac{1}{k_{23}}\left(1 + \frac{k_{21}}{\sigma_{12} * P}\right) \qquad 3.5$$

I plot *TimeON* as a function of the power and proceed with a fit according to Equation 3.5(Figure 3-5). Fit parameters have uncertainty below 15%. In his thesis, Bernd

Sontheimer expressed concern that when measuring quantum emitters, START-STOP approximation is commonly used, even though it's not always valid [160]. I calculate $\frac{k_{21}}{\sigma_{12}}$ using cross-correlation in a bunching regime. It will serve as a reference value to the σ_{12} and k_{21} that are calculated using START-STOP in the antibunching regime.

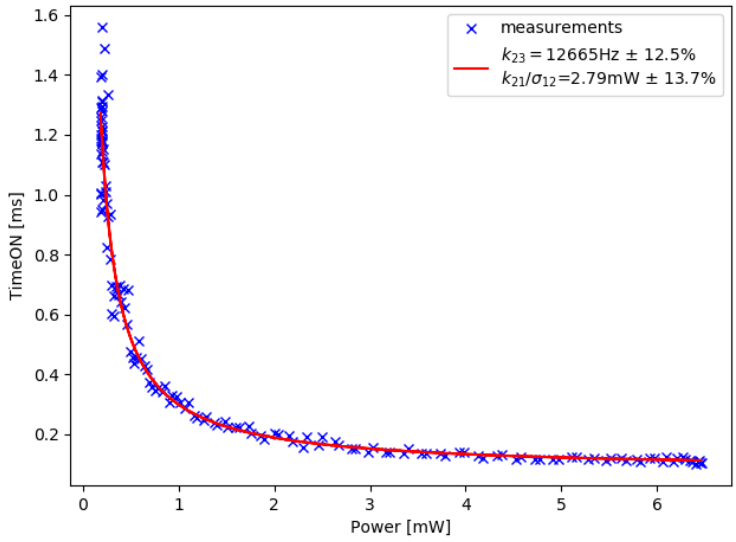

Figure 3-5. TimeON as a function of the power, data points (blue crosses) and the fit (red line).

To sum up, I've verified that at the minimal and maximum counts cross-correlation can be reliably fitted. I've assigned the power to each bin. Cross-correlation amplitude requires a few percent correction due to the background photoluminescence. By performing fits of *TimeOFF* and *TimeON* parameters, I calculated values and uncertainties of σ_{32}, k_T, $\frac{k_{21}}{\sigma_{12}}$ and k_{23}. The relative uncertainty of each rate varies and typically goes as $\delta\sigma_{32} < \delta k_T < \delta k_{23} < 20\%$. The magnitude of each rate uncertainty will be recalled later when discussing the population standard deviation (std) of the rates.

3.1.1.3. Antibunching (σ_{12}, k_{21})

The cross-correlation in the antibunching regime is approximated with a START-STOP approach [165]. The validity of this approximation was verified in Chapter 2 using Monte Carlo simulation and now, additionally, rates found with START-STOP will be verified

using ratio $\frac{k_{21}}{\sigma_{12}}$ found above from cross-correlation in the bunching regime. For time-delay τ much smaller than $\frac{1}{|\lambda_3|}$, second-order correlation approximates as:

$$g^{(2)}(\tau) = 1 - (1 + A)\, exp(\lambda_2 \tau) + A exp(\lambda_3 \tau) \xrightarrow{for\ \tau \ll \frac{1}{|\lambda_3|}} (1 + A)\big(1 - exp(\lambda_2 \tau)\big) \quad 3.6$$

For the term $exp(\lambda_2 \tau)$ to not uniformly equals 1, it is necessary that $|\lambda_3| \ll |\lambda_2|$.

As cross-correlation is approximated with a START-STOP approach, the unit changes to the Number of PhotonPairs (PP) within a bin of a given time width. It can be normalized to recover $g^{(2)}$ by using the formula [160]:

$$g^{(2)} = \frac{Acquistion\ time}{START - STOP\ bin\ width} * \frac{Number\ of\ PhotonPairs}{R(chan1) * R\ (chan2)} \quad 3.7$$

The first fraction is the number of channels in the histogram of START-STOP photon pairs. This means that A could be recovered from START-STOP also. However, START-STOP measurement with applied 200 ms per data point carries significant statistical noise and, without going into the details, A is fitted with higher accuracy from cross-correlation in the bunching regime, and these values are used instead throughout the manuscript.

Number of PhotonPairs (PP) and λ_2 values depend on the excitation. The smaller the excitation, the smaller the number of PP (tends to 0) and λ_2 (tends to k_{21}). However, $\lambda_2 \sim k_{21}$ indicates a large time constant, and thus START-STOP resolution can be decreased to compensate for small number of PP. To get a good fit across the entire power regime, START-STOP bin width has to be varied - larger bin widths (2048 ps) at low power and smaller bin width (512 ps) at high power. In Figure 3-6, I presented START-STOP histograms at maximum (1,5 Mcps) and minimum (0,1 Mcps) counts during Power Scan. Notice that Interchannel time is taken as positive or negative depending on the channel detection order, thus positive and negative delay.

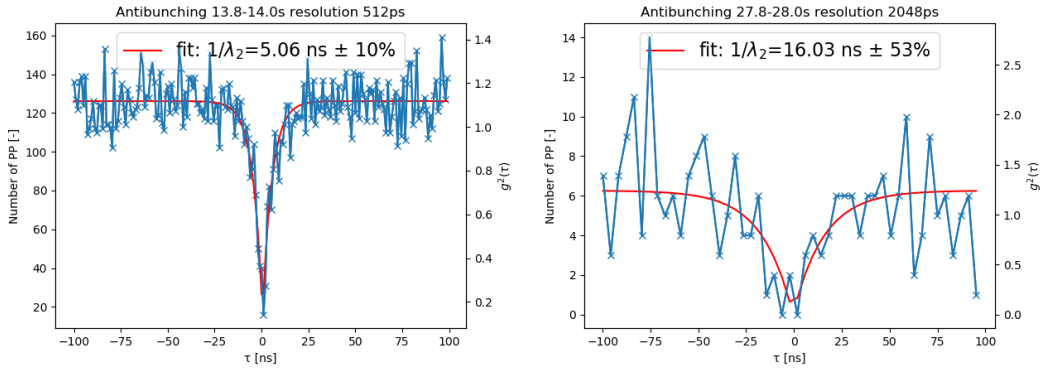

Figure 3-6. START-STOP histograms at 1,5 Mcps (left) and 0,1 Mcps (right) counts; data points (blue crosses), fit (red line).

The fit of the antibunching part at low photon flux yields very high uncertainty on the fitted parameters. However, I expect the fitting error to be random, and thus an average of many measurements should yield a proper value (Power Scan power-dependent speed). I proceed with the calculation of the rates according to the formula:

$$-\lambda_2 = \sigma_{12} * P + k_{21} \qquad 3.8$$

Fitted values of START-STOP histograms are plotted against the power and show good linearity (Figure 3-7). It turns out that both, the lowest and the highest power regimes have a large spread of the data. In the low power regime, it's the fit itself that is problematic (small Number of PPs and low resolution). It's not clear for me, why high power has a large data point spread – resolution is 20 times higher than the investigated time constant, and there are enough PPs to reduce the statistical noise. Nevertheless, the outliers in $\lambda_2 = k_{12} + k_{21}$ are not seen in counts on the detector, and explanation behind it depends on the excitation rate regime as counts are approximately proportional to $k_{12}k_{21}/(k_{12} + k_{21})$ – for $k_{12} \gg k_{21}$ counts stay constant within small variations of k_{12}, but are proportional to changes in k_{21}, while for $k_{12} \ll k_{21}$, counts are proportional to changes in k_{12} and stay constant within small variations of k_{21}. Therefore, noisy λ_2 at high incident power suggests fluorescence lifetime variations, but direct lifetime measurement with pulsed laser would be required to support this claim.

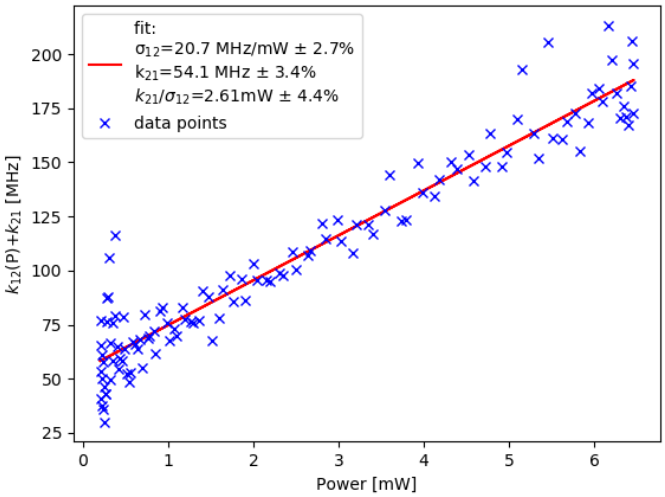

Figure 3-7. Sum of $k_{12}(P) + k_{21}$, that is -λ_2 as a function of the power, data points (blue cross) and linear fit (red line).

The uncertainties of σ_{12} and k_{21} stay typically below 10%. Note that ratio $\frac{k_{21}}{\sigma_{12}}$ found with START-STOP is consistent with that found with a cross-correlation – 2,61±0,12 mW and 2,79±0,38 mW, respectively.

To sum up, the uncertainty of the fit parameter goes from around 50% to 10% at the minimum and maximum photon flux, respectively. This is nearly twice the difference of the bunching curve fit uncertainty. I've calculated values of σ_{12} and k_{21} with their uncertainties, which have similar magnitude - unlike in the bunching regime, where each rate is calculated with a different uncertainty. I confirmed that the results of START-STOP are consistent with the cross-correlation.

The dataset for each molecule consists of the autocorrelation function parameters $(\lambda_2, \lambda_3, A)$ and counts for each time segment (at each power). Under the slow ISC approximation, λ_2 can be approximated by just two rates, but the other parameters remain depended on all 5 rates. Treating the rates separately by dividing the dataset into antibunching rate λ_2 (k_{12}, k_{21}), *TimeON* (k_{23}, k_{12}, k_{21}), *TimeOFF* (k_T, k_{32}) provides an insight into the rates – e.g., if atypical behavior in found in *TimeON(P)* but not in $\lambda_2(P)$, it can be stated directly, that k_{23} wasn't constant during the measurement. The origins of atypical observations are not easily interpreted from the shapes of λ_3 and A.

3.1.1.4. PhotonPairs Fraction ($k_R/k_{21}, C_{EFF}$)

In the Subsections above, I have calculated all 5 rates that govern the photon flux coming from the emitter. The number of counts (detected photons) and number of PhotonPairs within 100 ns depend not only on the rates, but also collection efficiency C_{EFF} of the set-up and radiative part of the excited singlet relaxation $\frac{k_R}{k_{21}}$. Those two parameters can't be determined separately from the autocorrelation parameters and are treated altogether as $\frac{k_R}{k_{21}} C_{EFF}$.

To tackle this problem, I take the calculated rates and implement them into Monte Carlo simulation of two detectors with deadtime of 90 ns (Appendix D.c). Subsequently, to find PhotonPair Fraction (PPF), which is a percentage of PP per counts, that matches the experiment, simulation has to adjust the value of $\frac{k_R}{k_{21}} C_{EFF}$.

The results are plotted in Figure 3-8. Simulation matches the experiment well in shape but there is a slight offset in the y-axis. However, $\frac{k_R}{k_{21}} C_{EFF}$ parameter cannot compensate for the y-axis offset as it changes solely the inclination (slope) of the fitted curve. Besides providing me with the value of $\frac{k_R}{k_{21}} C_{EFF}$, simulation also predicts that there should be around 7% count mismatch at the highest power due to the photon flux lost in the detectors' deadtime – recall, photons lost in the deadtime are equal to at least the number of PP detected.

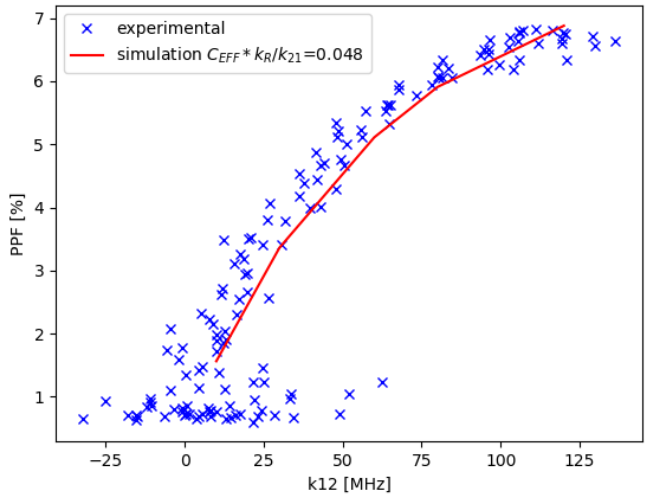

Figure 3-8. Simulation of the PPF using the calculated rates (red line) and the experimental PPF (blue crosses).

To sum up, I have found quantity that I've called PhotonPair Fraction (PPF), which depends on the k_{12}, k_{21} and C_{EFF}. PPF can be used to determine C_{EFF} of the system (once the two rates are determined using the antibunching regime).

3.1.1.5. Photon flux (verification)

The final step of Power Scan data treatment is validation, in which I compare the counts recalculated from the rates with the experimental observation. Counts can be recalculated with the formula:

$$R = \frac{k_R}{k_{21}} C_{EFF} \frac{\sigma_{12} * P * k_{21} * (\sigma_{32} * P + k_T)}{\lambda_2 * \lambda_3} \qquad 3.9$$

This formula actually comes from model B), and I use it for model C) – recall, model B) and C) are 3-level systems with and without rISC. In Chapter 2, I have validated that photon flux coming from both is nearly identical, and thus it is used here.

Photons collected from a molecule constitute of both, emitter's flux and background luminescence, which is not trivial to separate. Collecting the background luminescence few microns away from the emitter, and then subtracting it, is the easiest way to

approximate the counts coming from the emitter's flux only. I plot the calculated and experimental counts as a function of the power (Figure 3-9, left). The calculated and experimental counts show a good but not a perfect match. At the highest power mismatch reaches 12%, which is larger than the error bars calculated from the rate uncertainties.

To investigate it further, I plot their mismatch (Figure 3-9, right) and the deadtime loss predicted by the simulation. As can be seen, mismatch can't be fully compensated by the predicted loss but reduces it by half. Mismatch shows that counts are underestimated in the low power and overestimation in the high power by few percents (<6%). Mismatch of 5% at the lowest power is merely 5 k cps (~100 kcps counts) and 70 kcps at the highest power (flux 1400 kcps). If this mismatch was to be explain by the background, it would mean that background luminescence at the place of the emitter is double of that taken on the side (for this particular molecule). This is actually very probable as the background signal collected at different spots vary by a factor of 2-3. More precise study on the mismatch/background issue isn't really of interest, because I consider a mismatch of <6% (with deadtime loss correction) over nearly 60-fold incident power increase (0,1-6 mW) as a great result.

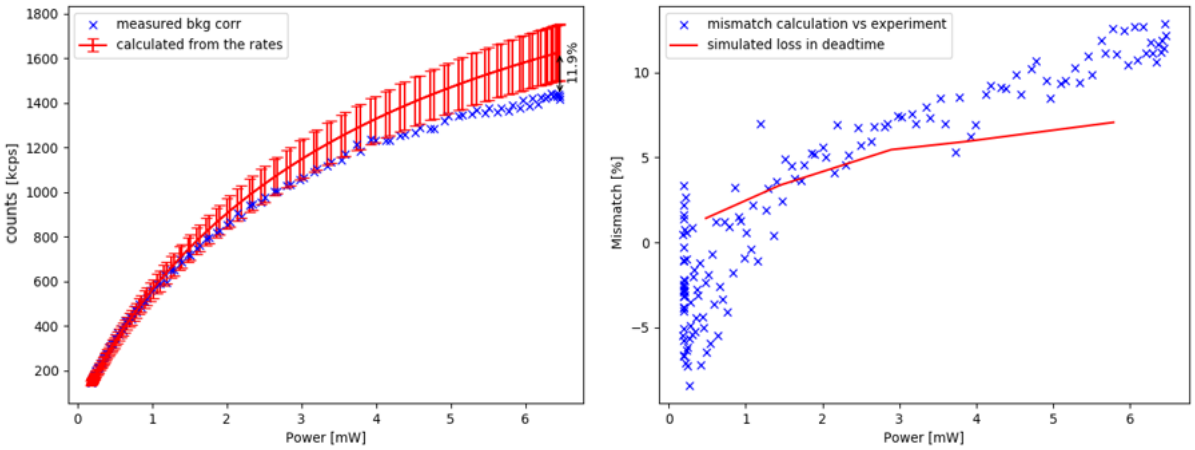

Figure 3-9. Counts calculated from the rates and experimental (left) and mismatch between the two (right) overlaid with the loss predicted by the simulation due to the detector deadtime.

To sum up, I've validated my calculations by matching the experimentally observed and recalculated counts that show 12% mismatch with background correction and only few percent (<6%) mismatch, when deadtime loss is taken into account.

3.1.2. Summary

Results are gathered in Table 3-1. Data processing for a single Power Scan is quite lengthy. In order to discuss the molecule-to-molecule variation in the subsequent Subsection, one has to be aware what is the measurement, fitting procedure, uncertainties, and their magnitude for each rate so that the photophysics can be distinguished from the influence of the data processing.

Table 3-1. Summary of the parameters calculated from Power Scan for a single T in sub-30 nm pT.

parameter	value	unit	Obtained with (regime)
k_T	2,56±0,22 2.6	kHz	Autocorrelation (Bunching)
σ_{32}	9,85±0,08 9.89	kHz/mW	Autocorrelation (Bunching)
k_{23}	12,66±1,58 13.3	kHz	Autocorrelation (Bunching)
k_{21}	54,1±1,8 / 53.24	MHz	START-STOP (Antibunching)
σ_{12}	20,7±0,56 22.7?	MHz/mW	START-STOP (Antibunching)
$\frac{k_R}{k_{21}} C_{EFF}$	0.048		Monte Carlo (Simulation)
Flux lost in deadtime	7	%	Monte Carlo (Simulation)

parameter	value	unit	Obtained with (regime)
Flux mismatch	12	%	Experiment vs Calculations

3.1.3. Population

Reports on measurements of T/pT rates at room temperature (RT) found in the literature don't include information about the fluorescence spectrum of the emitters, besides Kulzer et al. [30]. Therefore, I proceed with 2 separate studies in sub-30 nm pT. First, I collect a large population (43 molecules) without any spectral selection – a randomized study (spectra of each molecule wasn't taken.). Various exemplary fluorescence spectra of T/pT are plotted in Figure 3-10. Secondly, I carry out the experiments on a smaller population (16 molecules), but fluorescence spectrum of each molecule is verified and selected only if peak intensity (λ_{MAX}) is at 578±2 nm (blue line in Figure 3-10).

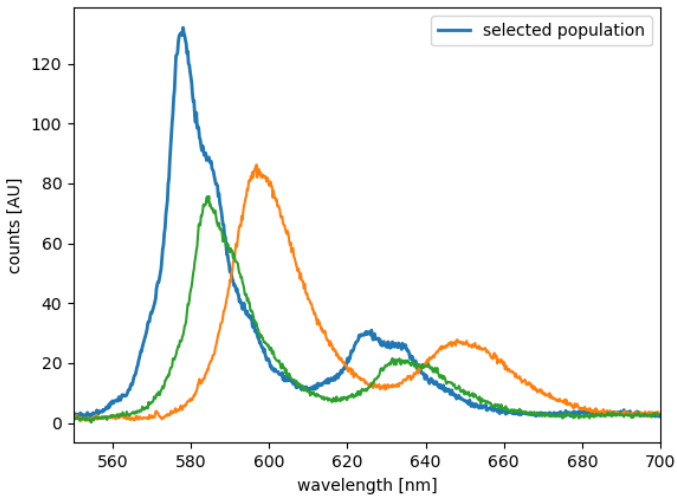

Figure 3-10. Fluorescence spectrum of various single T found in sub-30 nm pT.

I interpret the population std of the calculated rates as the result of both, photophysics and data processing (calculation error). And thus, if all emitters are photophysically

identical, particular rate's population std should be correlated with the typical uncertainty this rate calculation - σ_{32} <2%, σ_{12}, k_{21}<5%, k_T <10%, k_{23} <20%.

3.1.3.1. Randomized study

In Figure 3-11, I present the 5 rates ($\sigma_{12}, k_{21}, k_{23}, \sigma_{32}, k_T$) plotted in every possible combination to look for the correlations or clustering. Prior to analyzing the data, I have to clarify the definition behind two different standard deviation (std) that I refer to below. Every molecule has rates calculated from the fits. Thus the rate of each molecule has its std, which gives the confidence interval that this particular molecule's rate is within given range. On the other hand, for the population of molecules, I can calculate the population std, which gives the confidence interval that any molecule in sub-30nm pT has rates within this range. To not confuse the two concepts, I refer to std of the calculated rate as calculation uncertainty, and to statistics of the population as population std. If I assume that every molecule is photophysically identical, but the rates are calculated with a particular uncertainty, then the data treatment itself gives rise to molecule-to-molecule variation. The typical uncertainties of the rates calculation go as - $\delta\sigma_{32}$ <2%, $\delta\sigma_{12}, \delta k_{21}$<5%, δk_T <10%, δk_{23} <20%. In such a case, population std should be equal to uncertainty, and 99,7% confidence interval is given by 3-times the uncertainty. If the population stds is larger than the calculation uncertainties, then molecules are considered to have photophysical differences beyond the uncertainty (measurement resolution).

The calculation uncertainty are passed to the error bars to investigate whether molecule-to-molecule variation has photophysical or data treatment origins. Average and population std for each rate go as $\sigma_{12} = 16{,}9 \pm 4{,}5\ MHz$, $k_{21} = 53{,}3 \pm 7{,}3\ MHz$, $k_{23} = 12{,}4 \pm 4{,}3\ kHz$, $\sigma_{32} = 8{,}6 \pm 2{,}4\ kHz$, $k_T = 2{,}7 \pm 0{,}7\ kHz$ (27% for σ_{12}, 14% for k_{21}, 35% for k_{23}, 28% for σ_{32} and 26% for k_T). For all the rates, population std is at least 3-times the typical uncertainty (std of the calculated rate from the fit). This means that population 99,7% confidence interval given by ±3 population std is over ±9 uncertainty. Therefore, emitters must have different properties and the differences are larger than the calculation uncertainty.

Looking simply at the pattern in the graphs, it is evident that some rates contain outliers, while others do not. More precisely, graphs without k_T nor k_{23} have no outliers. This

means that an outlier in one rate is not necessarily an outlier in the other rates. The consequence of this statement is that there are physical factors that act on a particular rate exclusively.

The value of k_{21} changes drastically between the studies carried out in the bulk crystals and nanoscale pT – over 200 MHz and 40-67 MHz (Chapter 1, Table 1-2). Values of k_{21} found herein (53,3 MHz) corresponds well with the latter. Also the population std of k_{21} (14%) is 2-3 times smaller than the population std of other rates. The photophysical molecule-to-molecule variation of this rate is therefore dependent on the thickness and the depth inside the film (distance from the air interface). Chen et al. have calculated that in ~20 nm pT film on the glass substrate, range of k_{21} goes from to 60 MHz to 50 MHz, as the distance from the air interface changes from 16 nm to 4 nm [61], which matches well the population std found herein (53,3±7,3 MHz). Chen et al., as well as I herein, have also found experimentally molecules with ~40 MHz emission rate. It is unlikely that molecule is on the surface of pT (photostability), and therefore there might be some additional contribution to the emission rate. The Einstein coefficient predicts that spontaneous emission is proportional to the 3rd power of the emission frequency. If I assume that 50 MHz is the emission rate of the emitter at 578 nm (λ_{MAX} of blue trace, Figure 3-10), then emission rate of the emitter at 600 nm (orange trace, Figure 3-10) would be 45 MHz. Herein, I have found also some molecules with k_{21}~75 MHz that also have much lower C_{EFF} than the average of the population, which might be explained by additional non-radiative relaxation pathways of $k_{21} = k_R + k_{NR}$.

The average values of σ_{12} and σ_{32} should be set by T's oscillator strength of each transition and the environment. Moreover, as Power Scan has no information about the orientation of the transition dipole moment and the excitation polarization, the fitted σ_{12} and σ_{32} depend additionally on the angle between the transition moment and the excitation polarization. Such angle can be approximated (for a large population study), if the orientation of the emitter in the matrix is random, which is not the case for T/pT. Nevertheless, σ_{12} and σ_{32} are linearly correlated with Pearson correlation coefficient of 0,45 and p-value of 0,003 (<0.05 statistically significant) – graph 8) in Figure 3-11. This suggests that the transition moments of σ_{12} and σ_{32} may be somewhat aligned.

Rates k_T and k_{23} contain 1 and 2 outliers (more than 3 population std), respectively. The outlier number 1 has abnormal k_T, while the other rates are close to their average values. Outlier number 2, having the k_T and k_{23} of ~300% the average value, has σ_{12}, σ_{32} and k_{21} close to their average values. Larger k_T and larger k_{23} faster ISC (T1-S0 and S1-T1, respectively). Outliers don't seem to have any correlations between the rates, as outliers in 1 or 2 rates are within the population statistics of other rates.

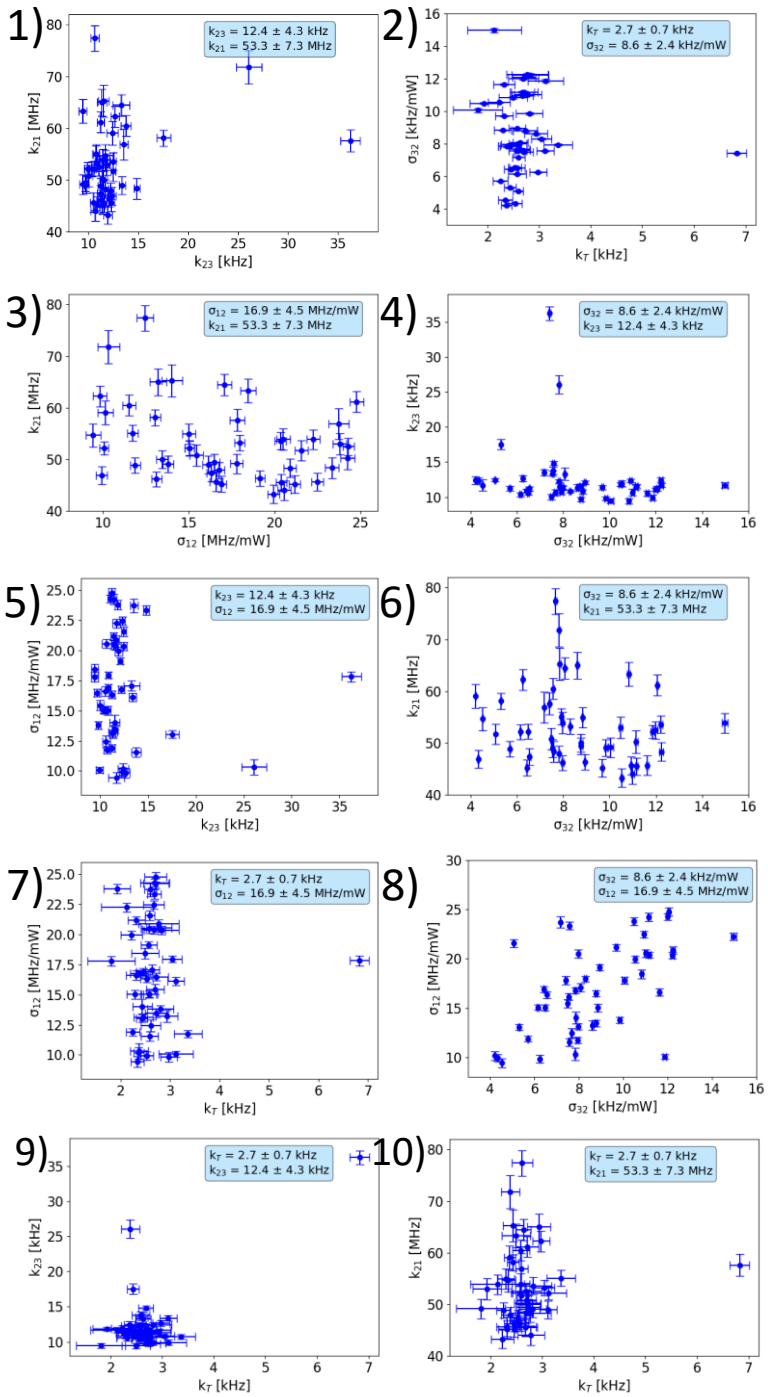

Figure 3-11. The 5 rates ($\sigma_{12}, k_{21}, k_{23}, \sigma_{32}, k_T$) plotted in every combination with the calculation uncertainty as error bars and population statistics in the captions.

To conclude, population std of each rate is at least 3-times larger than calculation uncertainty of that rate and thus molecules are considered photophysically different. The nanophotonic environment (film height and depth) can be considered as the dominant factor controlling the molecule-to-molecule variation in this transition. The excitation

coefficients σ_{12} and σ_{32} are correlated, (with Pearson correlation of 0,45) and thus I expect their transition moments to be colinear. An outlier in one rate is not necessarily an outlier in the other rates. Outliers are beyond the confidence interval of 3 population std (and calculation uncertainty), thus there must be some unknown factors that can affect the photophysics of T/pT that manifests itself through significant change in one or two rates only (outlier number 1 and 2), while the other rates remain close to the average values of the population.

3.1.3.2. Spectral subpopulation

I apply a spectral selection to further investigate the factors contributing to the molecule-to-molecule variation. In Figure 3-10, I presented some random examples of the fluorescence spectrum of T/pT. The redshift of the spectra results in a rapid decrease of the fluorescence intensity and a gradual loss of the vibronic pattern I focus on the most blue-shifted spectral subpopulation, which is the brightest and happens to have the most pronounced vibronic pattern.

In Figure 3-12, I plot histograms of the rates obtained within the random and spectrally selected study. It is evident that rates are much more clustered upon spectral selection, even though average values remain almost unchanged (within std). Average and population stds for each rate go as $\sigma_{12} = 20{,}1 \pm 1{,}6\ MHz/mW$, $k_{21} = 50{,}1 \pm 6{,}0\ MHz$, $k_{23} = 11{,}1 \pm 1{,}3\ kHz$, $\sigma_{32} = 9{,}9 \pm 1{,}1\ kHz/mW$, $k_T = 2{,}6 \pm 0{,}1\ kHz$ (8% for σ_{12}, 12% for k_{21}, 12% for k_{23}, 11% for σ_{32} and 4% for k_T).

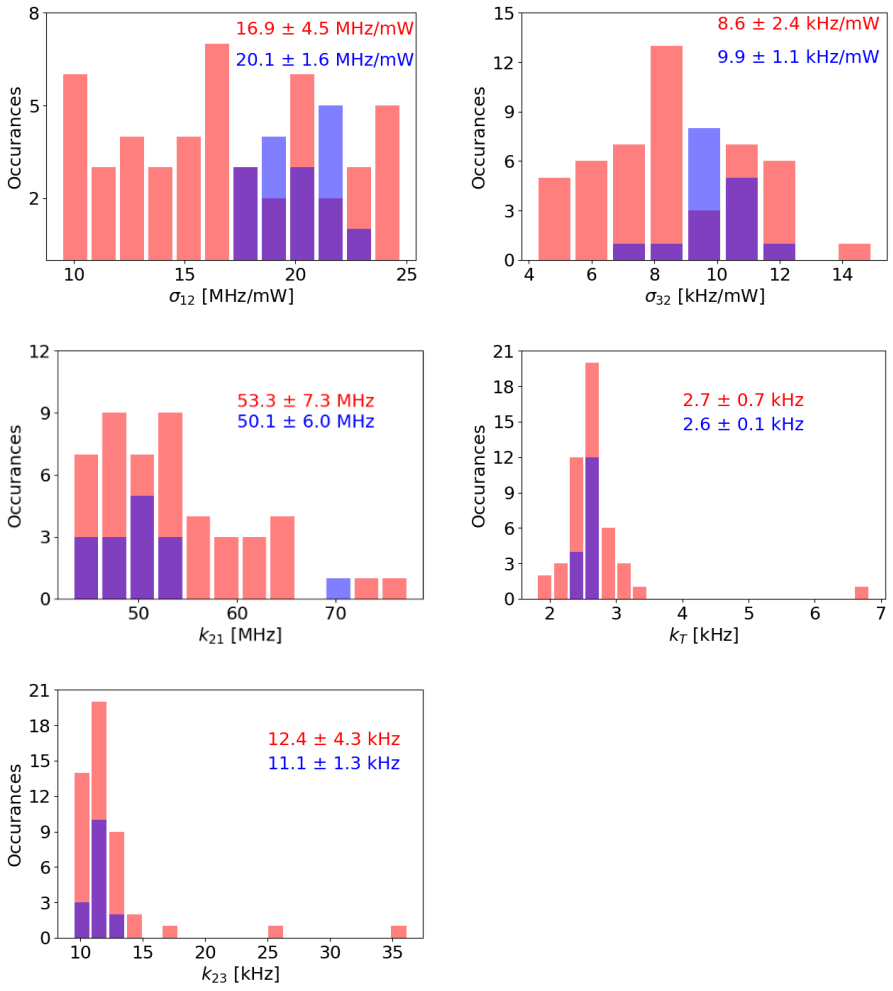

Figure 3-12. Histograms of the rates obtained in the random study (red) and spectral subpopulation (blue).

3.1.3.3. Discussion

The statistics of the rates found in the randomized study and spectrally selected are gathered in Table 3-2.

Table 3-2. Summary of the rates and population standard deviation for a random sample and spectrally biased sample.

	Randomized study (43 molecules)	Spectral subpopulation (16 molecules)

rate	Average	Standard deviation	Average	Standard deviation
σ_{12} [MHz/mW]	16,9	4,5	20,1	1,6
k_{21} [MHz]	53,3	7,3	50,1	6,0
k_{23} [kHz]	12,4	4,3	11,1	1,3
σ_{32} [kHz/mW]	8,6	2,4	9,9	1,1
k_T [kHz]	2,7	0,7	2,6	0,1

In contrast with excitation coefficients, average rates are nearly identical for the randomized study and spectral subpopulation. Population std of spectral subpopulation for each rate, compared to randomized study, goes as 3,3-fold decrease for σ_{12}, 1,2-fold decrease for k_{21}, 3,5-fold decrease for k_{23}, 2,5-fold decrease for σ_{32} and 6,5-fold decrease for k_T. This means that the molecule-to-molecule variation is indifferent to the spectral selection for one rate (k_{21} almost no change) and over a 2-fold decrease for other rates is observed.

Neither k_{21} dispersion nor average change from randomized to subpopulation study, which isn't consistent with Einstein coefficient – more blue-shifted fluorescence should have higher spontaneous emission rate. Thus, the thickness and depth, as well Einstein coefficient are not enough to explain both, the smallest k_{21}~40 MHz and the highest k_{21}~75 MHz. This molecule-to-molecule variation may be explained if I consider that each molecule has a somewhat constant radiative rate, and thus low $C_{EFF} = C_{setup} * k_R/(k_R + k_{NR})$ are a consequence of the additional non-radiative pathways (higher k_{21}). In fact, there is a correlation between calculated k_{21} and C_{EFF} (Figure 3-13) with Pearson coefficient of -0,83 and p-value of $3 \cdot 10^{-11}$.

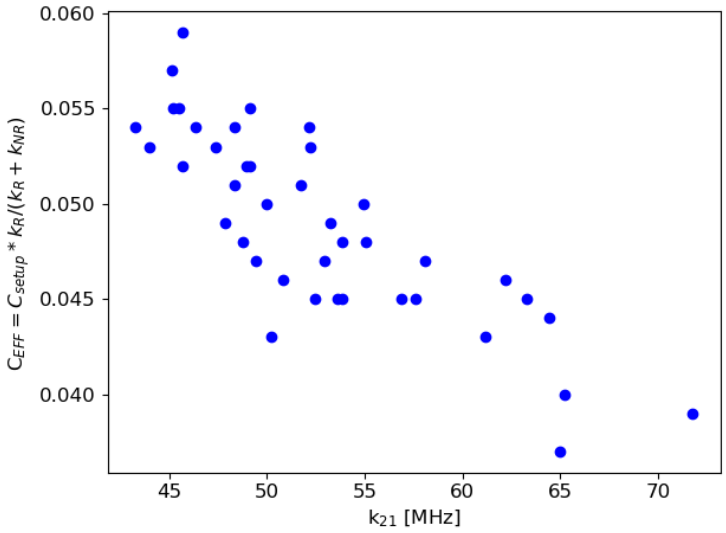

Figure 3-13. Scatter plot of C_{EFF} as a function of k_{21}, population statistics $C_{EFF} = 0{,}049 \pm 0{,}005$. Correlation Pearson coefficient of -0,83 and p-value of $3 \cdot 10^{-11}$.

The decrease in the std of σ_{12} is expected. The fluorescence spectrum is pinned by the absorption spectrum (mirror-like image) – assuming that every molecule experiences similar Stokes shift, which is set by pT matrix. In consequence, the excitation coefficient at laser wavelength remains constant and only misalignment of the transition moment with polarization remains, which is partially compensated by adjusting the polarization for maximum emission. Population std of ~10% indicates the molecules must have some limits to their orientation in space. This limitation manifests itself also through the doughnut-like image on the camera that all molecules poses – Figure 3-14, which implies that they must have significant out-of-plane alignment [72], with 7-15 deg tilt found in literature [55,61]. Note that the maximum value of σ_{12} found in the random sample and spectral subpopulation is the same ~24 MHz/mW. I could convert this value (using incident photon energy) to get $\sim 2 \cdot 10^{-16}$ cm^2 in the case of perfect collinearity of the excitation polarization and S0-S1 the transition dipole moment.

Figure 3-14. Wide-field fluorescence image of T/pT.

The difference in the spread of k_{23} and k_T is striking, 3,5-fold and 6,5-fold, respectively. I draw from this a very counterintuitive conclusion: although it may seem that the fluorescence spectrum (being a mirror-like image of the absorption spectrum) corresponding to the S0-S1 gap should be strongly correlated with the molecule-to-molecule variation of σ_{12} and k_{21}, it is, in fact, k_{23} and k_T that undergo the biggest changes. To understand this, we have to take a closer look at the fluorescence spectrum.

The fluorescence spectrum doesn't only redshift but also gradually changes its pattern. The vibronic pattern is independent of the environment, unless this environment changes Frank-Condon Factors (FCFs). The FCFs are related to the nuclei wavefunction overlap between the lowest excited singlet and vibrationally excited ground states. It seems that T indeed undergoes geometrical distortion inside pT, and this distortion is not step-wise but has a gradual character (various distortions – various fluorescence spectra). This geometric distortion results in the photon flux decrease (fluorescence spectrum in Figure 3-10). It strongly affects the population std in the rates that include horizontal transitions - k_{23} via ISC, k_T via IC. It seems logical, if I recall the energy diagram – the energy gap between S1 and T1 is ~1eV, thus k_{23} transition has to involve a vibrationally excited state of T1 (Energy Gap Law). Analogously, k_T requires the conversion of the lowest vibrational T1 to the vibrationally excited S0. The fact that transitions depend on the vibrationally excited states should make them particularly sensitive to the geometrical distortion of T as the potential energy surfaces and the crossing points should be affected.

Quantitatively, in the total of 59 measured molecules, I have found the smallest k_{23} to be 10 kHz and the largest k_{23} to be 37 kHz, which is a 3,7-fold difference. Meanwhile, the reported values of k_{23} in T/pT sublimated crystals vary by an order of magnitude (Chapter 1, Table 1-2). The whole purpose of using the sublimated crystal is its high quality, homogeneity and purity. It is therefore very surprising that spin coated film has a smaller population std, unless high crystallinity of pT causes actually larger geometrical distortions of the inserted T molecules. However, large molecule-to-molecule variations in ISC are also found in solution, where geometrical distortion cannot be considered. The standard dye such as Rhodamine6G (measured in ethanol) has a 2-orders of magnitude discrepancies in k_{23} between the different studies [158]. Even assuming the worst case scenario, it's very unlikely that different authors have committed 1-2 orders of magnitude mistakes in the data treatment process. It is unclear why I have not observed as large molecule-to-molecule variations in this study. By selecting a spectral subpopulation, the population std of k_{23} has decreased over 3-times. As connection between the spectrum vibronic pattern and geometrical distortion was already discussed, k_{23} must also be connected to this distortion.

Overall, I was expecting to find a molecule-to-molecule variation of 1-2 orders of magnitude (as reported in the literature) and correlate it with other rates and fluorescence spectrum to reveal the mechanisms of the ISC and factors contributing to the molecule-to-molecule variability. Instead, regardless of the spectrum, average value of k_{23} remains the same. Among the 59 molecules only 2 outliers were found and their values were merely a double and a triple of the average value (not an order of magnitude different). Moreover, one of the k_{23} outliers had all the other rates within the average values of the population, thus there was no correlation with the other rates. Another outlier was also an outlier in k_T.

Instead of gaining the insight into the mechanism of ISC in T/pT, results presented herein raise some questions about the literature on the ISC rate. Rates that can be measured directly with dedicated equipment such as σ_{12} (through molar extinction) with spectrophotometer and k_{21} with pulsed laser TCSPC module are consistent throughout the literature [174]. However, rate such as k_{23}, has to be recalculated from the data and often happens to have an order of magnitude spread within a single study and several orders between the studies, whether its T/pT or standard Rhodamine6G dye in the same

solution. Moreover, the way k_{23} is calculated/fitted also varies between the studies and I have shown also here (Appendix G) that the same dataset and equations may yield different rates by taking different approaches in the data treatment.

Just like Koenderink has mentioned in his review of nanoantennas [141], any field can benefit from setting commonly acclaimed methods to calculate a particular quantity and perform its validation, so that it can be readily compared with the different studies. In the field of single-molecules studies, such standardization of the way ISC rate is calculated would be extremely useful.

The value of σ_{12} in randomized study at 532 nm excitation ($1{,}4\pm0{,}4\cdot10^{-16}$ cm^2) – converted using incident power, molecule placed in the center of the gaussian beam with a FWHM of 1,5 μm and 532 nm excitation. This is within an order of magnitude with those reported in the literature for single molecules ($0{,}14\text{-}0{,}75\cdot10^{-16}$ cm^2, orientation not specified) at 514 nm excitation [32] and ensemble study in the solution ($7{,}8\cdot10^{-16}$ cm^2) at 557 nm excitation (wavelength of maximum molar absorption) [58]. For the record, the cross-section σ^{CS} was recalculated as $\varepsilon = 68000$ M^{-1}cm^{-1} and $\sigma^{CS} = 3{,}82 \cdot 10^{-21}\,\varepsilon$ and divided by 1/3 to account for the random orientation in the solution.

The value of σ_{32} (191±53 kHz/MWcm^{-2}) is consistent with the literature (200 and 50 kHz/MWcm^2) [32,45]. Statistically significant positive correlation (Pearson coefficient 0,45) was found between the σ_{32} and σ_{12}. To best of my knowledge, there are no reports on the relative orientation of the transition dipole moment of T1-T5/6 with respect to S0-S1 transition dipole moment.

The fluorescence lifetime $1/k_{21}$ herein (18,8 ± 2,7ns) is in perfect agreement with the literature (15-25 ns) for 20 nm T/pT [62]. The value of k_T (2,7± 0,7 kHz) is in agreement with 2 studies carried out at liquid helium temperature (2 kHz) [26,175] and within an order of magnitude of RT studies in sublimated crystals (3-19 kHz) [32,45].

The ISC related to k_{23} of 12,4±4,3 kHz found herein is in agreement with one study (0,1-14,7 kHz) and disagreement with another (0,1-2,3 MHz), both carried out on sublimated pT crystals [32,45].

3.1.4. Conclusions

I have dedicated a big part of this chapter to step-by-step data treatment and presented graphs at each step to showcase how Power Scan data is processed. To minimize the uncertainty of calculations and identify photophysical contribution of population std, Power Scans were adjusted to acquire observation of the emitter's photon flux at various powers, while minimizing the irradiation dosage and optimizing the photon budget. The counts observed experimentally were compared with the expected photon flux (implication of the calculated rates) to ensure consistency.

Subsequently, I have presented the randomized study (42 molecules), which shows that k_{23} and k_{21} have the largest and the smallest population std, respectively. The population std of each rate in randomized study is at least 3-times larger than the calculation uncertainty, which proves that molecules are indeed photophysically different (beyond the noise introduced by calculation uncertainty).

The population std was reduced with various magnitude for each rate, if only molecules with the most blue-shifted fluorescence spectra are selected (spectral subpopulation). The smallest reduction of population std was observed for k_{21} and the largest for k_T. In fact, population std of k_T in the spectral subpopulation is close to calculation uncertainty and thus molecule-to-molecule variation in this case cannot be interpreted as photophysics. The k_{21} is slightly higher in the randomized study than in the spectral subpopulation, which doesn't obey the frequency of Einstein spontaneous emission coefficient. Molecules with high k_{21} require low C_{EFF} to match the experimental counts. Thus I conclude that radiative QY most likely differs from a molecule to a molecule and prevents the observations predicted by Einstein coefficient. Values of the rates were compared with the literature and are within the order of magnitude, with an exception of one study that reported k_{23} in MHz range. The molecule-to-molecule variation of the rates are much smaller than those reported in the literature.

In spectral subpopulation, the population std of σ_{12} <10%, and doughnut-like image on camera, indicate that T isn't oriented randomly in pT, as reported in the literature. Moreover, σ_{12} has shown linear correlation with σ_{32}, which suggest alignment of those transition dipole moments. To investigate further the collinearity of the S0-S1 and T1-

T5/6, and to calculate the cross-sections, a 3D model of T and Angle Scans are introduced in the next Section.

3.2. Polarization Scan

In this Subsection, I will work on the spectrally-selected subpopulation only ($\lambda_{max} = 577 \pm 2\,nm$ (blue trace Figure 3-10). First, I present frame of reference and the idea behind Polarization Scan. Secondly, I show additional step in the treatment that was not used in Power Scan. Thirdly, I show that within a spectral subpopulation, molecules can be categorized into groups and species based on the particular pattern in Polarization Scan evolution of the rates. Lastly, the results of the field distribution simulation and Analyzer Scan are used to create a 3D model of each species.

Prior to step-by-step treatment, it's important to realize what happens during Polarization Scan and understand the idea behind it. It's obvious that the angle between the molecule absorption's transition dipole moment and the electric field of the excitation (polarization) will change when the polarization angle α_{EXC} of the laser rotates. However, there are some general properties to it. Let's view this problem in terms of linear algebra.

In what follows, I consider a linearly polarized plane wave of the incident excitation at fixed input power. Note that this is not valid for strongly focused beam [20], thus we a beam with FWHM of 1,5 μm at the focus. Moreover, I assume that the refractive index step at the sample interface is small enough so that the linear polarization is preserved.

To make discussion less abstract, first I present the cartesian coordinate system of the experiment, where Y-axis is aligned with s-polarization – Figure 3-15, left. The long axis of terrylene (LA) is expressed as a vector with spherical coordinates – Figure 3-15, right. The angle θ is the polar angle (between Z-axis and LA), such that 0 deg is a perfect Z-axis alignment. The angle φ is the azimuth angle (between Y axis and the projection of LA on XY plane), such as 0 deg is aligned with the Y-axis. And so a unit vector of the transition dipole moment oriented along LA is defined as:

$$\widehat{\mu^{(LA)}} = \begin{bmatrix} \sin\theta\cos\varphi \\ \sin\theta\sin\varphi \\ \cos\theta \end{bmatrix} \quad 3.10$$

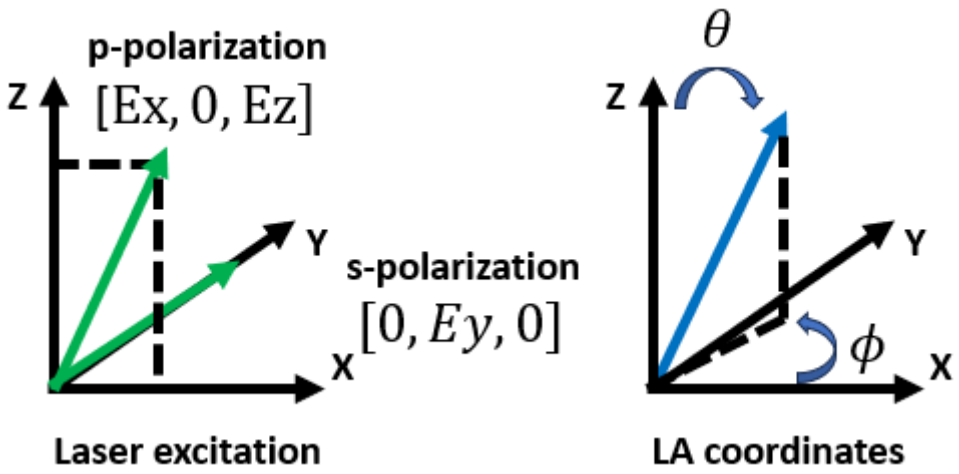

Figure 3-15. Frame of reference – cartesian coordinate system of the experiment with respect to the excitation (left) and the long axis of terrylene expressed in spherical coordinates (right).

As the polarization angle α_{EXC} of the excitation laser rotates by 360 deg, the polarization vector spans a plane – Figure 3-16, upper left. This plane contains vectors of all the possible polarization states. Note that this plane has a tilt angle with respect to the XY plane. This tilt angle would be zero in the normal incidence illumination (as the out-of-plane polarization component is negligible). When a laser is incident on the plane with an angle (as in TIRF illumination), all 3 axis components of the electric field become significant, and thus the out-of-plane tilt is formed.

The dipole moment $\vec{\mu}$ that governs the S0-S1 transition can be viewed as a vector, and is aligned with LA vector. The rate k_{12} at which S0-S1 excitation occurs depends on the dot product between $\vec{\mu}$ and excitation electric field vector $\vec{E}$, and thus on the angle γ between those 2 vectors:

$$k_{12} \propto \left|\overrightarrow{\mu_{12}} \cdot \vec{E}\right|^2 = |\overrightarrow{\mu_{12}}|^2 \cdot \left|\vec{E}\right|^2 \cos^2\gamma \quad 3.11$$

I can also write Equations 3.11 as a function of cartesian coordinates, assuming that S0-S1 excitation is coincident with the long axis of the emitter:

$$k_{12} \propto |\sin\theta\cos\varphi\, E_X + \sin\theta\sin\varphi\, E_Y + \cos\theta\, E_Z|^2 \qquad 3.12$$

Note that any excitation with the polarization vector $\vec{E}$ that is perpendicular to the dipole moment won't be able to excite the transition. Thus $\vec{\mu}$ is the normal vector to the plane that contains all the polarization states for which $k_{excitation} = 0$ (vectors perpendicular to the transition moment). I refer to the plane perpendicular to the transition dipole moment as perpendicular plane, for short. This plane is depicted in Figure 3-16, upper right. Notice that both planes – polarization plane and perpendicular plane –always have an inter Section line (common vectors).

From this inter Section, we get Polarization Scan property number 1 – any transition dipole moment, regardless of its orientation, won't be excitable at least twice during a 360 deg rotation of the excitation polarization. A particular case of property 1 occurs if a transition moment is perpendicular to the polarization plane and thus can never be excited as polarization plane and perpendicular plane are identical. In all the other cases, $k = 0$ only twice during the 360 deg rotation (perpendicular vector and its 180 deg rotation).

The transition moment orientation can be deduced from the perpendicular plane only, if there are 2 vectors. Only then, the perpendicular plane equation can be calculated and thus its normal vector, being the transition dipole moment. Unfortunately, Polarization Scan gives only 1 independent perpendicular vector (and its 180 deg rotation). Although 1 perpendicular vector doesn't allow to solve for $\vec{\mu}$, it limits the space of solutions to a plane. The perpendicular vector can be used as a normal vector to the surface, which contains $\vec{\mu}$ (solution plane).

Having only 1 perpendicular vector that belongs to the perpendicular plane doesn't allow to solve for $\vec{\mu}$, but it does limit the number of solutions – this perpendicular vector can be used as a normal to the plane, which contains the transition dipole (solution space)– Figure 3-16, bottom.

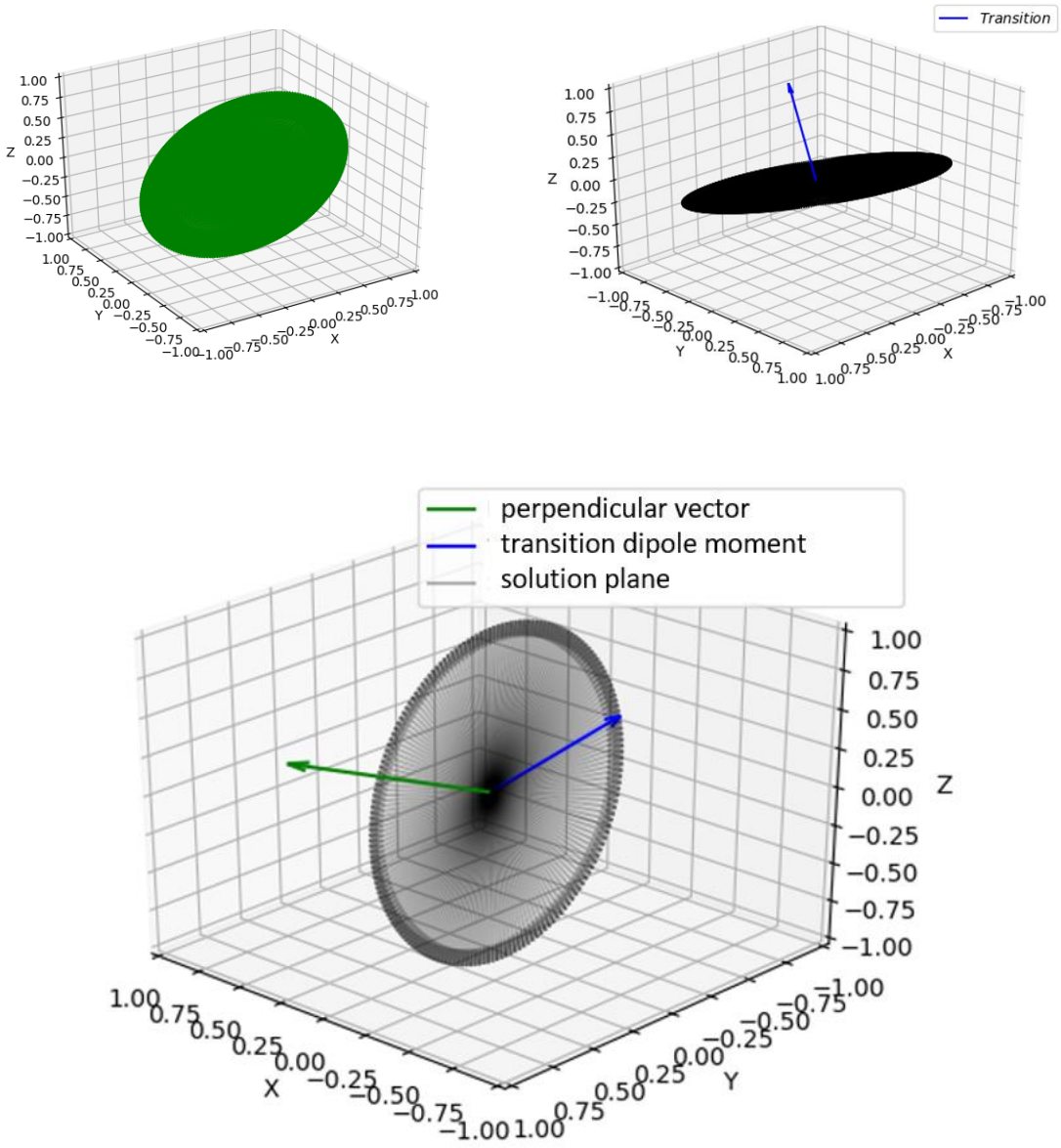

Figure 3-16. Exemplary representation of the polarization plane as α_{EXC} rotates by 360 deg (upper left). An arbitrary transition moment with its perpendicular plane (upper right). An arbitrary transition moment with its perpendicular vector, which is a normal vector to the solution plane that contains this transition dipole moment (bottom).

Polarization Scan property number 2 – the polarization at which excitation is the largest, doesn't mean that $\cos^2(\gamma)$=1. As polarization rotates from one perpendicular vector to its 180 deg rotation (from k=0 to k=0), it makes a 180 deg turn. However, 90 deg away from the k=0, the function takes a value of $I * \cos^2(\gamma)$, where intensity I depends on the field distribution. Therefore, there is a scale factor, which becomes very important when calculating the e.g. S0-S1 cross-section. In fact if $\overrightarrow{\mu_{12}}$ and $\vec{E}$ are not known, the calculated

S0-S1 ''absorption cross-section'' σ_{12} is not a cross-section per se, as it lacks $\cos^2(\gamma)$ correction and the field distribution factor. In TIRF illumination, even at the constant intensity (that enters the microscope objective), the intensity at the location of the emitter varies with polarization [20]. The true S0-S1 cross-section σ_{12}^{CS} must therefore depend on the polarization-dependent intensity $I(\alpha_{EXC})$, expressed in the unit of [$s^{-1} \cdot cm^{-2}$], and the polarization dependent angle γ between the electric field of the excitation and the S0-S1 transition dipole moment (fixed for a given molecule). Now excitation rate as a function of polarization angle can be expressed:

$$k_{12}(\alpha_{EXC}) = \sigma_{12}^{CS} * I(\alpha_{EXC}) * \cos^2 \gamma(\alpha_{EXC}) \qquad 3.13$$

To be more precise, intensity depends on the angle of incidence of the laser on the sample, depth at which T is embedded in pT and the refractive index of pT – the results of the simulation performed by Ludovic Douillard can be found in Section 2.1.5.

To sum up, 360 deg rotation of the excitation polarization spans a polarization plane. A transition dipole moment $\vec{\mu}$ is a normal vector to the perpendicular surface. Polarization Scan recovers only 1 independent perpendicular vector ($k_{excitation} = 0$), but two are required to find the orientation of $\vec{\mu}$. A single independent perpendicular vector is a normal vector to the solution plane, which contains $\vec{\mu}$. Calculating the cross-section σ^{CS} [cm^2] requires the information of the transition moment orientation and the excitation field distribution, otherwise σ remains an excitation coefficient.

3.2.1. Step-by-step data treatment

The step-by-step data treatment of Polarization Scan is analogous to Power Scan and will not be repeated here, apart from the uncertainty restriction step, which wasn't applied before. During Polarization Scan the incident power is constant (no need for power synchronization), speed of the polarization rotation element is constant (20 deg/s).

3.2.1.1. Uncertainty restriction

Recall Polarization Scan property number 1 – as polarization rotates by 360 deg, there will be at least 2 polarization vectors at which $k_{excitation}$=0 (perpendicular vector). This

means that at a certain α_{EXC} (and around it), T doesn't emit photons (or very few) – if it can't be excited, it won't relax radiatively. The data treatment script proceeds with the fitting regardless of the number of counts on the detector. Those fits yield physically unreasonable values with very high uncertainties because there are not enough photons – Figure 3-17, right column.

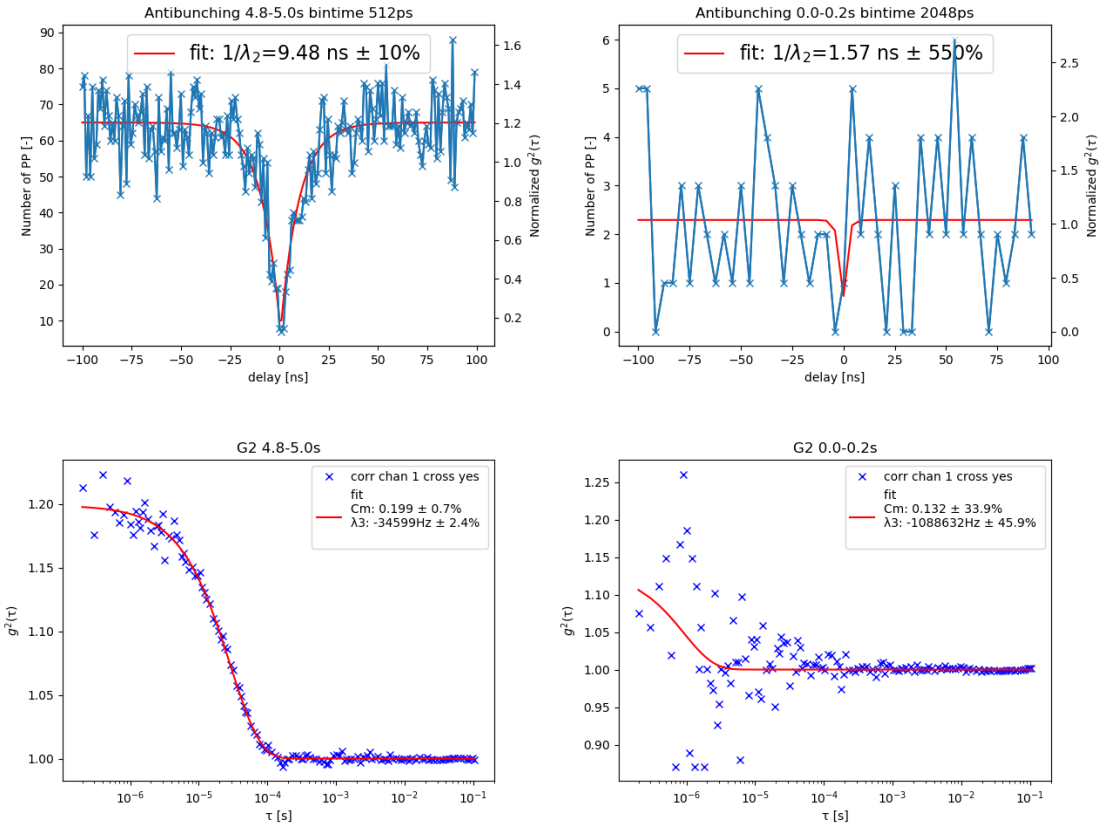

Figure 3-17. Examples of the START-STOP (top row) and cross-correlation (bottom row) at the 1,05 Mcps (left column) and near zero-excitation polarization vector (right column) during Polarization Scan.

Those observations must be removed from the dataset. To do this, I apply a condition that only data points having less than 30% uncertainty of λ_2 fit and less than 10% uncertainty of A and λ_3 fit are included in the dataset - Figure 3-18.

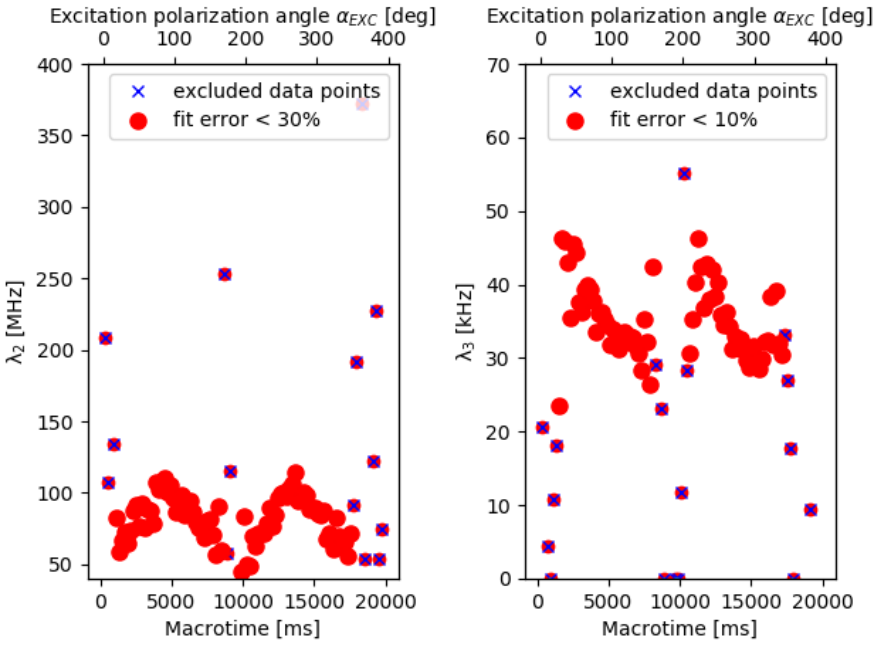

Figure 3-18. Time trace of the λ_2 and λ_3 parameters; data points (red dots) and data points that don't fulfill the uncertainty restrictions (blue crosses).

3.2.2. Species

I examine the dependence of the counts, $k_{12}(\alpha_{EXC}) + k_{21}$ and $k_{32}(\alpha_{EXC}) + k_T$ for 4 molecules as a function of the polarization angle α_{EXC} in Figure 3-19. Only k_{12} and k_{32} are considered polarization-dependent, because k_{21} and k_T are the relaxations rates (no stimulated emission/relaxation).

To categorize the emitters, I show that evolution of $k_{12}(\alpha_{EXC}) + k_{21}$ and $k_{32}(\alpha_{EXC}) + k_T$ can be approximated with an empirical formula:

$$B * \cos(\alpha_{EXC} - \beta)^2 + B0 \qquad 3.14$$

In the case of $k_{12}(\alpha_{EXC}) + k_{21}$, B relates to k_{12}, while $B0$ to k_{21}. In the case of $k_{32}(\alpha_{EXC}) + k_T$, such assignment can't be made – $B0$ is not k_T (explained below). The polarization angle, at which the excitation rate is maximum, is given by β.

The counts pattern (green crosses) exhibits a more or less pronounced flattening of its maxima, which is a typical sign of the saturation occurring at $k_{12} \gg k_{21}$. The maximum

counts are always aligned with the evolution of $k_{12}(\alpha_{EXC}) + k_{21}$, but not always with $k_{32}(\alpha_{EXC}) + k_T$. In the latter case, the counts are also slightly asymmetric around its maxima. The $k_{12}(\alpha_{EXC}) + k_{21}$ has a character of a single transition dipole moment. It has a squared cosine shape and its B0 is close to value of k_{21}, which means that perpendicular vector exists. In the case of $k_{32}(\alpha_{EXC}) + k_T$, B0 never reaches the value of k_T (~3 kHz), instead it stays as high as 26 kHz. The evolution of $k_{32}(\alpha_{EXC}) + k_T$ breaks Polarization Scan property number 1, because it can't be described by means of a single transition moment. This finding is consistent with the reported allowed transitions T1-T5 and T1-T6 (Chapter 1, Table 1-1), which are said to have cross-section of similar magnitude at the wavelengths of 2,26 eV and 2,42 eV nm, while the laser excitation used herein is 2,33 eV (almost at the identical distance in eV from both triplet transitions). Overall, this proves that description of k_{32}=$k_T \beta I$ as in reference [64] is incorrect physically, because it is not the T1-S0 transition that is power dependent.

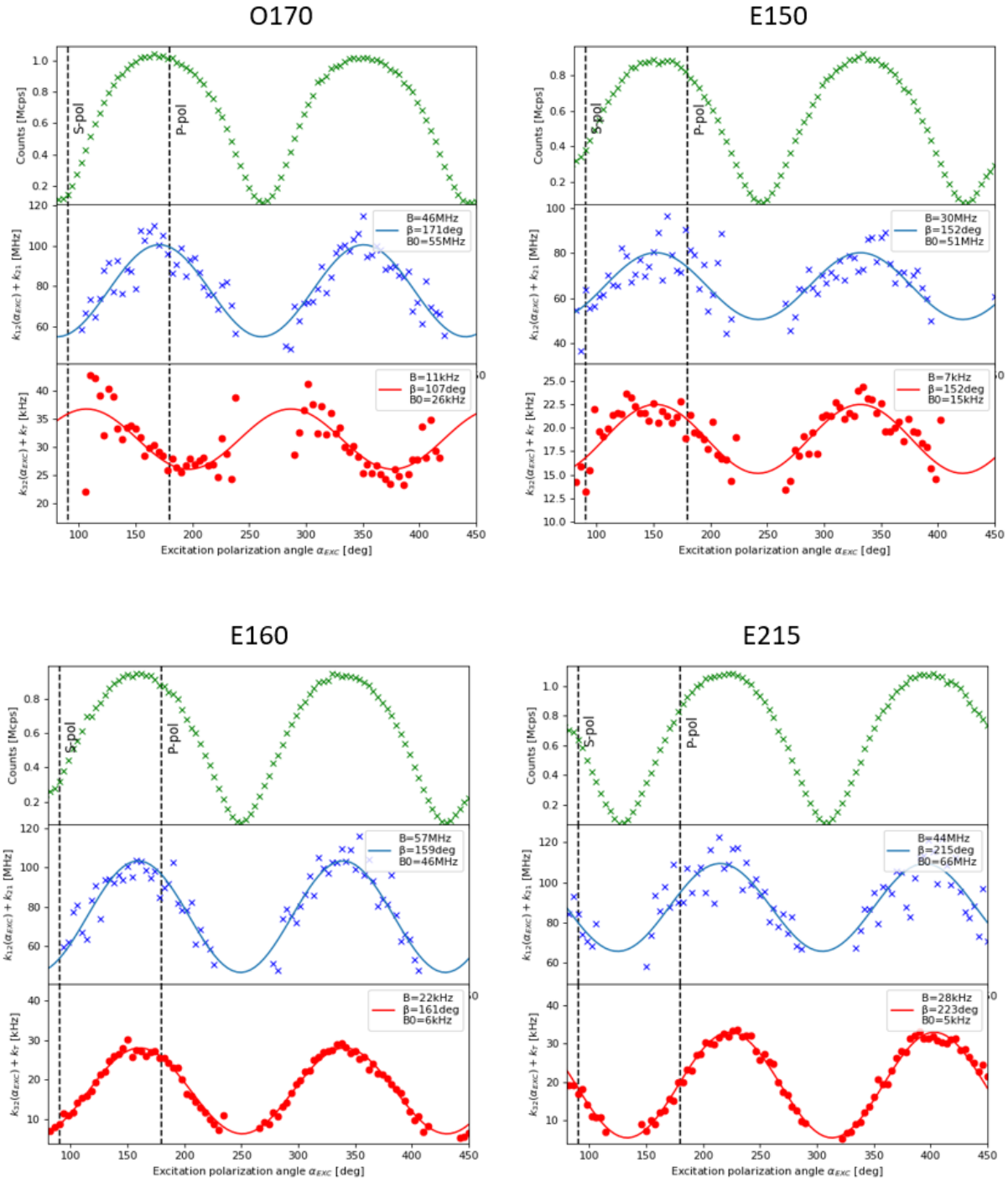

Figure 3-19. Four distinct Polarization Scan species (O170, E150, E160 and E215). Evolution of counts on the detectors (green cross), sum of excitation rate and spontaneous emission rate (blue cross) and triplet depopulation (red dots) as a function of excitation polarization angle. Datapoints were fitted with an empirical formula $B * cos^2(\alpha_{EXC} - \beta) + B0$ *as* k_{12}

and k_{32} are polarization-dependent, while k_{21} and k_T are independent. PP and PS polarization are indicated with a dashed black line.

The fits performed with this formula are represented as lines in Figure 3-19 and show that fitted β (Equation 3.14) in case of k_{12} and k_{32} evolution is not always identical. Based on this, the emitters can be categorized into 2 groups – even (E) and odd (O), which refers to the relation of β found for k_{12} and k_{32}. The visualization of E and O groups is best visible on the polar plots of k_{12} and k_{32} in Figure 3-20.

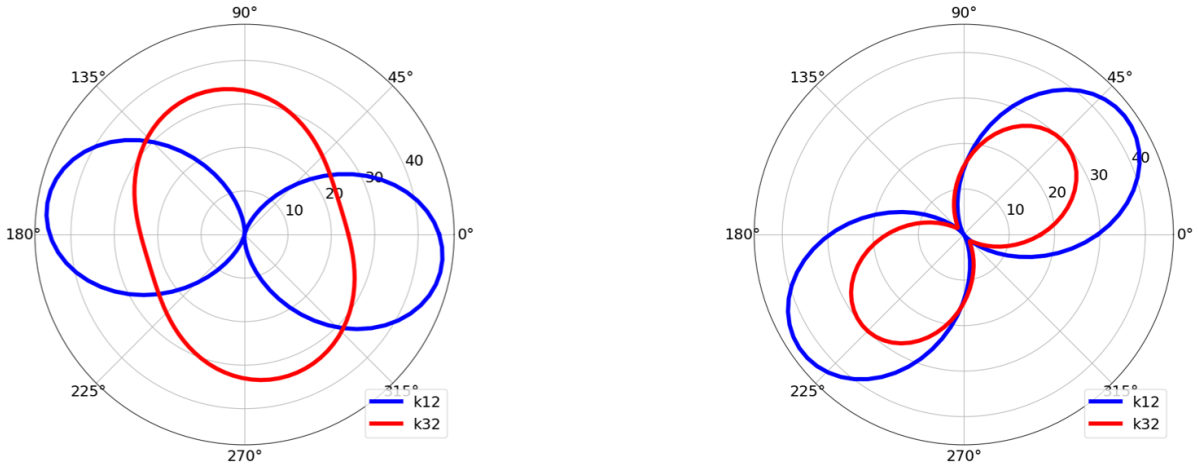

Figure 3-20. Polar plots of the singlet and triplet excitation rates (k_{12} and k_{32}) showing the odd group (left) and the even group (right).

Subsequently, the molecules within each group can be divided into species, based on the polarization angle at which k_{12} (or counts) is maximal. The assignment of the species presented in Figure 3-19 goes as:

- O170, which has a maximum k_{12} at $\alpha_{EXC} \approx 170$ deg and maximum k_{32} at α_{EXC} shifted by ~65 deg and $k_{32} + k_T$ evolution has an amplitude *B>B0* and $k_{32} + k_T$ evolution has parameters *B<B0* (Figure 3-19, upper left)
- E150, which has a maximum k_{12} and k_{32} at $\alpha_{EXC} \approx 150$ deg but its $k_{32} + k_T$ evolution has parameters *B<B0* (Figure 3-19, lower right).
- E160, which has a maximum k_{12} and k_{32} at $\alpha_{EXC} \approx 160$ deg and $k_{32} + k_T$ evolution has parameters *B>B0* (Figure 3-19, upper right)
- E215, which has a maximum k_{12} and k_{32} at $\alpha_{EXC} \approx 215$ deg and $k_{32} + k_T$ evolution has parameters *B>B0* (Figure 3-19, lower left)

Such identification of the species is very important. Later on, I will show that other molecules measured are just repetitions of those species. However, this doesn't mean that other species don't exist - some molecules have very low photon flux, whatever the α_{EXC}, which prevents me from taking the measurements with good counts SNR.

To verify if the 2 groups (E and O) are made of inherently different emitters exhibiting different photophysics, I've carried out Power Scans on 16 molecules. Out of 16, 8 molecules belong to E group and 8 molecules that belong to O group. Their population statistics is given in Table 3-3. The biggest difference between E and O was found for σ_{32} (12%), which is still within the population standard deviations of the 2 groups. Other rates have a difference below 7%. Altogether, with the identical maximum emission wavelength in the fluorescence spectrum, Based on the population statistics, I conclude that E and O groups cannot be distinguished with Power Scans only (are identical in rates), which highlights the importance of Polarization Scans.

Table 3-3. Average values of rates found with Power Scans for molecules divided into E (even) and O (odd) groups based on the evolution of $k_{12}(\alpha_{EXC}) + k_{21}$ and $k_{32}(\alpha_{EXC}) + k_T$ in Polarization Scans.

Rates from Power Scan	**E**	**O**	**Difference [%]**
k_T [kHz]	2,6±0,1	2,6±0,1	-
σ_{32} [kHz/mW]	10,6±0,7	9,3±0,9	12
k_{23} [kHz]	12,7±0,8	12,0±1,4	6
k_{21} [MHz]	48,6±3,6	51,5±7,5	6
σ_{12} [MHz/mW]	20,5±2,0	19,7±0,9	4

3.2.2.1. Polarization Scan vs Power Scan

Expression $B * \cos(\alpha_{EXC} - \beta)^2 + B0$ used to fit Polarization Scans is appropriate to fit the phase relation of the rates but not ideal to calculate the rates - it assumes that $\cos^2 \gamma = 1$ at $\alpha_{EXC} = \beta$.

To compare qualitatively the results of Power Scan and Polarization Scan, I calculate the cross-section and emission rate according to the relations $\sigma_{12} * P \sim B$ and $k_{21} \sim B0$ for 16 molecules and compare it with Power Scan results –Figure 3-21.

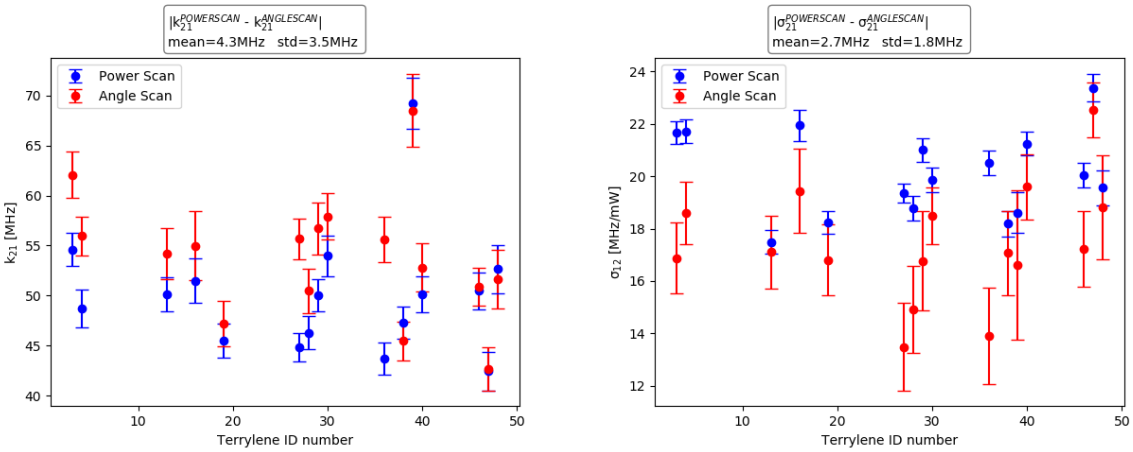

Figure 3-21. Spontaneous emission rate (k_{21}, left) and singlet excitation coefficient (σ_{12}, right) for 16 spectrally selected molecules calculated using Power Scan (blue dots) and Polarization Scan (red dots) cos² approximation. Error bars given by fit uncertainty.

The average mismatch between k_{21} calculated with Power and Polarization Scans approximation is equal to 4,3 MHz (9% of the average k_{21} from Power Scan) and 2,7MHz for σ_{12} (13% of the average σ_{12} from Power Scan). It's clear that mismatch is biased and not random – Polarization Scan tends to overestimate the k_{21} at the cost of σ_{12} underestimation. The main reason behind this deviation is the fact that the excitation rate doesn't evolve simply as cos², but requires a scale factor – if at some α_{EXC}, polarization is perfectly collinear with the dipole moment scale factor is equal to 1, otherwise <1. Moreover, dataset doesn't include the low excitation datapoints.

Remember that Power Scan also $\kappa \cdot \sigma_{12} \cdot \cos^2(\gamma)$ as angle between polarization and the molecule is unknown during Power Scan. Therefore, rates calculated with $B * \cos^2(\alpha_{EXC} - \beta) + B0$ formula carry the scaling factor. In the next Subsection, I will

describe the interaction and provide a coherent description of both Power and Polarization scan

3.2.3. The 3D model

In order to solve the 3D orientation and release the 3 cross-sections from the $\cos^2(\gamma)=1$ approximation, I have to consider the possible orientations of the 3 transition moments that were identified using Polarization Scans.

Recall that T belongs to the symmetry Point Group D_2h. If the geometry of T is not distorted, only transitions along the long axis (LA), short axis (SA) or out-of-plane axis are allowed (unless the transition is vibronic and vibrational mode breaks the symmetry). The S0-S1 (HOMO-LUMO) transition is a $\pi-\pi^*$ transition and is colinear with the LA of T. One of the triplet-triplet absorption components has proven to be aligned with $k_{12}(\alpha_{EXC})$ in Polarization Scans, and thus is also colinear with the LA. The second triplet-triplet excitation component has shown to be misaligned with $k_{12}(\alpha_{EXC})$. Since SA and out-of-plane axis are indistinguishable experimentally, for notation, I assign it to the SA of T. Therefore the cross-sections related to those triplet-triplet transitions are from now on referred to as $\sigma_{32}^{CS(LA)}$ and $\sigma_{32}^{CS(SA)}$. Thus the 3 transition dipole moments related to the excitation rates can be simplified to just 2 orientations – LA and SA (Figure 3-24 if description is unclear).

To describe $\sigma_{32}^{CS(SA)}$ in cartesian coordinates, where the cartesian components of the unit vector of $\widehat{\mu^{LA}}$ were defined in Equation 3.10as $\widehat{\mu_X^{LA}}=\sin\theta\cos\varphi$, $\widehat{\mu_Y^{LA}}=\sin\theta\sin\varphi$ and $\widehat{\mu_Z^{LA}}=\cos\theta$. Since the SA is perpendicular to the LA, I can define its components as:

$$\widehat{\mu_{X,0}^{SA}}=\sin\left(\theta+\frac{\pi}{2}\right)\cos\varphi \qquad 3.15$$

$$\widehat{\mu_{Y,0}^{SA}}=\sin\left(\theta+\frac{\pi}{2}\right)\sin\varphi \qquad 3.16$$

$$\widehat{\mu_{Z,0}^{SA}}=\cos\left(\theta+\frac{\pi}{2}\right) \qquad 3.17$$

Because $\widehat{\mu^{SA}}$ is free to rotate around the LA by angle φ', the unit vector related to $\sigma_{32}^{CS(SA)}$ can be calculated using the rotation matrix, where ξ is the angle of rotation (s=sin ξ and c=cos ξ):

$$\begin{bmatrix} \widehat{\mu_{X,\varphi_{SA}}^{SA}} \\ \widehat{\mu_{Y,\varphi_{SA}}^{SA}} \\ \widehat{\mu_{Z,\varphi_{SA}}^{SA}} \end{bmatrix} = \begin{bmatrix} \widehat{\mu_X^{LA}}^2(1-c)+c & \widehat{\mu_X^{LA}}\widehat{\mu_Y^{LA}}(1-c)-\widehat{\mu_Z^{LA}}s & \widehat{\mu_X^{LA}}\widehat{\mu_Z^{LA}}(1-c)+\widehat{\mu_Y^{LA}}s \\ \widehat{\mu_X^{LA}}\widehat{\mu_Y^{LA}}(1-c)+\widehat{\mu_Z^{LA}}s & \widehat{\mu_Y^{LA}}^2(1-c)+c & \widehat{\mu_Y^{LA}}\widehat{\mu_Z^{LA}}(1-c)-\widehat{\mu_X^{LA}}s \\ \widehat{\mu_X^{LA}}\widehat{\mu_Z^{LA}}(1-c)-\widehat{\mu_Y^{LA}}s & \widehat{\mu_Y^{LA}}\widehat{\mu_Z^{LA}}(1-c)+\widehat{\mu_X^{LA}}s & \widehat{\mu_Z^{LA}}^2(1-c)+c \end{bmatrix} \begin{bmatrix} \widehat{\mu_{X,0}^{SA}} \\ \widehat{\mu_{Y,0}^{SA}} \\ \widehat{\mu_{Z,0}^{SA}} \end{bmatrix} \quad 3.18$$

And thus in the spherical coordinates $\overrightarrow{\mu^{SA}}$ takes azimuthal angle of $\varphi_{SA} = \varphi + \xi$.

The emission dipole moment related to k_{21} can be safely assumed to be coincident with the LA. Therefore, if the orientation of the radiating dipole can be measured, $\widehat{\mu^{LA}}$ can be determined. This is done by performing Analyzer Scan – at fixed excitation power and polarization, the counts are recorded as the analyzer in front of the photon counter rotates. Experimental data is fitted assuming an emitter placed in the homogenous environment [73]. Note that every Analyzer Scan has 2 azimuthal solutions: φ and φ±180 deg (modulo 180) as the symmetry element of 180 deg rotation around the Z-axis is indistinguishable via Analyzer Scan. More details on Analyzer Scan can be found in Section 2.1.4.

Overall, the model has 12 parameters:

- Spherical coordinates of the S0-S1 transition dipole moment (σ_{12}^{CS}, φ, θ) – 3 unknowns
- Spherical coordinates of the LA triplet-triplet transition dipole moment ($\sigma_{32}^{CS\ (LA)}$, φ, θ) – 1 unknown
- Spherical coordinates of the SA triplet-triplet transition dipole moment ($\sigma_{32}^{CS\ (SA)}$, φ', θ') – 3 unknowns
- Rates and set-up (k_{21}, k_{23}, k_T, C_{EFF}) – 4 unknowns
- Distance from the glass interface at which emitter is embedded in pT (h) – 1 unknown

Now that the dipole moments are defined, I can link Power Scan and Polarization Scans. To use them both, its simpler to view it in terms of the effective intensity that the dipole 'sees'. This effective

intensity factor κ is a dot product between the electric field vector $\vec{E}$ and the unit vector $\hat{\mu}$ of the dipole moment:

$$\kappa = \hat{\mu} \cdot \vec{E} = |E(P, \alpha_{EXC})|^2 \cos^2 \gamma(\alpha_{EXC}) \quad 3.19$$

Effective intensity factor κ varies in both Scans but for different reasons. In Power Scan $\cos^2\gamma$ stays constant as α_{EXC} is fixed, but $|E|^2$ varies with incident power. In Polarization Scan, both the components vary, even though incident power is fixed, due to the filed distribution in TIRF illumination. Once κ is implemented, the model with 12 parameters can work on the dataset composed of Power and Polarization Scan.

Lastly, in order to recalculate the excitation coefficients into the cross-sections, intensity has to be expressed in photons/(s·cm^2):

$$I = \frac{\lambda_{EXC}}{\pi * \left(\frac{FWHM}{2}\right)^2 * c * h} \left[\frac{photons}{s * cm^2}\right] \quad 3.20$$

Where λ_{EXC} is the wavelength of excitation laser, $FWHM$ is 1,5µm of the beam PSF, c and h are speed of light and Plancks constant, respectively.

3.2.3.1. Species E170

I start with species E170. First, I plot Analyzer Scan data points and the fit in Figure 3-22 (Analyzer Scan details in Section 2.1.4.2), which yields $\theta = 25\ deg$, $\varphi = 342$ deg.

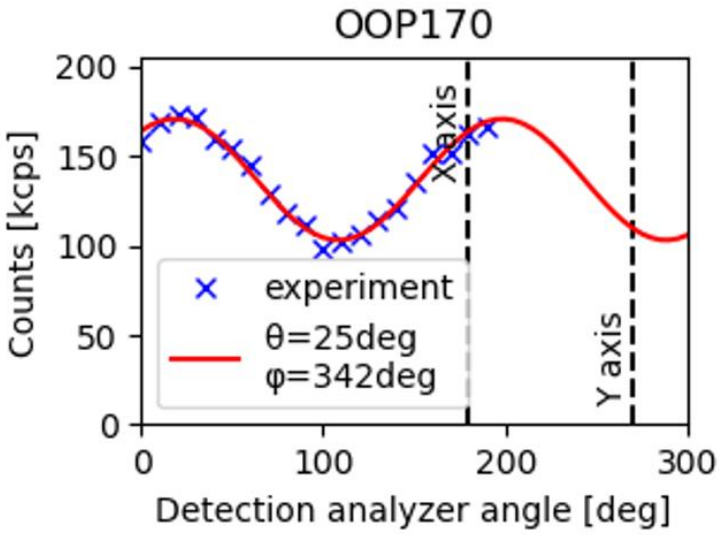

Figure 3-22. Analyzer Scan of E170 species with fitted polar and azimuthal angles ($\theta = 25\,deg$, $\varphi = 342$ or 162 deg); datapoints (blue crosses) and fit (red line). Axis of the cartesian coordinate system are given with dashed lines.

For now, I assume that φ and θ found with Analyzer Scan are the azimuthal and polar angles of $\widehat{\mu^{LA}}$. I apply those spherical coordinates as fixed and proceed with fitting the Power Scan and Polarization Scan (joined fit). The results of the (Analyzer-defined $\widehat{\mu^{LA}}$) joined fit are presented in Figure 3-23, with the parameters in the header. The model (lines) matches very well with the data points. There is no significant horizontal nor vertical offset between the two, besides a slight horizontal offset of $A(\alpha_{EXC})$ and $k_{32}(\alpha_{EXC}) + k_T$ (Figure 3-23, left column). The 3D model given by this solution is presented in Figure 3-24.

The model yields σ_{12}^{CS}~12·10^{-17}cm^2 at 532 nm, which is 6,5-times smaller than the cross-section found in the solution at 557 nm (σ_{12}^{CS}=78·10^{-17}cm^2 [58]) and larger than various $\kappa\,\sigma_{12}^{CS}\cos^2\gamma$ found in T/pT system at 514 nm (1-8·10^{-17} cm^2 [32]), where field distribution and orientation weren't discussed.

Analyzer-defined $\widehat{\mu^{LA}}$ is useful to find the order of magnitude of the cross-sections (σ_{12}^{CS}, $\sigma_{32}^{CS\,(LA)}$, $\sigma_{32}^{CS\,(SA)}$). The following species (E150, E160, E215) are fitted by fixing σ_{12}^{CS} to the value found in O170 (12·10^{-17}cm^2) without fixing $\widehat{\mu^{LA}}$ to Analyzer Scan. Such approach is taken because without defining $\widehat{\mu^{LA}}$ with Analyzer Scan, the latter can be used as an

independent reference to verify if both, Analyzer Scan and joined fit find consistent spherical coordinates of $\widehat{\mu^{LA}}$.

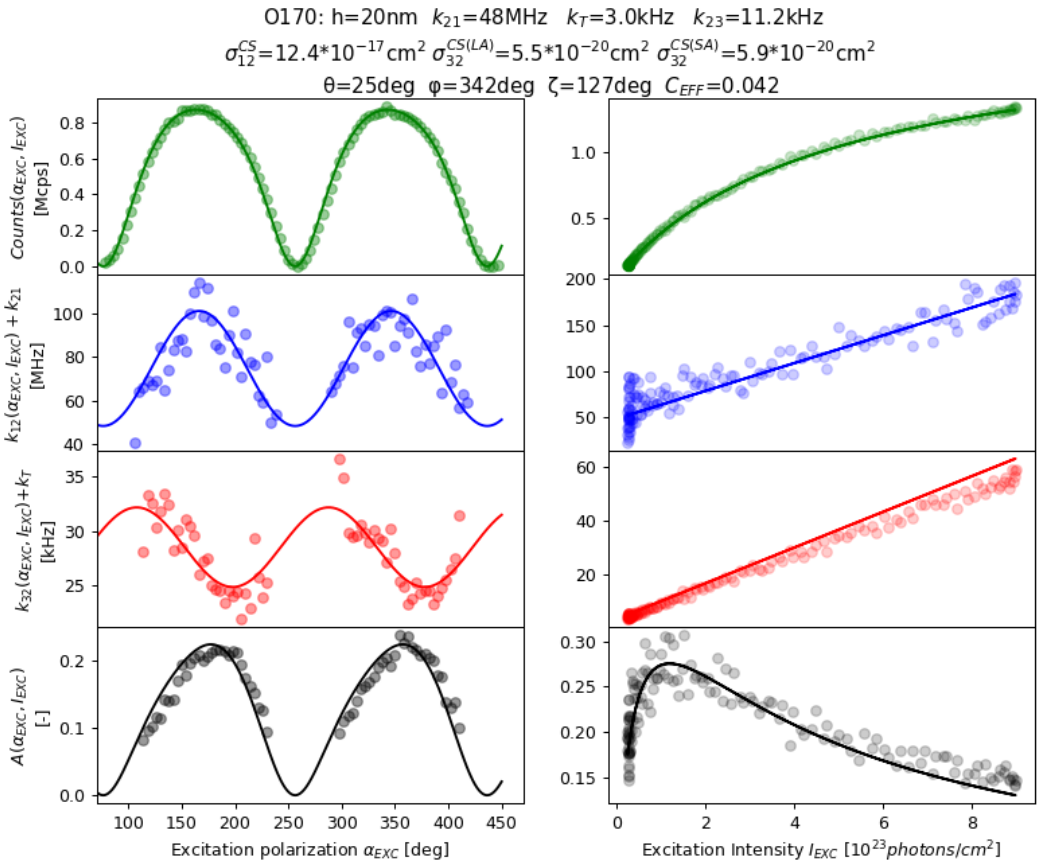

Figure 3-23. Joined fit (Analyzer-defined μ^{LA})– Angle (left) and Power Scan (right) fit of species O170. In top-down order: counts(α_{EXC}, I_{EXC}), $k_{12}(\alpha_{EXC}, I_{EXC}) + k_{21}$, $k_{32}(\alpha_{EXC}, I_{EXC}) + k_T$ and $A(\alpha_{EXC}, I_{EXC})$. Parameters of the fit are shown in the header of the figure. Data points in circles and model response in lines.

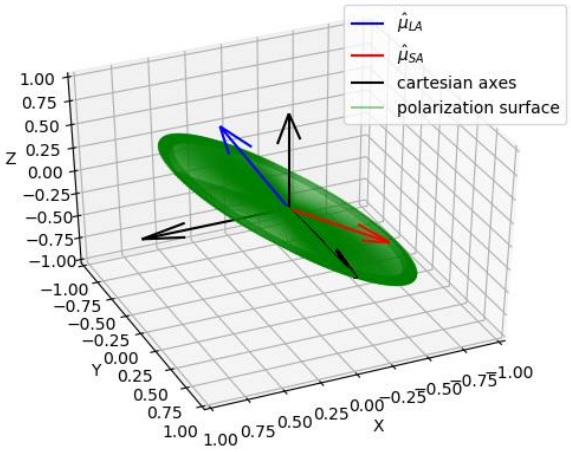

Figure 3-24. The 3D model of O170 species composed of 2 transition dipole moments, one oriented along LA, the other along SA of T molecule, cartesian axes and polarization plane for clearance (right).

3.2.3.2. Species E215 and E160 and E150

The fact that all the species can't be fitted with the model becomes apparent by simply looking at Analyzer Scans in Figure 3-25 (without even performing the joined fit). The 3 species (E215, E160 and E150) have nearly identical orientation according to Analyzer Scan (polar angle 18 deg<θ<22 deg and azimuthal angle 265 deg<φ<277 deg), but very different Polarization Scans (Figure 3-19). As mentioned earlier, every Analyzer Scan has two azimuthal angle results (modulo 180) and thus 2 out of those 3 species must be related by mirror-symmetry. The 3rd species cannot exist unless its photophysics is inherently different from the others.

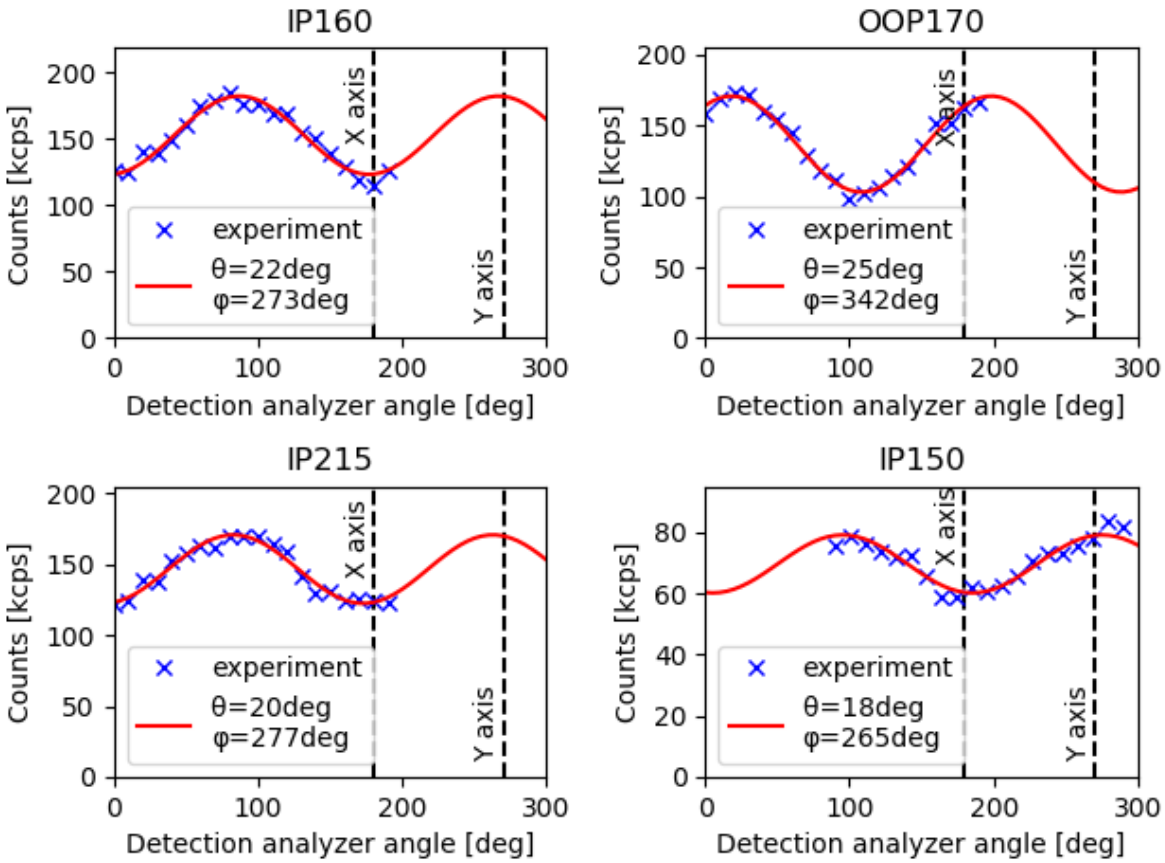

Figure 3-25. Analyzer Scans of 4 different species and the spherical coordinates – E160 (upper left), O170 (upper right), E215 (bottom left) and E150 (bottom right).

I start with a species E150. I fix σ_{12}^{CS}=12·10^{-17}cm^2 (based on species O170) and look for the spherical coordinates – Figure 3-26. The model matches the data well if the polar and azimuthal angle differs from Analyzer Scan by -5 deg and -1 deg, respectively. I consider this difference acceptable. Compared to the species O170, $\sigma_{32}^{CS\ (LA)}$ stays relatively constant (+15%), but $\sigma_{32}^{CS\ (SA)}$ decreases over 5-times. I have also tried to look for a fit by fixing all 3 cross-sections in E150 as in O170 (prohibit $\sigma_{32}^{CS\ (SA)}$ reduction), but there is no result that matches the experimental data. Besides that, there is a minor overestimation (few percents) of the slope in $k_{12}(P) + k_{21}$ (Figure 3-26, right column), which is also seen in $k_{12}(\alpha_{EXC}) + k_{21}$ (Figure 3-26, left column) – the majority of the data points are below the model continuous line. It's possible that the cross-section of this exact molecule may be few percents lower than 12·10^{-17}cm^2, but I consider this small difference negligible.

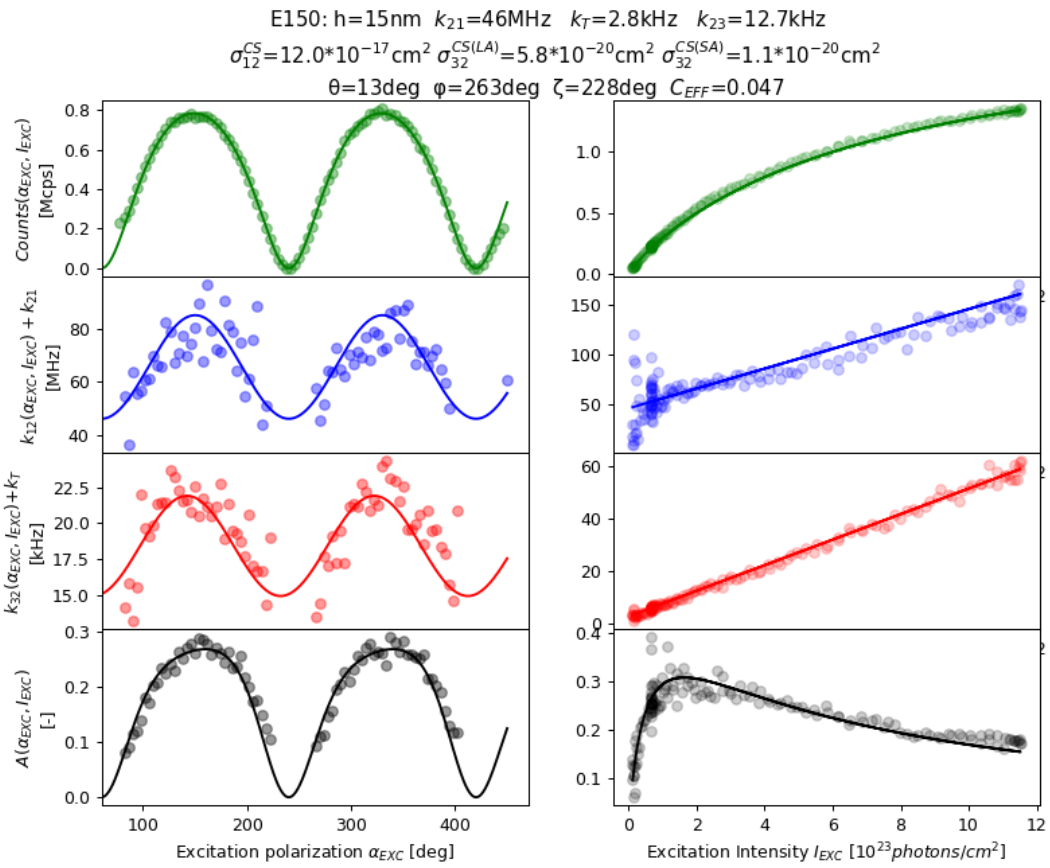

Figure 3-26. Joined fit (σ_{12}^{CS}-fixed) – Angle (left) and Power Scan (right) fit of species E150. In top-down order: counts(α_{EXC}, I_{EXC}), $k_{12}(\alpha_{EXC}, I_{EXC}) + k_{21}$, $k_{32}(\alpha_{EXC}, I_{EXC}) + k_T$ and $A(\alpha_{EXC}, I_{EXC})$. Parameters of the fit are shown in the header of the figure. Data points in circles and model response in lines.

Subsequently, I proceed with a species E215, which is equivalent to E150 by a symmetry element (azimuth modulo 180). If species E215 is fixed by σ_{12}^{CS}=12·10^{-17}cm^2 (as species O170 and E150), fit finds polar and azimuthal angle of 19 deg and 82 deg, which differs from Analyzer Scan by -1 deg and 15 deg (97 deg expected) – Figure 3-27. Besides large difference of azimuthal angle, fit fails to reproduce the experimental data of $k_{32}(\alpha_{EXC})$ due to a significant horizontal offset, which in consequence, propagates also into the A(α_{EXC}). Overall, joined fit fails to reproduce experimental data.

To verify if species E215 cannot be reproduced by the model, I measure another molecule of species E215. I obtain a perfect agreement between the experimental data and the fit – Figure 3-28. Fit was again fixed by σ_{12}^{CS}=12·10^{-17}cm^2 (as species O170 and E150). The

polar and azimuthal angle of ~20 deg and ~90 deg are typical for E215 specie. Joined fit finds $\sigma_{32}^{CS\ (LA)}$ (6,8·10^{-20}cm^2) higher than for O170 (5,5·10^{-20}cm^2) and E150 (5,8·10^{-20}cm^2).

In total, I have measured 8 molecules that are assigned as E215. Some of them can be fitted using the 3D model, and some of them can't. I suspect that some molecules have a broken symmetry and thus LA and SA don't exist anymore - the transition dipole moments no longer obey the model assumptions. Such misalignment of the transition dipole moments seems possible, when comparing $k_{32}(\alpha_{EXC})$ evolution in Figure 3-27 and Figure 3-28. However, more work is required to prove such symmetry breaking.

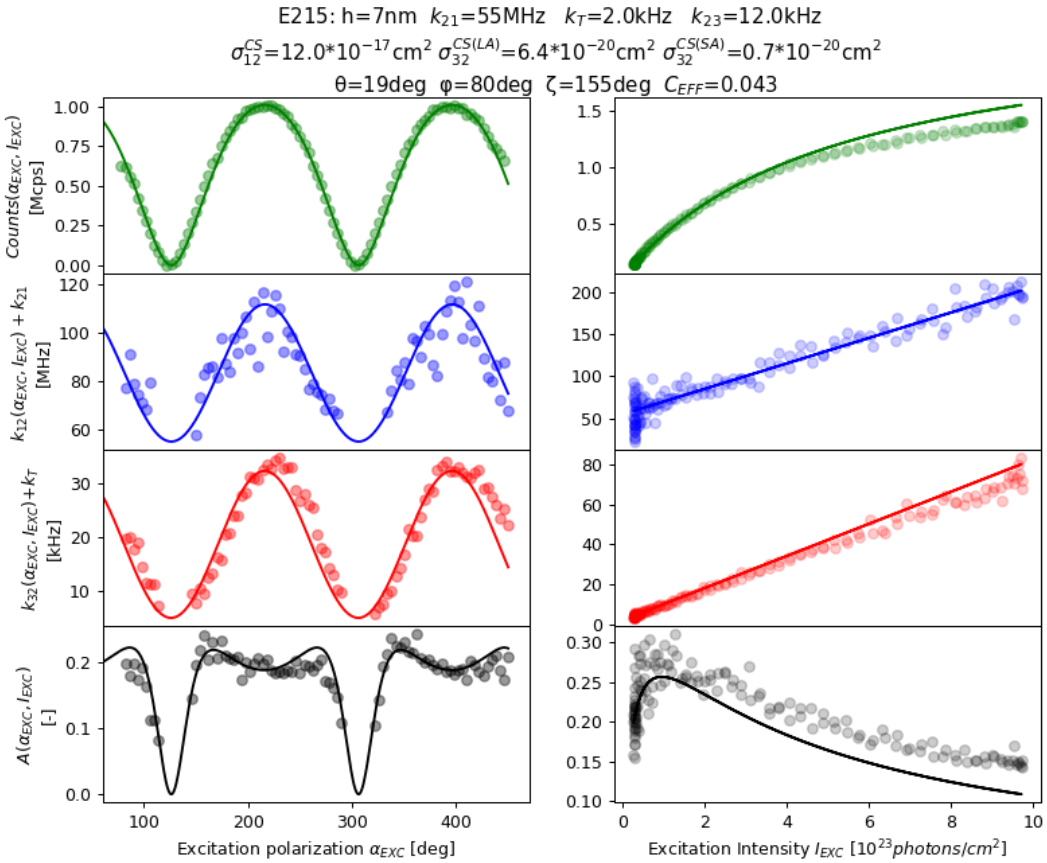

Figure 3-27. Joined fit (σ_{12}^{CS}-fixed) – Angle (left) and Power Scan (right) fit of species E215. In top-down order: counts(α_{EXC}, I_{EXC}), $k_{12}(\alpha_{EXC}, I_{EXC}) + k_{21}$, $k_{32}(\alpha_{EXC}, I_{EXC}) + k_T$ and (α_{EXC}, I_{EXC}). Parameters of the fit are shown in the header of the figure. Data points in circles and model response in lines.

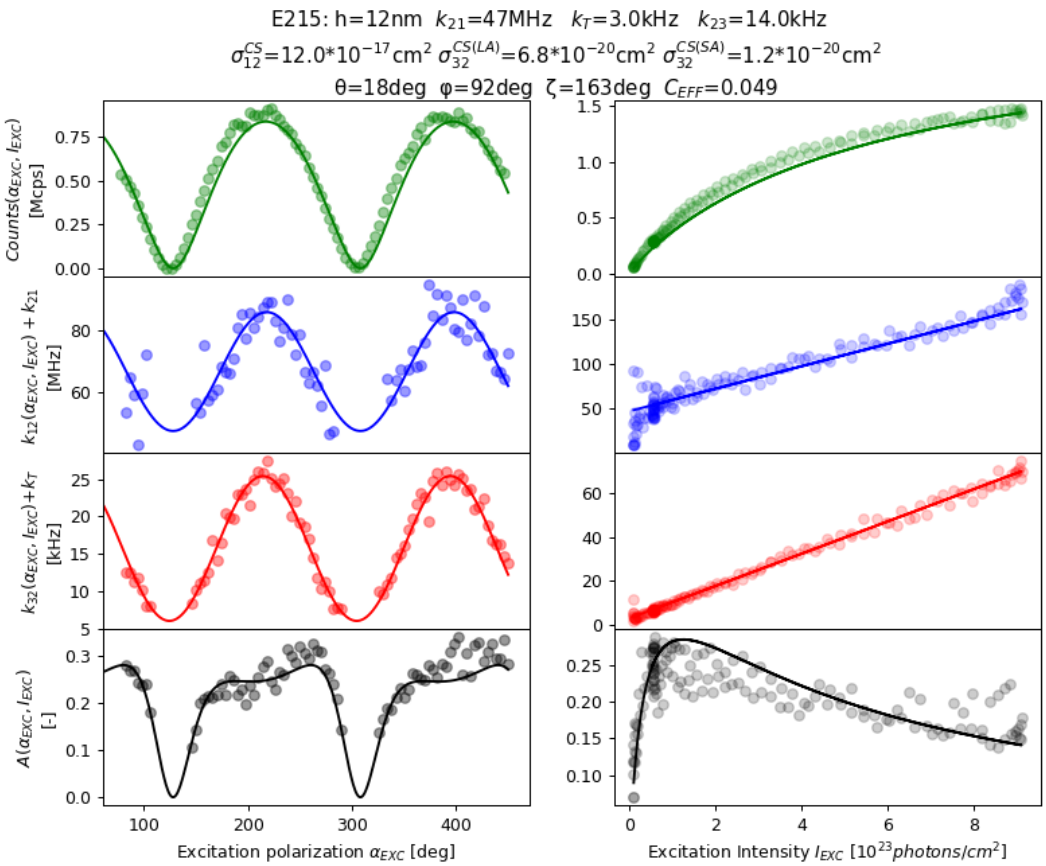

Figure 3-28. Joined fit (σ_{12}^{CS}-fixed) – Angle (left) and Power Scan (right) fit of species E215. In top-down order: counts(α_{EXC}, I_{EXC}), $k_{12}(\alpha_{EXC}, I_{EXC}) + k_{21}$, $k_{32}(\alpha_{EXC}, I_{EXC}) + k_T$ and (α_{EXC}, I_{EXC}). Parameters of the fit are shown in the header of the figure. Data points in circles and model response in lines.

Lastly, I proceed with a species E160. To recall, all 3 species E150, E160 and E215 have the same orientation according to Analyzer Scan, and so far, E150 and E215 were proven to be the two possible solutions of Analyzer Scan (~270 deg and ~90 deg, respectively). It is therefore evident that E160 cannot be photophysically identical to E150 and E215.

If E160 is fitted with σ_{12}^{CS}-fixed, the azimuthal angle differs from Analyzer Scan by 65 deg (polar angle differs by 3 deg only) – Figure 3-29. If E160 is fitted using Analyzer-defined μ^{LA}, there is no solution. I can also use solely the azimuthal angle of Analyzer Scan – such φ-fixed approached yields σ_{12}^{CS} of 16·10^{-17}cm^2 instead of 12·10^{-17}cm^2 and θ=10 deg, instead of 22 deg. It is unlikely that transition dipole moment related to S0-S1 is rotated by 65 deg with respect to S1-S0 emission and has σ_{12}^{CS} identical with the other species, nor that S0-S1 is

rotated by 12 deg and has 35% higher σ_{12}^{CS} than the other species. The lack of physically reasonable solution is not surprising, considering that both Analyzer Scan solutions were used to fit E215 and E150.

The failure of the model is case of E160 could be caused by the symmetry breaking as, but again, there are too many experimental unknowns – if pT matrix has a different refractive index in the areas where E160 is found, the field distribution (polarization surface) is also different. In such a case, it becomes evident that not all species can be fitted using the same polarization surface. Moreover, it wasn't verified experimentally if the simulated field matches exactly the field that the molecule experiences (in-situ). However, the fact that 3 species can be fitted with the same σ_{12}^{CS} and are the joined fit finds $\widehat{\mu^{LA}}$ consistent with Analyzer Scan is a strong indication that the simulation results are valid.

Notice also that $A(I_{EXC})$ (Figure 3-29, right column) matches at low excitation intensity, but the vertical offset between the model and experimental appears and increases as excitation intensity increases also. This issue will be discussed in Section 3.2.3.2.1.

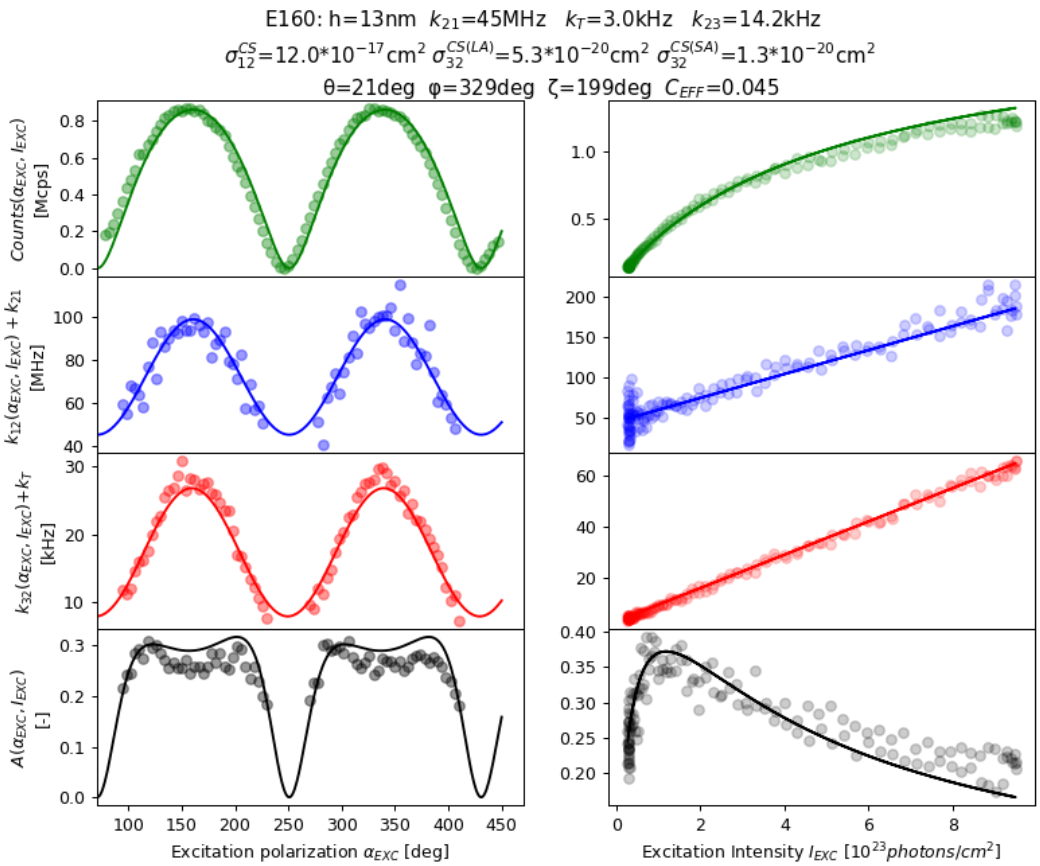

Figure 3-29. Joined fit (σ_{12}^{CS}-fixed) – Angle (left) and Power Scan (right) fit of species E160. In top-down order: counts(α_EXC,I_EXC), k_12 (α_EXC,I_EXC)+k_21, k_32 (α_EXC,I_EXC)+k_T and (α_EXC,I_EXC). Parameters of the fit are shown in the header of the figure.

Results of 4 fitted species are gathered in Table 3-4. Values of σ_{12}^{CS} are not compared as species were fixed to 12·10^{-17}cm^2 (found with O170). The orientation given by Analyzer Scan is noted using θ_{AS} and φ_{AS}, while θ_{FIT} and φ_{FIT} indicates the results of the joined fits.

All the species were fitted at the distance from glass interface h= 13,6 ± 5,4 nm. Rates independent of polarization were found to as follows, k_T = 2,7 ± 0,5 kHz, k_{23} = 12,5 ± 1,3 kHz and k_{21} = 48,5 ± 4,5 MHz, which is consistent with the population average found in Power Scan study of spectrally selected molecules (2,6 kHz, 12,4 kHz, 50,1 MHz, respectively). The triplet cross-section aligned with the LA and SA are 5,8 ± 0,4 · 10^{-20}cm^{-2} and 2,3 ± 2,4 · 10^{-20}cm^{-2}, respectively. While distribution of $\sigma_{32}^{CS\,(LA)}$ is narrow (std < 10%), for $\sigma_{32}^{CS\,(SA)}$ fit find results with either similar magnitude to $\sigma_{32}^{CS\,(LA)}$ (O170) or few times smaller (other species). All the species have similar polar angle

21,3 $\pm$ 3 deg according to Analyzer Scan and differ, on average, solely by 1,8 deg (19,5 $\pm$ 5,0 deg) compared to the joined fit results. Calculating an average of the azimuthal angle is senseless, instead for each species I calculate the difference between Analyzer Scan and full fit, which goes as 0 deg for O170 (Analyzer-defined μ^{LA}), 2 deg for E150, 17 deg for E215 and -48 deg for E160. Set-up C_{EFF} stays within 0,044±0,002 range.

Table 3-4. Full fit parameters for 4 distinct species and angles recovered from Analyzer Scan (θ_{DS} and φ_{DS}).

Specie	h	k_{23}	k_T	k_{21}	$\sigma_{32}^{CS\,(LA)}$	$\sigma_{32}^{CS\,(SA)}$	θ_{DS}	θ_{FIT}	φ_{DS}	φ_{FIT}	ζ	C_{EFF}
unit	*[nm]*	*[kHz]*		*[MHz]*	*[10^{-20} cm^{-2}]*		*[deg]*					
O170 (0108-48)	20	11,2	3,0	48,0	5,5	5,9	25	25	342	342	127	0,042
E150 (0107-20)	15	12,7	2,8	46,0	5,8	1,1	18	13	265	263	228	0,047
E215 (0108-3)	7	12,0	2,0	55,0	6,4	0,7	20	19	97	80	155	0,043
E160 (0108-47)	13	14,2	3,0	45,0	5,3	1,3	22	21	273	329	199	0,045
Average	**13,8**	**12,5**	**2,7**	**48,5**	**5,8**	**2,3**	**21,3**	**19,5**				**0,044**
Std	**5,4**	**1,3**	**0,5**	**4,5**	**0,4**	**2,4**	**3,0**	**5,0**				**0,002**

To sum up, the identified species are therefore related to their azimuthal angles (polar angle is ~20 deg for all species). Species O170, E150 and E215 have μ^{LA} aligned with +X (0 deg), -Y (270 deg) and +Y (90 deg) axes. All the species can be fitted using fixed σ_{12}^{CS}, but not all of them are consistent with Analyzer Scan (E160). Even the same species can be fitted or not, depending on the molecule measured, as shown in case of E215. There are too many experimental unknowns such as depth inside the pT, refractive index and distribution of the field (fitted, taken from the literature and simulated, respectively) to argue that some molecules have a broken symmetry and more work is required to support such claims.

I move to finer details that became apparent, while fitting the molecules – issue of $A(I_{EXC})$ mismatch that increases with increasing I_{EXC} (Section 3.2.3.2.1) and the fluorescence spectra of the species presented above (Section 3.2.3.2.2).

3.2.3.2.1. Contrast mismatch

The joined fit of E160 has a mismatch in power-dependence – Figure 3-29. Simultaneously, $k_{12}(\alpha_{EXC}, I_{EXC}) + k_{21}$ and $k_{32}(\alpha_{EXC}, I_{EXC}) + k_T$ were reproduced perfectly.

It's clear right away that if the rates k_{12}, k_{21}, k_{32} and k_T are reproduced by the joined fit, the only rate left to consider is k_{23}. The 3D model assumes that intersystem crossing rate is a constant value (polarization and power-independent). In the step-by-step treatment of Power Scan, this rate was calculated using $TimeON$. Yet, to explain the mismatch in A(α_{EXC}, I_{EXC}), it is simpler to transform the equation of A into:

$$k_{12} * k_{23} = A * (k_{32} + k_T) * -\lambda_2 \qquad 3.21$$

If the singlet excitation rate ($k12$) depends linearly on the excitation power and ISC (k_{23}) is independent of excitation power, the expression above yields a linear curve as a function of the excitation power. I track this expression for 4 molecules studied above – Figure 3-30. For clarity, a linear fit was overlaid with the data points to highlight the fact that 3 out of 4 molecules have a linear dependence on the power, while E160 has a nonlinear behavior. Recall that Power Scan has a bell-shaped curve – power is increased,

then decreased. This means that any hysteresis would be readily visible in the experimental data. Therefore, $k_{12} * k_{23}$ nonlinearity of E160 cannot be considered an instability of the molecule. The 4 species presented altogether clearly show that the model failed to reproduce the experimental data of $A(\alpha_{EXC}, I_{EXC})$ in E160.

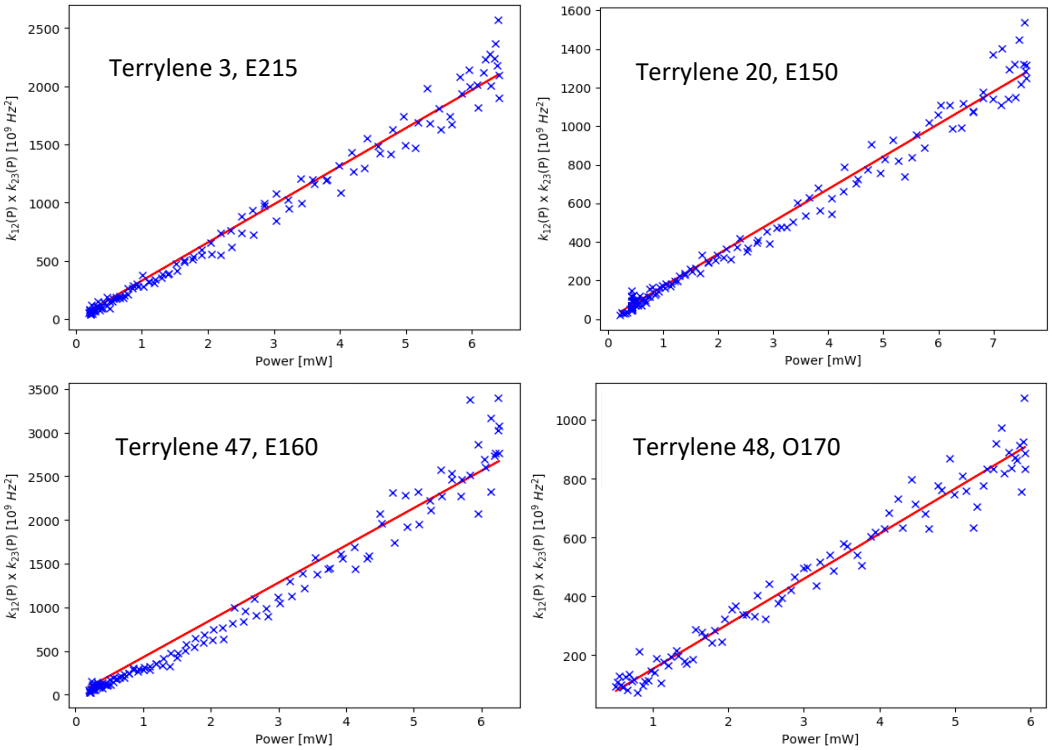

Figure 3-30. Product of excitation rate and intersystem crossing rate ($k12 * k23$) for 4 molecules treated with joined fit. Linear fit (red line) and data points (blue crosses).

There are 2 possible explanations to the behavior of E160 – background or power-dependent intersystem crossing (photoinduced ISC). The background measurement is necessary to correct A, and all molecules are corrected for the background taken a few micrometers away from the molecule. The value of the background is irrelevant to the shape of $k12 * k23$, only its power-dependence matters. Every background taken shows the same power-dependence – $1/SNR$ is approximately linear with the excitation power. Nonlinearity in $k12 * k23$ of E160 would be possible if background of this molecule had a quadratic SNR dependence, which is not the case.

The only other possible solution is that E160 indeed has a power-dependent ISC, which would require to describe by including excitation coefficient $k_{23}(P) = k_{23} + \sigma_{23} \cdot P$. The dependence of ISC, more precisely rISC, on power is already present in T/pT as k_{32} is

described with $\sigma_{32} * P$. In case of k_{23}, this mechanism is referred to as photoinduced ISC, because molecule has to be first pumped from T1 to higher triplet excited states, and then ISC occurs between higher levels prior to relaxation to the lowest excited state S1. If an analogous mechanism is to be proposed for $k_{23}(P)$, then S1 should be excitable (at 532 nm) to higher excited singlet states and then readily undergo ISC (into higher triplet states). Such an explanation needs to be supported by the energy diagram, however S2 is merely 1,38 eV (897 nm) above S1 (Chapter 1, Table 1-1). To the best of my knowledge, there are no reports on the energy level of singlets states higher than S2 (there are reports on high triplet states [56]). Thus, such mechanism cannot be argued due to the lack of the energy diagram of higher singlet states.

To sum up, this Subsection explains why $A(\alpha_{EXC}, I_{EXC})$ of E160 couldn't be fitted with the 3D model, which is a consequence of the nonlinear $k_{12} * k_{23}$ product. The energy diagram with higher singlet levels is required to support suspected mechanism. In the next chapter, I will study $k_{23}(P)$ of E160 molecules with and without dielectric nanoantenna to investigate this issue and verify if this is a particular property of this specie.

3.2.3.2.2. Spectra

Recall that all 3 E species have identical Analyzer Scans (orientation of the emission dipole), but different Polarization Scan, while the symmetry element allows only for 2 distinct insertions through 180 deg rotation around the Z-axis (E150 and E215).

All the species belong to the same spectral subpopulation $\lambda_{max} = 577 \pm 2$ nm, but there is another spectral property that was not discussed so far. In Figure 3-31, I present fluorescence spectra of E215, E160, and E150 species treated above. All 3 spectra are normalized to their maximum intensity. Such normalization is applied to clearly show the ratio between the first band 570-600 nm and the second band 610-650 nm. Even though each E species has the same 0-0 peak 577±2 nm (E160 at 576 nm, E210 at 578 nm, and E165 at 579 nm), they have a very different ratio of the two bands, while keeping an identical vibronic pattern.

Thus, all 3 species have similar orientations in Analyzer Scan, identical HOMO-LUMO energy gaps (±2 nm) and vibronic patterns, but the relative intensities of the second band can vary 2-fold. Note that the second band is composed of the high energy vibronic

relaxations (S1 to vibrationally excited S0) and thus depends on the Franck Condon Factors (FCF). This serves as a proof that 3 E species, are clearly not identical and geometrical distortion should be present. Yet, the energy of the vibrations must not be affected by such distortion as vibronic pattern persists.

The Differences in fluorescence spectra don't explain why $\sigma_{32}^{CS\,(SA)}$ varies so much between species, nor why some species don't obey Analyzer Scan restriction, but it certainly shows that there are some properties in the insertion sites of T/pT at room temperature that, to the best of my knowledge, weren't discussed in the literature.

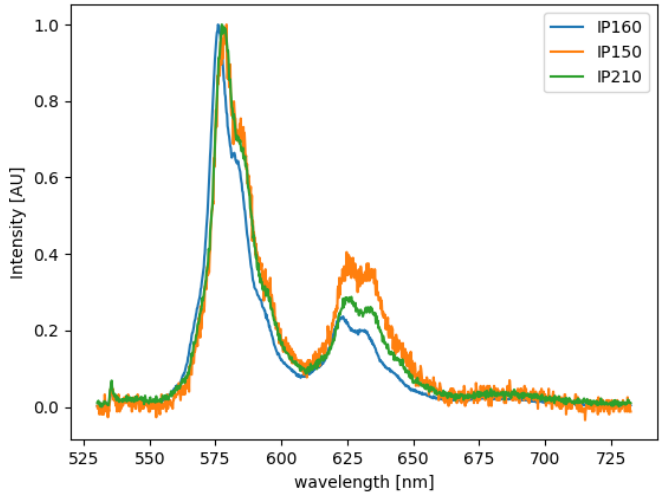

Figure 3-31. Fluorescence spectrum normalized of the 3 distinct E species (normalized to the maximum intensity).

3.3. Conclusions

In Chapter 3, I studied a well-known system, T/pT, but restricted to the nanoscale dimensions (sub-30 nm thickness). A complete 3-level model of T in sub-30 nm pT has not been reported so far in the literature (only in the bulk). I have used a standard experimental approach (in the field of single-molecule studies), which relies on collecting Time-Tagged-Time-Resolved (TTTR) measurements with a Hanbury-Brown Twiss (HBT) detection scheme at different excitation powers to calculate the rates. During my experimental works, I have noticed that the procedure commonly found in the literature - TTTR measurements collected at a couple of different excitation power – yield only a

couple of data points and thus calculated rates carry large uncertainties. This might be the potential reason of the large molecule-to-molecule rate variation reported in the literature even within a single study.

In order to understand the photophysical aspect of the molecule-to-molecule variation, I had to minimize the calculation uncertainties. To do this, more data points over a large range of excitation power must be recorded and thus the experimental method had to be adjusted. I have automatized the home-built setup to collect Power Scans – during 29 s of the acquisition time, the excitation power is varied continuously back and forth to record 145 data points over ~60-fold increase of the excitation power. I have presented the step-by-step data treatment to show the magnitude of uncertainty for each rate. Subsequently, I've conducted experiments on 43 randomly chosen molecules to investigate the population statistics. In the data treatment, some rates have typically smaller calculation uncertainties than the others ($\delta\sigma_{32} < \delta\sigma_{12}$, $\delta k_{21} < \delta k_T < \delta k_{23}$), but this order doesn't hold for the population standard deviation. Additionally, population standard deviation is at least 3-fold larger than calculation uncertainty, thus observed molecule-to-molecule variation must originate from physical factors. Nevertheless, molecule-to-molecule variation (population standard deviation) is quite small compared to the literature (27% for σ_{12}, 14% for k_{21}, 35% for k_{23}, 28% for σ_{32} and 26% for k_T). No correlation between the rates was found, besides a linear one between σ_{12} and σ_{32}. An outlier (values larger than 3 standard deviations of the population) in one rate is not necessarily an outlier in other rates. To investigate further, which physical factors could affect one rate, while leaving the others invariant, I have proceeded with a second population study (16 molecules) but this time applying a spectral selection of $\lambda_{max} = 577 \pm 2$ nm. This spectral selection has drastically changed the population standard deviation for all the rates, besides k_{21}.

To discuss the factors that contribute to the molecule-to-molecule variation I have considered the non-random orientation of the transition dipole moments, the fluorescence spectrum (mirror-like absorption spectrum) and its vibronic pattern (Franck Condon Factors), the Einstein spontaneous emission rate coefficient, the depth in the pT film and dependence on the fluorescence lifetime (QY).

The orientation of the transition dipole moment plays a big in molecule-to-molecule variation of the absorption cross-sections. The standard experimental approach

(measurements at different excitation power) is inherently blind to the orientation of the emitter. The calculated values are rather an excitation coefficient σ, than a cross-section σ^{CS}, because they are coupled with the field distribution factor κ and the angle γ between the transition dipole moment and the excitation polarization ($\kappa \cdot \sigma^{CS} \cos^2 \gamma$).

To troubleshoot this experimental limitation, I have implemented Polarization Scan (360 deg rotation of the excitation polarization). I have laid out some specific algebraic properties of Polarization Scan. The results of Polarization Scans allowed to categorize the molecules by investigating the evolution of the rates with respect to the polarization angle α_{EXC}. The species were assigned based on the α_{EXC} at which counts reach maximum value and divided into groups based on evolution of $k_{12}(\alpha_{EXC})$ and $k_{32}(\alpha_{EXC})$. Group E has synchronized (even) evolution of the two rates, while group O is out-of-sync (odd). I have found 3 species within E group and 1 species within O group. Triplet depopulation (through triplet-triplet absorption) proved to be composed of at least 2 transition dipole moments, while singlet absorption has a single transition character. This work can be considered as a proof of concept that Polarization Scan can provide insight into the spatial character of the transitions, which is complementary to magnitude-only information gathered with Power Scan.

Finally, to recover the cross-sections (without κ and $\cos^2 \gamma$) and thus the 3D orientation of the transition moments, I have created a 3D model of my emitter. To get the field distribution in sub-30 nm pT, I have used analytical equations and simulation results. To find the orientation of the transition dipole moments, I have used the joined fit method, which simultaneously fits Power and Polarization Scan. Nevertheless, 3D model has many parameters and thus many solutions can be found for the same experimental dataset. I have recorded Analyzer Scan to get the polar and azimuthal angles for each species (μ^{LA}) and compared it with the results of joined fit fixed to σ_{12}^{CS}=12·10^{-17}cm^2. All the species have a polar angle of ~20 deg, but various azimuthal angles.

Besides one exception (E160), species could be fitted with fixed σ_{12}^{CS} and spherical coordinates consistent with Analyzer Scan. The triplet-triplet cross-section aligned with the long axis (LA) of terrylene $\sigma_{32}^{CS(LA)}$ has shown little variation between species (std <10%), but the short axis (SA) aligned cross-sections varies substantially $\sigma_{32}^{CS(SA)}$ between O and E group. The ratio of the triplet cross-sections is similar to that reported in the

literature. The exception (E160) must be photophysically different, because 3 species (E150, E160 and E215) have identical Analyzer Scan, while only 2 orientations are possible for a given Analyzer Scan (φ±180 deg).

To conclude, this work is a proof of concept that both value and spatial dependence of the rates can be investigated with Power and Polarization Scans. This allows to use a 3-level model, taking into account the 3D orientation of the molecule (and the excitation field). This modelization provides a deeper insight into the photophysics of the single photon emitter. Such studies are of interest especially for the emitters inside solid matrixes, which sometimes tend to distort the emitter's structure.

Chapter 4

Placing a nanoobject that is able to modify the photon statistics of the emitter (nanoantenna) offers a possibility of tuning the performance of the devices based on the single molecules. Moreover, such modifications are also interesting to investigate fundamental science of light-matter interactions. The nanoantennas used in this manuscript are quite simple and one can think of much complicated shapes and materials that could be used as a nanoantenna. However, the pulled glass fiber and gold pyramid were chosen in order to develop necessary protocols/methods and start this new activity in our laboratory. Therefore, besides the nanoantenna effect, a lot of attention is paid also to the technical side. I propose certain SNOM experiments that can be used to verify whether that the nanoantenna is well aligned, drift and regulation are negligible, emitter is stable and its photon statistics can be measured before and after removing the nanoantenna.

In this chapter, I present the results of experiments carried out with a dielectric nanoantenna (pulled glass fiber) and plasmonic nanoantenna (gold pyramid). I showcase the experimental data in a step-by-step treatment to carefully investigate modification of each rate. Simultaneously, I also argue the successful application of all the technical considerations made in Chapter 2, by tracking factors such as height regulation, evolution of tip's shape and misalignment of the tip and the nanoantenna during the measurement. Nevertheless, measurements carried out on the emitter before and after approaching it with a nanoantenna are not identical (show hysteresis), but not for all the rates.

4. Nanoantenna effect on a single molecule

4.1. Molecule and a dielectric nanoantenna

The dielectric tip has a negligible absorption in the visible range, and thus provides counts enhancement at the cost of very little background luminescence. This results in the increase of the *SNR.* To once again focus on the molecule-to-molecule variability (rather than tip-to-tip variability), all of the measurements (besides Z-spectroscopy) presented in this chapter were done using a single probe (the same tip).

The maximum power was reduced 2-fold (molecule alone) and 4-fold (molecule-nanoantenna) with respect to the measurements presented in Chapter 3. This is related to photon budget/photostability considerations (Section 2.1.4.1) and the fact that the photon flux enhanced with the dielectric tip.

4.1.1. Raster Scan and Z-spectroscopy

Firstly, I performed calibration of the probe's oscillation amplitude. The calibration yields oscillation amplitude of 800 nm/V, and thus driving voltage V_{EXC} was fixed to 10 mV, and thus ~8 nm oscillation amplitude. Probe used for the experiments below has the resonance quality factor of 285 and resonant frequency f_{RES} of 32,3 kHz. Thus gluing the pulled glass fiber redshifts the nominal resonant frequency by 500 Hz. Typical closed loop parameters of the Z-controller are 4 ms time constant and 0,3 nm/Hz proportional gain and setpoint of 1 Hz, but those parameters are constantly adjusted throughout the session.

Before conducting a measurement on the tip-emitter system, it is necessary to align the tip with the emitter. To do this, I have to gather information about the spatial dependence of the counts enhancement. Such dependence is difficult to carry out experimentally in all 3 directions at once and thus XY-scan (raster scan) and Z-spectroscopy are made separately – Figure 4-1.

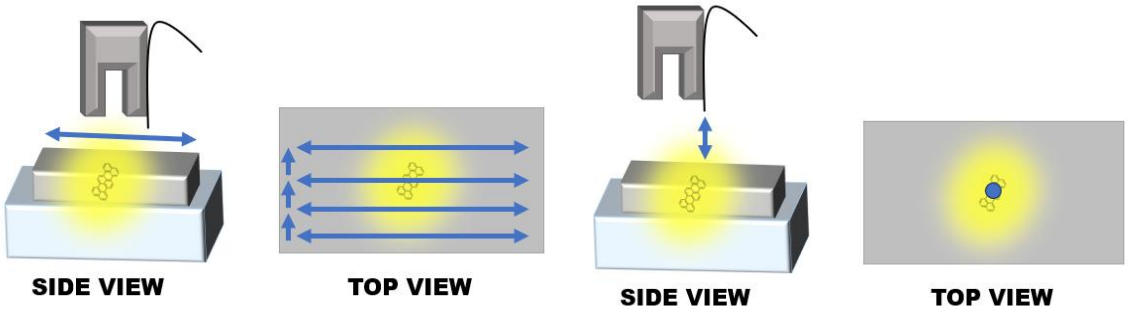

Figure 4-1. Schematic of the tip back and forth XY-scan raster scan (left) and Z-spectroscopy (right).

Note that XY- scan works in a closed loop regulation (shear force), while Z-spectroscopy varied the absolute value of the piezostage, without updating the surface contact point. Due to this, Z-spectroscopy can't be considered as tip-sample distance (TSD) scan,

because Z position of the sample and probe may change during the experiment (in- and out-of-contact tip snapping due to adhesion forces).

By performing a raster scan, I can construct a XY map of the flux incident on the detector $counts(X, Y)$ – Figure 4-1 upper left. The image clearly shows a circular pattern of the counts enhancement (3-fold) and I refer to this pattern as the PSF (Point Spread Function) of my tip. The horizontal and vertical cross-sections of the PSF are used to fit a Gaussian curve (Figure 4-1, upper right), which yields a FWHM of 45 nm. There is no analytical expression that would allow me to recalculate diameter of the pulled fiber apex from the PSF. Nevertheless, counts enhancement (LDOS) must be related to the apex diameter. I expect the tip's apex to be a flat plateau of ~45 nm, which fulfills the condition Radius of Curvature (RoC) $\ll \lambda$, and thus observed phenomenon is a near-field interaction.

To ensure that counts change has nothing to do with the change in pT topography, I plot also the back and forth height image obtain simultaneously with the counts XY-scan (Figure 4-1, lower). As back and forth scans are very different, I can assume that pT film is flat over the area of 230 nm x 230 nm and the observed height images are just the regulation noise. If I calculate height roughness as regulation noise, I get ±0,5 nm (5 nm peak-to-peak). However, it must be pointed out that regulation noise doesn't mean anything unless the scan details are defined. Recall that regulation closed loop is keeping the Z position around (unknown) TSD fixed by a setpoint. A very slow scans (long dwelling time per pixel) shows no regulation noise, because pixel value is a time-averaged Z position (TSD), while instantaneous Z position (deviations from TSD) are lost in the averaging process.

Raster scan presented in Figure 4-2 is made of 128 pixels per line and 32 lines (4096 pixels in total) acquired during 15,4 s, which gives 3,76 ms per pixel (close to regulation gain time constant) and at scan speed of 1 μm/s (230 nm x 230 nm). Due to the fact that pixel dwelling time is close to the time constant of the closed loop, ±0,5 nm regulation noise can be considered as close to the instantaneous TSD deviation. The shorter the acquisition time, the larger the speed scan and thus larger regulation noise. Fast scan on small areas are a very demanding challenge for the closed loop regulation as tip has to change direction every 235 ms (2x32, lines back and forth).

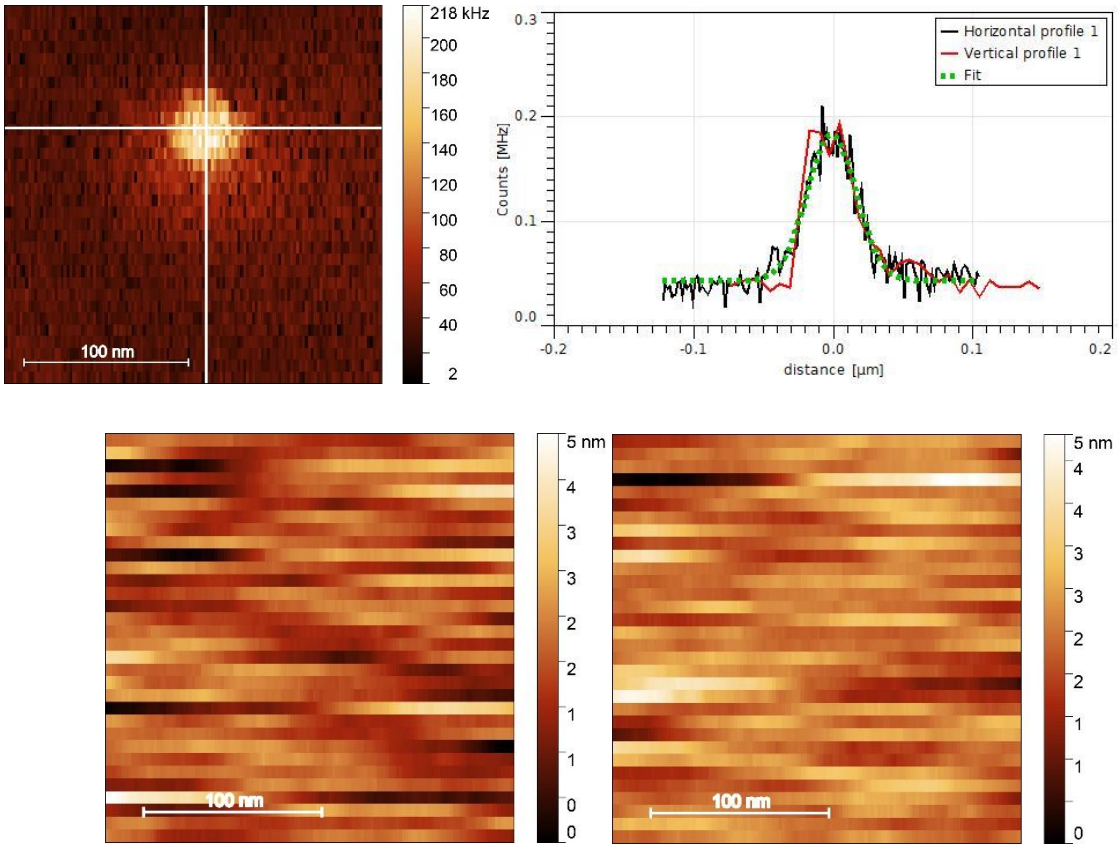

Figure 4-2. Counts on the detector as the dielectric tip is scanned above a single T in sub-30 nm pT (upper left). The PSF's vertical and horizontal cross-sections with a Gaussian fit that yields 45 nm FWHM (upper right) and counts enhancement of ~3. Back and forth height images of the same area (lower) recorded simultaneously.

The $counts(X,Y)$ map is measured on each molecule, because it is required to align the tip and the emitter – once the map is measured, the tip is moved to the center of the PSF. However, everyone with a practical experience in AFM knows that very often apex changes as the probe is used; it ''wears off'. I have rechecked the FWHM repeatedly throughout the entire experiment (7 days). In Figure 4-3, I present FWHM that corresponds to the molecules that are later presented in Table 4-2. By doing it, I ensure that any variations in nanoantenna effect are not a consequence of changes in the PSF. As it is shown in Figure 4-3, FWHM indeed changes but only at the beginning of the experiment (1st day of using the probe ~60 nm) and then stays basically constant (~45 nm). throughout the entire experiment. Purposely, on Figure 4-2, I show the raster scan with tip of ~45 nm FWHM, to show that it has a perfectly circular XY projection and gaussian shape in the counts profile. It is unclear why FWHM became smaller.

Nevertheless, PSF retains appropriate PSF (XY projection circular) and counts enhancement response (Gaussian) through the entire experiment of 7 days. Moreover, the pattern in $counts(X, Y)$ proves that tip must indeed oscillate at <10 nm. Tip's oscillation is unidirectional and thus if the oscillation amplitude wasn't much smaller than RoC, it would elongate the circular pattern in one direction, thus making it ellipsoidal. Overall, FWHM is nearly identical (±10%) for 5 out of 6 molecules and within 40-65 nm for all the molecules, which is very satisfactory.

Note that evolution of FWHM is a very important detail. One cannot discuss molecule-to-molecule variation if PSF varies throughout the experiment. It is difficult to keep tip apex relatively constant throughout several days (time required to measure many molecules). Sometimes tip crushes due to the external factors (transmitted vibrations due to the activity of other people present in the lab), especially when working at such a small oscillation amplitude (<10 nm) and very subtle closed loop regulation required to keep small TSD deviations (<1 nm).

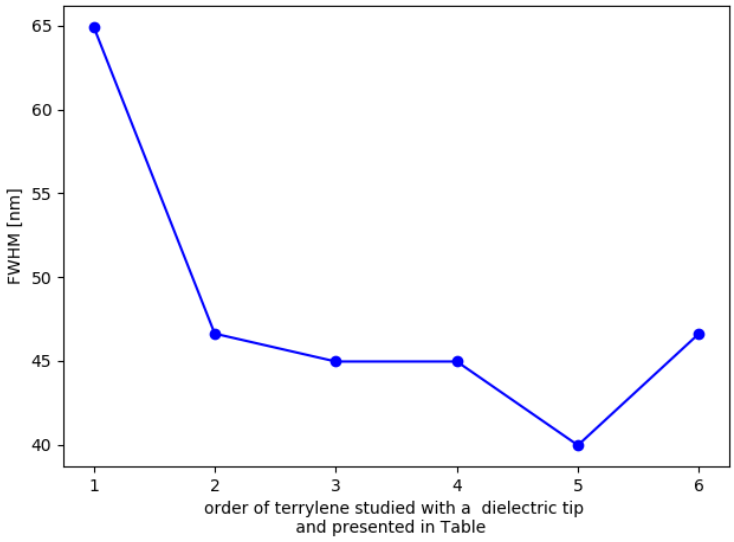

Figure 4-3. Evolution of the full width half maximum (FWHM) of the counts(X, Y) measured and corresponding to the molecules presented in Table 4-2.

Subsequently, I can track the Z-dependence of the count enhancement. To do this, I conduct Z-spectroscopy – once the tip is moved to the center of the Gaussian, XY coordinates are kept constant, while the Z position of the piezo stage is varied to approach (forward) and retract (backward) the tip from the surface. As noted in the chapter header,

Z-spectroscopy are conducted with a different tip, because they result in the degradation of the tip.

As tip approaches the surface, it reaches a contact point, which is identified based on the drastic change in the frequency shift (Δf) gradient with respect to Z – Figure 4-4, left. The exact positions of the contact points are not easy to identify due to the attractive forces and adhesion forces, which result in snapping of the tip in- and out-of-contact, respectively (hence the degradation of the tip). This snapping introduces an error in the tip-sample-distance (TSD) between the tip and the surface, that Nanonis tracks by measuring only the Z position of the piezo stage (assumption of the perfectly rigid assembly). I refer to the distance given by Nanonis as Z relative to keep in mind this issue. Overall, $counts(Z)$ experiences 2-fold enhancement over $\sim$50 nm, which proves near-field nature of this phenomenon. Nevertheless, the exact values and enhancement gradient is impossible to calculate due to the motion caused by adhesive forces.

The tip effect on the counts can be tracked simultaneously with $\Delta f(Z)$ to better resolve the contact points. According to the $counts(Z)$ in Figure 4-4, right, the contact points of forward and backward are not consistent between directions $\sim$20 nm and $\sim$5 nm, respectively. Moreover, $counts(Z)$ on the forward direction have a higher gradient than on the backward direction. This proves that the tip must be in the attractive regime, where the movement in the forward direction is accelerated (contact point reached sooner). On the other hand, movement in the backward direction is deaccelerated. Due to the attractive force, it's impossible to assess the real-space Z-dependence of the count enhancement.

The forward contact point corresponds to 0,05 Hz. Counts saturate and Δf rises rapidly as Z position continues to approach another 20 nm. Based on the $\Delta f(Z)$, there seem to be 2 candidates for the backward contact point, but altogether with $counts(Z)$, the contact point corresponds to 0,15 Hz. Note that $counts(Z)$ at 90 nm are identical for both directions, which proves that after contact the tip approached closer but hasn't altered the physical system. I hypothesize that the sample Z-position changes with the tip (not-rigid assembly). I can't really prove it in-situ (to protect the tip), but I have carried 2 experiments to prove the non-rigid assembly. Firstly, I optimize the focus to get a sharp image of pT, when placed a small weight ($\sim$30g) on the sample, which made the image

blurry. Subsequently, I removed the weight to regain exactly the same sharp image as initially. Secondly, I can force (another) tip to crash slightly, which also changes the focus, and then retract it to regain the focus. The two experiments mentioned above are not a prove that in Z-spectroscopy tip hasn't dug into pT, but they prove that set-up is not a perfectly rigid assembly.

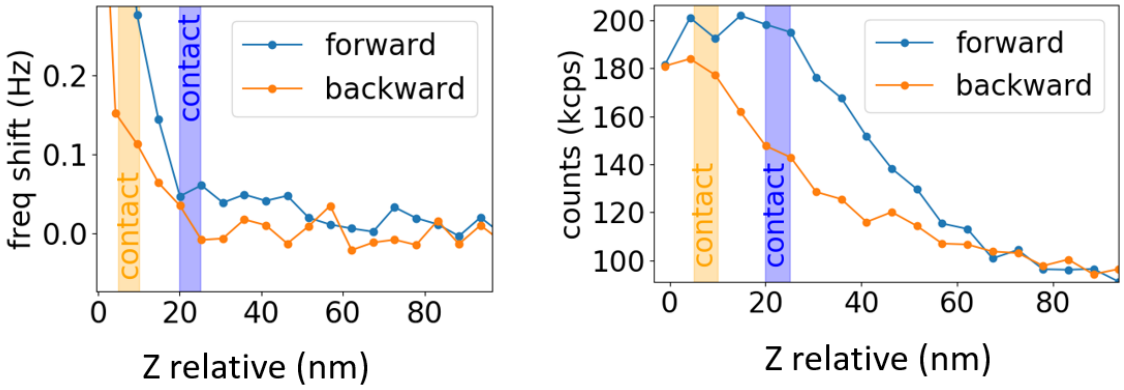

Figure 4-4. Frequency shift Δf (left) and counts on the detector (right) measured during Z-spectroscopy above a single molecule.

To sum up, $counts(X,Y)$ and $counts(Z)$ investigate not only nanoantenna affect but can be used also for several technical check-up. Principally, $counts(X,Y)$ is necessary to align the nanoantenna with a single molecule. The PSF found in $counts(X,Y)$ can be fitted with a Gaussian to get FWHM (~45 nm) and counts enhancement (~3). The counts enhancement (according to field distribution Section 2.1.5) will be related to the depth in pT, but FWHM is not (add simulation). Therefore, PSF of $counts(X,Y)$ can be used to track the evolution of apex RoC throughout the experiment. The PSF cannot be used to calculate the oscillation amplitude, but knowing that the apex of the pulled glass fiber is circular (SEM images, Section 2.2.3.1), I can check if given oscillation amplitude doesn't result in ellipsoidal PSF (circle elongated along axis of prong displacement). If forward and backward height images are not correlated, I can assume that the $Z(X,Y)$ (height image) recorded during $counts(X,Y)$ is my time-averaged regulation noise at a given scan speed, closed loop parameters and pixel dwelling time. With $counts(Z)$ counts enhancement in Z-axis can be investigated. Unfortunately, Z-axis cannot be viewed as TSD, due to the unknown motion caused by the adhesive forces. Nevertheless, the range of the interaction can be approximated using back- and forward Z-spectroscopy. Approximately, near the

contact point 10 nm Z change causes 10% change in counts. This sets a quantitative condition for Z regulation. Additionally, Δf of the contact point can be found. Setpoint is typically set to $10\Delta f\,(contact\ point)$ for good operation of the probe – to place the probe linear-like regime of $\Delta f\,(Z)$. If $\Delta f\,(Z)$ is approximately linear, then error signal created by TSD deviation towards and away from the surface is symmetric and closed loop regulation is more stable.

4.1.2. Signal-to-noise ratio of the dielectric tip

There two ways two assess the signal-to-noise ratio (SNR) experimentally. One can either collect counts from the T/pT with the tip approached above the molecule, and then from the tip alone – similarly to SNR from T/pT and then pT taken on the side. This method evaluates the background, but assumes that background at the location of the emitter is equal to the background few microns away from the emitter. As was shown in Section 3.1.1.1, SNR of the molecule alone changes from nearly 40 to 20 as incident power increases (up to 6 mW). However, as the dielectric tip is very weakly luminescent and provides ~2 fold counts enhancement, it keep SNR~40 – Figure 4-5.

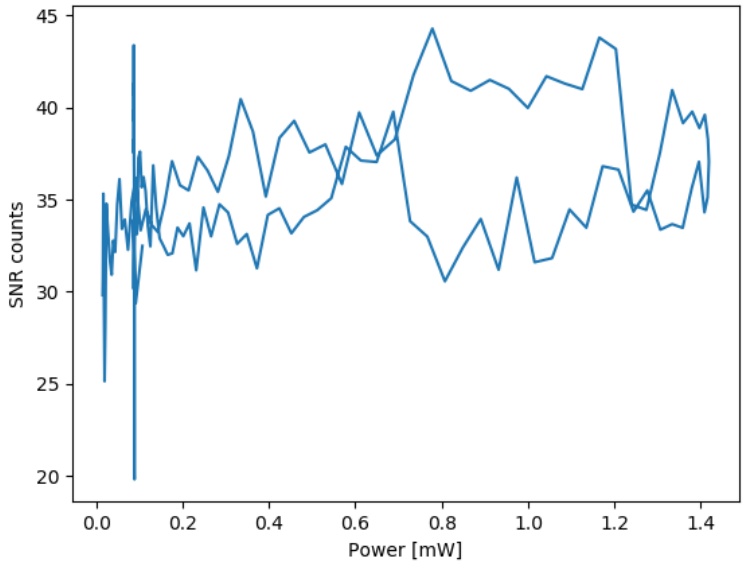

Figure 4-5. Signal-to-noise ratio taken as a ratio of counts T/pT with the dielectric tip and the dielectric tip and pT taken few microns away from the emitter.

For a perfect single photon source $g^{(2)}(0)$ is equal to 0. Non-zero $g^{(2)}(0)$ may originate from multiphoton emission events (in quantum light sources like 2D materials or

quantum dots) or background luminescence. To classify the light source as a single photon emitter $g^{(2)}(0)$ <0,5 is commonly used. Because terrylene is a perfect single photon emitter, any deviation from 0 are simply due to the background luminescence. I plot START-STOP antibunching curves at highest incident power – Figure 4-6. In the presence of the dielectric tip and incident power of 1,4 mW, START-STOP measurement shows that molecule-nanoantenna system has $g^{(2)}(0)$ ~0,15, compared to ~0,06 of the molecule alone. Both are well below single photon source limitation (dashed black line). This proves that single molecule and the dielectric tip system can be treated as a single photon source.

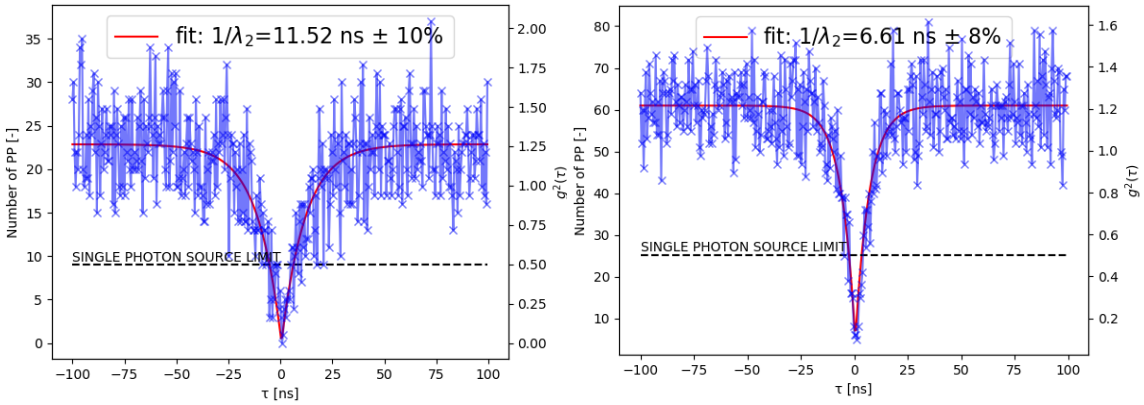

Figure 4-6. START-STOP measurement of T/pT (left) and T/pT approached with the dielectric tip (right). Both measurements taken at the incident power of 1,4 mW. Limit value of single photon source classification $g^{(2)}(0)$=0,5 plotted with a dashed line.

4.1.3. Effect on the rates (Power Scan)

In this Subsection, I will follow the order similar to the step-by-step Power Scan treatment for one of the emitters measured. I refer to the measurement on the emitter alone as a ''retracted'' and to the measurement on the very same molecule with the tip as ''approached''. To ensure that the potential change in the rates is an antenna-effect (reversible in nature), every emitter was measured 3 times – 1) retracted before the approach, referred to as ''pre-approached'', 2) in the approached state, 3) retracted after the approach as ''post-approached''. The photostability is assessed based on the total number of photons detected and visual inspection of the time traces (no sudden jumps in rates, nor counts). If total number of photons in the pre- and post-approached

measurement vary by less than 15%, molecule is considered photostable. Otherwise, molecule is excluded from the dataset.

Each graph represents rates fitted as a function of power for the post-/pre-approached and approached measurements for an exemplary molecule. At the end of this Subsection, the results from the measurements on 6 molecules (2 E215 and 4 E160) are gathered.

The enhancement factors are superscribed pre or post refereeing to the chosen reference:

$$Enh_k^{pre/post} = \frac{k^{app}}{k^{pre/post}} \tag{4.1}$$

The average enhancement factor Enh_k^{AVG} is an equal-weighted average of the pre- and post- enhancement factor.

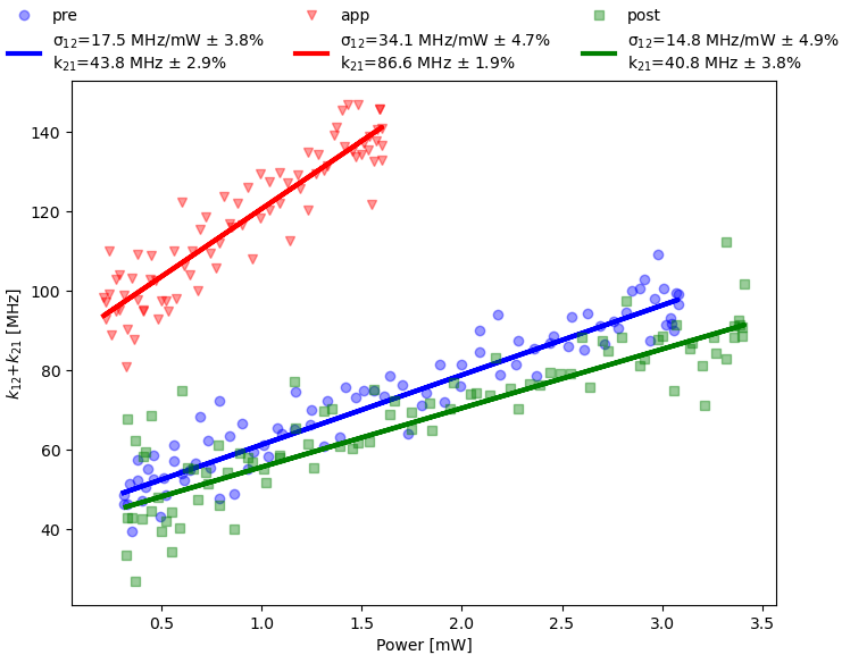

Figure 4-7. Sum of the excitation rate (k_{12}) and spontaneous emission rate (k_{21}) as a function of the excitation laser power. The pre-approached (blue dots), approached (red triangles) and post-approached (green squares) with linear fits (lines) and fit parameters given in the inset.

The parameter $\lambda_2 = k_{12} + k_{21}$ is plotted as a function of the excitation power in Figure 4-7. Both rates increase 2-fold due to the presence of the dielectric tip. In the case of k_{21}, $Enh_{k_{21}}^{AVG}$ is referred to as the Purcell factor and yields a value of 2,04. The lifetime of the excited state remains unchanged between pre- and post- measurements (within the uncertainties). However, defining the enhancement of the excitation rate is more complicated as the slope of pre- and post- measurement varies significantly (beyond the uncertainties). Values of $Enh_{k_{12}}^{pre}$ and $Enh_{k_{12}}^{post}$ are 1,84 and 2,25, respectively, and thus $Enh_{k_{12}}^{AVG}$ is equal to 2,04. Therefore, for this molecule the excitation rate is enhanced by the same factor as the emission rate. Despite the stokes shift, the increase in photon density of states is the same.

Subsequently, the parameter $\frac{1}{TimeOFF} = k_{32} + k_T$ is plotted as a function of the excitation power in Figure 4-8. Triplet depopulation is effectively accelerated ($TimeOFF$ is shortened) by the dielectric tip, as k_{32} increases 2-fold, even thought k_T decreases by 25%. Once again, I observe no hysteresis in the power-independent rate such as k_T for which $Enh_{k_T}^{AVG}$=0,77. In the case of power-dependent k_{32}, $Enh_{k_{32}}^{pre}$ and $Enh_{k_{32}}^{post}$ yield 1,83 and 2,26. Note that those values are identical (within uncertainties) with the factors found for $Enh_{k_{12}}$ (1,84 and 2,25). Fact that $Enh_{k_{12}}$ and $Enh_{k_{32}}$ are equal in pre- and post- (experience the same hysteresis) is expected for emitters belonging to E group. This group has triplet depopulation dominated the transition aligned with the LA ($\sigma_{32}^{CS(LA)} \gg \sigma_{32}^{CS(SA)}$), which is colinear with the transition dipole moment of the singlet absorption (Chapter 3, Table 3-4).

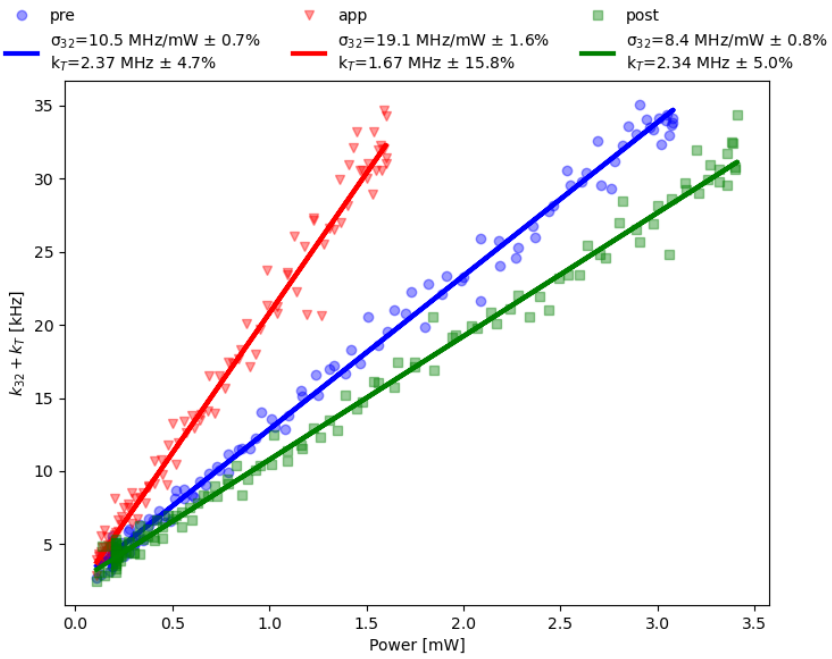

Figure 4-8. TimeOFF as a function of the excitation laser power. The pre-approached (blue dots), approached (red triangles) and post-approached (green squares) with linear fits (lines) and fit parameters given in the inset.

The fact that hysteresis in k_{12} and k_{32} coincides indicates that they have the same physical origin.

The last rate to be verified is k_{23} – Figure 4-9. Compared to pre-approached, there is a slight increase and decrease of k_{23} in the approached and post-approached measurement, respectively. However, all those changes are within the uncertainties. The pre- and approached measurement are very similar and fitted curves overlay on the graph, even though fitted parameters are slightly different. The post-approached measurement clearly deviates from the two. This suggests that 1) dielectric tip has little to no effect on the intersystem crossing rate and affects excitation and emission rate almost equally, because of the small change in k_{21}/σ_{12}, and 2) the hysteresis seen in the post-approached measurement has not been caused by the tip (pre- and app overlay), and emitter (or its environment) must have changed of state after the approached measurement.

Notice that k_{21}/σ_{12} as evaluated from the bunching part only is consistent with rates fitted in the antibunching part. Moreover, as in the post-approached measurement k_{21}

didn't change, while σ_{12} has decreased (according to the antibunching part), ratio of the two has increased from 2,38-2,56 mW (pre- and approached) to 2,71 mW.

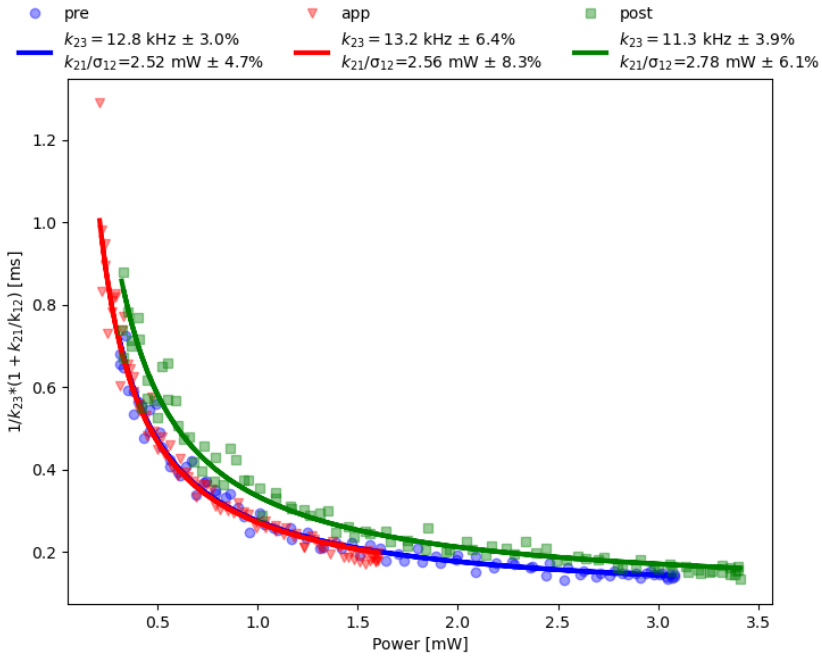

Figure 4-9. TimeON as a function of the excitation laser power. The pre-approached (blue dots), approached (red triangles) and post-approached (green squares) with fits (lines) and fit parameters given in the inset.

Because maximum power was reduced, Power Scan doesn't reach plateau required to find asymptotic limit $1/k_{23}$ (fit finds many solutions). Thus correct k_{23} can be found only if ratio $\frac{k_{21}}{\sigma_{12}}$ is fixed based on the fit in Figure 4-7 ($k_{12} + k_{21}$).

Now the change in the radiation pattern of the emitter is indirectly assessed through C_{EFF} – whether a different fraction of the radiation is emitted outside the solid angle collected by the microscope objective due to the dielectric tip. The counts calculated from the rates are corrected for the deadtime (Chapter 2) and plotted as a function of the excitation power altogether with the experimental counts. As expected, C_{EFF} remains the same for the pre- and post-approached measurement. The dielectric tip enhanced the collection efficiency by 30% (0,61 to 0,79). This result suggests that dielectric tip may redirects the radiation from the upper hemisphere (above glass slide) towards the microscope objective. This finding is in contradiction to the simulation results with predicts that C_{EFF} should decrease. According to the simulation, the tip redirects larger fraction of the total

radiated power towards the upper hemisphere (not collected with microscope objective) than it is radiated without the tip.

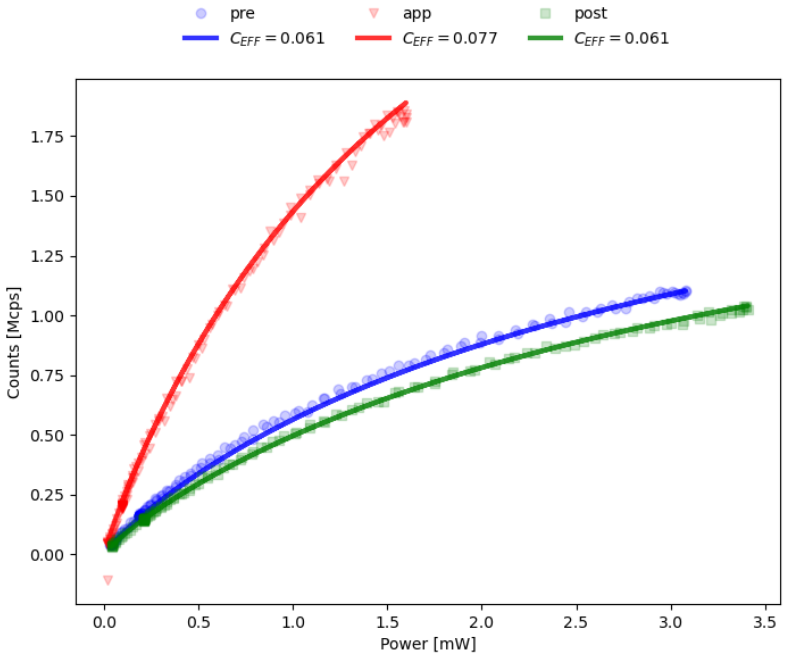

Figure 4-10. Counts on the detectors as a function of the excitation laser power. The pre-approached (blue dots), approached (red triangles) and post-approached (green squares) with counts calculated from the rates and corrected for the deadtime (lines) and adjusted collection efficiency given in the inset.

Recall that Power Scan has a bell-shape (power-increase and power-decrease slopes). It was mentioned repeatedly through the manuscript that such shape can be used to asses tip-molecule misalignment throughout the measurement. In Figure 4-10, the two directions (power increase and decrease) are hardly seen, thus it proves that for the dielectric tip with a FWHM ~45 nm, the tip drift during 29 s is negligible.

Table 4-1. Pre-, approached and post-approached calculated rates and enhancement factors for the T above.

	σ_{12}	k_{21}	σ_{32}	k_T	k_{23}	C_{EFF}
Pre	17,5 ± 0,7	43,8 ± 1,3	10,5 ± 0,1	2,37 ± 0,11	12,8 ± 0,4	0,061
App	34,1 ± 1,6	86,6 ± 1,6	19,1 ± 0,3	1,67 ± 0,26	13,2 ± 0,8	0,077
Post	14,8 ± 0,7	40,8 ± 1,6	8,4 ± 0,1	2,34 ± 0,12	11,3 ± 0,4	0,061
Enh^{pre}	1,9	2,0	1,8	0,7	1,0	1,3
Enh^{post}	2,3	2,1	2,3	0,7	1,2	1,3
$\boldsymbol{Enh^{AVG}}$	**2,1**	**2,0**	**2,0**	**0,7**	**1,1**	**1,3**

To sum up, presence of the dielectric antenna has affected the radiation pattern and all the rates besides k_{23}. While changes in the rates that involve emission or absorption of a photon (k_{12}, k_{21} and k_{32}) are expected to be affected by the LDOS, it is unclear why k_T would change by 20%. If this transition was radiative, change similar to other rates would be expected, and if it was nonradiative, there should be no change. The influence of the dielectric antenna on k_T requires further verification with other T molecules.

The hysteresis of an equal value in k_{12} and k_{32} is present in the post-approached measurement – hysteresis of σ_{12} is equal to 18% (17,9 to 14,7 MHz/mW) and hysteresis of σ_{32}^{IP} is equal to 19% (10,5 to 8,5 kHz/mW). Most probably, this hysteresis comes from the rotation of the emitter inside pT matrix. Unfortunately, pre- and post-approach Detection Scans weren't taken.

4.1.3.1. Population study

In the example shown above, the enhancements of k_{12}, k_{21} and k_{32} were similar. Such a relation can be expected only from E species, because the contribution of $\sigma_{32}^{(SA)}$ to the overall σ_{32} is negligible (Section 3.2.3.2). To investigate it further, 6 molecules (2x E215 and 4x E160) were studied. The pre- and post-enhancement factors are gathered in Table 4-2. Overall, enhancement factor is nearly 2 for k_{12}, k_{21} and k_{32}, which is consistent with the example above. Doubling of the counts and emission rate is consistent with results reported using dielectric tip of FWHM~35 nm [150]. On average, k_T is reduced by 20% due to the presence of the dielectric tip, while k_{23} remains unchanged. On average, there is also no change in C_{EFF}. Only 2 out of 6 molecules show no hysteresis (<10%), while the others have up to 30% hysteresis.

In the case of 4 out of 6 molecules, the enhancement factors for k_{12}, k_{21} and k_{32} are equal within ± 10% range. For the 2 last ones, they have distinct behaviors: all enhancements are different (molecule E) or only 2 of them are similar (molecule B). While the nanoantenna effect on those 4 molecules supports collinearity of the transition moments (through equal enhancement), molecule E (IP215) shows basically no enhancement in k_{32}. This means that for T molecule E the 3D model introduced in Chapter 2 is not valid – there cannot be 2-fold enhancement in k_{12} and no enhancement in k_{32} if the transition moments are spatially aligned. There are two E215 species studied with the dielectric tip, and one of them (molecule A) has equal enhancement for those 3 rates, while the other doesn't.

When it comes to k_T change, the results vary from no change to 40% reduction. Whether direct T1-S0 relaxation is radiative or not, I would expect only enhancement or no change in this rate, but not a decrease in the presence of a nanoantenna. I don't see any clear correlation with other enhancements, as two molecules having similar enhancements of k_{12}, k_{21} and k_{32} and being the same species (molecule F and molecule D) show no change and 20% decrease, respectively. Neither do I see a correlation with k_{23}, as if the dielectric tip would somehow decrease the probability of the intersystem crossing. I wouldn't also consider tip mechanical influence, as the change is perfectly reversible, unless the mechanical tip effect is elastic.

On average there is no change in k_{23}. Interestingly enough, the one molecule, which was mentioned as an exception before (+10% in k_{32} and +100% in k_{12}) is also molecule that shows 30% change in k_{23} upon approach with the tip. This proves that assignment of the groups and species is not enough to predict behavior of the emitter upon approach with the dielectric tip.

Lastly, C_{EFF} is related to how nanoantenna affect the emission pattern of the emitter. Ideally, nanoantenna should result in C_{EFF} increase. The dielectric tip, on average, doesn't change C_{EFF}. This means that fraction of radiated power, within the solid angle collected by the microscope objective, remains unchanged. Unexpectedly, C_{EFF} value changes between pre- and post-approach measurement instead of staying constant. The most obvious causes of the change in C_{EFF} between pre- and post-approached is the drift of the sample/misalignment with pinhole/detectors. However, there is one molecule with a negative and one with a positive change in C_{EFF}, while misalignment should always result in negative change (smaller C_{EFF}). Moreover, as measurements with a tip, which is much more sensitive to spatial misalignment, shows no hysteresis (no misalignment of the laser PSF/tip/molecule/detector), it is not logical to explain changes in C_{EFF} in pre- and post- with the misalignment.

I suspect the pre/post-approach changes in C_{EFF} to be related with changes in $\frac{k_R}{k_{21}}$. I can analyze possibility nonradiative rate increase. Let's assume a molecule with k_{21}=k_R+k_{NR}, which has a given C_{EFF}. If in post-approached measurement k_{21} increases due to increase in k_{NR}, C_{EFF} decreases. Then $Enh_{C_{EFF}}^{post} > Enh_{C_{EFF}}^{pre}$, because C_{EFF}^{app} is divided by $C_{EFF}^{post} < C_{EFF}^{pre}$. Simultaneously, changes must follow $Enh_{k_{21}}^{post} < Enh_{k_{21}}^{pre}$, because k_{21}^{app} is divided by $k_{21}^{post} > k_{21}^{pre}$. This is exactly the case of molecule D. An analogous situation, when molecule decreases in k_{NR} is seen in molecule C and conditions for pre/post enhancements are inversed accordingly. Thus, experimental results are consistent with the analysis of changes in non-radiative S1 relaxation, however more experiments would be required to fully support such claim.

Table 4-2. The pre- and post-enhancement factors for 6 molecules.

ID number (polarization specie)		$Enh_{\sigma_{12}}$	$Enh_{k_{21}}$	$Enh_{\sigma_{32}}$	Enh_{k_T}	$Enh_{k_{23}}$	$Enh_{C_{EFF}}$
molecule A (IP215)	pre	1.9	2.0	1.8	0.7	1.0	1.3
	post	2.3	2.1	2.3	0.7	1.2	1.3
molecule B (IP160)	pre	1.9	1.8	1.4	0.7	1.0	1.0
	post	2.1	1.4	1.4	0.7	0.8	1.0
molecule C (IP160)	pre	1.9	2.1	1.9	0.9	1.2	1.0
	post	2.0	2.4	1.9	0.9	1.1	0,8
molecule D (IP160)	pre	2.4	2.2	2.1	0.8	0.9	1.0
	post	2.1	2.0	2.1	0.8	1.0	1.3
molecule E (IP215)	pre	2,0	1,5	1,1	0,7	0,7	0,9
	post	2,1	1,5	1,1	0,6	0,7	0,9
molecule F (IP160)	pre	2,2	2,2	2,3	1,0	1,1	1,0
	post	2,2	2,1	2,2	1,0	1,1	1,1
avg ± std	pre	2,1 ± 0,2	2,0 ± 0,3	1,8 ± 0,4	0,8 ± 0,1	1,0 ± 0,2	1,0 ± 0,1

ID number (polarization specie)		$Enh_{\sigma_{12}}$	$Enh_{k_{21}}$	$Enh_{\sigma_{32}}$	Enh_{k_T}	$Enh_{k_{23}}$	$Enh_{C_{EFF}}$
	post	2,1 ± 0,1	1,9 ± 0,4	1,8 ± 0,5	0,8 ± 0,1	1,0 ± 0,2	1,1 ± 0,2

4.1.4. Intersystem Crossing and Quantum Yield

In chapter 3, Section 3.2.3.2.1, I have discussed a nonlinear behavior of $k_{12}k_{23}$ product, which invalidates the assumption of a constant ISC rate. However, the power-dependence of k_{23} (in Chapter 3) was in the order of background correction and thus this argumentation was tricky. Herein, I calculate directly k_{23} according to the formula:

$$k_{23} = A * \frac{(k_{32} + k_T) * -\lambda_2}{k_{12}} \qquad 4.2$$

I consider 2 molecules – molecule C and molecule A, which exhibit very different behavior in $k_{23}(P)$ (Figure 4-11 left). Molecule C nearly doubles it's k_{23} over the 0-3 mW range (10 to 20 kHz). On the other hand, molecule A (Figure 4-11 right) shows typical small increase of k_{23} on the order of 10%. The 2-fold increase in k_{23} would require +100% background correction of A, while typical correction is ~10%. Therefore, background contribution may be discarded.

Notice also that from Equation 4.2, any error made in fitting σ_{12} (or σ_{32}) affects only the range of k_{23} values, but its slope persists. To explain this – a linear curve multiplied by any non-zero value, would still give a doubling of k_{23}, but range of the values changes. Additionally, in both cases, presence of the dielectric tip increases significantly the slope of $k_{23}(P)$, but has a small to no effect on the intercept. This suggest that indeed there must be a connection between excitation field and calculated k_{23}. As has been said in Chapter 3, Section 3.2.3.2.1, S1-S2 excitation and subsequent ISC cannot be argued due to the lack of the energy diagram of higher singlet states.

Note that little change in k_{23}, and simultaneous 2-fold enhancement of k_{21} means that dielectric tip decreases by half the efficiency of S1 depopulation through ISC pathway $\eta_{k_{23}}^{-S1}$. Meaning that, probability that S0 excitation event ends up in a triplet state is 2 times lower, and so QY_{ISC} is also cut in half.

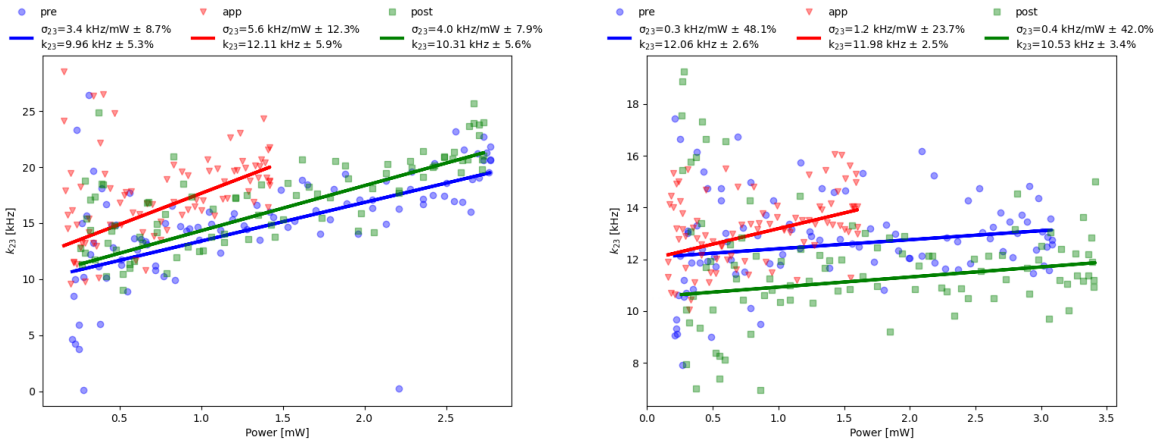

Figure 4-11. Calculated power-dependence of the k_{23} rate for molecule C (left) and molecule A (right). The linear fit parameters in the inset.

4.1.5. Effect on the field distribution (Polarization Scan)

The field distribution changes when nanoantenna approaches the surfaces. Though simulation of the field distribution with the dielectric tip were carried out (by Ludovic Douillard), it showed that C_{EFF} should decrease by half, as part of the radiated power couples into the fiber and gets lost in the upper hemisphere (microscope objective below the sample). Since I didn't observe following changes in C_{EFF} – on average C_{EFF} didn't change in Power Scans – simulation results cannot be used to treat Polarization Scans with the dielectric tip. Instead, I have to redefine field distribution and solve for it using experimental data of Polarization Scan.

To find how each component of the electric field (E'_x, E'_y, E'_z) is modified by the dielectric tip, I start by defining the intensity I_{APP} in the presence of the dielectric tip (approached):

$$I_{APP} = E_X'^2 + E_Y'^2 + E_Z'^2 \qquad 4.3$$

To limit the number of parameters that are implemented in the fit, I simplify the problem and consider that each cartesian field component N in the presence of the nanoantenna is the field without nanoantenna, multiplied by some constant S_{NN}:

$$E'_N = S_{NN} E_N \tag{4.4}$$

The orientation and the rates are fitted using the pre-approached measurement only and taken as fixed values in the approached measurement fit. The results of the fit are presented in Figure 4-12. It should be noted that fit yields physically unreasonable uncertainties, which means that there is more than 1 set of values that can fit the data. This was confirmed as the solution depends on the initial guess. Polarization scans require further work, both experimental and data processing.

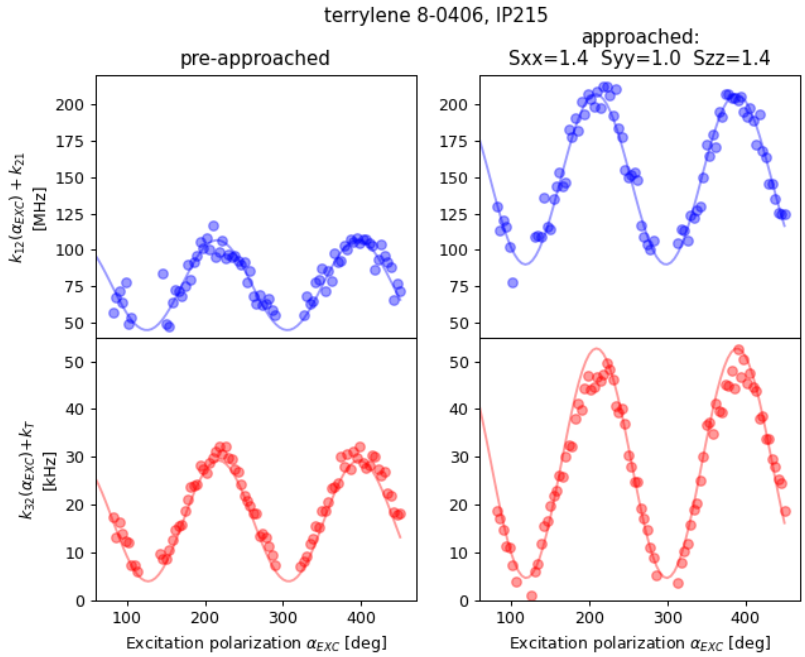

Figure 4-12. Pre- and approached Angle Scans measured at 2,7 mW and 3,1 mW, respectively. The spherical coordinates of the transition moments are fixed for approached fit based on the values recovered with the pre-approached measurement and go as $\theta = 24$ *deg,* $\phi = 49$ *deg,* $\gamma = 320$ *deg,* $\sigma_{12} = 11 * 10^{-17} cm^2$, $\sigma_{32}^{IP} = 4{,}5 * 10^{-20} cm^2$ *and* $\sigma_{32}^{IP} = 0{,}1 * 10^{-20} cm^2$. *In the approached fit only the 3 field distribution factors (Sxx, Syy, Szz) are taken as parameters and results are plotted in the header.*

4.1.6. Conclusions

The dielectric tip has proven to change the rates of processes that involve a photon, such as singlet-singlet absorption, fluorescence and triplet-triplet absorption. All of those transitions were enhanced nearly equally (2-fold) in case of the spatially-aligned transition moments. The enhancement of the spontaneous emission rate is viewed as Purcell factor and thus proportional to the change in LDOS. The equivalent enhancements in the absorption rates prove that T/pT obeys electromagnetic reciprocity. On average, the dielectric tip didn't change the rate of the horizontal S1-T1 transition but slightly decreased the rate of the T1-S0 one. Both pathways require a spin flip and results vary from a molecule to a molecule. This decrease in the RISC rate, which is surprising in view of LDOS increase, might be of non-electromagnetic origin. Overall, the dielectric tip has increased the photon flux by accelerating S1 depopulation via S1-S0 transition, decreasing triplet population (lowering QY_{ISC}) and increasing the triplet depopulation selectively through the T1-T5/6-S2 pathway, instead of T1-S0 pathway.

Thanks to the sensitive and careful SPM control coupled with low excitation power, the emitters remained photostable enough to carry out pre- and post- controls and the average enhancement of the excitation rate has as little as 10% standard deviation (population of 6 molecules).

Very few molecules have power-dependent ISC rate, the slope of this dependence gets increased in the presence of the dielectric tip. Further studies and hypothetical mechanism is required to explain such a dependence. The experiments with the tip didn't provide any clarification to this issue.

The modification of the field distribution due to the presence of the tip cannot be solved using the experimental data due to the underdetermination issue (many solutions).

4.2. Molecule and a plasmonic nanoantenna

4.2.1. Fabrication and characterization

The top-down fabrication of gold pyramids was done by Lola Chamot and Simon Vassant, following the reference [176] and details can be found in the Appendix I. The pyramids

were imaged with SEM in order to verify the geometry. It was found that instead of a sharp, point-like apex, the pyramids have a wedge-like apex – Figure 4-13. Pyramids of various sizes were fabricated and all of them suffered from the same wedge-like apex. Pyramid used for the emitter-nanoantenna experiments had a square base 100 μm x 100 μm.

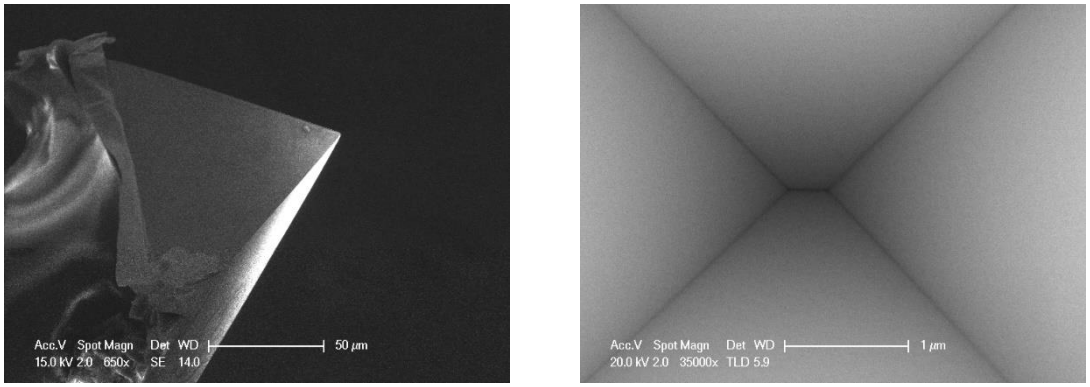

Figure 4-13. SEM images of the pyramids picked-up with the optical fiber and UV glue (left), zoom on the tip of the gold pyramid (base 200 μm x 200 μm) showing ~200 nm rectangle-like, instead of the point-like apex (right).

A similar topology was also found in-situ with the tip raster scans counts(X,Y). The count-enhancement rectangle-like area of 80x300 nm was found and the corresponding height image is shown – Figure 4-14 upper left and upper right, respectively.

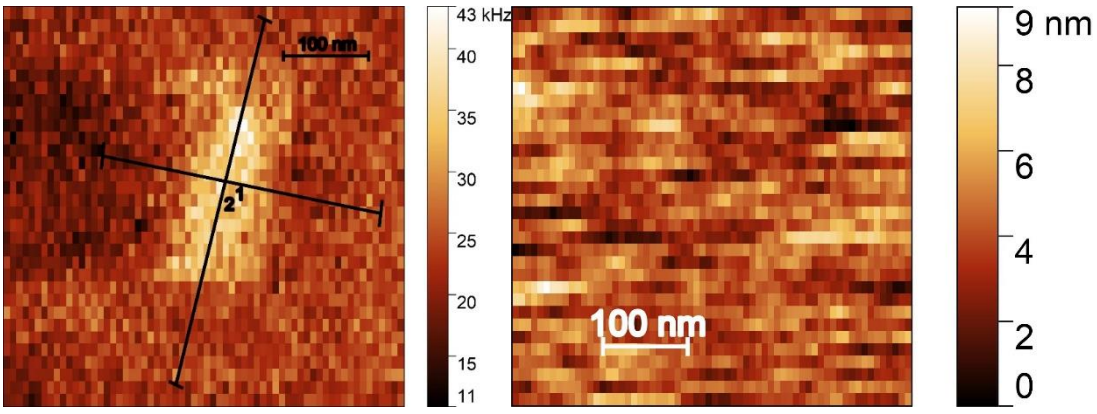

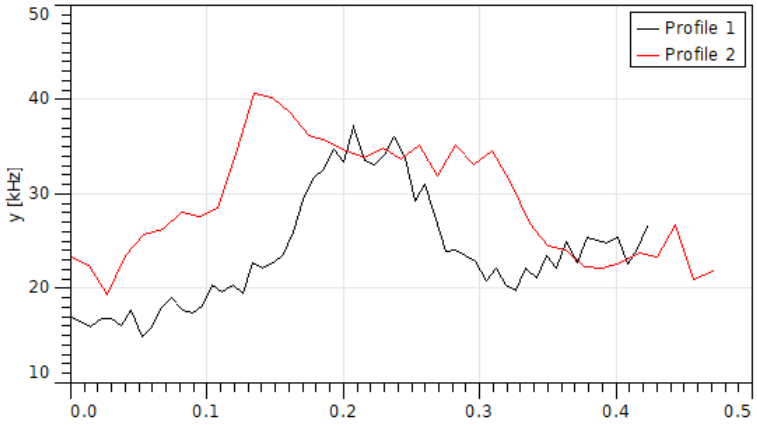

Figure 4-14. The gold pyramid raster scan Counts(X,Y) with 2 cross-section lines. (upper left) and the corresponding height image (upper right). The counts profile of the respective cross-section lines indicating the counts enhancement over the 80x300 nm rectangle-like area (lower).

4.2.2. Signal-to-noise ratio of the gold pyramid

As mentioned in Section 4.1.2, experiments on the molecule alone has shown 50<SNR<20 and SNR~40 in the presence of the dielectric tip. In the presence of the gold pyramid SNR falls rapidly with incident power increase from 20 to single digit numbers – Figure 4-15.

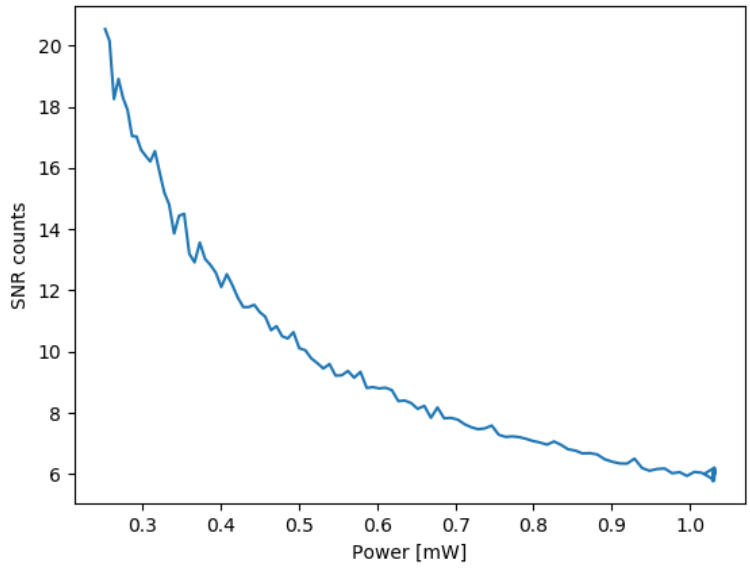

Figure 4-15. Signal-to-noise ratio taken as a ratio of counts T/pT with the gold pyramid and gold pyramid and pT taken few microns away from the emitter.

I plot START-STOP antibunching curves at the lowest and at the highest incident power – Figure 4-16. In the presence of the gold pyramid, START-STOP measurement shows that molecule-nanoantenna system oscillates at the limit of the single photon source classification. This shows that enhancement of the gold pyramid comes at the cost of large gold photoluminescence, so that the system (molecule and gold pyramid) can be hardly viewed as a single photon source.

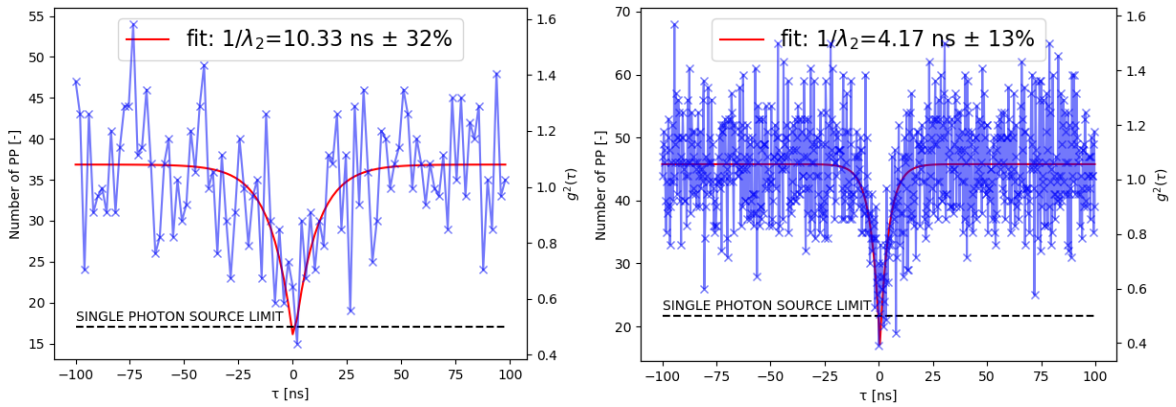

Figure 4-16. START-STOP measurement of T/pT approached with the gold pyramid at the lowest and the highest incident power of 0,2mW (left) and 1mW (right). Limit value of single photon source classification $g^{(2)}(0)$=0,5 plotted with a dashed line.

4.2.3. Effect on the rates (Power Scan)

To confirm that upon approach with the gold pyramid (plasmonic) nanoantenna, the system remains in the weak-coupling regime, the fluorescence spectrum was taken – Figure 4-17.

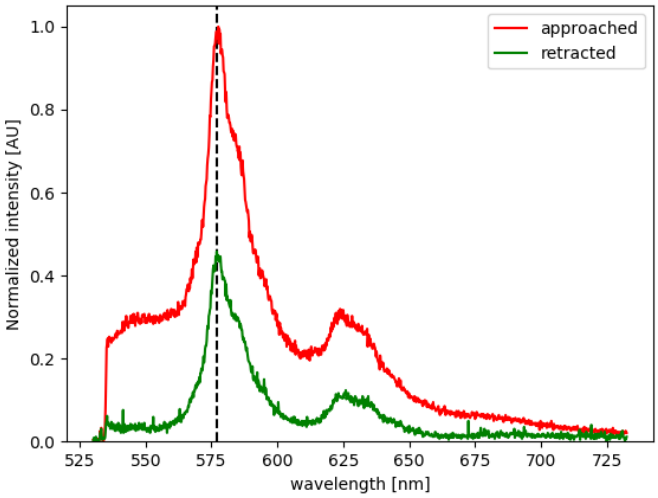

Figure 4-17. Fluorescence spectrum of T/pT with the approached (red) and retracted (green) gold pyramid.

As seen from the fluorescence spectrum presented above, pyramid introduces very large background due to gold fluorescence and thus a bandpass filter (570-610 nm) is placed in front of the detectors to increase SNR of the TTTR2 measurements. Besides, the fluorescence spectrum intensity is consistent with the ~1,5 counts enhancement seen in the counts(X,Y) raster scan. Thus, gold pyramid, even with the rectangle-like apex, enhances the fluorescence rather than quenching the excited state.

When treating the molecule alone or molecule with a dielectric tip, the background correction was often mentioned, but its magnitude was negligible (<10% correction) due to high SNR (~20). In the case of a gold pyramid, even with the bandpass filter, the SNR falls down to single digit (Figure 4-15) and correction of correlation function amplitude A reaches up to 50% of the raw value – Figure 4-18. If the autocorrelation amplitude is undervalued, triplet population (k_{23}) and depopulation (k_{32} and k_T) will be undervalued and overvalued, respectively. Meanwhile, the singlet excitation and excited singlet lifetime remain unaffected as they are calculated from λ_2 of START-STOP histogram.

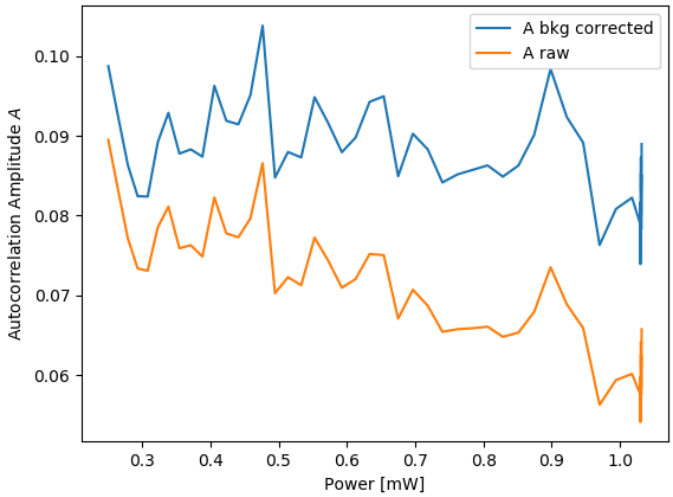

Figure 4-18. Autocorrelation amplitude in the presence of gold pyramid without background correction (orange) and with background correction (blue).

The excitation and emission rates are both enhanced by the gold pyramid but inequivalently (Figure 4-19) – around 5-fold and 2-fold, respectively. There is no hysteresis between pre- and post-approached measurement but low power range datapoints (<0.8 mW) had to be cut out due to the emitter instability.

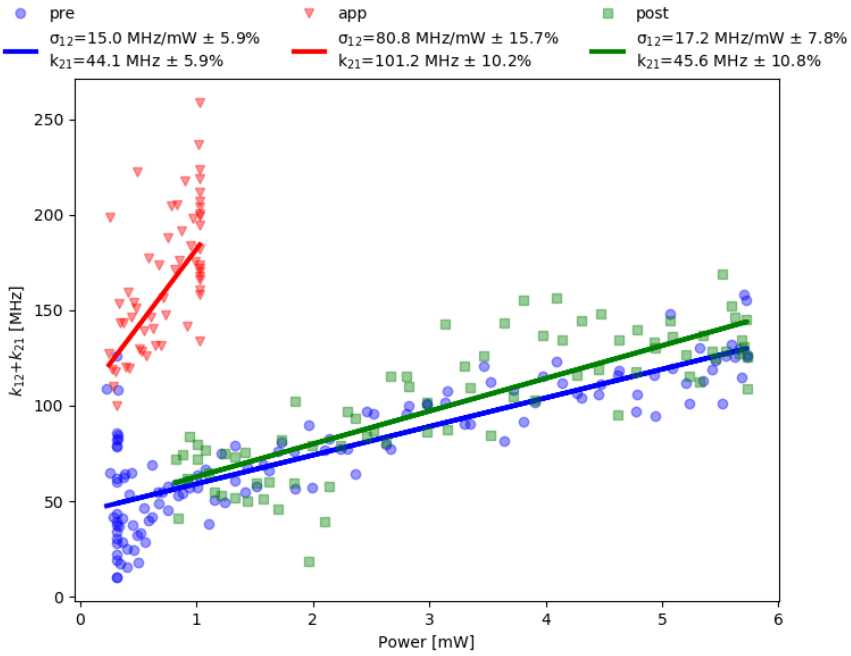

Figure 4-19. Sum of the excitation rate (k_{12}) and spontaneous emission rate (k_{21}) as a function of the excitation laser power. The pre-approached (blue dots), approached (red

triangles) and post-approached (green squares) with linear fits (lines) and fit parameters given in the inset.

Triplet depopulation rates are changed significantly, with σ_{32} enhanced over 3-fold and k_T reduced 6-fold – Figure 4-20. Moreover, even though low power regime datapoints were discarded due to instability, the emitter jumps between slower and faster triplet depopulation states also in the higher power regime during the post-approached measurement.

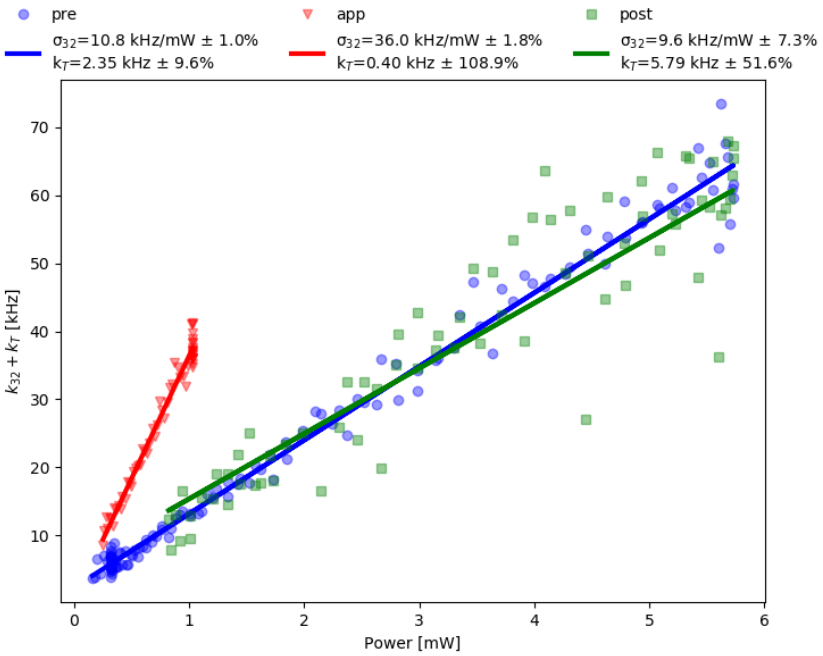

Figure 4-20. TimeOFF as a function of the excitation laser power. The pre-approached (blue dots), approached (red triangles) and post-approached (green squares) with linear fits (lines) and fit parameters given in the inset.

Calculating the intersystem crossing with the gold pyramid is technically difficult. To reach high precision, high power is required, but emitters become extremely unstable in the presence of pyramid at high excitations. Nevertheless, according to the fit, k_{23} is reduced by half in the approached measurement - Figure 4-21. Those findings are inconsistent with study of Rhodamine dye in plasmonic nanoholes, which reported 7-fold enhancement of the ISC rate [157]. However, it must be noted that emitter-nanoantenna distance is widely different in the experimental set-ups – freely diffusing emitter inside

the nanoaperture and emitter trapped in a solid matrix and approached with a nanoantenna.

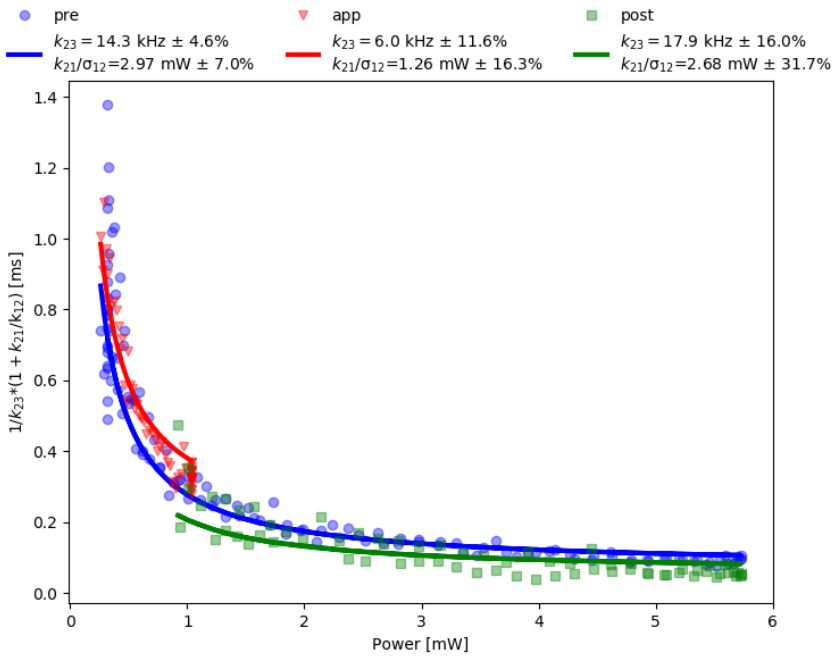

Figure 4-21. TimeON as a function of the excitation laser power. The pre-approached (blue dots), approached (red triangles) and post-approached (green squares) with fits (lines) and fit parameters given in the inset.

Increased photon flux is readily visible in Figure 4-22. Notice that C_{EFF} doesn't change significantly between the pre- and approached measurement. This means that LDOS is entirely radiative and pyramid doesn't introduce any losses. This is quite surprising, considering that gold pyramid is highly luminescent, and thus must also highly absorb. The distribution of LDOS around the gold pyramid wasn't simulate. The distance between the emitter and nanoantenna can be estimated to be around 25 nm (~15nm depth in pT and 10 nm TSD). It's possible that such range prevents the increase of the non-radiative rates through short-range dipole-dipole interaction.

The rules set for data selection (less than 15% difference in the number of photons for pre- and post-approached measurement) cannot be applied for the gold pyramid. The emitters rarely remain photostable during approached measurement and just 1 molecule was found to ''survive'' all 3 measurements (pre, app,post). I consider this instability to

be caused by the gold pyramid as emitters were proven to be stable, when using the dielectric tip.

Large population study with the gold pyramid and Polarization Scans study has been halted for the time of writing my manuscript and I restrict myself to the example presented above. Experiments with gold pyramid are especially tedious as gold pyramid probes often struggle to stay approached, wear off gradually, and render the emissions highly unstable.

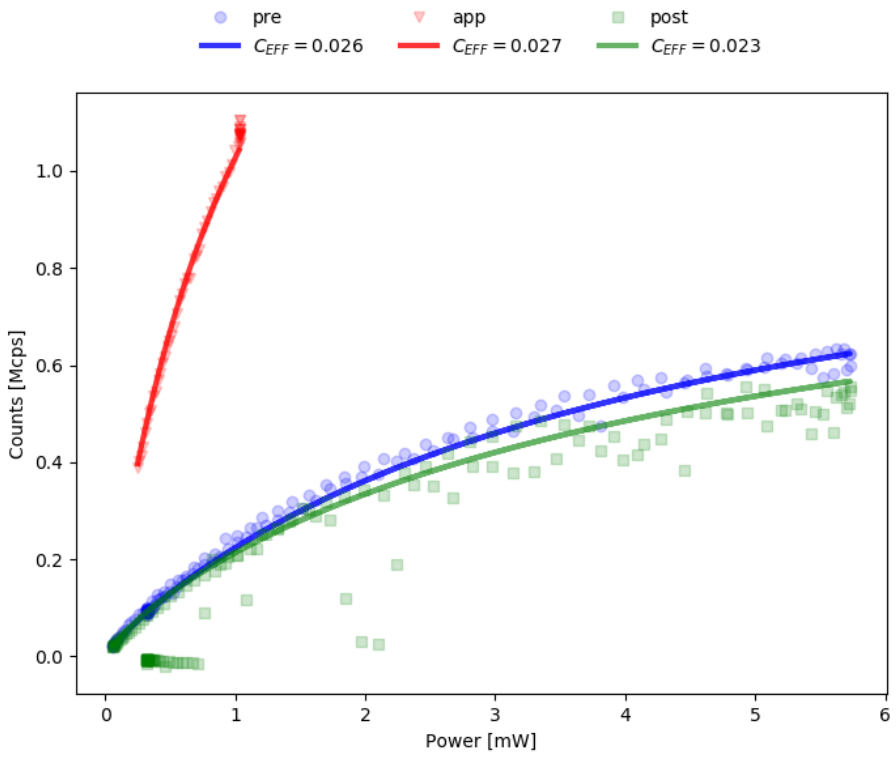

Figure 4-22. Background corrected counts on the detectors as a function of the excitation laser power. The pre-approached (blue dots), approached (red triangles) and post-approached (green squares) with counts calculated from the rates and corrected for the deadtime (lines) and adjusted collection efficiency given in the inset.

The rates and their enhancements in the presence of gold pyramid are gathered in Table 4-3.

Table 4-3. Pre-, approached (gold pyramide) and post-approached calculated rates and enhancement factors for the T above.

	σ_{12}	k_{21}	σ_{32}	k_T	k_{23}	C_{EFF}
Pre	15,0 ± 0,9	44,1 ± 2,6	10,8 ± 0,2	2,35 ± 0,23	14,3 ± 0,7	0,026
App	80,8 ± 12,7	101,2 ± 10,3	36,0 ± 0,7	0,40 ± 0,44	6,0 ± 0,7	0,027
Post	17,2 ± 1,3	45,6 ± 4,9	9,6 ± 0,7	5,8 ± 2,98	17,9 ± 2,9	0,023
Enh^{pre}	5,4	2,3	3,3	0,17	0,4	1,1
Enh^{post}	4,7	2,2	3,8	0,07	0,3	1,2
$\boldsymbol{Enh^{AVG}}$	**5,0**	**2,3**	**3,5**	**0,12**	**0,4**	**1,2**

4.2.4. Conclusions

The fabricated gold pyramids suffer from wedge-like shape instead of point-like shape at the apex. The wedge-like apex results in rectangle-like PSF when performing raster scan above a single molecule. The gold pyramid is highly photoluminescent, which results in START-STOP histograms that barely fulfill single photon source condition $g^{(2)}(0)$<0,5. Weak coupling regime was confirmed by measuring fluorescence spectrum of the emitter with and without the pyramid. On the contrary to the other measurements, background correction of the correlation function amplitude requires up to 50% correction and thus shouldn't be neglected.

Effect of the gold pyramid has shown inequivalent enhancement of the excitation (5-fold) and emission rate (2-fold). Simultaneously, large decrease in ISC was observed. Similar situation was also observed in 1 of the 6 molecules studies with the dielectric tip. Due to

the lack of large population study, its difficult to predict whether inequivalent enhancements of the S0-S1 and S1-S0 transition dipole moments are an effect of the pyramid or just present for this exact molecule. The direct T1-S0 relaxation also undergoes significant decrease in the presence of the gold pyramid, though mechanism through which such change would occur is unclear. The decrease in those rates is inconsistent with studies carried out with Rhodamine dye in plasmonic nanoapertures [157], but experimental approaches (emitter-nanoantenna distance) are very different. There is no change in C_{EFF} and thus gold pyramid doesn't increase non-radiative rates through energy transfer to the gold. As gold pyramid is highly absorbing at this wavelength, it's most likely the distance between the emitter and nanoantenna that prevents energy transfer through dipole-dipole interactions.

Considering population dynamics, the gold pyramid has shown very similar effects to the dielectric tip. The spontaneous emission rate is enhanced, while intersystem crossing rate is reduced, which results in the decrease of the triplet state population (reduction of QY_{ISC}). Triplet depopulation is simultaneously enhanced selectively via triplet-triplet optical transition and subsequent rISC, instead of direct lowest excited triplet to ground singlet transition.

Summary and outlook

The subject of this work was to understand how systems made of a single molecule and a nanoantenna can be used to surpass physical limitations to the photon flux set by state dynamics of the quantum photon source. Work was divided into two main parts.

Firstly, the photophysics of single molecules was investigated by implementing novel Scan methods. By using Scans in the excitation power and in excitation polarization, one extract the single molecule transition rates and find the absorption cross-sections and their transition dipole moments orientation. Such a complete characterization is required to understand photophysics of the emitters inside solid matrixes and thus predict the performance of the devices based on single molecules. Secondly, the photophysics of single molecules was studied in the presence of dielectric and plasmonic nanoantennas to investigate how such photon sources could be further tuned. Both antennas, in various magnitudes, result in an overall acceleration of the excited singlet state selectively via fluorescence, which simultaneously decreases the triplet state population by two distinct processes. The first is a reduction of the intersystem crossing quantum yield. The other is the depopulation of the triplet state is accelerated selectively via triplet-triplet absorption and subsequent photo-induced reversed intersystem crossing, which brings the system to the excited singlet state instead of the ground singlet. Thus, both nanoantennas successfully affect two main factors that set the limit of the maximal photon flux – the fluorescence lifetime and dark triplet bottle-neck effect. The following changes in population dynamics are desired for quantum emitters as they increase the efficiency of the light source.

In the first Chapter (and Appendix), I review, to the best of my knowledge, all the reports in the literature. This provides an insight into the rates and photophysics of terrylene. In thin films of nanoscale thickness spontaneous emission rate reduces few folds, however there are no reports of intersystem crossing and triplet relaxation in such samples. Meanwhile, studies in bulk report order of magnitude variation in the rates of those two transitions. Moreover, the triplet lifetime was shown to depend on the excitation power and triplet-triplet transition was proposed, but there is no information about the number and orientation of those transitions. Subsequently, I present state-of-the-art of molecule-nanoantenna studies to identify experimental approaches, outcomes, limitations, and

challenges. Finally, I show how the photon flux of quantum emitters can be treated with various models to calculate the parameters necessary to describe the temporal behavior of such a light source.

In the second Chapter, I show the methods, protocols and general ''know-how'' of the molecule-nanoantenna experiments. I describe in detail the novel implementation of Power and Polarization Scans and discuss the factors to be considered in order to optimize them for a given emitter. Then, the field distribution in thin film is presented, which is necessary to treat Polarization Scans. Subsequently, I go through the nanopositioning control, fabrication, and calibration of the probe and the sample, as well as some experimental details necessary to avoid the molecule-nanoantenna misalignment during measurements.

In the third Chapter, I focus solely on the molecule in order to find the answers to several questions that I have stumbled upon in the first Chapter. I start by showing how and with what uncertainty each rate is calculated. Then, I present the results of a large population study. Even in the random study, the population standard deviation is relatively small compared to studies found in the literature. I've measured the spontaneous emission rate of 53,3 MHz…, . Subsequently, the orientation of the transition dipole moments and the cross-sections of the transitions are calculated. We discover that, In order to describe the polarization and intensity response of terrylene in para-terphenyl, one singlet-singlet transition and two triplet-triplet transitions are required. One of the triplet-triplet transitions is colinear with the singlet-singlet transition (emission and absorption dipole moments), while the other triplet-triplet transition is perpendicular to those. The molecules of various orientations could be fitted using the same absorption cross-section for singlet-singlet transition. The cross-section of the perpendicular triplet-triplet transition has aclarger molecule-to-molecule variation than the colinear one. It remains unclear why some molecules show identical orientation of the emission dipole moment but different polarization-resolved response. The geometrical distortion of terrylene molecule in their insertion sites inside the para-terphenyl film is suspected based on the molecule-to-molecule variation in the relative intensities of the vibronic bands in the fluorescence spectrum. This chapter therefore highlights the complexity of the photophysics of single organic molecules trapped in a solid matrix and constitutes a proof of concept that Power and Polarization scans can be used to retrieve the photophysical

rates, and the full orientation of the molecule. Thanks to the two orthogonal triplet-triplet transitions, it is possible to gain information on the long-axis orientation (aligned with the singlet emission dipole) but also to the rotation of the molecule around this long axis. To the best of my knowledge, such information was so far no accessible experimentally at the single molecule level.

In the fourth Chapter, I show the results of the experiments with dielectric (pulled glass fiber) and plasmonic nanoantenna (gold pyramid). The purity of the single photon source with the pulled glass fiber is comparable to that of the molecule alone. The dielectric nanoantenna typically doubles the singlet excitation rate, emission rate and triplet excitation rate equivalently. This supports the proposed 3D model. On average, the intersystem crossing rate remains constant, as expected. It is unclear why the lifetime of the direct triplet-singlet relaxation is slightly increased (on average 20%). However, there are some exceptional molecules where each rate is enhanced differently and even intersystem crossing is reduced.

The gold pyramids provide much higher enhancements than the pulled glass fiber. However, due to the substantial photoluminescence of gold, the molecule-gold pyramid system can hardly be considered as a single photon source. The intersystem crossing rate was reduced by half in one molecule, but population statistics couldn't be carried out as emitters become very unstable in the presence of the gold pyramid.

As for the outlook, Scans are a promising tool for precise and robust characterization of single emitter in solid matrixes. This work constitutes a proof of concept that they can be used on single photon emitters to calculate their rates, absorption cross-sections, and orientation of the transition dipole moment related to the excitation rates. Such properties of the emitter are necessary to predict the performance of the devices based on the single molecules and could be applied in the characterization of other organic single molecules.

The emitter-nanoantenna experiments were carried out with relatively simple nanoantennas. This was required to develop the necessary protocols and general know-how to start a new activity in our laboratory. In the future, more complicated nanoantennas will studied to move closer to real-life applications.

Some molecules couldn't be fitted using our model. They displayed unexpected enhancement factors in the presence of the nanoantenna and fluorescence spectrum with various relative intensities of vibronic transitions. It remains unexplained why some molecules behave differently than others but our results suggest a perturbation of the emitters' geometry. For fundamental research and practical applications, it would be potentially interesting to carry out more work on such ''exceptional'' molecules. Perhaps, such studies could clarify the connection between orientation of the transition dipole moment and relative intensity of the vibronic bands. In perspective, such knowledge could be used to optimize fabrication protocols in order to create more efficient single molecule devices.

Appendices

A. Sequence of processes

The validity of describing a sequence of processes (transitions) as a single effective transition is theoretically incorrect. In the literature, words 'much faster' or 'much slower' are used when giving reasoning for neglecting a process without giving exact order of magnitude. Below I try to answer the question of how much faster a rate has to be with respect to the other rate, so it can be neglected without compromising an exponential distribution. To do this, I will recover *CDF* of a sequential process and compare it with *CDF* if this transition was governed by a slower process only.

I simplify the problem to 2 processes in a sequence. To give it some meaning, I consider a single S1-S0 relaxation event that occurs through the VR-Fluo sequence. At the time $t = 0$, molecule was excited to the υ_N vibrational level of S1, then according to Kasha's rule, it undergoes VR, and emission happens from the lowest vibrational level of S1. The overall average time that molecule spends in S1 prior to relaxing to S0 corresponds to the time of VR and Fluo with rates k_{VR} and k_{Fluo}. The probability of state occupancy makes a sequence:

$$P[S1^{\upsilon_N}] \xrightarrow{k_{VR}} P[S1^0] \xrightarrow{k_{Fluo}} P[S0] \qquad \text{A.1}$$

where *P[SY^Z]* refers to the probability of finding a molecule in *SY* electronic and *Z* vibrational level, respectively. On the other hand, I take a direct transition by neglecting vibrational levels:

$$P[S1^0] \xrightarrow{k_{Fluo}} P[S0] \qquad \text{A.2}$$

Now *CDF* of a single transition (Equation A.2) takes a form of a single exponential, but *CDF* of S0 population in a sequential transition (Equation A.1) has to be calculated. I start with describing the highest state, which follows a single exponential and gives boundary conditions of:

$$P[S1^{\upsilon_N}](0) = 1 \; and \; P[S1^{\upsilon_N}]\left(t \gg \frac{1}{k_{VR}}\right) = 0 \tag{A.3}$$

Dynamics of the highest state can be written as:

$$P[S1^{\upsilon_N}](t) = P[S1^{\upsilon_N}](0) * \exp\left(-k_{VR} * t\right) \tag{A.4}$$

To describe a change in the probability ΔP within the time Δt, which refers to a molecule leaving the highest state to the middle state:

$$\Delta P[S1^{\upsilon_N}](\Delta t) = P[S1^{\upsilon_N}](t) - P[S1^{\upsilon_N}](t + \Delta t) \tag{A.5}$$

The probability of leaving the highest state becomes a positive probability of occupying the middle state. Middle state probability at time $t+\Delta t$ can be written as the sum of 3 factors: i) $P[S1^0](t)$ being a middle state probability at time t ii) $\Delta P[S1^{\upsilon_N}](\Delta t)$ incoming from the highest state during Δt iii) $\Delta P[S0](\Delta t)$ flux leaving $S1^0$ that populates the lowest state S0 (from middle to the lowest state):

$$P[S1^0](t + \Delta t) = P[S1^0](t) + \Delta P[S1^{\upsilon_N}](\Delta t) - \Delta P[S0](\Delta t) \tag{A.6}$$

Flux $\Delta P[S0]$ that leaves the middle state to the lowest state is a bit more complex. Every $\Delta P[S1^{\upsilon_N}](\Delta t)$ came to the middle state at a different time t, and thus experiences different duration time inside this level. It's convenient to switch to discrete form, where time is defined as N number of very small time segments, $t = N * \Delta t$:

$$\Delta P[S0]_N = \sum_{J=0}^{J=N-1} \Delta P[S1^{\upsilon_N}]_J * \left[1 - \exp\left(-k_F * (N * \Delta t - J * \Delta t\,)\right)\right] \tag{A.7}$$

And the probability of leaving the middle state to populate the lowest state at each time segment is a sum of all the probability fractions that have entered this state and multiplied by a decay with a duration time $(N * \Delta t - J * \Delta t\,)$ calculated since its entrance time.

Factor J is used to account for different duration time inside the middle level of each $\Delta P[S1^{\upsilon_N}]$ that have entered this state.

As a verification step, middle state population can be calculated from adapting Bateman equation for the sequence of the radioactive decays [177,178]:

$$P[S1^0](t) = \frac{k_{Fluo} * k_{VR}}{k_{Fluo} - k_{VR}}(e^{-k_{VR}t} - e^{-k_{Fluo}t}) \quad \text{A.8}$$

As an additional verification step, I check if at each time t - molecule occupies one of the 3 states:

$$P[S1^{\upsilon_N}](t) + P[S1^0](t) + P[S0](t) = 1 \quad \text{A.9}$$

In Figure A-1 upper, I present the probability of states occupancy as a function of time t post-excitation obtained from discrete treatment and verified using the Bateman equation and A.9. If the rates are of similar magnitude, *CDF* of S0 becomes sigmoidal (S-shape) instead of exponential (green line). This means that it has to be treated as 2 separate transitions. Subsequently, I calculate an absolute error between the *CDF* of S0 probability in case of transition governed by Fluo only and when 2 processes (VR-Fluo) are sequential but have a different ratio of their rates (Figure A-1, lower). The higher the ratio, the smaller the error between the *CDF* of a single and sequential transition. At the ratio of 2 maximum error reaches 0,25, and thus molecule state occupancy is assessed with only 75% precision at this time. However, as the ratio reaches 100, the maximal error stays below 1%.

To conclude, 2 subsequent processes that change the state of the molecule, and thus are considered as 2 transitions according to the Fermi golden rule, can be approximated with a single transition if the rates vary by 2 orders of magnitude at least. The effective rate of this sequential transition is equal to the slower transition. This has particular implications to this thesis such as, rates k_{ij} can be simply understood as time spend in the state i prior to transitioning to state j, thus neglecting the vibrational transitory levels (VR) if those exist.

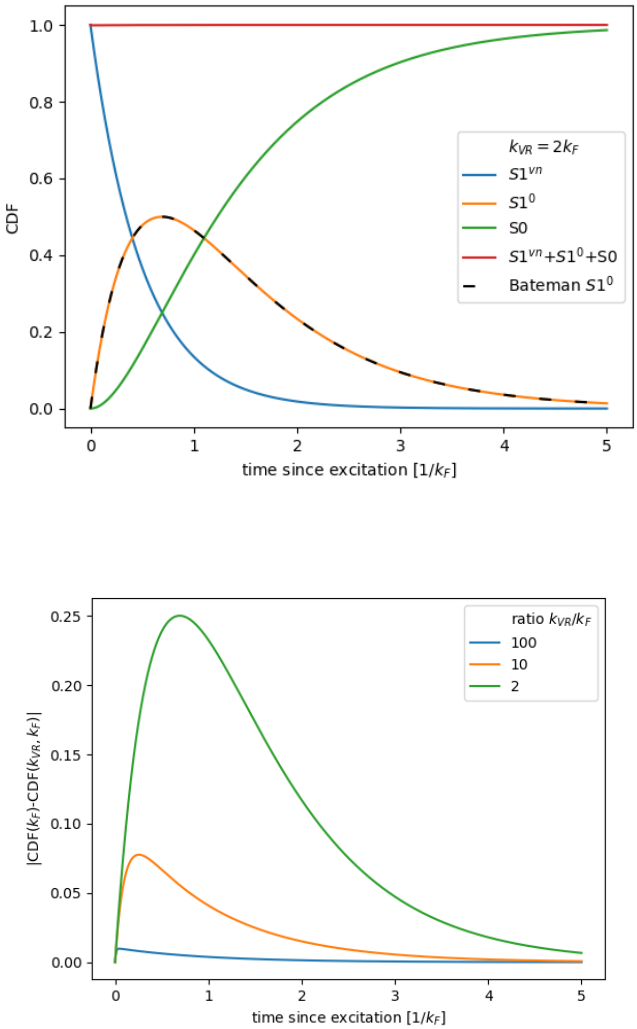

Figure A-1. Transient probability of states occupancy as a function of time since molecule was excited to the vibrational level of the excited singlet $S1^{\upsilon_N}$ (upper) and transient absolute error when a sequential process is approximated with the slower process only for different ratios of the rates.

B. Other interactions

a. Host triplet energy level

If different sites of T/pT were to be responsible for the differences in rates found in the literature, they would have to be explained by a particular set of interactions with the host molecules around the guest. Therefore below, I review host-guest interactions reported for T to verify how rates are affected.

T in anthracene crystals at LT have nearly 3 orders of magnitude lower photon flux than in naphthalene or pT, which was attributed to a similar increase in intersystem crossing yield [39, 38]. In this particular case, the triplet is populated via intermolecular intersystem crossing - from T's S1 to the host's T1 and finally to T's triplet. Authors suggest that such a ''ping-pong'' process may appear in any host-quest system with a host's T1 energy level below the guest's S1 and above guest's T1 energy level and proceed accordingly with the EGL.

b. Heavy atom effect

Heavy atom effect is used to increase spin-orbit coupling and thus is generally applied to accelerate intersystem crossing [179]. Terrylene-doped para-dichlorobenzene and dichloronaphthalene crystals were reported [42,60]. In the former, intersystem crossing wasn't directly investigated, while in the latter no significant change was seen. The authors explained the lack of external heavy atom effect by referring to the energy diagram of the electronic states of terrylene - arguing that it prevents efficient SOC between S1 and T1 or T2 states. Indeed, S1 and T1 have a large energy offset (~1 eV). The energy of S1 and T2 are matched, however, their direct spin-orbit coupling is symmetry forbidden [49].

To sum up, in order to change the T1 population or depopulation: 1) triplet energy level of a host can be changed. 2) even if a heavy atom is introduced, the large energy gap between S1 and T1 prevents T1 population change, and it is unlikely that this gap changes from site to site.

c. Pressure

If we consider a matrix from a mechanical point of view, what can vary from site to site is the stress inside the material that could, in consequence, disturb structure of T. The pressure effect on zero phonon lines in T/pT has shown reversible redshift up to 1,48 MHz/hPa and was proven to be independent of their crystallographic sites [180]. The author calculated that such a redshift is attributed solely to Lennard-Jones type interaction (and not molecule's deformation), only if the vacuum absorption wavelength of T is 509±11 nm. A separate study on the fluorescence excitation spectroscopy of T in helium supersonic jet was measured to recover 0-0 line at 520 nm [66]. Altogether, those

findings suggest that exerted force doesn't induce conformational changes of T/pT but could induce a negligibly small redshift in order of MHz/hPa.

To sum up, this is promising for measurements with a tip approached above the film, and it could be easily experimentally verified with fluorescence measurement if the tip indeed induces a negligible redshift.

d. Stark effect

Site-to-site variations may also have a nanoscopic origin, which depends on the guest's nearest neighbors. However, measuring the organization of pT molecules around T insertion is not directly possible experimentally.

The DC stark effect of terrylene was first studied in polyethylene, which yielded various signs and values due to different orientations inside the host [35]. Terrylene in p-terphenyl has shown linear, quadratic [181] as well as anomalous Stark shifts- sometimes inverted relation between polarizabilities of the ground and excited state [36]. Authors have explained this anomaly through a supermolecule model. In this model, the first shell of the host molecules has to be taken into consideration altogether with each guest molecule. The authors suggest possible mechanism of host central phenyl ring flip and guest naphthalene unit tilt creating asymmetric π-conjugation. Moreover, the authors warn, I quote: ''any mechanical force exerted (…) annihilates normal terrylene insertion'', which is somehow in contradiction to the studies cited in Appendix B.c. of this manuscript.

The same measurements were performed on T/pT system in SNOM configuration to study shifts and linewidth changes as a function of tip voltage. Since linewidth changes are reversible and tuned by voltage, authors attributed it to the electric-field effect (no mechanical influence from the tip)[123].

To sum up, studies of the electric field effect have proven that the shell of the nearest neighbors varies between T/pT sites. Suggestions were made that those shells may affect the geometry of T and even lower π-conjugation. Change in π-conjugation would manifest itself directly through the HOMO-LUMO bandgap and directly affect the transition moment related to the S0-S1 transition. This leads to the hypothesis that fluorescence spectrum, σ_{12} and k_{23} may be somewhat correlated.

e. Zeeman effect

Under a magnetic field, terrylene S0-S1 transition in n-hexadecane Shpol'skii matrix has shown redshift quadratic in magnetic field up to 8 MHz/T^2 [182]. Authors have expected blueshift due to ring currents in the π-system (diamagnetic effect of aromatic compounds). Instead, a major contribution of van Vleck's paramagnetism was found but couldn't be explained quantitatively. Qualitatively redshift instead of blueshift indicates that the ground state has a larger extension of the π-conjugation than the first excited state (typically opposite situation). On the other hand, this explanation seems somewhat inconsistent with the suggested distorted geometry in S0 that reduces π-conjugation according to the previously discussed vibronic study (Section 1.2.2). I have found no studies that would investigate the effect of Zeeman splitting triplet level population dynamics in T.

C. Model B)

In this paragraph, I proceed with the derivation of rates in model B). Solutions are well-known in the literature [20,160], and scientific community commonly takes advantage of slow ISC approximation [32,158,162–164].

First, for each level *L*, the probability of occupation has to be described at time *t*:

$$L_X(t) = L_X(0) * e^{-kt} \qquad \text{C.1}$$

Where parameter *k* reflects the rate at which the process occurs. For a model B) in Figure 1-14, a set of differential equations is used to describe the change of occupation in time:

$$\frac{d}{dt}L1(t) = -k_{12} * L1(t) + k_{21} * L2(t) + k_{31} * L3(t) \qquad \text{C.2}$$

$$\frac{d}{dt}L2(t) = k12 * L1(t) - (k_{21} + k_{23}) * L2(t) \qquad \text{C.3}$$

$$\frac{d}{dt}L3(t) = k_{23} * L2(t) - k_{31} * L3(t) \quad \text{C.4}$$

those yield 3 eigen values:

$$\lambda_1 = 0,\ \lambda_{2/3} = \frac{-P \pm \sqrt{P^2 - 4Q}}{2} \quad \text{C.5}$$

Where *P* and *Q* are defined as:

$$P = k_{12} + k_{21} + k_{23} + k_{31};\ Q = k_{31}(k_{12} + k_{21}) + k_{23} * (k_{12} + k_{31}) \quad \text{C.6}$$

As signal is made of photon detection events, its autocorrelation correspond directly to the level *L2* that emits and is written as:

$$g^2(\tau) = \frac{L2(\tau)}{L2(\tau = \infty)} \quad \text{C.7}$$

$$g^2(\tau) = 1 - (1 + A)\exp(\lambda_2\tau) + Aexp(\lambda_3\tau) \quad \text{C.8}$$

Where parameter *A* is defined as:

$$A = \frac{\lambda_2(k_T + k_{32} + \lambda_3)}{(k_T + k_{32})(\lambda_3 - \lambda_2)} \quad \text{C.9}$$

Photon flux *F* is then calculated as:

$$F = \frac{k_{12}k_R k_{31}}{\lambda_2\lambda_3} \quad \text{C.10}$$

Where k^R is a radiative part of the *L2-L1* deexcitation rate.

To sum up, autocorrelation of the model B) yields 2 monoexponential components - λ_2 and λ_3, which correspond to the antibunching and bunching regimes.

In the case of T/pT, slow intersystem crossing approximation is commonly used (k_{12} and k_{21} are much larger than k_{31} and k_{23}) [162]. Equations C.5 and C.9 simplify to:

$$\lambda_2 = -(k_{12} + k_{21}) \quad \text{C.11}$$

$$\lambda_3 = -(k_{31} + \frac{k_{12}\, k_{23}}{\lambda_2}) \quad \text{C.12}$$

$$A = \frac{k_{12}k_{23}}{-k_{31}\lambda_2} \quad \text{C.13}$$

$$F = \left(\frac{1}{k_{21}} + \frac{1}{k_{12}}\right)^{-1} \left(\frac{1}{1+A}\right) \frac{k_R}{k_{21}} \quad \text{C.14}$$

Note that rate k_{31} can be directly calculated from bunching part by plugging Equation C.12 into C.13 that yields:

$$k_{31} = \frac{-\lambda_3}{1+A} \quad \text{C.15}$$

D. Population method

In this Section, I will proceed with derivations to introduce the population method for calculating photon statistics of a single emitter. Developing this method is necessary in order to simulate photon flux coming from a theoretical emitter (model with a particular set of rates) through Monte Carlo simulation.

I assume that the system is observed during a time much longer than the inverse of the slowest rate and therefore takes advantage of the law of large numbers (LLN).

Observation time becomes a very large number of multiple realizations of the different cycles in the mathematical model. Every cycle starts with L1 excitation and ends up with deexcitation back to L1. Characteristic cycle C is defined as a cycle made of subsequent transitions which makes an individual pathway – e. g. 2-level model (Figure 1-14A.) has only 1 characteristic cycle *L1-L2*. Therefore the number of excitations during observation time is equal to N_{TOT} and, in the case of the 2-level model, is made of *L1-L2* repetitions only.

In general case, N_{TOT} is a sum of repetitions of each characteristic cycle CM.

$$N_{TOT} = \sum_{0}^{M} N_{CM} \qquad \text{D.1}$$

Each characteristic cycle has its average duration time $t_{AVG}(CM)$ and probability of occurrence *P[CM]* (both depend on the pathway). The sum of their products (realization probability weighted average) gives the average time per cycle:

$$t_{AVG} = \sum_{0}^{M} t_{AVG}(CM) * P[CM] \qquad \text{D.2}$$

I can calculate number of cycles that have taken place during observation time t_{ACQ}:

$$N_{TOT} = \frac{t_{ACQ}}{t_{AVG}} \qquad \text{D.3}$$

In the next 2 Subsection, I will identify characteristic cycles and their probability for models B) and C) to compare the two models.

a. Model B)

I can distinguish 2 characteristic cycles (Figure 4-2A.) and their average times. Slow ISC approximation is applied when sign $'\cong'$ is used instead of $'='$. Average time $t_{AVG}(LX - LY)$ indicates time spent in a level X prior to transitioning to the level Y:

$$cycle\ of\ type\ 1\colon (L1 - L2 -)\ as\ C1$$

$$t_{AVG}(C1) = t_{AVG}(L1 - L2) + t_{AVG}(L2 - L1) = \frac{1}{k_{12}} + \frac{1}{k_{21}} \quad \text{D.4}$$

$$cycle\ of\ type\ 2\colon (L1 - L2 - L3 -)\ as\ C2$$

$$t_{AVG}(C2) = t_{AVG}(L1 - L2) + t_{AVG}(L2 - L3) + t_{AVG}(L3 - L1) = \quad \text{D.5}$$

$$= \frac{1}{k_{12}} + \frac{1}{k_{21}} + \frac{1}{k_{31}} \cong \frac{1}{k_{31}}$$

The probability that each excitation ends up following a particular characteristic cycle is given as:

$$P[C1] = 1 - \eta_{k_{23}(-L2)} \quad \text{D.6}$$

$$P[C2] = \eta_{k_{23}(-L2)} \quad \text{D.7}$$

where $\eta_{k_{23}(-L2)}$ is the efficiency with which rate k_{23} depopulates level L2. The number of each characteristic cycle's repetitions that takes place during observation time, which is also a number of emission events and triplet state events, is given as:

$$N_{C1} = N_{TOT} * P[C1] \quad \text{D.8}$$

$$N_{C2} = N_{TOT} * P[C2] \quad \text{D.9}$$

I can define a contrast A, which is a ratio of time that is spent cycling in the two pathways:

$$A = \frac{N_{C1} * t_{AVG}(C1)}{N_{C2} * t_{AVG}(C2)} \cong \frac{k_{23}k_{12}}{k_{31}(k_{21} + k_{12})} \quad \text{D.10}$$

This result is coherent with the equations under slow ISC approximation presented in Appendix C.

Finally, average duration time of a cycle for the model B):

$$t_{AVG_{B)}} = \frac{1}{k_{12}} + \frac{1}{k_{21}} + \frac{\eta_{k_{23}(-L2)}}{k_{31}} \quad \text{D.11}$$

To sum up, model B) consists of 2 possible characteristic cycles and the ratio between time spent in each of them is given by Equation D.10. This formula is identical with Equation 1.33, which relates to the autocorrelation function amplitude. Within observation time t_{ACQ} there will be N_{C1} photon emission events and N_{C2}- triplet state events.

b. Model C)

Identification of characteristic cycles in model C) is tricky as the number of combinations is infinite due to reversed ISC process – molecule could get trapped in the ISC-rISC pathway on repeat. Let's define all the possible characteristic cycles and their average times:

$$M\ different\ cycles\ of\ Trap1\ type: (L1 - [L2 - L3 - L2]^M -)\ as\ C1_M$$

$$t_{AVG}(C1_M) = \frac{1}{k_{12}} + \left(\frac{M+1}{k_{21}}\right) + \left(\frac{M}{k_{32} + k_T}\right) \quad \text{D.12}$$

$$M\ different\ cycles\ of\ Trap2\ type: (L1 - [L2 - L3 - L2]^M - L3 -)\ as\ C2_M$$

$$t_{AVG}(C2_M) = \frac{1}{k_{12}} + \left(\frac{M+1}{k_{21}}\right) + \left(\frac{M+1}{k_{32} + kT}\right) \quad \text{D.13}$$

Note that *L3* is a double decay process, and thus it has an effective rate - sum of both decay rates. Model C) cycles of the 0th order are the same as *C1* and *C2* in model B). I define probability that each excitation ends up following a particular characteristic cycle that depends on $\eta_{k_{23}}^{-2}$ and $\eta_{k_T}^{-3}$:

$$P[C1_M] = \left[\eta_{k_{23}(-L2)} * \left(1 - \eta_{k_T(-L3)}\right)\right]^M * \left(1 - \eta_{k_{23}(-L2)}\right) \quad \text{D.14}$$

$$P[C2_M] = \left[\eta_{k_{23}(-L2)} * \left(1 - \eta_{k_T(-L3)}\right)\right]^M * \eta_{k_{23}(-L2)} * \eta_{k_T(-L3)} \quad \text{D.15}$$

To verify orders that are significant to the photon statistics, I assume rates of k_{12}=50MHz, k_{21}=50MHz, k_{23}=50kHz, k_T=3kHz, k_{32}=30kHz and plot the percentage of the total time that is spent circulating in each characteristic cycle in Figure D-1. The percentage of the total time of 3 characteristic cycles ($C1_0$, $C1_1$ and $C2_0$) sums up to 99,92%, so I deem other orders negligible.

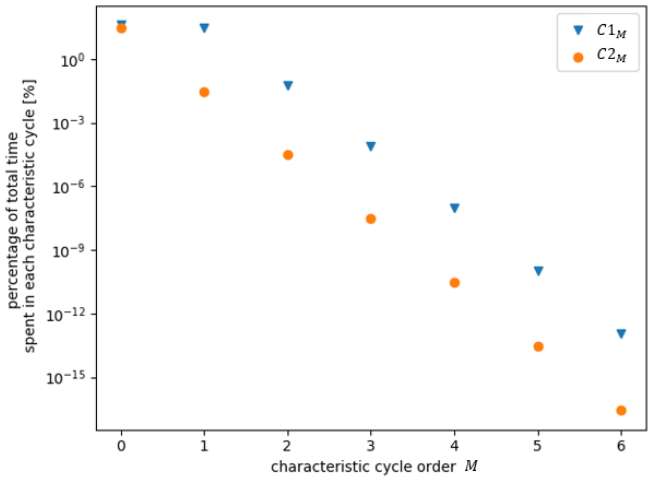

Figure D-1. The percentage of the total observation time that model having rates k_{12} =50 MHz, k_{21} =50 MHz, k_{23} =50 kHz, k_T =3 kHz, k_{32} =30 kHz would spend in each characteristic cycle up to the 6th order.

It is important to realize that the autocorrelation function looks at the delay between the photons. Cycles of type 1 with an order higher than 0 contribute to the photon bunching phenomenon ($1/k_{32} >> 1/k_{12} + 1/k_{21}$). Therefore contrast goes as:

$$A = \frac{\sum_0^M C2_M * t_{AVG}(C2_M) + \sum_1^M C1_M * t_{AVG}(C1_M)}{N_{C1^0} * t_{AVG}(C1^0)} \quad \text{D.16}$$

Finally, the average time per cycle in model C) goes as follows:

$$t_{AVG_{C)}} = \sum_0^N P[C1^N] * t_{AVG}(C1^N) + \sum_0^N P[C2^N] * t_{AVG}(C2^N) \quad \text{D.17}$$

With infinite characteristic cycles of model C) reduced to 3 dominant characteristic cycles, I recalculated parameters for each model to compare them qualitatively. I use the same rates as above and gather results in Table D-1. Both models yield the same number of photons and triplet states within 0,2% precision. There are 824 trapped states of type 1 2nd order cycle and nearly 1 million triplet states overall within 1 billion random realizations.

Table D-1. Parameters of models B) and C) calculated accordingly to the population method.

parameter	Model B)	Model C)
N_{C1_0} [10^8]	9,990	9,990
N_{C1_1} [10^5]	-	9,073
N_{C1_2}		824
N_{C2_0} [10^5]	9,990	0,908
N_{C2_1}	-	82
Total Photons [10^8]	9,990	9,999

parameter	Model B)	Model C)
Total Triplet states [10^5]	9,990	9,990
A	0,758	0,757

To conclude this part, I've introduced the population method to photon statistics of a single molecule. In the next Subsection, I will proceed with Monte Carlo simulations to verify if the autocorrelation of the simulated flux is consistent with solutions of the set of steady-state differential equations of population dynamics.

c. Monte Carlo simulations

In Monte Carlo simulations, every photon is treated as a random realization of a cycle. In this context, N emitted photons are simply N independent and random realizations (N cycles). Each cycle constitutes a series of realizations of random variables (transition rates). Every subsequent transition depends on the previous event – e.g. after k_{12} only k_{21} and k_{23} are possible. Therefore it can be considered a Markov process. It is more convenient to view the system as a Markov process diagram instead of 3-level visualization – Figure D-2.

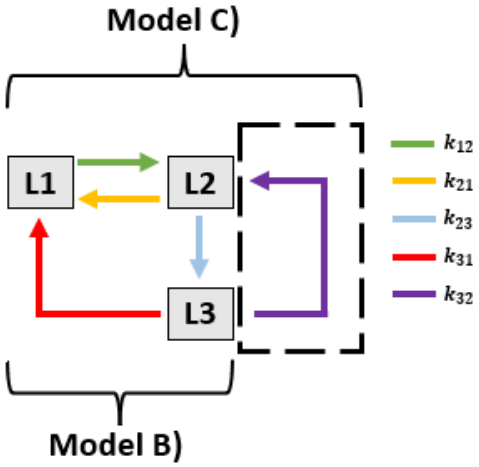

Figure D-2. Markov process diagram of the models B) and C) used for Monte Carlo simulations.

I can build my temporally-resolved photon flux cycle per cycle. Firstly, I have to draw a random variable from an equal probability distribution that defines, which characteristic cycle is being realized. Secondly, I draw random duration times from the exponential distributions for each transition that takes place in this characteristic cycle. Finally, I draw a random variable from an equal probability distribution that accounts for the limited photon collection C_{EFF}. To verify whether my simulation is correct, I calculate the correlation function of the simulated temporally-resolved flux of a model C) and overlay it with the theoretical correlation function for this model - Figure D-3

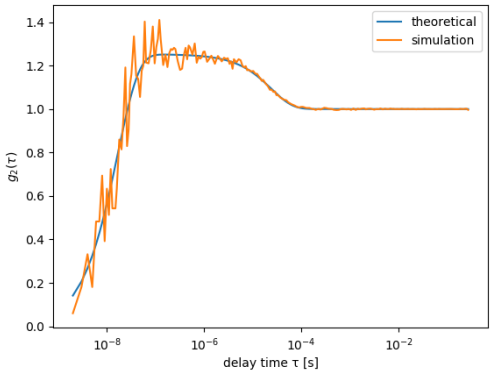

Figure D-3. Rate equation of autocorrelation function (blue line) of the model C) and calculated autocorrelation of the Monte-Carlo simulated flux (orange).

Once simulation is verified, it can be used for other purposes such as fitting the set-up C_{EFF} through detected Photon Pairs, which will be introduced in Chapter 2 of this manuscript.

E. Field distribution

Analytical calculations were done by Simon Vassant and compared with simulations of Ludovic Douillard to yield a perfect agreement – Figure E-1.

I follow derivations by Simon Vassant based on Axelrod [183], Hecht et al. [20] and Born et al. [184]). I present the analytical calculations necessary to obtain the electric field profile for the excitation in the experimental scheme (Section 2.1.5). The objective is to get the spatial dependence of the electric field in TE and TM polarization as a function of depth in pT film.

The system under study is a thin pT film of thickness h, on a glass substrate, and with air as the superstrate. The refractive indexes are respectively n_1=1.5717 for glass, n_2=1.8 for pT and, n_3=1 for air. The substrate plane is considered in the x-y plane, and z is the propagation direction. Light is incident from the glass side. Wavevector υ (to not confuse with a transition rate k) is defined as:

$$\upsilon_0 = \frac{2\pi}{\lambda} \qquad \text{E.1}$$

with λ = 532nm the incident wavelength. The plane wave is incident at an angle ψ_1 from the normal, so that:

$$\upsilon_x = n_1 k_0 \sin\psi_1 \qquad \text{E.2}$$

$\upsilon_x$is constant through the propagation. We can now calculate υ_z component in all the layers:

$$\upsilon_{zi} = \sqrt{\epsilon_i k_0^2 - k_x^2} \qquad \text{E.3}$$

with i ranging from 1 to 3, and $\epsilon_i = n_i^2$. The angle of refraction in subsequent layers is given by:

$$\psi_i = \arctan(\upsilon_x/\upsilon_{zi}) \qquad \text{E.4}$$

Fresnel coefficients at the different interfaces for the electric field by Hecht et al. [20]:

$$r_{ij}^{TM} = \frac{\epsilon_j \upsilon_{zi} - \epsilon_i \upsilon_{zj}}{\epsilon_j \upsilon_{zi} + \epsilon_i \upsilon_{zj}} \qquad \text{E.5}$$

$$t_{ij}^{TM} = \frac{2\epsilon_j v_{zi}}{\epsilon_j v_{zi} + \epsilon_i v_{zj}} \sqrt{\frac{\epsilon_i}{\epsilon_j}} \tag{E.6}$$

$$r_{ij}^{TE} = \frac{v_{zi} - v_{zj}}{v_{zi} + v_{zj}} \tag{E.7}$$

$$t_{ij}^{TE} = \frac{2v_{zi}}{v_{zi} + v_{zj}} \tag{E.8}$$

Overall reflection coefficients are given by Born et al. [184]:

$$r_{13}^{TM} = \frac{r_{12}^{TM} + r_{23}^{TM} \exp(2iv_{z2}h)}{1 + r_{12}^{TM} r_{23}^{TM} \exp(2iv_{z2}h)} \tag{E.9}$$

$$r_{13}^{TE} = \frac{r_{12}^{TE} + r_{23}^{TE} \exp(2iv_{z2}h)}{1 + r_{12}^{TE} r_{23}^{TE} \exp(2iv_{z2}h)} \tag{E.10}$$

The expression for the electric fields in medium 2 (pT) at depth d inside pT are given by Axelrod [183]:

$$E_{2x}(d, \psi_3) = \cos\psi_2 \frac{[t_{12}^{TM} \exp(iv_{z2}h) \exp(iv_{z2}d) - r_{23}^{TM} \exp(-iv_{z2}d)]}{1 - r_{23}^{TM} r_{21}^{TM} \exp(2iv_{z2}h)} \tag{E.11}$$

$$E_{2y}(d, \psi_3) = \frac{t_{12}^{TE} \exp(iv_{z2}h) \exp(iv_{z2}d) + r_{23}^{TM} \exp(-iv_{z2}d)}{1 - r_{23}^{TE} r_{21}^{TE} \exp(2iv_{z2}h)} \tag{E.12}$$

$$E_{2z}(d, \psi_3) = \sin\psi_2 \frac{[t_{12}^{TM} \exp(iv_{z2}h) \exp(iv_{z2}d) + r_{23}^{TM} \exp(-iv_{z2}d)]}{1 - r_{23}^{TM} r_{21}^{TM} \exp(2iv_{z2}h)} \tag{E.13}$$

The equations for the field in medium 1 (glass) and medium 3 (air) are given as in Axelrod.

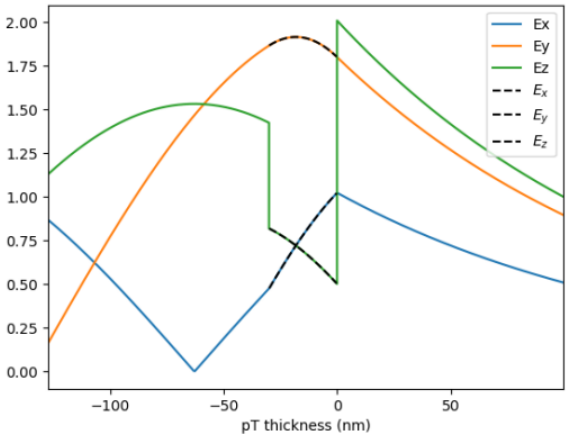

Figure E-1. Comparison of the electric field distribution between analytical solutions and simulation (dashed).The pT film is located bewteen -30nm and 0nm.

F. SPM stability

a. Drifts

There are 2 types of drifts present in AFM. Mechanical drift causes spatial misalignment in a manner that doesn't require an explanation. However, drift of the probe parameters is more complicated in its consequences.

To asses mechanical drift in XY direction (in-plane), light can be coupled into the pulled glass fiber and its drift can be observed on the microscope. This drift (few hours after mounting it on the setup) is not bigger than hundreds of nanometers per hour and after several days (without manipulations on the setup) can be hardly seen. It's important to note that nanoantenna-emitter experiments couldn't be carried out the same day that probe is mounted on the set-up. Also, once probe is mounted, one should perform as little manual manipulations on the set-up as required.

However, there is also a drift in Z-axis. To study the drift in Z-axis, I have left the tip scanning for 2h a single line of pT film on repeat, which is seen as high frequency modulation in probe's Z position in Figure F-1, left. The low frequency modulation in Z position is the Z-axis drift, which turns out to be sinusoidal with an amplitude of ~100 nm and period of ~45 min. Overall, this Z-drift is very large, but by leaving the tip scanning

pT on repeat, I have verified that this drift isn't problematic – tip never loses contact or never crashes into the sample; it is able to follow the drift.

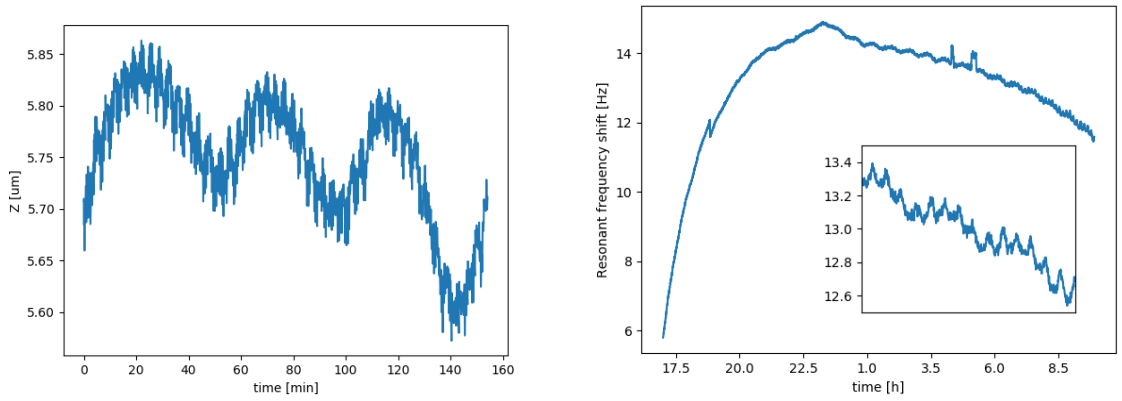

Figure F-1. Height profile of tip scanning on repeat sub-40 nm pT matrix – high-frequency component due to the matrix height variations, slow frequency due to the drift of TSD (left). Probe's f_{res} overnight in the retracted state; inset shows the zoomed range at night (right).

Finally, drift of the probe's parameters is more or less troubling. Recall that fixing Δf, fixes also TSD. The largest drift, and thus the most impactful, is observed for the resonant frequency of the probe – presented in Figure F-1, right. The evolution of the resonant frequency drift is very confusing - it has a large exponential component within first few hours post-mounting and then some high frequency modulated slow decay. As will be shown in Chapter 4, to not damage pT film mechanical, setpoint as small as possible should be applied (as little force exerted as possible). Let's assume a setpoint of Δf =1 Hz and look at the drift in Figure F-1, right. Within first 2h post-mounting, the probe drifts from 6 to 12 Hz. Depending on the direction of the frequency drift (towards lower or larger frequency), the tip would either lose contact with the surface or exert much higher force (-1 Hz from the initial f_{RES} is -13 Hz from f_{RES} +12Hz). Thus probe cannot be operated right after mounting and is always left to rest on the setup overnight prior to carrying out the experiments.

b. Radius of Curvature effect

It could be expected that the larger the tip (but still in nanoscale range), the easier it is to align the emitter and the nanoantenna. This view is true, but there are other factors, such

as regulation, that influence the alignment. Recall, that proper regulation requires near-zero error signal (Section 2.2.2) and so far I have used simplification that fixing Δf also fixed TSD, which is not entirely true. Fixing Δf fixes the average TSD, but instantaneous TSD depends on the closed loop regulation and its gains. Below, I evaluate how error signal influences this instantaneous TSD.

To investigate it, using the very same probe, I have measured the same area with a tip of RoC ~80 nm (Figure F-2) and ~200 nm (Figure F-3). RoC was determined with raster scan on a single molecule. Change of the RoC without changing the probe was achieved by performing controlled crush of the tip – tens of nm crash results in breaking of the long, thin, nonelastic pulled glass fiber at a certain height of the fiber (not at the apex). By doing so, fiber can be broken off, thus increasing the diameter. Initial tip (Figure F-2) has a gaussian-like shape in the counts profile, while the crashed tip has a more trapezoidal shape – the tip clearly broke not perpendicularly to the long axis of the fiber, because apex is not flat. Smaller tip result in ~2 fold increase of the counts, while broken tip results in nearly 3-fold enhancement of the counts. Main takeaway is that dielectric tip, which is 3-fold larger in diameter produces higher counts enhancement than the intial tip. This may seem counterintuitive, one could expect that the smaller the tip, the larger the enhancement. In fact, I consider this enhancement increase as a consequence of a broken tip shape and roughness. Rough tips produce various enhancements in the population study (its difficult to align a rough tip identically for each molecule) and thus results from rough tips are not presented in Chapter 4.

In Figure F-4, I show height image of pT (left) scanned with ~80 nm RoC up to half the image, then I perform the crash outside the scanned area, then I go back to the area and continue the scan. Phase of 0 deg is my setpoint, and any phase different than 0 deg is my error signal. This error signal image (phase image) is plotted in Figure F-4, center. The two profile lines are taken on the error signal image, where one profile corresponds to ~80 nm tip and ~200 nm broken tip, and plotted in Figure F-4, right. As phase is my error signal, I can treat it as noise and calculate its Root Mean Square, which relates to the power of this noise. The tip ~80 nm diameter has a RMS of 0,42°, while the broken tip ~200 nm has a RMS of 1,52°.

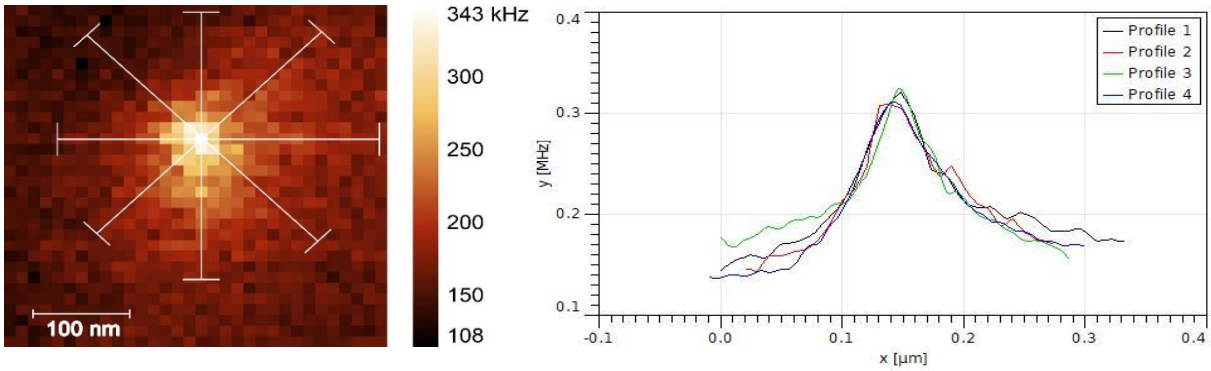

Figure F-2. Counts on the detector as the tip is scanned above a single T (left) and cross-sections yielding a ROC of 80 nm (right).

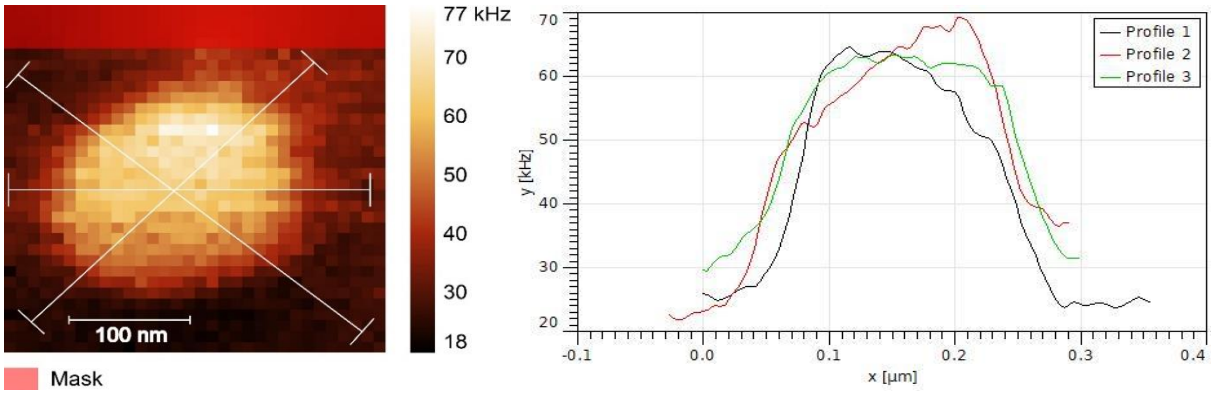

Figure F-3. Counts on the detector as tip after controlled crush is scanned above a single T (left) and radial cross-sections yielding a ROC of 200 nm (right).

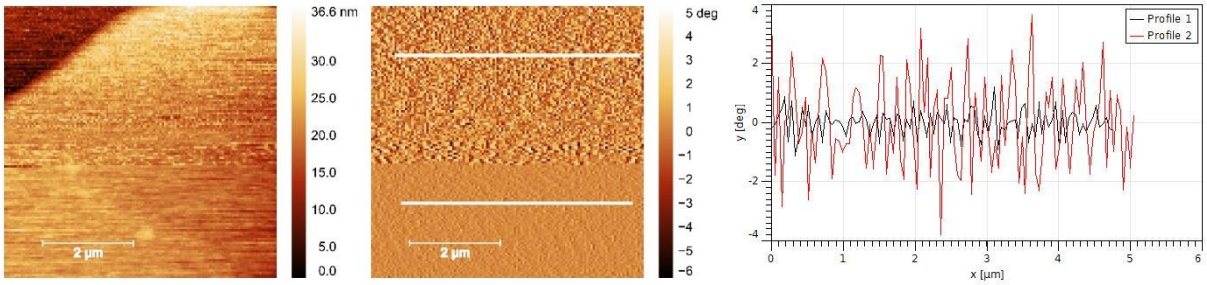

Figure F-4. Height image, phase image and cross-sections of the phase image taken before (Profile 1, black) and after (Profile 2, red) controlled crush, yielding RMS of 0,42° and 1,52°, respectively.

However, error signal, which gets multiplied by feedback loop parameters, nor parameters themselves doesn't really give an idea of what really happens with the Z position of the tip. Note that every error signal can be always made near-zero if feedback

loop parameters are very small. Therefore, to gain insight of into the real space fluctuation of the tip, I also calculated RMS of Z-command (voltage sent to regulate piezostage, which holds the tip). Z-command yields RMS of 200 μV and 500 μV for initial and broken tip, respectively. According to the piezostage calibration, the tips were regulated at ±0,30 nm and ±0,75 nm precision, which can be understood as the range instantaneous deviation around the average TSD. Recall studies reviewed in Section 1.3.6.1, (over 10 nm away from the surface) few nanometer changes in nanoantenna-emitter distance are required to significantly change the photon statistics. Thus I consider regulation smaller than ±1 nm as satisfactory.

To sum up, in this Section I discussed very briefly how diameter and shape of the pulled glass fiber tip affects the counts enhancement and how such rough tips may produce higher counts enhancement but also produce larger error signals. To draw conclusions (rather than observations) from the error signal, more elaborate discussion would be required – tip volume (and shape) results in the change of the tip's vdW potential. To give real meaning to the error signal considerations I calculate RMS of the voltage sent to regulate Z-position of the probe. It shows that the regulation stays within ±0,30 nm and ±0,75 nm (instantaneous deviation), around the average TSD given by a setpoint, for the initial and broken tip, respectively. Such regulation noise shouldn't be problematic for the emitter-nanoantenna experiments.

G. Global treatment

The sequential treatment presented above can be viewed as a somewhat of a serial approach to calculate the rates. A parallel approach to calculate the rates would be to perform a global fit, where the entire autocorrelation function (antibunching and bunching part together) obtained at each power is fitted simultaneously.

If we look at the fitting as the least square optimization (minimization of squared residuals), then each datapoint is treated with the same weight in theory, but its overall contribution to the fit results depends on the values – e.g. 10% mismatch with a datapoint of value 1 is less important (for the least square method) than 10% mismatch with a datapoint of value 100. However, from a perspective of the rates calculation, it is not obvious if the absolute residual or the relative residual is more appropriate. Secondly,

antibunching part has incident power-varying resolution (to compensate for PP increase and time constant decrease). This means that not only the bunching part and antibunching part may not have an equal number of datapoints but also the ratio of the datapoints changes with incident power. Thirdly, antibunching part has much higher noise than the bunching part and therefore raises concerns that maybe indeed one part should be treated with ''higher importance '' as it is less noisy (more reliable). All of the issues above, make it extremely difficult to define what is the correct way to extract the rates from the data.

As a comparison with the serial approach, I treat the very same molecule using the parallel approach. First, I treat in a parallel way – 145 autocorrelation curves with power assigned to them are fitted at once. First, I do this only for the bunching part of the autocorrelation, and thus calculate only the triplet dynamics (k_T, k_{32} and k_{23}). Then I repeat this with antibunching and bunching curve, because under slow ISC approximation, the antibunching part shouldn't affect k_T, k_{32} and k_{23}.

I start with global fit of the bunching part only. In Figure G-1, I present a global fit (upper left) and zoomed region (upper right) of the autocorrelation curve in the bunching regime (the same dataset as in sequential treatment). Rates recovered go as $k_{23} = 14{,}4\ kHz, \sigma_{32} = 10{,}4\ kHz, k_T = 2{,}0\ kHz$, which compared to the sequential treatment is respectively an increase by 14%, increase by 6% and decrease by 22%. Ideally, a global fitting should recover exactly the same rates as calculated with sequential treatment, but it's not the case. To understand where does this change come form, I plot the datapoints (each autocorrelation curve fitted separately) and overlay it with the global and sequential fit lines (Figure G-1, lower). The global fit (red line) clearly follows the upper edge of the dataset, while sequential fit (green line) goes through the middle of the dataset.

Sequential treatment reduces every cross-correlation curve to a data point, and thus a local minima of the residue is searched for the equally weighted time segments. Global fit searches for a local minima of the residues for ~20000 equally weighted data points.

As stated above, in the slow ISC approximation $k_{12}, k_{21} \gg k_{23}, k_{32}, k_T$ antibunching parameter can be simplified to $\lambda_2 = k_{12} + k_{21}$. In Figure G-2, I show the results of

antibunching and bunching global fit. Rates go as $\sigma_{12} = 23{,}9\frac{MHz}{mW}$, $k_{21} = 51{,}1\ MHz$, $k_{23} = 11{,}2\ kHz$, $\sigma_{32} = 8{,}8\frac{kHz}{mW}$ and k_T=4,9 kHz. There are 2 reasons why global fit can be readily recognized as wrong. First, global fit value of $k_T \sim 5\ kHz$ (being a triplet depopulation at zero incident power) is actually larger than the $\lambda_3/(1+A) = k_T + k_{32}$ measured in the low incident power regime (P<0,3mW). Secondly, under slow ISC approximation, introducing the antibunching part into the dataset, shouldn't affect the triplet depopulation significantly. The curve_fit python package may not be optimal for such long arrays of nonlinear shape and multiparameter fits.

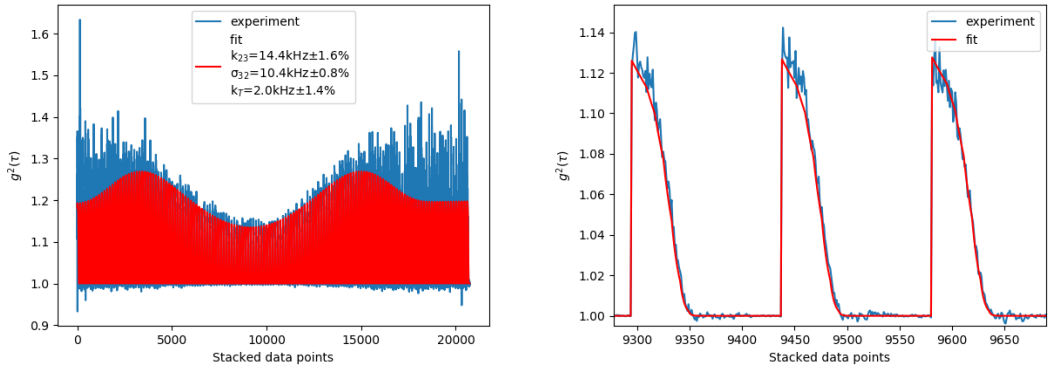

Figure G-1. Global fit of the bunching part – one array made of 145 cross-correlation at different incident power (left) and zoomed-in region (right).

To conclude, global fit and sequential fit method are not mathematically equivalent as one optimizes the residues for the ~20000 datapoint array made of 145 correlation curves, while the other proceeds in two steps. In the first step, fit searches for the residuals minima for each correlation curve separately. In the second step, the rates are fitted by searching the residue minima in equally weighted fit parameters obtained in the first step. This Subsection was included to show the reader that even with the same equations and dataset, the calculated rates may vary depending on the data processing approach. I have not found any reports that would discuss optimal data processing methods for such type of data. Due to the lack of such guidelines, I have taken a decision to treat anti- and bunching part separately (valid under slow ISC approximation) and proceed with the sequential approach.

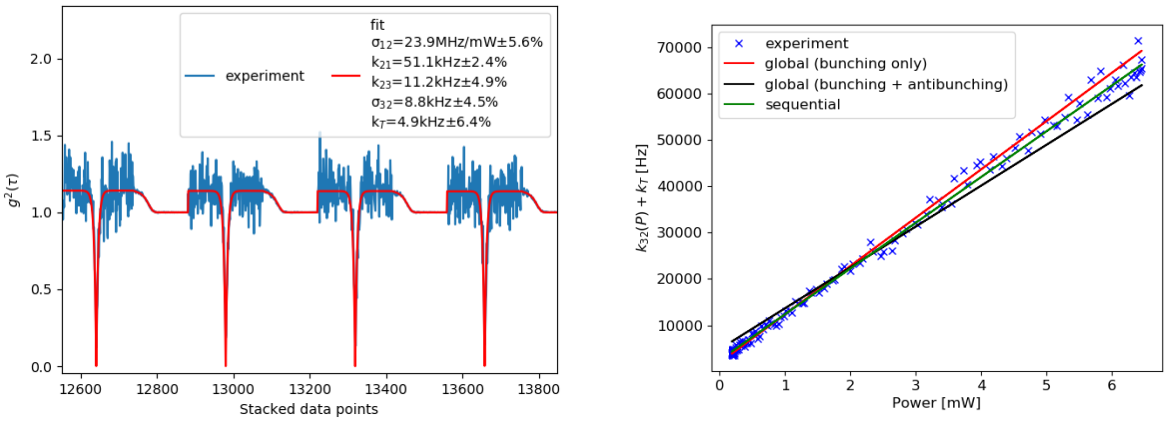

Figure G-2. Zoomed-in region of the stacked antibunching and bunching global fit (upper). The comparison of the global using bunching part only (red line) or antibunching and bunching part (black line) and sequential fit (green line) with the experimental data (blue crosses).

H. Height, photostability and temporal behavior

The spin coated sample of T/pT evolves with time even in the dark. This can be observed under the microscope in a matter of hours (the in-plane dimension of the film shrink and the film height increases) and in a matter of days by naked eye (pattern and transparency of the spin coated film changes). Such a behavior raises the concerns whether the environment of the inserted T molecules changes with post spin-coating time. To verify whether film shrinking affects the rates, height of the film and post spin-coating time were assigned to each molecule.

In Figure H-1, I present the results for k_{21}. Figures are separated into several columns as each column represents another pT area that was measured. The time indicated in the graphs reflects the time that has elapsed since spin coating. The height measured with the AFM was found to be in the 20-30 nm range. I indicate below the height and the ratio of the number of T molecules that were photostable enough to treat the data to all the T found within a given area (column). This also means that areas investigated in each column were not exposed to irradiation, when carrying out experiments on the molecules

belonging to other columns. Lastly, I indicate the density of molecule per area in $1/\mu m^2$ (also the unstable once); areas of 100-200 μm^2 were investigated.

Firstly, there is no clear trend in the values of k_{21} as a function of post-spin coating time nor in the thickness, and the same applies to the other rates (not shown). This suggests that 1) although pT changes with time, the rates don't change (up to a few days) 2) within the range of 20-30 nm, rates take similar values regardless of the thickness. There is one exception from the statement above – in the samples 72h+ post-spin coating, besides T with k_{21} around the average value, there are T with much higher k_{21}. Interestingly enough, T with a high k_{21} exhibit low $C_{EFF}\, k_R/k_{21}$ as estimated by matching the experimental counts. Thus the increase in k_{21} must be non-radiative.

Secondly, for readers experienced with the single molecules, it is not a surprise that not every emitter found can be measured (single molecules photobleach). However, I have decided to disregard from the dataset also the molecules that simply fluctuate, that is exhibit jumps or drifts in the counts. The motivation behind it is that if the rates change with time, I cannot expect to recover consistent sets of values by fitting the curves presented in the step-by-step data treatment. Fractions given in the columns show that there is no preference for photostability with time nor thickness. Overall, around 29% of the measured molecules are considered photostable after investigating the time traces.

Lastly, the number of T per μm^2 is given and shows no clear dependence on the time nor thickness.

To conclude, the rates show no clear dependence on the time nor thickness other than some low $\frac{k_R}{k_{21}}$ species that coexist with the typical species in the samples older than 72h. Regardless, even the low $\frac{k_R}{k_{21}}$ have other rates within the population statistics.

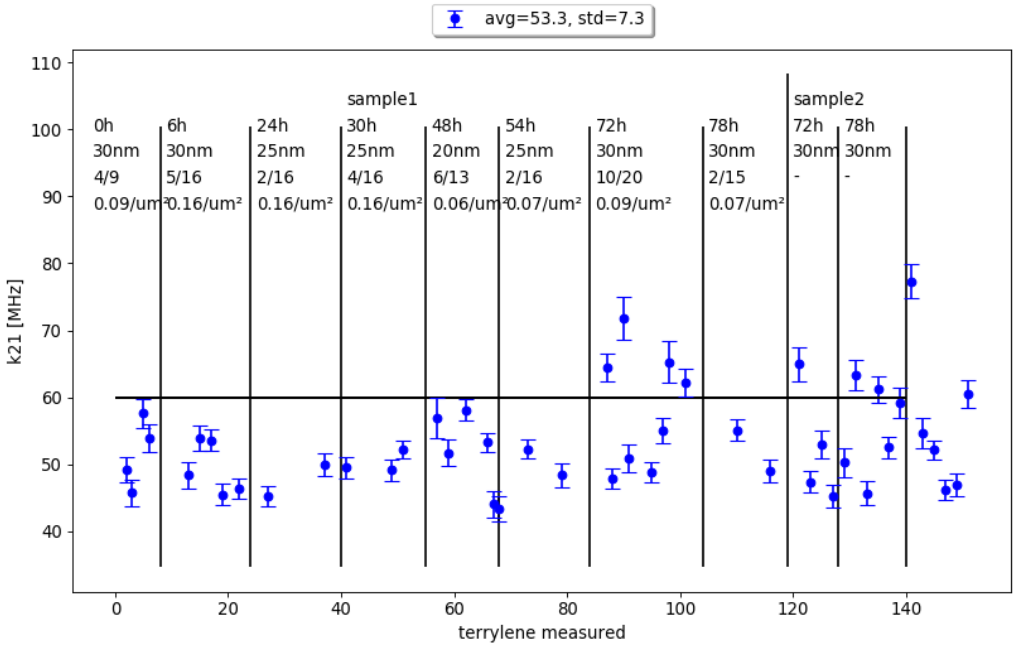

Figure H-1. S1-S0 relaxation rate k_{21} of T/pT measured with different post-spin coating times and areas of various thickness. X axis represents all of the measured emitters, while fraction given in each columns indicated how many emitters were photostable. Density of number of emitters per area is given with a unit of μm^{-2}. Photostable emitters are treated and plotted with error bars being the uncertainty of the fit.

I. Gold pyramid nanofabrication

The nanofabrication of the gold pyramids was based on Johnsons et al [176] and developed during the stage of Lola Chamot in our laboratory and under the supervision of Simon Vassant [185].

Briefly, 30 nm of Al is evaporated onto a Si substrate with 800 nm SiN_x layer. Photoresist AZ5214 is spin-coated, exposed to (positive) UV photolithography with the mask. The photoresist and Al are developed in MF319 for 60 s. Leftover photoresist is then removed with acetone, leaving Al with the mask pattern on top of the $SiSiN$ substrate. Subsequently, Reactive Ion Etching (O_2/SF_6) is used to etch SiN_x. Wet etching with KOH is used to as anisotropic etching of $Si(110)$. Then, 200 nm gold is evaporated and finally upon HF bath SiN_x is removed, which leaves only gold pyramids inside the Si holes.

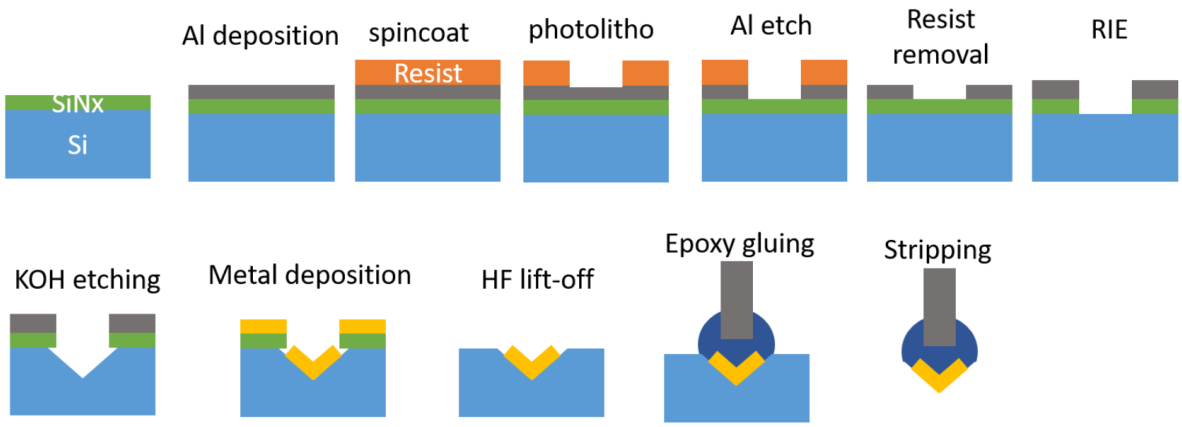

Figure I-1. Scheme of the fabrication protocol [185].

List of Acronyms

Abs	Absorption
AFM	Atomic Force Microscopy
avg	Average
CDF	Cumulative Distribution Function
C_{EFF}	Collection Efficiency
EGL	Energy Gap Law
ESSC	Electron Spin-Spin Coupling
FCF	Franck-Condon Factors
FCS	Fluorescence Correlation Spectroscopy
Fluo	Fluorescence
FWHM	Full Width Half Maximum
HFI	Hyperfine Interaction
HOMO	Highest Occupied Molecular Orbital

IC	Internal Conversion
ISC (rISC)	Intersystem Crossing (reversed Intersystem Crossing)
k_{XY}	Transition rate from level X to level Y
LA	Long axis of terrylene
LDOS	Local Density Of States
LUMO	Lowest Occupied Molecular Orbital
LT	Low Temperature
NP (AuNP)	nanoparticle (gold nanoparticle)
PF	Purcell Factor
Ph	Phosphorescence
PP	PhotonPair
PPF	Photon Pair Fraction
PSF	Point Spread Function
pT	para-terphenyl
QY	Quantum Yield
RT	Room Temperature
SA	Short axis of terrylene
SX	Singlet state level X
SOC	Spin-Orbit Coupling
SPM	Scanning Probe Microscopy
std	Standard Deviation

T(/pT)	Terrylene (in para-terphenyl)
TX	Triplet state level X
TIRF	Total Internal Reflection Fluorescence
TSD	Tip-Sample Distance
VR	Vibrational Relaxation
δ	relative uncertainty expressed as $\frac{\Delta x}{x}$
Δ	uncertainty expressed in a unit of the variable
Δf	frequency shift
λ	wavelength
$\sigma_{XY}/\sigma_{XY}^{(CS)}$	absorption coefficient between levels X and Y [Hz/mW]/ cross-section of the transition between levels X and Y [cm^2]
θ	radial angle in spherical coordinates
φ	azimuthal angle in spherical coordinates

List of Figures

List of Tables

References

(1) Nemova, G. *Field Guide to Light-Matter Interaction*; 2022. https://doi.org/10.1117/3.2611513.

(2) Zhang, J. M.; Liu, Y. Fermi's Golden Rule: Its Derivation and Breakdown by an Ideal Model. *Eur J Phys* **2016**, *37* (6). https://doi.org/10.1088/0143-0807/37/6/065406.

(3) Toninelli, C.; Gerhardt, I.; Clark, A. S.; Reserbat-Plantey, A.; Götzinger, S.; Ristanović, Z.; Colautti, M.; Lombardi, P.; Major, K. D.; Deperasińska, I.; Pernice, W. H.; Koppens, F. H. L.; Kozankiewicz, B.; Gourdon, A.; Sandoghdar, V.; Orrit, M. Single Organic Molecules for Photonic Quantum Technologies. *Nature Materials*. 2021. https://doi.org/10.1038/s41563-021-00987-4.

(4) Bharadwaj, P.; Deutsch, B.; Novotny, L. Optical Antennas. *Adv Opt Photonics* **2009**, *1* (3). https://doi.org/10.1364/aop.1.000438.

(5) Mulliken, R. S. Spectroscopy, Molecular Orbitals, and Chemical Bonding. *Science (1979)* **1967**, *157* (3784). https://doi.org/10.1126/science.157.3784.13.

(6) Loudon, R.; von Foerster, T. The Quantum Theory of Light. *Am J Phys* **1974**, *42* (11). https://doi.org/10.1119/1.1987930.

(7) Kimber, P.; Plasser, F. Energy Component Analysis for Electronically Excited States of Molecules: Why the Lowest Excited State Is Not Always the HOMO/LUMO Transition. *J Chem Theory Comput* **2023**, *19* (8), 2340–2352. https://doi.org/10.1021/acs.jctc.3c00125.

(8) *https://www.edinst.com/us/blog/jablonski-diagram-2/*. [2023/05/23].

(9) Struve, WalterS.; Mills, I. Fundamentals of Molecular Spectroscopy. *Vib Spectrosc* **1990**, *1* (1). https://doi.org/10.1016/0924-2031(90)80014-u.

(10) The Effect of Environment on Singlet-Triplet Transitions of Organic Molecules. *Proc R Soc Lond A Math Phys Sci* **1960**, *255* (1280). https://doi.org/10.1098/rspa.1960.0049.

(11) Del Valle, J. C.; Catalán, J. Kasha's Rule: A Reappraisal. *Physical Chemistry Chemical Physics* **2019**, *21* (19). https://doi.org/10.1039/c9cp00739c.

(12) Avlasevich, Y.; Kohl, C.; Müllen, K. Facile Synthesis of Terrylene and Its Isomer Benzoindenoperylene. *J Mater Chem* **2006**, *16* (11). https://doi.org/10.1039/b516264e.

(13) Balzani, Vincenzo, Ceroni, Paola, Juris, A. *Photochemistry and Photophysics*; Wiley-VCH, Weinheim, 2014.

(14) Marian, C. M. Understanding and Controlling Intersystem Crossing in Molecules. *Annual Review of Physical Chemistry*. 2020. https://doi.org/10.1146/annurev-physchem-061020-053433.

(15) Fedorov, D. G.; Koseki, S.; Schmidt, M. W.; Gordon, M. S. Spin-Orbit Coupling in Molecules: Chemistry beyond the Adiabatic Approximation. *International Reviews in Physical Chemistry*. 2003. https://doi.org/10.1080/0144235032000101743.

(16) Bissesar, S.; van Raamsdonk, D. M. E.; Gibbons, D. J.; Williams, R. M. Spin Orbit Coupling in Orthogonal Charge Transfer States: (TD-)DFT of Pyrene—Dimethylaniline. *Molecules* **2022**, *27* (3). https://doi.org/10.3390/molecules27030891.

(17) Lawetz, V.; Orlandi, G.; Siebrand, W. Theory of Intersystem Crossing in Aromatic Hydrocarbons. *J Chem Phys* **1972**, *56* (8). https://doi.org/10.1063/1.1677816.

(18) El-Sayed, M. A. Spin-Orbit Coupling and the Radiationless Processes in Nitrogen Heterocyclics. *J Chem Phys* **1963**, *38* (12). https://doi.org/10.1063/1.1733610.

(19) Kandrashkin, Y. E. Hyperfine Interaction Promoted Intersystem Crossing. *Appl Magn Reson* **2019**, *50* (9). https://doi.org/10.1007/s00723-019-01131-x.

(20) Novotny, L.; Hecht, B. *Principles of Nano-Optics*; 2006; Vol. 9780521832. https://doi.org/10.1017/CBO9780511813535.

(21) Griffiths, D. J.; Schroeter, D. F. *Introduction to Quantum Mechanics*; 2018. https://doi.org/10.1017/9781316995433.

(22) Moerner, W. E.; Kador, L. Optical Detection and Spectroscopy of Single Molecules in a Solid. *Phys Rev Lett* **1989**, *62* (21). https://doi.org/10.1103/PhysRevLett.62.2535.

(23) Ambrose, W. P.; Basché, T.; Moerner, W. E. Detection and Spectroscopy of Single Pentacene Molecules in a P-Terphenyl Crystal by Means of Fluorescence Excitation. *J Chem Phys* **1991**, *95* (10). https://doi.org/10.1063/1.461392.

(24) Tchénio, P.; Myers, A. B.; Moerner, W. E. Vibrational Analysis of the Dispersed Fluorescence from Single Molecules of Terrylene in Polyethylene. *Chem Phys Lett* **1993**, *213* (3–4). https://doi.org/10.1016/0009-2614(93)85140-J.

(25) Werley, C. A.; Moerner, W. E. Single-Molecule Nanoprobes Explore Defects in Spin-Grown Crystal. *Journal of Physical Chemistry B* **2006**, *110* (38), 18939–18944. https://doi.org/10.1021/jp057570b.

(26) Kummer, S.; Basché, T.; Bräuchle, C. Terrylene in P-Terphenyl: A Novel Single Crystalline System for Single Molecule Spectroscopy at Low Temperatures. *Chem Phys Lett* **1994**, *229* (3), 309–316. https://doi.org/10.1016/0009-2614(94)01043-9.

(27) Basché, T.; Kummer, S.; Bräuchle, C. Direct Spectroscopic Observation of Quantum Jumps of a Single Molecule. *Nature*. 1995, pp 132–134. https://doi.org/10.1038/373132a0.

(28) Kummer, S.; Kulzer, F.; Kettner, R.; Basché, T.; Tietz, C.; Glowatz, C.; Kryschi, C. Absorption, Excitation, and Emission Spectroscopy of Terrylene in p-Terphenyl: Bulk Measurements and Single Molecule Studies. *Journal of Chemical Physics* **1997**, *107* (19), 7673–7684. https://doi.org/10.1063/1.475107.

(29) Kulzer, F.; Kummer, S.; Matzke, R.; Bräuchle, C.; Basché, T. Single-Molecule Optical Switching of Terrylene Inp-Terphenyl. *Nature* **1997**, *387* (6634), 688–691. https://doi.org/10.1038/42674.

(30) Kulzer, F.; Koberling, F.; Christ, T.; Mews, A.; Basché, T. Terrylene in P-Terphenyl: Single-Molecule Experiments at Room Temperature. *Chem Phys* **1999**, *247* (1), 23–34. https://doi.org/10.1016/S0301-0104(99)00100-7.

(31) Harms, G. S.; Irngartinger, T.; Reiss, D.; Renn, A.; Wild, U. P. Fluorescence Lifetimes of Terrylene in Solid Matrices. *Chem Phys Lett* **1999**, *313* (3–4), 533–538. https://doi.org/10.1016/S0009-2614(99)01061-1.

(32) Fleury, L.; Segura, J. M.; Zumofen, G.; Hecht, B.; Wild, U. P. Nonclassical Photon Statistics in Single-Molecule Fluorescence at Room Temperature. *Phys Rev Lett* **2000**, *84* (6), 1148–1151. https://doi.org/10.1103/PhysRevLett.84.1148.

(33) Hübner, C. G.; Renn, A.; Renge, I.; Wild, U. P. Direct Observation of the Triplet Lifetime Quenching of Single Dye Molecules by Molecular Oxygen. *Journal of Chemical Physics* **2001**, *115* (21). https://doi.org/10.1063/1.1421382.

(34) Fleury, L.; Sick, B.; Zumofen, G.; Hecht, B.; Wild, U. P. High Photo-Stability of Single Molecules in an Organic Crystal at Room Temperature Observed by Scanning Confocal Optical Microscopy. *Mol Phys* **1998**, *95* (6), 1333–1338. https://doi.org/10.1080/00268979809483263.

(35) Orrit, M.; Bernard, J.; Zumbusch, A.; Personov, R. I. Stark Effect on Single Molecules in a Polymer Matrix. *Chem Phys Lett* **1992**, *196* (6). https://doi.org/10.1016/0009-2614(92)86000-8.

(36) Bordat, P.; Orrit, M.; Brown, R.; Würger, A. The Anomalous Stark Effect of Single Terrylene Molecules in P-Terphenyl Crystals. *Chem Phys* **2000**, *258* (1), 63–72. https://doi.org/10.1016/S0301-0104(00)00173-7.

(37) Zondervan, R.; Kulzer, F.; Orlinskii, S. B.; Orrit, M. Photoblinking of Rhodamine 6G in Poly(Vinyl Alcohol): Radical Dark State Formed through the Triplet. *Journal of Physical Chemistry A* **2003**, *107* (35). https://doi.org/10.1021/jp034723r.

(38) Kol'chenko, M. A.; Kozankiewicz, B.; Nicolet, A.; Orrit, M. Intersystem Crossing Mechanisms and Single Molecule Fluorescence: Terrylene in Anthracene Crystals.

Optics and Spectroscopy (English translation of Optika i Spektroskopiya) **2005**, *98* (5). https://doi.org/10.1134/1.1929053.

(39) Nicolet, A.; Kol'chenko, M. A.; Kozankiewicz, B.; Orrit, M. Intermolecular Intersystem Crossing in Single-Molecule Spectroscopy: Terrylene in Anthracene Crystal. *Journal of Chemical Physics* **2006**, *124* (16). https://doi.org/10.1063/1.2184311.

(40) Sigl, A.; Orrit, M.; Reinot, T.; Jankowiak, R.; Friedrich, J. Terrylene in Hexadecane Revisited: A Hole Burning Study. *Journal of Chemical Physics* **2007**, *127* (8). https://doi.org/10.1063/1.2768960.

(41) Orrit, M. Chemical and Physical Aspects of Charge Transfer in the Fluorescence Intermittency of Single Molecules and Quantum Dots. *Photochemical and Photobiological Sciences*. 2010, pp 637–642. https://doi.org/10.1039/b9pp00192a.

(42) Navarro, P.; Tian, Y.; Van Stee, M.; Orrit, M. Stable Single-Molecule Lines of Terrylene in Polycrystalline Para-Dichlorobenzene at 1.5 K. *ChemPhysChem* **2014**, *15* (14). https://doi.org/10.1002/cphc.201402200.

(43) Kozankiewicz, B.; Orrit, M. Single-Molecule Photophysics, from Cryogenic to Ambient Conditions. *Chemical Society Reviews*. 2014, pp 1029–1043. https://doi.org/10.1039/c3cs60165j.

(44) Banasiewicz, M.; Wiacek, D.; Kozankiewicz, B. Structural Dynamics of 2,3-Dimethylnaphthalene Crystals Revealed by Fluorescence of Single Terrylene Molecules. *Chem Phys Lett* **2006**, *425* (1–3). https://doi.org/10.1016/j.cplett.2006.04.105.

(45) Banasiewicz, M.; Morawski, O.; Wiącek, D.; Kozankiewicz, B. Triplet Population and Depopulation Rates of Single Terrylene Molecules in P-Terphenyl Crystal. *Chem Phys Lett* **2005**, *414* (4–6), 374–377. https://doi.org/10.1016/j.cplett.2005.08.120.

(46) Banasiewicz, M.; Dresner, J.; Morawski, O.; Wiącek, D.; Kozankiewicz, B. Purely Electronic and Vibronic Fluorescence Excitation of Single Terrylene Molecules in a

Naphthalene Crystal. *Acta Phys Pol A* **2007**, *112* (SUPPL.). https://doi.org/10.12693/aphyspola.112.s-85.

(47) Wiacek, D.; Kozankiewicz, B. Non-Planar Distortion of Single Molecules Revealed by Vibronic Fluorescence Excitation: Terrylene in p-Terphenyl and Naphthalene Crystals. *Chem Phys Lett* **2008**, *462* (4–6). https://doi.org/10.1016/j.cplett.2008.08.002.

(48) Kociesza, R.; Luzina, E.; Wicek, D.; Dresner, J.; Kozankiewicz, B. Photo-Stability of Single Terrylene Molecules in 2,3-Dimethylnaphthalene Crystals. *Mol Phys* **2009**, *107* (18). https://doi.org/10.1080/00268970802603515.

(49) Deperasińska, I.; Karpiuk, E.; Banasiewicz, M.; Kozankiewicz, B. On the Photo-Stability of Single Molecules. Dibenzoterrylene in 2,3-Dimethylnaphthalene Crystals. *Chem Phys Lett* **2010**, *492* (1–3). https://doi.org/10.1016/j.cplett.2010.04.025.

(50) Kozankiewicz, B.; Deperasińska, I.; Karpiuk, E.; Banasiewicz, M.; Makarewicz, A. On Photo-Oxidation of Single Molecules. *Opt Mater (Amst)* **2011**, *33* (9). https://doi.org/10.1016/j.optmat.2011.02.023.

(51) Białkowska, M.; Makarewicz, A.; Banasiewicz, M.; Kozankiewicz, B. Spin-Lattice Relaxation and Intersystem Crossing in Single Molecules of Terrylene Embedded in a p-Terphenyl Crystal. *Chem Phys Lett* **2013**, *555*, 131–134. https://doi.org/10.1016/j.cplett.2012.11.001.

(52) Białkowska, M.; Deperasińska, I.; Makarewicz, A.; Kozankiewicz, B. Anomalous Doping of a Molecular Crystal Monitored with Confocal Fluorescence Microscopy: Terrylene in a p -Terphenyl Crystal. *Journal of Chemical Physics* **2017**, *147* (11). https://doi.org/10.1063/1.4989983.

(53) Halasinski, T. M.; Weisman, J. L.; Ruiterkamp, R.; Lee, T. J.; Salama, F.; Head-Gordon, M. Electronic Absorption Spectra of Neutral Perylene (C20H12), Terrylene (C30H16), and Quaterrylene (C40H20) and Their Positive and Negative Ions: Ne Matrix-Isolation Spectroscopy and Time-Dependent Density Functional Theory

Calculations. *Journal of Physical Chemistry A* **2003**, *107* (19). https://doi.org/10.1021/jp027394w.

(54) Sepioł, J.; Jasny, J.; Keller, J.; Wild, U. P. Single Molecules Observed by Immersion Mirror Objective. The Orientation of Terrylene Molecules via the Direction of Its Transition Dipole Moment. *Chem Phys Lett* **1997**, *273* (5–6), 444–448. https://doi.org/10.1016/S0009-2614(97)00622-2.

(55) Pfab, R. J.; Zimmermann, J.; Hettich, C.; Gerhardt, I.; Renn, A.; Sandoghdar, V. Aligned Terrylene Molecules in a Spin-Coated Ultrathin Crystalline Film of p-Terphenyl. *Chem Phys Lett* **2004**, *387* (4–6), 490–495. https://doi.org/10.1016/j.cplett.2004.02.040.

(56) Minami, T.; Ito, S.; Nakano, M. Theoretical Study of Singlet Fission in Oligorylenes. *Journal of Physical Chemistry Letters* **2012**, *3* (18). https://doi.org/10.1021/jz3011749.

(57) Greiner, J.; Sundholm, D. Calculation of Vibrationally Resolved Absorption and Fluorescence Spectra of the Rylenes. *Physical Chemistry Chemical Physics* **2020**, *22* (4). https://doi.org/10.1039/c9cp06089h.

(58) Meyer, Y. H.; Plaza, P.; Müllen, K. Ultrafast Spectroscopy of Soluble Terrylene and Quaterrylene. *Chem Phys Lett* **1997**, *264* (6), 643–648. https://doi.org/10.1016/S0009-2614(96)01386-3.

(59) Nonn, T.; Plakhotnik, T. Fluorescence Excitation Spectroscopy of Vibronic Transitions in Single Molecules. *Chem Phys Lett* **2001**, *336* (1–2). https://doi.org/10.1016/S0009-2614(01)00084-7.

(60) Białkowska, M.; Chaładaj, W.; Deperasińska, I.; Drzewiecka-Antonik, A.; Koziol, A. E.; Makarewicz, A.; Kozankiewicz, B. Single Molecules of Terrylene in Di-Substituted Naphthalenes Crystallizing in the Herringbone Pattern. *RSC Adv* **2017**, *7* (5). https://doi.org/10.1039/c6ra27167g.

(61) Chen, X. W.; Lee, K. G.; Eghlidi, H.; Götzinger, S.; Sandoghdar, V. Enhancing the Radiative Emission Rate of Single Molecules by a Plasmonic Nanoantenna Weakly

Coupled with a Dielectric Substrate. *Opt Express* **2015**, *23* (26). https://doi.org/10.1364/oe.23.032986.

(62) Buchler, B. C.; Kalkbrenner, T.; Hettich, C.; Sandoghdar, V. Measuring the Quantum Efficiency of the Optical Emission of Single Radiating Dipoles Using a Scanning Mirror. *Phys Rev Lett* **2005**, *95* (6). https://doi.org/10.1103/PhysRevLett.95.063003.

(63) Yüce, M. Y.; Kiraz, A. Single-Molecule Fluorescence of Terrylene Embedded in Anthracene Matrix: A Room Temperature Study. *Chem Phys Lett* **2012**, *547*, 47–51. https://doi.org/10.1016/j.cplett.2012.08.014.

(64) Treussart, F.; Clouqueur, A.; Grossman, C.; Roch, J.-F. Photon Antibunching in the Fluorescence of a Single Dye Molecule Embedded in a Thin Polymer Film. *Opt Lett* **2001**, *26* (19), 1504. https://doi.org/10.1364/ol.26.001504.

(65) Han, S.; Qin, C.; Song, Y.; Dong, S.; Lei, Y.; Wang, S.; Su, X.; Wei, A.; Li, X.; Zhang, G.; Chen, R.; Hu, J.; Xiao, L.; Jia, S. Photostable Fluorescent Molecules on Layered Hexagonal Boron Nitride: Ideal Single-Photon Sources at Room Temperature. *Journal of Chemical Physics* **2021**, *155* (24). https://doi.org/10.1063/5.0074706.

(66) Deperasińska, I.; Zehnacker, A.; Lahmani, F.; Borowicz, P.; Sepioł, J. Fluorescence Studies of Terrylene in a Supersonic Jet: Indication of a Dark Electronic State below the Allowed Transition. *Journal of Physical Chemistry A* **2007**, *111* (20). https://doi.org/10.1021/jp070337o.

(67) Kummer, S.; Mais, S.; Basché, T. Measurement of Optical Dephasing of a Single Terrylene Molecule with Nanosecond Time Resolution. *Journal of Physical Chemistry* **1995**, *99* (47). https://doi.org/10.1021/j100047a005.

(68) Vogel, M.; Gruber, A.; Wrachtrup, J.; Von Borczyskowski, C. Determination of Intersystem Crossing Parameters via Observation of Quantum Jumps on Single Molecules. *Journal of Physical Chemistry* **1995**, *99* (41), 14915–14917. https://doi.org/10.1021/j100041a003.

(69) Brouwer, A. C. J.; Groenen, E. J. J.; Schmidt, J. Detecting Magnetic Resonance through Quantum Jumps of Single Molecules. *Phys Rev Lett* **1998**, *80* (18), 3944–3947. https://doi.org/10.1103/PhysRevLett.80.3944.

(70) Lang, J.; Sloop, D. J.; Lin, T. S. Dynamics of P-Terphenyl Crystals at the Phase Transition Temperature: A Zero-Field EPR Study of the Photoexcited Triplet State of Pentacene in p-Terphenyl Crystals. *Journal of Physical Chemistry A* **2007**, *111* (22). https://doi.org/10.1021/jp070251v.

(71) Reilly, P. D.; Skinner, J. L. Spectral Diffusion of Individual Pentacene Molecules in P-Terphenyl Crystal: Stochastic Theoretical Model and Analysis of Experimental Data. *J Chem Phys* **1995**, *102* (4). https://doi.org/10.1063/1.468886.

(72) Backlund, M. P.; Lew, M. D.; Backer, A. S.; Sahl, S. J.; Moerner, W. E. The Role of Molecular Dipole Orientation in Single-Molecule Fluorescence Microscopy and Implications for Super-Resolution Imaging. *ChemPhysChem*. 2014. https://doi.org/10.1002/cphc.201300880.

(73) Fourkas, J. T. Rapid Determination of the Three-Dimensional Orientation of Single Molecules. *Opt Lett* **2001**, *26* (4). https://doi.org/10.1364/ol.26.000211.

(74) Kim, J.; Chacón, R.; Wang, Z.; Larquet, E.; Lahlil, K.; Leray, A.; Colas-des-Francs, G.; Kim, J.; Gacoin, T. Measuring 3D Orientation of Nanocrystals via Polarized Luminescence of Rare-Earth Dopants. *Nat Commun* **2021**, *12* (1). https://doi.org/10.1038/s41467-021-22158-4.

(75) Beausang, J. F.; Shroder, D. Y.; Nelson, P. C.; Goldman, Y. E. Tilting and Wobble of Myosin v by High-Speed Single-Molecule Polarized Fluorescence Microscopy. *Biophys J* **2013**, *104* (6). https://doi.org/10.1016/j.bpj.2013.01.057.

(76) Ward, I. M. Determination of Molecular Orientation by Spectroscopic Techniques; 1985. https://doi.org/10.1007/3-540-13779-3_18.

(77) Koziol, P.; Kosowska, K.; Liberda, D.; Borondics, F.; Wrobel, T. P. Super-Resolved 3D Mapping of Molecular Orientation Using Vibrational Techniques. *J Am Chem Soc* **2022**, *144* (31). https://doi.org/10.1021/jacs.2c05306.

(78) Starukhin, A.; Gorski, A.; Dobkowski, J. Temperature Dependence of Singlet Oxygen Generation by Different Photosensitizers. *EPJ Web Conf* **2019**, *220*. https://doi.org/10.1051/epjconf/201922001012.

(79) Schuster, J.; Cichos, F.; Von Borczyskowski, C. Influence of Self-Trapped States on the Fluorescence Intermittency of Single Molecules. *Appl Phys Lett* **2005**, *87* (5). https://doi.org/10.1063/1.2006217.

(80) Wustholz, K. L.; Bott, E. D.; Kahr, B.; Reid, P. J. Memory and Spectral Diffusion in Single-Molecule Emission. *Journal of Physical Chemistry C* **2008**, *112* (21). https://doi.org/10.1021/jp711687j.

(81) Valĺe, R. A. L.; Tomczak, N.; Vancso, G. J.; Kuipers, L.; Van Hulst, N. F. Fluorescence Lifetime Fluctuations of Single Molecules Probe Local Density Fluctuations in Disordered Media: A Bulk Approach. *Journal of Chemical Physics* **2005**, *122* (11). https://doi.org/10.1063/1.1861881.

(82) Vallée, R. A. L.; Tomczak, N.; Kuipers, L.; Vancso, G. J.; van Hulst, N. F. Single Molecule Lifetime Fluctuations Reveal Segmental Dynamics in Polymers. *Phys Rev Lett* **2003**, *91* (3). https://doi.org/10.1103/PhysRevLett.91.038301.

(83) Drexhage, K. H. Influence of a Dielectric Interface on Fluorescence Decay Time. *J Lumin* **1970**, *1–2* (C). https://doi.org/10.1016/0022-2313(70)90082-7.

(84) Dovzhenko, D. S.; Ryabchuk, S. V.; Rakovich, Y. P.; Nabiev, I. R. Light-Matter Interaction in the Strong Coupling Regime: Configurations, Conditions, and Applications. *Nanoscale*. 2018. https://doi.org/10.1039/c7nr06917k.

(85) Chikkaraddy, R.; De Nijs, B.; Benz, F.; Barrow, S. J.; Scherman, O. A.; Rosta, E.; Demetriadou, A.; Fox, P.; Hess, O.; Baumberg, J. J. Single-Molecule Strong Coupling at Room Temperature in Plasmonic Nanocavities. *Nature* **2016**, *535* (7610). https://doi.org/10.1038/nature17974.

(86) Krasnok, A. E.; Slobozhanyuk, A. P.; Simovski, C. R.; Tretyakov, S. A.; Poddubny, A. N.; Miroshnichenko, A. E.; Kivshar, Y. S.; Belov, P. A. An Antenna Model for the Purcell Effect. *Sci Rep* **2015**, *5*. https://doi.org/10.1038/srep12956.

(87) Vos, W. L.; Koenderink, A. F.; Nikolaev, I. S. Orientation-Dependent Spontaneous Emission Rates of a Two-Level Quantum Emitter in Any Nanophotonic Environment. *Phys Rev A* **2009**, *80* (5). https://doi.org/10.1103/PhysRevA.80.053802.

(88) Anger, P.; Bharadwaj, P.; Novotny, L. Enhancement and Quenching of Single-Molecule Fluorescence. *Phys Rev Lett* **2006**, *96* (11). https://doi.org/10.1103/PhysRevLett.96.113002.

(89) Taminiau, T. H.; Stefani, F. D.; van Hulst, N. F. Enhanced Directional Excitation and Emission of Single Emitters by a Nano-Optical Yagi-Uda Antenna. *Opt Express* **2008**, *16* (14). https://doi.org/10.1364/oe.16.016858.

(90) Bedingfield, K.; Demetriadou, A. On the Excitation and Radiative Decay Rates of Plasmonic Nanoantennas. *Nanophotonics* **2022**, *11* (10). https://doi.org/10.1515/nanoph-2022-0015.

(91) Frey, H. G.; Witt, S.; Felderer, K.; Guckenberger, R. High-Resolution Imaging of Single Fluorescent Molecules with the Optical near-Field of a Metal Tip. *Phys Rev Lett* **2004**, *93* (20). https://doi.org/10.1103/PhysRevLett.93.200801.

(92) Eghlidi, H.; Lee, K. G.; Chen, X. W.; Götzinger, S.; Sandoghdar, V. Resolution and Enhancement in Nanoantenna-Based Fluorescence Microscopy. *Nano Lett* **2009**, *9* (12). https://doi.org/10.1021/nl902183y.

(93) Saemisch, L.; Liebel, M.; Van Hulst, N. F.; Van Hulst, N. F. Control of Vibronic Transition Rates by Resonant Single-Molecule-Nanoantenna Coupling. *Nano Lett* **2020**, *20* (6). https://doi.org/10.1021/acs.nanolett.0c01381.

(94) Taminiau, T. H.; Stefani, F. D.; Segerink, F. B.; Van Hulst, N. F. Optical Antennas Direct Single-Molecule Emission. *Nat Photonics* **2008**, *2* (4). https://doi.org/10.1038/nphoton.2008.32.

(95) Singh, A.; Calbris, G.; Van Hulst, N. F. Vectorial Nanoscale Mapping of Optical Antenna Fields by Single Molecule Dipoles. *Nano Lett* **2014**, *14* (8). https://doi.org/10.1021/nl501819k.

(96) Lee, K.-G.; Eghlidi, H.; Chen, X.-W.; Renn, A.; Götzinger, S.; Sandoghdar, V. Spontaneous Emission Enhancement of a Single Molecule by a Double-Sphere Nanoantenna across an Interface. *Opt Express* **2012**, *20* (21). https://doi.org/10.1364/oe.20.023331.

(97) Gopinath, A.; Miyazono, E.; Faraon, A.; Rothemund, P. W. K. Engineering and Mapping Nanocavity Emission via Precision Placement of DNA Origami. *Nature* **2016**, *535* (7612). https://doi.org/10.1038/nature18287.

(98) Kongsuwan, N.; Demetriadou, A.; Chikkaraddy, R.; Benz, F.; Turek, V. A.; Keyser, U. F.; Baumberg, J. J.; Hess, O. Suppressed Quenching and Strong-Coupling of Purcell-Enhanced Single-Molecule Emission in Plasmonic Nanocavities. *ACS Photonics* **2018**, *5* (1). https://doi.org/10.1021/acsphotonics.7b00668.

(99) Punj, D.; Mivelle, M.; Moparthi, S. B.; Van Zanten, T. S.; Rigneault, H.; Van Hulst, N. F.; García-Parajó, M. F.; Wenger, J. A Plasmonic "antenna-in-Box" Platform for Enhanced Single-Molecule Analysis at Micromolar Concentrations. *Nat Nanotechnol* **2013**, *8* (7). https://doi.org/10.1038/nnano.2013.98.

(100) Schuck, P. J.; Fromm, D. P.; Sundaramurthy, A.; Kino, G. S.; Moerner, W. E. Improving the Mismatch between Light and Nanoscale Objects with Gold Bowtie Nanoantennas. *Phys Rev Lett* **2005**, *94* (1). https://doi.org/10.1103/PhysRevLett.94.017402.

(101) Mivelle, M.; Van Zanten, T. S.; Neumann, L.; Van Hulst, N. F.; Garcia-Parajo, M. F. Ultrabright Bowtie Nanoaperture Antenna Probes Studied by Single Molecule Fluorescence. *Nano Lett* **2012**, *12* (11). https://doi.org/10.1021/nl303440w.

(102) Maksymov, I. S.; Staude, I.; Miroshnichenko, A. E.; Kivshar, Y. S. Optical Yagi-Uda Nanoantennas. *Nanophotonics* **2012**, *1* (1). https://doi.org/10.1515/nanoph-2012-0005.

(103) Puchkova, A.; Vietz, C.; Pibiri, E.; Wünsch, B.; Sanz Paz, M.; Acuna, G. P.; Tinnefeld, P. DNA Origami Nanoantennas with over 5000-Fold Fluorescence Enhancement and Single-Molecule Detection at 25 Mm. *Nano Lett* **2015**, *15* (12). https://doi.org/10.1021/acs.nanolett.5b04045.

(104) Hasan, M. R.; Hellesø, O. G. Dielectric Optical Nanoantennas. *Nanotechnology*. 2021. https://doi.org/10.1088/1361-6528/abdceb.

(105) Rolly, B.; Bebey, B.; Bidault, S.; Stout, B.; Bonod, N. Promoting Magnetic Dipolar Transition in Trivalent Lanthanide Ions with Lossless Mie Resonances. *Phys Rev B Condens Matter Mater Phys* **2012**, *85* (24). https://doi.org/10.1103/PhysRevB.85.245432.

(106) Sanz-Paz, M.; Ernandes, C.; Esparza, J. U.; Burr, G. W.; Van Hulst, N. F.; Maitre, A.; Aigouy, L.; Gacoin, T.; Bonod, N.; Garcia-Parajo, M. F.; Bidault, S.; Mivelle, M. Enhancing Magnetic Light Emission with All-Dielectric Optical Nanoantennas. *Nano Lett* **2018**, *18* (6). https://doi.org/10.1021/acs.nanolett.8b00548.

(107) Kerker, M.; Wang, D. S.; Giles, C. L. ELECTROMAGNETIC SCATTERING BY MAGNETIC SPHERES. *J Opt Soc Am* **1983**, *73* (6). https://doi.org/10.1364/JOSA.73.000765.

(108) Palombo Blascetta, N.; Lombardi, P.; Toninelli, C.; Van Hulst, N. F. Cold and Hot Spots: From Inhibition to Enhancement by Nanoscale Phase Tuning of Optical Nanoantennas. *Nano Lett* **2020**, *20* (9). https://doi.org/10.1021/acs.nanolett.0c02607.

(109) Oldenburg, S. Light Scattering from Gold Nanoshells. **2000**.

(110) Grand, J.; Le Ru, E. C. Practical Implementation of Accurate Finite-Element Calculations for Electromagnetic Scattering by Nanoparticles. *Plasmonics* **2020**, *15* (1). https://doi.org/10.1007/s11468-019-01014-8.

(111) Evlyukhin, A. B.; Chichkov, B. N. Multipole Decompositions for Directional Light Scattering. *Phys Rev B* **2019**, *100* (12). https://doi.org/10.1103/PhysRevB.100.125415.

(112) McPeak, K. M.; Jayanti, S. V.; Kress, S. J. P.; Meyer, S.; Iotti, S.; Rossinelli, A.; Norris, D. J. Plasmonic Films Can Easily Be Better: Rules and Recipes. *ACS Photonics* **2015**, *2* (3). https://doi.org/10.1021/ph5004237.

(113) Kneipp, K.; Wang, Y.; Kneipp, H.; Perelman, L. T.; Itzkan, I.; Dasari, R. R.; Feld, M. S. Single Molecule Detection Using Surface-Enhanced Raman Scattering (SERS). *Phys Rev Lett* **1997**, *78* (9). https://doi.org/10.1103/PhysRevLett.78.1667.

(114) Kühn, S.; Håkanson, U.; Rogobete, L.; Sandoghdar, V. Enhancement of Single-Molecule Fluorescence Using a Gold Nanoparticle as an Optical Nanoantenna. *Phys Rev Lett* **2006**, *97* (1). https://doi.org/10.1103/PhysRevLett.97.017402.

(115) Muskens, O. L.; Giannini, V.; Sánchez-Gil, J. A.; Gómez Rivas, J. Strong Enhancement of the Radiative Decay Rate of Emitters by Single Plasmonic Nanoantennas. *Nano Lett* **2007**, *7* (9). https://doi.org/10.1021/nl0715847.

(116) Kinkhabwala, A.; Yu, Z.; Fan, S.; Avlasevich, Y.; Müllen, K.; Moerner, W. E. Large Single-Molecule Fluorescence Enhancements Produced by a Bowtie Nanoantenna. *Nat Photonics* **2009**, *3* (11), 654–657. https://doi.org/10.1038/nphoton.2009.187.

(117) Santhosh, K.; Bitton, O.; Chuntonov, L.; Haran, G. Vacuum Rabi Splitting in a Plasmonic Cavity at the Single Quantum Emitter Limit. *Nat Commun* **2016**, *7*. https://doi.org/10.1038/ncomms11823.

(118) Bitton, O.; Haran, G. Plasmonic Cavities and Individual Quantum Emitters in the Strong Coupling Limit. *Acc Chem Res* **2022**, *55* (12). https://doi.org/10.1021/acs.accounts.2c00028.

(119) Mertens, H.; Koenderink, A. F.; Polman, A. Plasmon-Enhanced Luminescence near Noble-Metal Nanospheres: Comparison of Exact Theory and an Improved Gersten and Nitzan Model. *Phys Rev B Condens Matter Mater Phys* **2007**, *76* (11). https://doi.org/10.1103/PhysRevB.76.115123.

(120) Wenger, J.; Gérard, D.; Dintinger, J.; Mahboub, O.; Bonod, N.; Popov, E.; Ebbesen, T. W.; Rigneault, H. Emission and Excitation Contributions to Enhanced Single Molecule Fluorescence by Gold Nanometric Apertures. *Opt Express* **2008**, *16* (5). https://doi.org/10.1364/oe.16.003008.

(121) Seelig, J.; Leslie, K.; Renn, A.; Kühn, S.; Jacobsen, V.; Van De Corput, M.; Wyman, C.; Sandoghdar, V. Nanoparticle-Induced Fluorescence Lifetime Modification as

Nanoscopic Ruler: Demonstration at the Single Molecule Level. *Nano Lett* **2007**, *7* (3). https://doi.org/10.1021/nl0627590.

(122) Kühn, S.; Mori, G.; Agio, M.; Sandoghdar, V. Modification of Single Molecule Fluorescence Close to a Nanostructure: Radiation Pattern, Spontaneous Emission and Quenching. *Mol Phys* **2008**, *106* (7). https://doi.org/10.1080/00268970802002510.

(123) Gerhardt, I.; Wrigge, G.; Sandoghdar, V. Control and Imaging of Single-Molecule Spectral Dynamics Using a Nano-Electrode. *Mol Phys* **2009**, *107* (18), 1975–1979. https://doi.org/10.1080/00268970903188358.

(124) Lee, K. G.; Chen, X. W.; Eghlidi, H.; Kukura, P.; Lettow, R.; Renn, A.; Sandoghdar, V.; Götzinger, S. A Planar Dielectric Antenna for Directional Single-Photon Emission and near-Unity Collection Efficiency. *Nature Photonics*. 2011. https://doi.org/10.1038/nphoton.2010.312.

(125) Chen, X.-W.; Götzinger, S.; Sandoghdar, V. 99% Efficiency in Collecting Photons from a Single Emitter. *Opt Lett* **2011**, *36* (18). https://doi.org/10.1364/ol.36.003545.

(126) Bharadwaj, P.; Novotny, L. Plasmon-Enhanced Photoemission from a Single Y3N@C80 Fullerene. *Journal of Physical Chemistry C* **2010**, *114* (16). https://doi.org/10.1021/jp911226p.

(127) Lu, X.; Ye, G.; Punj, D.; Chiechi, R. C.; Orrit, M. Quantum Yield Limits for the Detection of Single-Molecule Fluorescence Enhancement by a Gold Nanorod. *ACS Photonics* **2020**, *7* (9). https://doi.org/10.1021/acsphotonics.0c00803.

(128) Devilez, A.; Stout, B.; Bonod, N. Compact Metallo-Dielectric Optical Antenna for Ultra Directional and Enhanced Radiative Emission. *ACS Nano* **2010**, *4* (6). https://doi.org/10.1021/nn100348d.

(129) Zambrana-Puyalto, X.; Bonod, N. Purcell Factor of Spherical Mie Resonators. *Phys Rev B Condens Matter Mater Phys* **2015**, *91* (19). https://doi.org/10.1103/PhysRevB.91.195422.

(130) Rolly, B.; Stout, B.; Bidault, S.; Bonod, N. Crucial Role of the Emitter–Particle Distance on the Directivity of Optical Antennas. *Opt Lett* **2011**, *36* (17), 3368. https://doi.org/10.1364/ol.36.003368.

(131) Devilez, A.; Zambrana-Puyalto, X.; Stout, B.; Bonod, N. Mimicking Localized Surface Plasmons with Dielectric Particles. *Phys Rev B Condens Matter Mater Phys* **2015**, *92* (24). https://doi.org/10.1103/PhysRevB.92.241412.

(132) Gérard, D.; Wenger, J.; Devilez, A.; Gachet, D.; Stout, B.; Bonod, N.; Popov, E.; Rigneault, H. Strong Electromagnetic Confinement near Dielectric Microspheres to Enhance Single-Molecule Fluorescence. *Opt Express* **2008**, *16* (19). https://doi.org/10.1364/oe.16.015297.

(133) Busson, M. P.; Rolly, B.; Stout, B.; Bonod, N.; Bidault, S. Accelerated Single Photon Emission from Dye Molecule-Driven Nanoantennas Assembled on DNA. *Nat Commun* **2012**, *3*. https://doi.org/10.1038/ncomms1964.

(134) Wientjes, E.; Renger, J.; Cogdell, R.; Van Hulst, N. F. Pushing the Photon Limit: Nanoantennas Increase Maximal Photon Stream and Total Photon Number. *Journal of Physical Chemistry Letters* **2016**, *7* (9), 1604–1609. https://doi.org/10.1021/acs.jpclett.6b00491.

(135) Flauraud, V.; Regmi, R.; Winkler, P. M.; Alexander, D. T. L.; Rigneault, H.; Van Hulst, N. F.; García-Parajo, M. F.; Wenger, J.; Brugger, J. In-Plane Plasmonic Antenna Arrays with Surface Nanogaps for Giant Fluorescence Enhancement. *Nano Lett* **2017**, *17* (3). https://doi.org/10.1021/acs.nanolett.6b04978.

(136) Holzmeister, P.; Pibiri, E.; Schmied, J. J.; Sen, T.; Acuna, G. P.; Tinnefeld, P. Quantum Yield and Excitation Rate of Single Molecules Close to Metallic Nanostructures. *Nat Commun* **2014**, *5*. https://doi.org/10.1038/ncomms6356.

(137) Acuna, G. P.; Bucher, M.; Stein, I. H.; Steinhauer, C.; Kuzyk, A.; Holzmeister, P.; Schreiber, R.; Moroz, A.; Stefani, F. D.; Liedl, T.; Simmel, F. C.; Tinnefeld, P. Distance Dependence of Single-Fluorophore Quenching by Gold Nanoparticles Studied on DNA Origami. *ACS Nano* **2012**, *6* (4). https://doi.org/10.1021/nn2050483.

(138) Caldarola, M.; Albella, P.; Cortés, E.; Rahmani, M.; Roschuk, T.; Grinblat, G.; Oulton, R. F.; Bragas, A. V.; Maier, S. A. Non-Plasmonic Nanoantennas for Surface Enhanced Spectroscopies with Ultra-Low Heat Conversion. *Nat Commun* **2015**, *6*. https://doi.org/10.1038/ncomms8915.

(139) Sortino, L.; Zotev, P. G.; Phillips, C. L.; Brash, A. J.; Cambiasso, J.; Marensi, E.; Fox, A. M.; Maier, S. A.; Sapienza, R.; Tartakovskii, A. I. Bright Single Photon Emitters with Enhanced Quantum Efficiency in a Two-Dimensional Semiconductor Coupled with Dielectric Nano-Antennas. *Nat Commun* **2021**, *12* (1). https://doi.org/10.1038/s41467-021-26262-3.

(140) Su, Q.; Jiang, C.; Gou, D.; Long, Y. Surface Plasmon-Assisted Fluorescence Enhancing and Quenching: From Theory to Application. *ACS Applied Bio Materials*. 2021. https://doi.org/10.1021/acsabm.1c00320.

(141) Koenderink, A. F. Single-Photon Nanoantennas. *ACS Photonics*. 2017, pp 710–722. https://doi.org/10.1021/acsphotonics.7b00061.

(142) Celebrano, M.; Kukura, P.; Renn, A.; Sandoghdar, V. Single-Molecule Imaging by Optical Absorption. *Nat Photonics* **2011**, *5* (2). https://doi.org/10.1038/nphoton.2010.290.

(143) Liu, S. Y.; Huang, L.; Li, J. F.; Wang, C.; Li, Q.; Xu, H. X.; Guo, H. L.; Meng, Z. M.; Shi, Z.; Li, Z. Y. Simultaneous Excitation and Emission Enhancement of Fluorescence Assisted by Double Plasmon Modes of Gold Nanorods. *Journal of Physical Chemistry C* **2013**, *117* (20), 10636–10642. https://doi.org/10.1021/jp4001626.

(144) Taminiau, T. H.; Moerland, R. J.; Segerink, F. B.; Kuipers, L.; Van Hulst, N. F. λ/4 Resonance of an Optical Monopole Antenna Probed by Single Molecule Fluorescence. *Nano Lett* **2007**, *7* (1). https://doi.org/10.1021/nl061726h.

(145) Knight, M. W.; Wu, Y.; Lassiter, J. B.; Nordlander, P.; Halas, N. J. Substrates Matter: Influence of an Adjacent Dielectric on an Individual Plasmonic Nanoparticle. *Nano Lett* **2009**, *9* (5). https://doi.org/10.1021/nl900945q.

(146) Gurbatov, S.; Vitrik, O.; Kulchin, Y.; Kuchmizhak, A. Mapping the Refractive Index with Single Plasmonic Nanoantenna. *Sci Rep* **2018**, *8* (1). https://doi.org/10.1038/s41598-018-21395-w.

(147) Vahala, K. J. Optical Microcavities. *Nature*. 2003. https://doi.org/10.1038/nature01939.

(148) Steiner, M.; Hartschuh, A.; Korlacki, R.; Meixner, A. J. Highly Efficient, Tunable Single Photon Source Based on Single Molecules. *Appl Phys Lett* **2007**, *90* (18). https://doi.org/10.1063/1.2736294.

(149) Zambrana-Puyalto, X.; Bonod, N. Tailoring the Chirality of Light Emission with Spherical Si-Based Antennas. *Nanoscale* **2016**, *8* (19). https://doi.org/10.1039/c6nr00676k.

(150) Kühn, S.; Sandoghdar, V. Modification of Single Molecule Fluorescence by a Scanning Probe. *Appl Phys B* **2006**, *84* (1–2). https://doi.org/10.1007/s00340-006-2233-y.

(151) Trabesinger, W.; Kramer, A.; Kreiter, M.; Hecht, B.; Wild, U. P. Single-Molecule near-Field Optical Energy Transfer Microscopy with Dielectric Tips. *J Microsc* **2003**, *209* (3), 249–253. https://doi.org/10.1046/j.1365-2818.2003.01124.x.

(152) Regmi, R.; Berthelot, J.; Winkler, P. M.; Mivelle, M.; Proust, J.; Bedu, F.; Ozerov, I.; Begou, T.; Lumeau, J.; Rigneault, H.; García-Parajó, M. F.; Bidault, S.; Wenger, J.; Bonod, N. All-Dielectric Silicon Nanogap Antennas to Enhance the Fluorescence of Single Molecules. *Nano Lett* **2016**, *16* (8). https://doi.org/10.1021/acs.nanolett.6b02076.

(153) Vaskin, A.; Mashhadi, S.; Steinert, M.; Chong, K. E.; Keene, D.; Nanz, S.; Abass, A.; Rusak, E.; Choi, D. Y.; Fernandez-Corbaton, I.; Pertsch, T.; Rockstuhl, C.; Noginov, M. A.; Kivshar, Y. S.; Neshev, D. N.; Noginova, N.; Staude, I. Manipulation of Magnetic Dipole Emission from Eu 3+ with Mie-Resonant Dielectric Metasurfaces. *Nano Lett* **2019**, *19* (2). https://doi.org/10.1021/acs.nanolett.8b04268.

(154) Kalkbrenner, T.; Håkanson, U.; Sandoghdar, V. Tomographic Plasmon Spectroscopy of a Single Gold Nanoparticle. *Nano Lett* **2004**, *4* (12). https://doi.org/10.1021/nl048694n.

(155) Gillett, A. J.; Pershin, A.; Pandya, R.; Feldmann, S.; Sneyd, A. J.; Alvertis, A. M.; Evans, E. W.; Thomas, T. H.; Cui, L. S.; Drummond, B. H.; Scholes, G. D.; Olivier, Y.; Rao, A.; Friend, R. H.; Beljonne, D. Dielectric Control of Reverse Intersystem Crossing in Thermally Activated Delayed Fluorescence Emitters. *Nat Mater* **2022**, *21* (10). https://doi.org/10.1038/s41563-022-01321-2.

(156) Mukherjee, A.; Feist, J.; Börjesson, K. Quantitative Investigation of the Rate of Intersystem Crossing in the Strong Exciton-Photon Coupling Regime. *J Am Chem Soc* **2023**, *145* (9). https://doi.org/10.1021/jacs.2c11531.

(157) Wenger, J.; Cluzel, B.; Dintinger, J.; Bonod, N.; Fehrembach, A. L.; Popov, E.; Lenne, P. F.; Ebbesen, T. W.; Rigneault, H. Radiative and Nonradiative Photokinetics Alteration inside a Single Metallic Nanometric Aperture. *Journal of Physical Chemistry C* **2007**, *111* (30). https://doi.org/10.1021/jp0726135.

(158) Widengren, J.; Mets, Ü.; Rigler, R. Fluorescence Correlation Spectroscopy of Triplet States in Solution: A Theoretical and Experimental Study. *Journal of Physical Chemistry* **1995**, *99* (36). https://doi.org/10.1021/j100036a009.

(159) Eisaman, M. D.; Fan, J.; Migdall, A.; Polyakov, S. V. Invited Review Article: Single-Photon Sources and Detectors. *Review of Scientific Instruments*. 2011. https://doi.org/10.1063/1.3610677.

(160) Bernd Sontheimer. Characterization and Utilization of Novel Solid-State Qantum Emitters, 2020.

(161) Lee, K. G. Statistical Analysis of Photons from a Single Terrylene Molecule for the Study of the Energy Level Scheme. *Journal of the Korean Physical Society* **2014**, *64* (12). https://doi.org/10.3938/jkps.64.1792.

(162) Widengren, J.; Rigler, R.; Mets, Ü. Triplet-State Monitoring by Fluorescence Correlation Spectroscopy. *J Fluoresc* **1994**, *4* (3). https://doi.org/10.1007/BF01878460.

(163) Blom, H.; Chmyrov, A.; Hassler, K.; Davis, L. M.; Widengren, J. Triplet-State Investigations of Fluorescent Dyes at Dielectric Interfaces Using Total Internal Reflection Fluorescence Correlation Spectroscopy. *Journal of Physical Chemistry A* **2009**, *113* (19). https://doi.org/10.1021/jp8110088.

(164) Berthel, M.; Mollet, O.; Dantelle, G.; Gacoin, T.; Huant, S.; Drezet, A. Photophysics of Single Nitrogen-Vacancy Centers in Diamond Nanocrystals. *Phys Rev B Condens Matter Mater Phys* **2015**, *91* (3). https://doi.org/10.1103/PhysRevB.91.035308.

(165) Reynaud, S. La Fluorescence de Résonance : Etude Par La Méthode de l'atome Habillé. *Ann Phys (Paris)* **1983**, *8*, 315–370. https://doi.org/10.1051/anphys/198308080315.

(166) Kurtsiefer, C.; Mayer, S.; Zarda, P.; Weinfurter, H. Stable Solid-State Source of Single Photons. *Phys Rev Lett* **2000**, *85* (2), 290–293. https://doi.org/10.1103/PhysRevLett.85.290.

(167) Giessibl, F. J. Advances in Atomic Force Microscopy. *Reviews of Modern Physics*. 2003. https://doi.org/10.1103/RevModPhys.75.949.

(168) Giessibl, F. J. Forces and Frequency Shifts in Atomic-Resolution Dynamic-Force Microscopy. *Phys Rev B Condens Matter Mater Phys* **1997**, *56* (24). https://doi.org/10.1103/PhysRevB.56.16010.

(169) Dagdeviren, O. E.; Miyahara, Y.; Mascaro, A.; Grütter, P. Calibration of the Oscillation Amplitude of Electrically Excited Scanning Probe Microscopy Sensors. *Review of Scientific Instruments* **2019**, *90* (1). https://doi.org/10.1063/1.5061831.

(170) Qin, Y.; Reifenberger, R. Calibrating a Tuning Fork for Use as a Scanning Probe Microscope Force Sensor. *Review of Scientific Instruments* **2007**, *78* (6). https://doi.org/10.1063/1.2743166.

(171) Nanonis, G. Piezoelectric Quartz Tuning Forks for Scanning Probe Microscopy. In *Nanonis GmbH*; 2005.

(172) Beveratos, A.; Kühn, S.; Brouri, R.; Gacoin, T.; Poizat, J. P.; Grangier, P. Room Temperature Stable Single-Photon Source. In *European Physical Journal D*; 2002; Vol. 18. https://doi.org/10.1140/epjd/e20020023.

(173) Beveratos, A.; Brouri, R.; Gacoin, T.; Poizat, J. P.; Grangier, P. Nonclassical Radiation from Diamond Nanocrystals. *Phys Rev A* **2001**, *64* (6). https://doi.org/10.1103/PhysRevA.64.061802.

(174) Boens, N.; Qin, W.; Basarić, N.; Hofkens, J.; Ameloot, M.; Pouget, J.; Lefèvre, J. P.; Valeur, B.; Gratton, E.; VandeVen, M.; Silva, N. D.; Engelborghs, Y.; Willaert, K.; Sillen, A.; Rumbles, G.; Phillips, D.; Visser, A. J. W. G.; Van Hoek, A.; Lakowicz, J. R.; Malak, H.; Gryczynski, I.; Szabo, A. G.; Krajcarski, D. T.; Tamai, N.; Miura, A. Fluorescence Lifetime Standards for Time and Frequency Domain Fluorescence Spectroscopy. *Anal Chem* **2007**, *79* (5). https://doi.org/10.1021/ac062160k.

(175) Basché, T.; Kummer, S.; Bräuchle, C. Direct Spectroscopic Observation of Quantum Jumps of a Single Molecule. *Nature*. January 12, 1995, pp 132–134. https://doi.org/10.1038/373132a0.

(176) Johnson, T. W.; Lapin, Z. J.; Beams, R.; Lindquist, N. C.; Rodrigo, S. G.; Novotny, L.; Oh, S. H. Highly Reproducible Near-Field Optical Imaging with Sub-20-Nm Resolution Based on Template-Stripped Gold Pyramids. *ACS Nano* **2012**, *6* (10), 9168–9174. https://doi.org/10.1021/nn303496g.

(177) Cruz-López, C. A.; Espinosa-Paredes, G. Fractional Radioactive Decay Law and Bateman Equations. *Nuclear Engineering and Technology* **2022**, *54* (1). https://doi.org/10.1016/j.net.2021.07.026.

(178) Verberk, R.; Orrit, M. Photon Statistics in the Fluorescence of Single Molecules and Nanocrystals: Correlation Functions versus Distributions of on- and off-Times. *Journal of Chemical Physics* **2003**, *119* (4). https://doi.org/10.1063/1.1582848.

(179) Caldwell, R. A.; Jacobs, L. D.; Nalley, E. A.; Laboy, J.; Furlani, T. R.; Nalley, E. A. Conformationally Dependent Heavy Atom Effect of Chlorine on Alkene Triplet Lifetimes. Experimental and Ab Initio Calculations. *J Am Chem Soc* **1992**, *114* (5). https://doi.org/10.1021/ja00031a013.

(180) Müller, A.; Richter, W.; Kador, L. Pressure Effects on Single Molecules of Terrylene in P-Terphenyl. *Chem Phys Lett* **1995**, *241* (5–6), 547–554. https://doi.org/10.1016/0009-2614(95)00670-Y.

(181) Kulzer, F. Nonphotochemical Hole Burning Investigated at the Single-Molecule Level: Stark Effect Measurements on the Original and Photoproduct State. *Journal of Physical Chemistry A* **1999**, *103* (14). https://doi.org/10.1021/jp9839448.

(182) Bauer, M.; Kador, L. Zeeman Effect of Single-Molecule Lines. *Chem Phys Lett* **2005**, *407* (4–6). https://doi.org/10.1016/j.cplett.2005.03.131.

(183) Axelrod, D. Fluorescence Excitation and Imaging of Single Molecules near Dielectric-Coated and Bare Surfaces: A Theoretical Study. *J Microsc* **2012**, *247* (2). https://doi.org/10.1111/j.1365-2818.2012.03625.x.

(184) Born, M.; Wolf, E. Principles of Optics: 60th Anniversary Edition. *Principles of Optics* **2019**.

(185) Lola Chamot. Contrôle de La Fluorescence d'une Molécule Unique Par Une Nano-Antenne Optique, Sciences Sorbonne Universite, 2023.

Publications and scientific contributions

Peer-reviewed articles:

Trojanowicz, R.; Douillard, L.; Sosa-Vargas, L.; Charra, F.; Vassant, S. "Photophysical characterization of single Terrylene molecules in a thin para-terphenyl film: rates and full orientation using triplet-triplet absorption" (in submission)

Fabre, N.; Trojanowicz, R.; Moreaud, L.; Fiorini-Debuisschert, C.; Vassant, S.; Charra, F. '' Structure and photonic properties of a perylenediimide monolayer assembled by the Langmuir-Blodgett technique'', Langmuir **2023** 39 (50), 18252-18262. https://doi.org/10.1021/acs.langmuir.3c02038

Oral presentations at conferences:

Trojanowicz, R. ''Dielectric tip influence on the rates of a single molecule'', European Optical Society Annual Meeting, Dijon, France, 2023.

Trojanowicz, R. ''Structure and photonic properties of a perylenediimide monolayer assembled by the Langmuir-Blodgett technique'', NANOP, Barcelona, Spain, 2023.

Poster presentations at conferences:

Trojanowicz, R. ''Enhancement of a single molecule triplet depopulation rate by a dielectric nanoantenna'', META, Paris, France, 2023.